université PARIS-SACLAY

Hydrogen production by anoxic corrosion of steel under gamma radiation

-

Etude de la production d'hydrogène par corrosion anoxique des aciers sous rayonnement gamma

Thèse de doctorat de l'université Paris-Saclay

École doctorale n° 571: Sciences chimiques: molécules, matériaux, instrumentation et biosystèmes (2MIB)
Spécialité de doctorat : Chimie
Graduate School : Chimie. Référent : Faculté des sciences d'Orsay

Thèse préparée dans les unités de recherche **LIDYL** (Université Paris-Saclay, CEA, CNRS) et **LECEV** (IRSN), sous la direction de **Gérard BALDACCHINO**, Directeur de Recherche CEA, le co-encadrement de **Charles WITTEBROODT**, Docteur (IRSN), et le co-encadrement d' **Hortense DESJONQUERES**, Ingénieure-chercheure (IRSN)

Thèse soutenue à Paris-Saclay, le 30 mars 2022, par

Stavroula-Isidora GIANNAKANDROPOULOU

Composition du Jury

Mehran MOSTAFAVI Professeur, Université Paris-Saclay, France	Président
Nathalie MONCOFFRE Directrice de Recherche CNRS, IP2I Lyon, France	Rapporteure & Examinatrice
Mats JONSSON Professeur, KTH, Stockolm, Suède	Rapporteur & Examinateur
Barbara PASTINA Docteur, Posiva, Finlande	Examinatrice
Philippe REFAIT Professeur, La Rochelle Université, France	Examinateur
Gérard BALDACCHINO Directeur de Recherche CEA, CEA Paris-Saclay, France	Directeur de thèse

THESE DE DOCTORAT

NNT : 2022UPASF028

université PARIS-SACLAY

ÉCOLE DOCTORALE
Sciences Chimiques : Molécules, Matériaux, Instrumentation et Biosystèmes (2MIB)

Titre : Etude de la production d'hydrogène par corrosion anoxique des aciers sous rayonnement gamma

Mots clés : Acier carboné, corrosion anoxique, irradiation gamma, radiolyse de l'eau, hydrogène gazeux

Résumé : Ces travaux de thèse sont consacrés à l'étude des effets que les rayonnements gamma peuvent avoir sur le processus de corrosion anoxique de l'acier carbone et sur la production d'hydrogène qui en découle. Le concept de multi-barrières, associé au projet français de site de stockage géologique des déchets HA-MAVL, implique l'utilisation de grande quantité d'éléments métalliques. Ces éléments métalliques, exposés aux rayonnements ionisants provenant des déchets radioactifs, vont être progressivement soumis à un phénomène de corrosion anoxique sous irradiation. Parallèlement aux probables modifications des processus de corrosion liées à la néoformation des espèces radiolytiques, les phénomènes de corrosion anoxique et de radiolyse de l'eau produisent ensemble de l'hydrogène gazeux dont l'accumulation pourrait affecter sensiblement la sûreté de l'installation de stockage à moyen-long terme.

Afin de contribuer à l'évaluation de sûreté à long terme d'une telle installation souterraine, cette étude a pour objectif de développer un dispositif expérimental permettant de distinguer la production d'hydrogène provenant de la radiolyse de l'eau de celle associée à la corrosion anoxique. La mesure en continu des productions d'hydrogène correspondant à trois étapes importantes (la pré-irradiation, l'irradiation et la post-irradiation) nous a permis d'estimer l'évolution de la vitesse de corrosion se produisant avant, pendant et après l'irradiation gamma pour des échantillons d'acier carboné immergés dans différentes solutions.

Les résultats obtenus, associés aux caractérisations post mortem des échantillons liquide et solide correspondant indiquent que : (i) la présence de soluté et/ou d'un pH élevé entraîne une diminution de la production d'hydrogène radiolytique, (ii) la composition chimique initiale de la solution à un impact direct sur les vitesses de corrosion mesurées avant irradiation, (iii) les rayonnements gamma n'entraînent pas d'augmentation significative de la vitesse de corrosion, (iv) la dégradation progressive de la couche de magnétite, causée par les variations des conditions redox induites par les espèces radiolytiques néoformées, peut engendrer des modifications structurales pouvant impacter à la fois la croissance et les propriétés de passivation associées à l'évolution moyen-long terme d'un film d'oxyde formé sur la surface métallique et (v) la modélisation peut aider à prédire l'évolution des concentrations de certaines espèces radiolytiques clefs susceptibles d'impacter le processus de corrosion anoxique sous irradiation.

université PARIS-SACLAY

ÉCOLE DOCTORALE
Sciences Chimiques : Molécules, Matériaux, Instrumentation et Biosystèmes (2MIB)

Title : Hydrogen production by anoxic corrosion of steel under gamma radiation

Keywords : Carbon steel, anoxic corrosion, gamma radiation, water radiolysis, hydrogen gas

Abstract : The present thesis work reports an investigation of the impact of gamma radiation on carbon steel anoxic corrosion process and the resultant hydrogen gas production. The multi-barriers concept associated to the French HL-ILW waste deep geological disposal project implies the use of large amount of metallic elements. These metallic elements, exposed to ionizing radiations originating from nuclear waste, will be progressively submitted to anoxic corrosion under irradiation processes. In addition to the fact that neoformed radiolytic species are prone to modify the corrosion processes, both anoxic corrosion and water radiolysis phenomena generate hydrogen gas whose accumulation may significantly affect mid- and long-term safety of the disposal facility.

To contribute to the long-term safety assessment of such underground installation, this work aimed to develop an experimental setup allowing to distinguish between the H_2 production related to water radiolysis and the one related to anoxic corrosion. By measuring continuously the hydrogen gas production corresponding to three important stages (pre-irradiation, irradiation and post-irradiation phases), we were able to estimate corrosion rate values evolution occurring before, during and after gamma-irradiation for carbon steel samples immersed in different solutions.

The obtained experimental results, associated to the corresponding liquid and solid samples post mortem characterisations, indicate that: (i) both the presence of solute and/or higher pH conditions induce a decrease of radiolytic hydrogen production, (ii) initial chemical composition of the solution impacts directly the pre-irradiation phase corrosion rate values, (iii) gamma radiation does not induce any significant increase of the corrosion rate values, (iv) progressive alteration of magnetite layer caused by radiolytic induced redox variations could cause structural modifications that may impact both growth and passivating properties associated to mid and long term evolution of the oxide film formed on the metallic surface and (v) modelling can help to predict the concentration evolution associated to key radiolytic species prone to impact anoxic corrosion under irradiation processes.

Résumé étendu en français

En France, la gestion des déchets radioactifs est prise en charge par l'Andra (Agence Nationale des Déchets Radioactifs). Le projet Cigeo propose de stocker les déchets de haute activité et les déchets de moyenne activité à vie longue (HAVL et MAVL respectivement) en couche géologique profonde. Son objectif principal est la protection de l'environnement et de la biosphère. Or, les déchets HAVL contiennent des radioisotopes ayant des durées de vie longues les rendant radiotoxiques pendant des centaines de milliers d'années. De plus, ces déchets, qui proviennent pour la plupart du traitement des combustibles des centrales nucléaires, présentent des radionucléides en concentrations élevées ce qui nécessite leur stockage en milieu confiné. Pour cette raison, un concept de multi-barrières dont l'objectif est de s'opposer à la dispersion des polluants radioactifs dans l'environnement est privilégié. Ainsi, pour les déchets HAVL, la matrice vitreuse contenant les déchets est coulée dans des conteneurs en acier inoxydable. Ces conteneurs sont ensuite incorporés dans des sur-conteneurs en acier au carbone et ces sur-conteneurs sont enfin placés dans des alvéoles de stockage équipées d'un chemisage en acier au carbone. Depuis 2014, l'Andra envisage d'injecter un coulis ciment-bentonite dans l'espace entre le chemisage métallique et la roche pour éviter une augmentation de la vitesse de corrosion du chemisage au contact de l'argilite.

Pendant la phase d'exploitation du site de stockage et pendant les premières années suivant sa fermeture, les sur-conteneurs ainsi que le chemisage des alvéoles subiront une première dégradation en présence d'oxygène (corrosion en conditions oxiques). Après une période de plusieurs dizaines d'années suivant la fermeture du site de stockage, l'oxygène aura complètement disparu et les éléments métalliques subiront une deuxième phase de dégradation (corrosion en conditions anoxiques). Dans ces conditions la corrosion anoxique va entrainer la libération d'hydrogène en phase gazeuse et la dissolution de fer ionique en solution.

En parallèle, les déchets radioactifs émettront des rayonnements ionisants qui vont provoquer le processus de radiolyse de l'eau se trouvant en champ proche des alvéoles de stockage, et ainsi créer des espèces radiolytiques. Leur formation est gouvernée par un paramètre, le rendement radiolytique qui est défini comme le rapport du nombre d'espèces formées sur la quantité d'énergie déposée par la particule ionisante. L'une des espèces radiolytiques moléculaires est l'hydrogène.

Ainsi, les phénomènes de corrosion anoxique et de radiolyse de l'eau vont entrainer une production d'hydrogène gazeux au sein de l'installation de stockage. Cette production d'hydrogène engendre différents problèmes de sûreté du fait de son accumulation. L'un d'eux est lié au caractère inflammable et explosif de l'hydrogène pendant la phase d'exploitation. Un autre aspect pénalisant lié à cette production d'H_2 pendant la phase post-fermeture, est le

phénomène de surpression capable de retarder et/ou de limiter la re-saturation des noyaux de scellement en bentonite, créant ainsi des chemins préférentiels pour la migration des radionucléides. Par conséquent, il est nécessaire d'obtenir l'épaisseur appropriée du chemisage en acier au carbone pour faire face à une éventuelle surpression, ce qui assurera une protection suffisante de l'installation. Pour cette raison, il est crucial d'étudier la vitesse de corrosion de l'acier au carbone en présence d'irradiation dans des conditions anoxiques.

Les travaux de cette thèse vise à donner de nouvelles données expérimentales relatives à l'évolution de la production d'hydrogène en conditions anoxiques : la corrosion pure, la corrosion radiolytique et la corrosion post-irradiation. Pour ces trois phases, la production d'hydrogène est régie par différents mécanismes et est fonction de paramètres tels que la température, les conditions physico-chimiques du milieu aqueux, le Transfert d'Energie Linéique (TEL) ou encore le débit de dose des rayons ionisants. L'approche expérimentale suivie pour étudier cette problématique est d'irradier en conditions anoxiques avec des rayonnements gamma deux systèmes : le premier contenant une solution aqueuse désaérée et des échantillons d'acier carbone et le second uniquement une solution aqueuse désaérée. Ceci nous permettra de distinguer l'hydrogène moléculaire produit provenant exclusivement de la radiolyse de l'eau et celui produit par les processus de corrosion anoxique. Cette dernière distinction nous permet d'estimer la vitesse de corrosion pour les trois phases successives testées (pré-irradiation, pendant l'irradiation, post-irradiation) et nous aide à conclure sur l'impact des rayonnements ionisants sur la corrosion anoxique de l'acier. Les essais sont réalisés en utilisant l'irradiateur expérimental IRMA (^{60}Co) de l'IRSN à Saclay, en utilisant différents types de solutions afin de tester en parallèle l'impact de la présence de solutés et de l'alcalinité sur le processus de corrosion sous irradiation. En outre, des analyses post mortem sont effectuées sur la surface des échantillons métalliques pour identifier les produits de corrosion néoformés, et les caractéristiques chimiques de la solution sont déterminées. Enfin, pour comprendre les cinétiques des systèmes, les simulations complètent ce travail dans le but d'expliquer les données expérimentales.

Les résultats obtenus, indiquent que notre approche expérimentale a permis l'acquisition d'une grande quantité de données. Les essais en utilisant des solutions complexes représentatives des eaux de l'environnement du lieu de stockage montrent que la présence de solutés ou d'un pH plus élevé peut donner lieu à une diminution de la production d'hydrogène sous irradiation. En plus, la production d'hydrogène gazeux n'implique pas une augmentation significative des vitesses de corrosion sous rayonnement gamma en utilisant des solutions avec un pH entre 6.5 - 8.2. Cependant, les vitesses de corrosion obtenues après irradiation sont légèrement supérieures à celles de la phase de pré-irradiation. Ceci pourrait signifier que la couche de magnétite formée sous les surfaces métalliques est progressivement dégradée par la présence

d’espèces radiolytiques, en impliquant éventuellement des altérations structurelles, susceptibles de modifier les propriétés à moyen et long terme de la couche de corrosion. Ceci pourrait impacter les propriétés de passivation du métal.

Enfin, la modélisation des espèces radiolytiques semble être en bon accord avec la majorité de nos résultats expérimentaux, nous faisant conclure que ce travail de modélisation pourrait aider à prédire l’évolution de certaines espèces radiolytiques susceptibles d’impacter le processus de corrosion anoxique sous irradiation.

Acknowledgements

First of all, I would like to thank Mehran Mostafavi (President), Barbara Pastina and Philippe Refait for accepting the invitation to be examiners and members of the jury for this PhD thesis, as well as Nathalie Moncoffre and Mats Jonsson for being in addition reviewers of this work.

I would also like to express my sincere thanks to my thesis director, Gerard Baldacchino for giving me the opportunity to work with him, for supervising my work and for helping me with the simulation work that I have performed. His guidance including our useful discussions, with exceptional pedagogy, allowed me to complete this work.

Furthermore, I would like to thank Hortense Desjonqueres, for co-supervising my work in IRMA installation at Saclay. Her presence was important to resolve a lot of technical problems that we faced during these three years.

Moreover, I would like to thank my supervisor Charles Wittebroodt, for being by my side from the very beginning of this journey. His advices throughout all the process of conducting my study was essential to the present work. Despite the difficulties we encountered due to the sanitary crisis, he was always there and available to discuss and listen to my concerns regarding my research, even by distance, and this was enough to encourage me all this time.

Furthermore, it is important to mention people who contributed to the obtained results of this thesis. Starting with the structural characterization of the solid samples that has been performed, I would like to thank Michel Schlegel for his contribution. In addition, concerning the analyzes of the liquid samples, I would like to deeply thank Gilles, Olivier and Cyrielle for their help at the LETIS laboratory at Fontenay aux Roses. Also, I would like to thank from LECEV laboratory at Saclay, Stephane and Benoit for their help into IRMA installation.

Lastly, I want to thank my family for encouraging me in every decision that I made. I am grateful for all the support that I have received, especially during this thesis.

.

Στον παππού μου Νίκο

Table of Contents

Introduction

Deep geological disposal of high-level radioactive waste (HLW) is foreseen by several countries to protect living organisms from long-term radioactive contamination. In France, according to the multi-barrier concept developed by Andra (French radioactive waste management agency), HLW would be embedded in a glass matrix cooled in a stainless-steel container. This package would be then encapsulated into cylindrical carbon steel overpack and inserted in a carbon steel casing tube within horizontal micro-tunnel drilled in the highly impermeable Callovo-Oxfordian (COx) clay rock of the Paris Basin [1, 2]. If carbon steel casing should ensure adequate mechanical function over a century to allow the nuclear waste to be retrieved from the deep geological disposal concept, carbon steel overpack must remain leakproof for a few thousand years to prevent porewater seeping from the clay formation from reaching the vitrified waste during the thermal phase. Throughout the duration of the operational phase of the project and long after the closure of the disposal facility, several corrosion processes are expected. They could occur in a series of distinct environments: in oxic or anoxic conditions, in contact with liquid or vapour phase porewater, in contact with evolutive chemistry porewater. These conditions will gradually impair the carbon steel component and finally induce its breakage. Predominant over the long term, carbon steel anoxic corrosion process will progressively attack the metallic elements, iron interacting with water to produce ferrous hydroxide ($Fe(OH)_2$) and hydrogen gas (H_2). Under these conditions, corrosion rate values should progressively decrease from 10 to 0.1 $\mu m.year^{-1}$ thanks to the gradual formation of a protective corrosion product layer on the metallic surface [2, 3].

In addition, it is noteworthy that all these corrosion processes will take place on carbon steel component exposed to ionizing radiations originating from nuclear waste. These radiations will lead to the radiolysis of percolated porewater which forms radiolytic species such as radicals (e_{aq}^-, $H^\bullet$, $^\bullet OH$), molecular products (H_2O_2, H_2) and ionic species (H_3O^+) [4]. These chemical species, whose concentrations are radiation parameters dependent (energy, LET, dose rate), are prone to modify the physico-chemical conditions at the metal-water interface, and thus, to impact the corrosion processes and the associated corrosion rate. Furthermore, these formed radiolytic species include H_2, meaning that porewater radiolysis will also lead to an additional production of hydrogen gas. Accumulation of H_2 gas may significantly affect mid- and long-term safety of the disposal facility. On the one hand, its highly flammable and explosive properties represent a risk during the operational phase. On the other hand, the consequent overpressure is liable to either lead to incomplete saturation of bentonite sealing plugs or to create the formation of preferential pathway enhancing the radionuclides migration through disposal installation.

Therefore, to contribute to the long-term safety assessment of such deep geological disposal, dedicated research programs have been committed to study steel corrosion under irradiation and the associated hydrogen gas production. The various experimental techniques that have been used to measure uniform corrosion rates can be grouped as follow: weight loss measurements, hydrogen gas production monitoring and electrochemical measurements. While a range of individual studies has been performed to understand the impact of several parameters such as the dose rate (or total dose), the temperature or the physico-chemical properties of the solution, the observed effects of ionizing radiation on steel corrosion are still conflicting. Even though, most studies demonstrate that carbon steel corrosion rate is enhanced by radiation exposure, some others tend to indicate the contrary. In parallel, while a large majority of the works cited above agreed on the fact that magnetite (Fe_3O_4) is the predominant corrosion product which is form under such experimental conditions, many key questions regarding the mid- and long-term evolution of this oxide film properties, induced by the physico-chemical modifications of the solution caused by irradiation, remain unanswered.

The primary motivation of this thesis work is to investigate the impact of gamma radiation on carbon steel anoxic corrosion processes in order to (i) quantify the H_2 production and (ii) estimate the associated corrosion rate allowing an accurate dimensioning of the metallic elements. While almost all studies dealing with the impact of ionizing radiations on steel corrosion processes have been performed in closed systems, the present work is meant to get closer to the real disposal conditions by working in a semi-open system. This experimental setup allows to distinguish between the H_2 production related to water radiolysis and the one related to anoxic corrosion, making possible the estimation of associated corrosion rate. Finally, *post mortem* analyses are performed on the metallic samples surface to identify neoformed corrosion products, and chemical characteristics of the solution are determined. In parallel, obtained experimental data are compared to simulated results arising from modelling exercises.

This thesis is organised into six chapters. The first chapter recalls the general context of French radioactive waste management in which this study takes place. The second chapter states a bibliographic review focusing firstly on the different corrosion processes that should take place in an underground disposal facility. Thereafter, the whole water radiolysis phenomenon is described by introducing the main reactions involved, the associated neoformed radiolytic species and also the factors that can impact their radiolytic yields. Finally, studies that combine the two parallel phenomena, i.e., effect of water radiolysis on carbon steel corrosion systems under anoxic conditions, are discussed. The third chapter is dedicated to a general presentation of our experimental approach, including the description of the original experimental setup that we used to monitor H_2 production evolution and also the presentation of the analytical tools used for samples *post mortem* characterisation. The associated experimental results are

extensively presented in the fourth chapter. The fifth chapter presents the simulation results that have been obtained in parallel to be compared to the experimental ones. Finally, chapter six is dedicated to a detailed discussion of the experimental data, which allows to highlight several tendencies and to propose some mechanisms that should take place under the different examined conditions.

References

[1] D. G. Bennett and R. Gens, "Overview of European concepts for high-level waste and spent fuel disposal with special reference waste container corrosion," J. Nucl. Mater., vol. 379, no. 1–3, pp. 1–8, 2008.

[2] Andra, "Referentiel du site Meuse/Haute-Marne, Présentation Générale," Rap. C.RP.ADS.04.0022, Andra, Chatenay-Malabry, France, 2005.

[3] D. Crusset, V. Deydier, S. Necib, J. M. Gras, P. Combrade, D. Feron, E. Burger, "Corrosion of carbon steel components in the French high-level waste programme: evolution of disposal concept and selection of materials," Corros. Eng. Sci. Technol., vol. 2782, pp. 17–24, 2017.

[4] Y. Hatano, Y. Katsumura, and A. Mozumder, "Charged Particle and Photon Interactions with Matter," CRC Press, 2010.

Chapter 1: General Context

1.1 The radioactive waste

1.1.1 Origin and classification of radioactive waste

Since its discovery over a century ago, radioactivity has been used in various fields such as energy production, military or medical applications and research activities. Because of nucleus transformation of radioactive isotopes generate waste materials that need specific treatment to protect mankind and the environment from the harmful effects of radioactivity. Radioactive substances are considered as radioactive waste when no other use is planned or envisaged for them. We define for each radioactive isotope a period (or half-life) which is the time required for the disintegration of 50% of the quantity initially present. This gradual decrease in radioactivity is called radioactive decay.

There are three types of radiation:

i) Alpha rays (α): emission of particles composed of poorly penetrating helium atom nuclei (with a range in the air about a few centimeters). This energy is in the order of MeV.

ii) Beta rays (β): electrons that penetrate several meters in the air with an energy range at tens of keV.

iii) Gamma rays (γ): electromagnetic radiation having about MeV energy, can penetrate much more (several centimeters of lead or several decimeters of concrete are needed to sufficiently attenuate it).

The ionizing radiation emitted by short-lived (or intermediate) radionuclides mainly consists of β particles and γ photons, while those emitted by long-lived radionuclides include mainly α particles (Andra, 2005a).

Radioactive wastes are classified according to their activity (very low, low, intermediate, and high), i.e., the intensity of the radiation emitted, and the decay period of the main radionuclides they contain. This allows the duration estimation of their harmful activity. An initial distinction is made between short-lived radioactive waste (Low/Intermediate level) and long-lived waste (Low/Intermediate/High level). There are also very short-lived waste (half-life less than 100 days). Wastes are thus classified into 6 categories (Andra, 2020b):

i) Very Short-Lived Waste (VSLW) with a half-life less than 100 days. There is no specific storage for this type of waste as they remain radioactive for a very short

time. They are stored on site for a few days or months, while their radioactivity decreases sufficiently. Then they join a conventional waste management system (Figure 1.1.1).

ii) Very Low-Level Short-Lived Waste (VLLW) with an activity of less than 100 Becquerels per gram, are very slightly contaminated. They result from dismantling/operation of nuclear installations or conventional industries using naturally radioactive materials or can also come from rehabilitation of old sites polluted by radioactivity.

iii) Low and Intermediate-Level Short-Lived Waste (LILW-SL) are mainly small equipment contaminated during maintenances and operation of nuclear facilities. These wastes mostly contain radionuclides with half-life of less than 31 years and arise from research laboratories, hospitals, and universities. However, LILW-SL wastes may also contain long-lived radionuclides in very small quantities. A LILW-SL waste package is made up of 15-20% radioactive waste and 80 to 85% coating material in order to confine the radioactivity inside the package. They are stored at Andra's Aube storage center (CSA) in France.

iv) Low-Level Long-Lived Waste (LLW-LL); Long-lived low-level waste are essentially old waste. Different types of waste are grouped together, such as so-called "radium-bearing" waste, resulting mainly from the use of slightly radioactive ores, or "graphite" waste, coming from the first generations of nuclear power plants in operation in the 1960s (Natural Uranium Graphite Gas).

v) Intermediate-Level Long-Lived Waste (ILW-LL); is mainly produced by the nuclear power industry and research centers. They cover a wide variety of objects, mainly metallic objects (sheaths, shells, caps), but there are also inorganic and organic (plastics, cellulose, etc.) compounds. Their β-γ activity is low or medium, so they have little or no thermal release. Although, their content in long-lived radioactive elements justifies containment of very long lasting. According to their nature, they are conditioned in bitumen, in concrete or by compaction (for shells and end caps and technological waste). Wastes are placed in concrete or steel containers (Andra, 2005a; Andra, 2005e).

vi) High-Level Waste (HLW) with an activity of the order of several billion Becquerels per gram. Most of these wastes come from the nuclear power industry

and related research activities as well as, in a smaller extent, from national defence activities. They mainly consist of non-recoverable substances resulting from the reprocessing of spent fuel. Most of them are incorporated into glass and then packaged in stainless steel containers. Due to their high radioactivity, these wastes have an important thermal release (Andra, 2005a). Thus, deep geological disposal is necessary to store certain types of waste such as HLW and ILW-LL which are produced mainly by the nuclear energy sector. Figure 1.1.1 gathers all these categories and the adopted solutions for their treatment.

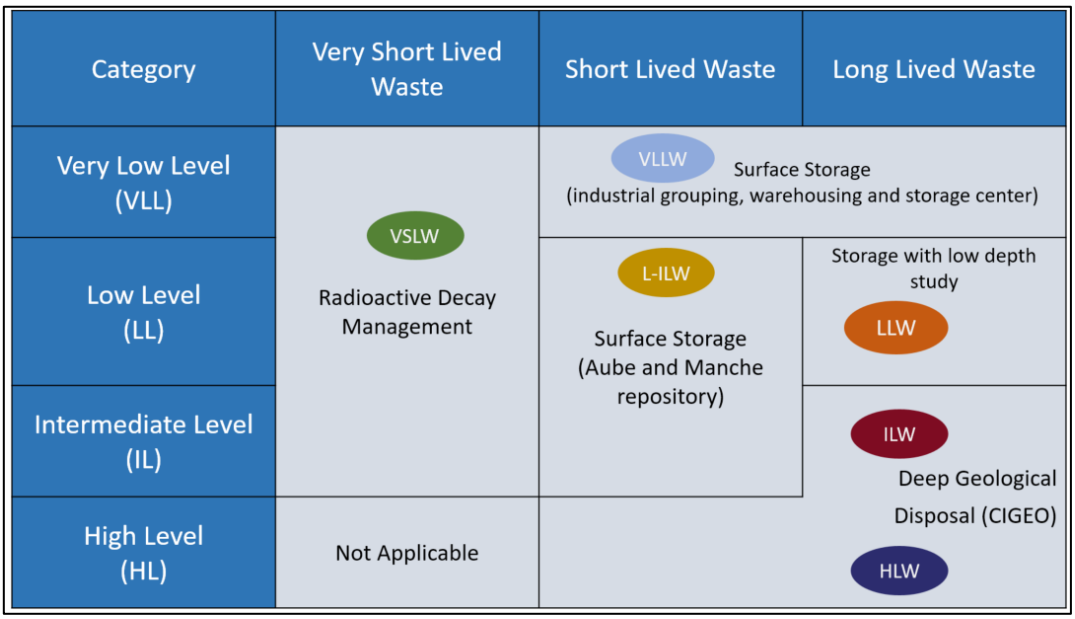

Figure 1.1.1: Classification of the waste against their nuclear activity (Andra, 2020b)

1.1.2 Pre-existing storage situation

Until the early 1960s, the volume of radioactive wastes was remaining relatively low. They remained under the responsibility of industries; they were kept on the site of their production. However, the development of the nuclear industry and associated research makes an inevitable increase of the waste volume. The authorities quickly became aware of the situation: anticipating the management of present and especially future waste became a necessity. Immersion of radioactive waste at sea was practiced by several countries. It was considered by the international scientific community as an appropriate solution, that the marine environment provided sufficient assurance in terms of dilution and isolation time of radioactivity. In 1967 and 1969, France took part in this plan, although, it was decided that immersion wouldn't

remain the management solution and these were the only participations on sea immersion storage. This decision is based on the idea of isolation of waste in deep geological disposal (Andra, 2020b). The national agency for the management of Radioactive waste (ANDRA) was created in 1979 after government demand to the French Atomic Energy Commission (CEA), to create an organization within it that will take the management of all this waste under its direct responsibility. Using the law of 1991, the Parliament registered the French policy in a prospect of search for long term and safe solutions for the radioactive waste. The vast majority of these waste benefit from solutions that are already operational as almost 90% of the total volume of radioactive waste produced each year in France are today stored in centers of Andra. High Level (HLW) and Intermediate Level Long-Lived (ILW-LL) waste cannot be stored for long time period in facilities located at the surface or at shallow depth. Therefore, in 2005, Andra proposed the construction of a deep geological disposal facility for high-level waste and intermediate-level long-lived waste, as the only solution capable of ensuring the long-term safety of this radioactive waste, while limiting the burdens weighing on future generations. This was a major step forward for radioactive waste management in France. The following year, the law of June 28th instructed Andra to design and install Cigeo (Centre Industriel de stockage GEOologique). If its creation is authorized, Cigeo will be located in eastern France, at the border of the departments of Meuse and Haute-Marne (Andra, 2005d).

1.2 Deep geological disposal of radioactive waste

1.2.1 The Cigeo project

The Cigeo geological disposal facility designed by Andra must enable HL and IL-LL waste packages to be disposed of and potentially retrieved over a period of at least 100 years (‘reversibility’ requirement) and ensure that radioelements are fully confined for several centuries. If agreed, the future deep geological disposal will be built in Grand-Est region, within the departments of Meuse and Haute-Marne (Andra, 2020a).

This project will have to take in charge of HL and IL-LL wastes that already exist as well as those which will inevitably be produced. Pending the commissioning of Cigeo, the HL and IL-LL waste packages already produced are temporary stored in constructions on their production site, mainly in La Hague (Manche), Marcoule (Gard), Cadarache (Bouches-du-Rhône) and Valduc (Côte-d´Or) (Andra, 2013).

This deep geological disposal facility consists of placing the radioactive waste packages into profound constructions at a depth about 500m, expecting to cover an underground area of 29 km^2. This depth will permit their isolation without generating important operational and geomechanical limitations (Andra, 2020a).

The high-level waste disposal will meet various requirements levels at different stages of the disposal facility lifetime. Initially, a metallic overpack, containing the stainless-steel primary canister, and secondly, a metallic liner, which must enable waste packages to be disposed of and potentially removed during the reversibility period. Furthermore, the rock hosting the deep geological disposal facility is of great importance, acting as a final protection barrier. For this reason, the deep geological disposal facility will be built in the Callovo-Oxfordian claystone layer (about 130 m thickness and 155 million years old) as a result of its favourable properties to ensure an efficient confinement of the radioactive waste.These argillaceous formations are characterized by very low permeability (order of 10^{-13} m/s), very slow water circulation, low porosity (depending on the content of carbonates 14%-19.5%) and with porous size lower than 1μm. Moreover, the argillaceous minerals are composed of microscopic crystals, electrically charged in their surface, permitting high retention capacity of positively charged radio-elements possibly released from the facility (Andra 2005d).

High Level Waste (HLW) disposal cell

Due to their significant radioactivity levels, High Level Waste (HLW) require specific treatment in order to ensure their efficient confinement. They represent about 1% by volume of total radioactive waste and they correspond to materials contained in solutions resulting from the treatment of spent fuels in COGEMA plants.

Their high β-γ rays activity induces a significant thermal release which decreases over time, mainly with the radioactive decay of the products of medium fission period (^{137}Cs, ^{90}Sr). They are incorporated into a borosilicate glass matrix with a containment capacity particularly high and durable (several hundred thousand years). Radionuclides are thus distributed homogeneously in the vitreous matrix. These vitrified wastes are poured into stainless steel packages to form the primary canister of vitrified waste. The primary canisters are placed in a carbon steel-container, with thickness of which approximately at 55 mm which should make it waterproof throughout the thermal phase. The installation of vitrified waste induces an increase of the temperature within the disposal areas and on the surrounding geological environment. The emitted quantity of heat can be several hundred to several thousand watts. Over time, the temperature reaches a maximum, followed by a decrease in natural geothermal heat (~22°C). The required time to obtain a temperature up to 50°C inside the waste package varies between

200 and 1400 years depending on the type of the package (Andra, 2005c). However, the temperature in the level of the metallic liner remains below 90°C with the maximum value reached approximately 15 years after the waste package emplacement (Bennet & Gens, 2008).

As it is shown in Figure 1.2.1, waste packages are placed in horizontal boreholes, approximately 700 mm of excavated diameter, and of limited length to about 100 m. They are placed into a carbon steel metallic liner, which provides support for installation and their eventual recovery.

Carbon steel has been chosen for the overpack and the metallic liner as it is known for its durability over time and its corrosion processes have been extensively studied. Its lifetime is evaluated at several thousand years, which extends the thermal phase of the waste (around one thousand years maximum). In addition, carbon steel is less prone to localized corrosion than passive materials, such as stainless steel or nickel-based alloys (Feron et al., 2008).

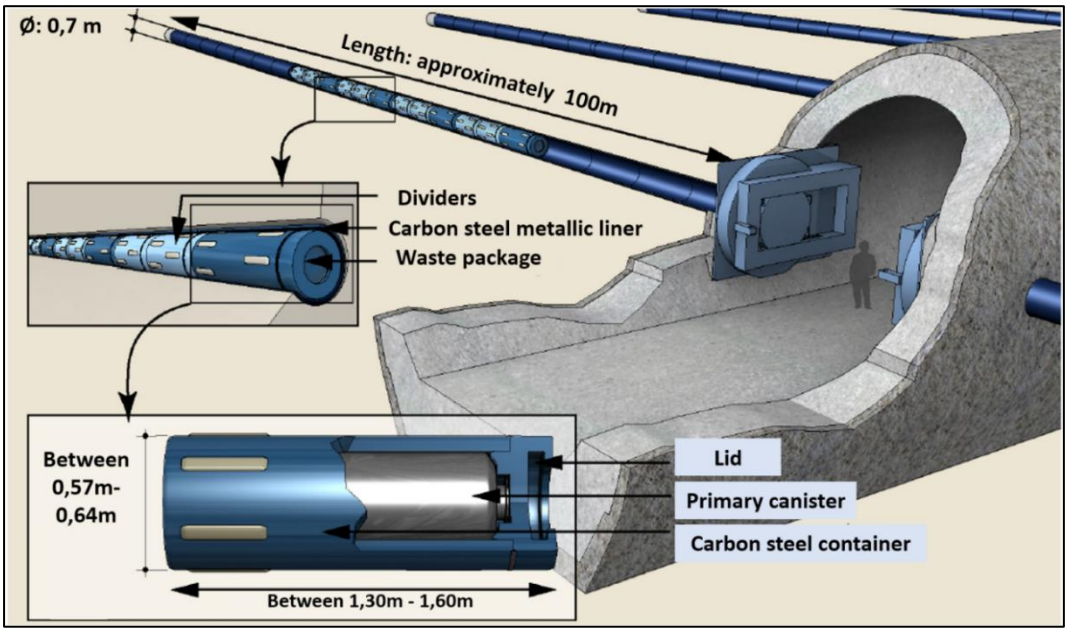

Figure 1.2.1: Schematic view of HL vitrified waste gallery

For packages with high thermal release, a minimum storage period of 60 to 70 years is predicted before their disposal into the gallery, in order to limit thermal disturbances. The residual thermal energy still needs to be separated by dividers in the same HLW gallery. Once the cell is closed, it is sealed by a plug of swelling clay placed in contact with the argillite. The latter is held in place by a concrete plug.

It is also planned to inject a low pH (9 < pH < 12) cement-bentonite grout/"Matériau de Remplissage de l'espace annulaire" (MREA), in the space between the metallic liner and the host rock (Figure 1.2.2). The objective is (i) to neutralize the transient acidic disturbance caused by the oxidation of pyrites during excavation and drilling operation, (ii) to limit the residual presence of oxygen and (iii) to promote general corrosion at slow rates (Crusset et al. 2017).

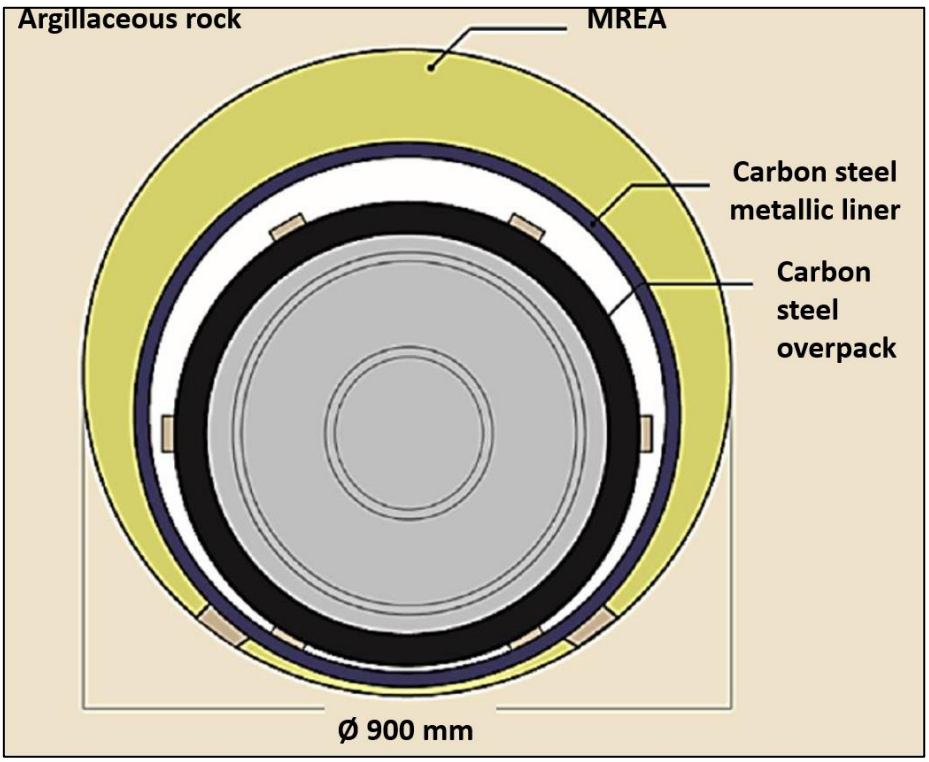

Figure 1.2.2: Cross-sectional schematic view of HL waste cell (Verron, 2020)

1.2.2 Evolution of the disposal conditions over time

Even if the design of the deep geological disposal facility aims to limit chemical interactions within the installation, a series of chemical processes are occurring. After the closure of the facility, all the residual oxygen during the operation phase will be gradually consumed by several processes e.g., pyrite oxidation, metal corrosion or microbial activity.

Through this transition phase, the metallic elements present in the disposal facility undergo a primary degradation (dry oxidation), forming multiple corrosion layers upon their surface. The gradual natural pore water incoming into the HL disposal cell will lead to its resaturation and thus, to aqueous corrosion processes. In parallel, oxygen consumption leads to corrosion processes occurring under anoxic conditions. This transient period has consequences on the

redox of the aqueous medium passing from oxidising to reducing conditions (Eh < -100mV) in the first ten years as it is shown in Figure 1.2.3.

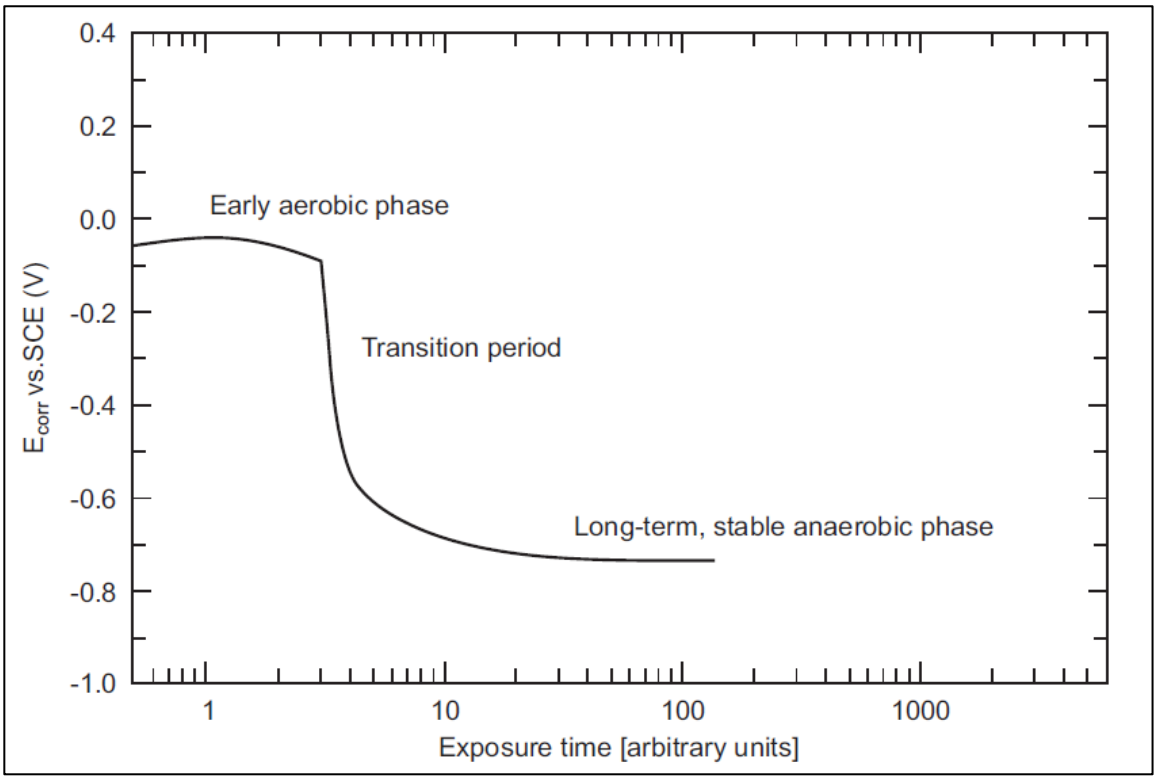

Figure 1.2.3: Expected evolution of the corrosion potential of a carbon steel canister (King, 2008)

Under such conditions, anoxic corrosion of carbon steel generate hydrogen gas (H_2) production. The accumulation of H_2 gas may significantly affect the mid- and long-term repository safety. If hydrogen cannot be evacuated at the rate at which it is produced, there will be gas accumulation. Due to the hydrostatic pressure and the low permeability of clay barriers, very high hydrogen pressures could theoretically develop. This production of hydrogen generates various safety problems. One the one hand, its highly flammable and explosive properties create a risk during the operational phase. On the other hand, the consequent overpressure is capable of delaying and/or limiting the resaturation of the bentonite sealing, creating preferential paths for the migration of radionuclides (Andra, 2005b; Schlegel et al., 2021).

The transition from aerobic to anoxic conditions will lead to different corrosion processes by formatting a passive layer thorough the available surface of metallic elements, causing a gradual decrease on the corrosion rate and an iron release in the aqueous medium (Andra, 2005b; Diomidis, 2014).

In addition, the influence of microbial activity on corrosion processes of carbon steel should be taken into account. All metallic materials immersed in a non-sterile aqueous medium will lead to the formation of a "biofilm" composed by organic/inorganic substances and micro-organisms. Biofilm's existence remains independent of big temperature ranges and pH evolution (from very acid to very basic values). Metal corrosion is highly dependent on oxidation/reduction conditions, which could lead to the formation of different growth-type biofilms. Under aerobic conditions (operation phase), sulphur-oxidising bacteria generate sulphuric acid, causing rapid degradation of metals. Also, pyrite (FeS), is present in many clay environments and its oxidation result in a highly acidic environment. Moreover, ferro-oxidising bacteria, can oxidize ferrous ion into ferric ion and accelerate metal corrosion, particularly in the presence of chloride ions. Under anaerobic conditions (post-closure phase), localized corrosion may be induced by the presence of anaerobic bacteria. However, it should be mentioned that this type of bacteria could potentially have positive effects like the consumption of hydrogen, or the formation enhancement of protective corrosion products (Ferron & Crusset, 2014).

Besides, all the other chemical procedures, spent nuclear fuel emits alpha, beta, gamma, and neutron radiation. The relative intensity of the different types of radiation depends on the fuel age and the distance from the fuel. In the disposal conditions, taking into account the designed multi-barrier system, only γ-rays are to be considered for water radiolysis in the level of the metallic liner, with a debit dose up to 10 $Gy.h^{-1}$ (Andra, 2005b; Bennett & Genns, 2008). Once the pore water or humid air will come into contact with the containers, undergoes radiolysis under the effect of ionizing radiation emitted by the waste packages. The water decomposition will create different chemical species, whose concentrations depend on the radiation, and can intervene in the corrosion phenomena in particular by modifying the redox conditions of the medium at vicinity of the container. Moreover, solutes presence in pore water will influence radiation chemistry of the near environment. The oxidising/reducing species from water radiolysis will react with solutes present in pore water and the redox potential will become dependent of the solutes type and concentration. Thus, it is important to have knowledge of the solution chemistry to estimate the final outcome of water radiolysis (Andra, 2005b; Eriksen & Jacobsson, 1983; Holmboe et al., 2012; Jonsson, 2012).

1.3 Summary

The deep geological disposal facility for HL and IL waste has been designed according to specialised needs. Its primary function is to isolate the waste from surface activities. The second function is to confine the radioactive substances and control possible pathways which in long term may bring radionuclides into contact with the biosphere. These phenomena operate over very long-time scales, during which the waste becomes less hazardous owing to radioactive decay. During this long period, the evolution of the disposal conditions should be taken into account with the intention of the assurance of the facility safety. As it has been described, it is planned the utilization of large volumes of metallic elements. These metallic elements will undergo a progressive anoxic corrosion degradation which will induce the release of H_2 and the creation of ferrous ions dissolved in the aqueous medium in contact with the metallic surfaces. Simultaneously, the water radiolysis process caused by the ionizing radiation emitted of the waste can lead to an additional production of hydrogen.

If hydrogen cannot be evacuated, the gas accumulation will generate various safety problems. These parallel phenomena, anoxic corrosion of steel and water radiolysis, will become sources of hydrogen production within the facility, therefore it is crucial to study them separately in order to better understand the way that one intervenes in the other. The following chapter is dedicated to the bibliographic review of metal corrosion and water radiolysis in order to achieve a better comprehension of their co-existence, anoxic corrosion under irradiation, within the disposal facility.

Chapter 2: State of the art

2.1 Corrosion of metallic elements

Corrosion is the process that concludes in the deterioration of the performance of a metallic material, the result of which is corrosion damage. Corrosion may be defined as: “a physico-chemical interaction, leading to a significant deterioration of the functional properties of either a material, or the environment with which it has interacted, or both”. The definition includes processes that combine environmental (e.g., chemical and/or electrochemical) deterioration where these are additionally influenced by applied/residual stresses in the material, and by the material microstructure because of manufacture or service (Feron, 2012).

2.1.1 General information about metal corrosion

Corrosion of metals results from electrochemical process, a chemical reaction in which there is electron transfer from one chemical element to another. The characteristic property of metals is to lose electrons during a reaction, called oxidation. The metal M can be oxidised according to the following reaction:

$$M \rightarrow M^{n+} + ne^- \qquad \text{(R2.1)}$$

The upper reaction is called anodic reaction. For example, iron is oxidized as follows:

$$Fe \rightarrow Fe^{2+} + 2e^- \qquad \text{(R2.2)}$$

The electrons generated from every metal atom which is oxidized are transferred in order to become part into another chemical element, during a process which is called reduction (cathodic reaction). For example, some metallic elements are corroded in acidified medium with high concentration on protons (H^+). The protons are reduced as follows:

$$2H^+ + 2e^- \rightarrow H_2 \qquad \text{(R2.3)}$$

All oxidation-reduction reactions, consist of two partial reactions. Therefore, the overall reaction of the partial anodic reaction (R2.2), and partial cathodic reaction (R2.3) is the following:

$$Fe + 2H^+ \rightarrow Fe^{2+} + H_2 \qquad \text{(R2.4)}$$

Thus, in this overall electrochemical reaction, each atom of iron that passes into solution implies the exchange of two electrons between the metal and the protons (Callister, 2000).

Corrosion forms

The corrosion behavior can be influenced by many factors such as temperature, microstructure and chemical composition of the metal, mechanical forces etc. Consequently, it is more convenient to classify corrosion according to the way it is expressed. Eight forms of most frequent corrosion types are reported: uniform, galvanic, crevice, pitting, intergranular, selective leaching, erosion and stress corrosion cracking (Callister, 2000; Landolt, 2007).

-Uniform corrosion: it is expressed with similar intensity on the exposed metallic surface by leaving usually a corrosion layer/film. Redox reactions occur randomly upon the surface, it is the most frequent corrosion type and also the easier in order to predict the degradation rate.

-Galvanic corrosion: it is noted when two metals or alloys with different compositions are connected while they are exposed in the same electrolyte. The more reactive metal in this type of environment will be corroded close to the connection region. The rate of galvanic corrosion is affected by the anode-cathode specific surface as well as by the surface exposed to the electrolyte. A selective attack within cracks and at other sites of poor oxygen access is frequently observed.

-Crevice corrosion: is a result of different ion concentration/gaseous concentration in the electrolyte medium and between two regions of the same metallic element. In this element, crevice corrosion will take place in a region of the lower concentration.

-Pitting corrosion: formed in small pits in an almost vertical direction to the surface of the material, usually quite difficult to be identified.

-Intergranular corrosion: is a selective attack of grain boundaries. Often, it is related to thermal treatments that lead to preferred precipitation of phases at grain boundaries.

-Selective corrosion: takes place in alloys where implies the selective dissolution of one of the components. It leads to the formation of a porous layer made of the more noble metal.

-Erosion corrosion: results from chemical attack combined with material loss by mechanical wear due to impingement of solids or a fluid.

-Stress corrosion cracking: results from combined energy from mechanical stress and corrosive electrolyte.

Corrosion rate

With the term of “corrosion rate” we can define the rate at which any metal in a specific environment deteriorates. The corrosion rate can be expressed in different ways depending on the application:

• loss of mass per unit area and per unit time (mg/(dm^2day))

• in number of moles transformed per unit of surface and per unit of time (mole/m^2s)

• in depth corroded per unit of time (mm/year)

• in current density (A/m^2)

The rate of corrosion determines the life of metal-based materials. This reality dictates the choice of metals used for different purposes and in different environments. It also determines the maintenance requirements for structures: a metal structure in a humid environment may require more frequent maintenance than a similar structure in a drier place (Landolt, 2007).

2.1.2 Nature of formed phases during iron corrosion

Corrosion of iron (Fe (0)) induces the formation of ferrous ions (Fe (II)) and/or ferric ions (Fe (III)). Other valences exist in a stable or metastable state (I, IV, V and VI) but they are very rare as a corrosion product (Bouniol, 2010). As we can see in Table 2.1, there are five main categories of iron corrosion products:

Family	Phase	Chemical Formula	Oxydation Degree
Oxy-hydroxides of iron	Goethite	α-FeOOH	Fe (III)
	Akaganéite	β-FeOOH	Fe (III)
	Lepidocrocite	γ-FeOOH	Fe (III)
	Feroxyhyte	δ-FeOOH	Fe (III)
	Ferrihydrite	Fe_2O_3, nH_2O	Fe (III) / Fe (II)
	Green Rust	$Fe_6(OH)_{12}SO_4$. $8H_2O$	Fe (III) / Fe (II)
Iron oxides	Hematite	α-Fe_2O_3	Fe (III)
	Maghemite	γ-Fe_2O_3	Fe (III)
	Magnetite	Fe_3O_4	Fe (III) / Fe (II)
Iron hydroxides	Ferrous iron hydroxide	$Fe(OH)_2$	Fe (II)
	Ferric iron hydroxide	$Fe(OH)_3$	Fe (III)
Iron carbonates	Siderite	$FeCO_3$	Fe (II)
	Chukanovite	$Fe_2(OH)_2CO_3$	Fe (II)
Iron sulfides	Pyrite	FeS_2	Fe (II)
	Mackinawite	FeS	Fe (II)

Table 2.1: Iron corrosion products

i) Iron oxides

The iron oxides only contain iron and oxygen atoms in their structure. Among these phases, we find two polymorphic compounds: i) the oldest known Fe oxide in minerals and extremely stable hematite (α-Fe_2O_3) and ii) maghemite (γ-Fe_2O_3), occurring in soils as a weathering product of magnetite or as the product of heating of other Fe-oxides. These two phases are compounds containing iron under its valence (III). Magnetite (Fe_3O_4) is a ferrimagnetic mineral

containing both Fe (II) and Fe (III) in the form of Fe_3O_4 and which can tolerate small deviations from the stoichiometric composition. This phase has a low resistivity, although three to four times higher than that of metallic iron. This is due to the possibility of electron transfer between Fe (II) and Fe (III) (Cornell & Schwertmann, 2003).

ii) Iron hydroxides, with general formula $Fe_x(OH)_y$:

Two types of hydroxides are known: ferrous hydroxide $Fe(OH)_2$ and ferric hydroxide $Fe(OH)_3$. Ferrous hydroxide is unstable in an aerated medium and corresponds to an intermediate reaction. Any experiment on the conductivity of ferrous hydroxide is made difficult because of its instability in air. Also, ferric hydroxides ($Fe(OH)_3$) are obtained from dissolution and aerial oxidation of ferrous hydroxides, in strongly alkaline medium, acting also as intermediate product before the precipitation to Fe(III) oxy-hydroxides (Misawa et al., 1974).

iii) Iron oxy-hydroxides, with general formula FeOOH:

There are four main types of polymorphic iron oxy-hydroxides, goethite (α-FeOOH), akaganite (β-FeOOH), lepidocrocite (γ-FeOOH) and feroxyhyte (δ-FeOOH). They all have iron at a degree of oxidation (III). Furthermore, disordered ferrihydrite ($Fe_2O_3.nH_2O$) phases are also classified among the oxy-hydroxides. Goethite, lepidocrocite or ferrihydrite have very high resistivities, 10 to 12 orders of magnitude higher than that of iron and can be considered as electrical insulators (Cornell & Schwertmann, 2003). In addition, there are non-stable reaction intermediates containing iron in the Fe (II) and Fe (III) state: green rusts. These structures are poorly crystallized, and their general chemical formulas vary depending on climatic conditions and the duration of exposure to aerobic conditions. Rust is a complex of different phases, once green complexes or green rusts are formed as intermediates, further oxidation is governed by their existence. This is why, their structures, compositions and formation processes are essential for rusting of iron at pH value around neutrality (Genin et al., 2006; Misawa et al., 1974).

iv) Iron carbonates and sulfides

In carbonated media, dissolved carbonate ions tend to associate with iron to produce carbonate iron compounds. In the study of Saheb et al. (2010), two crystalline phases are noted on archaeological artefacts buried in anoxic media: siderite ($FeCO_3$) and chukanovite ($Fe_2(OH)_2CO_3$). They have iron at a degree of oxidation (II).

In a sulfur-containing medium, the sulfur species can recombine with the aqueous iron to form different species. As iron chemistry in sulfur medium can be complex, we present here the most common forms without considering their hydration and the many existing intermediates. In a reducing medium, pyrite (FeS_2) or mackinawite (FeS) can be formed by association of sulphide ions (S^{2-}) with Fe (II) (Novakova et al., 1997).

Corrosion products (CP)

The nature of the corrosion products formed during the deterioration of the metal will depend on the material and the physico-chemical conditions of degradation. Atmospheric corrosion leads to the formation of a rust layer composed of different phases of iron oxides and hydroxides. In the work of Dillmann et al. (2004) regarding archeological objects, the three main constituents distributed non-homogeneously in the rust layer are: i) goethite (α-FeOOH), ii) lepidocrocite (γ-FeOOH) and iii) magnetite (Fe_3O_4). It has been shown that the presence of different oxides affects the morphology of the corrosion layer by creating different inner layers. More specifically, goethite is found rather at the metal/oxide interface while lepidocrocite is more evident at the external interface. In another study with ancient artefacts, Monnier et al. (2010) confirms the presence of goethite and lepidocrocite and also identifies akageneite (β-FeOOH) in the outer layer of the corrosion layer, but it is linked with the presence of chlorides. In the presence of neutral or basic medium, corrosion products are slightly soluble, thus, the formation of a layer cannot act as a shield against the metal deterioration, although it can decrease the corrosion rate (Bouniol, 2010; Cornell & Schwertmann, 2003). In anoxic conditions, it has been found that unalloyed steel is mainly covered with a magnetite-type oxide (Fe_3O_4) or, in some cases, siderite ($FeCO_3$) (Andra, 2005b).

2.1.3 Corrosion under anoxic conditions

The lifetime of the deep geological disposal facility will be divided into several phases. The construction and the operational phase, during which oxygen will be present in the installation, will give rise to corrosion processes under oxic conditions. Then, during the post-closure phase of the site, the oxygen present in the installation will gradually be consumed via the oxic corrosion mechanisms and the oxidation of minerals sensitive to redox conditions (e.g., pyrite FeS_2), then leaving make way for anoxic corrosion processes. Corrosion studies with duration up to three years using argillaceous pore water indicate final rates varying between 3 and 10 $\mu m.year^{-1}$ (Mohamed-Said et al., 2017; Necib et al., 2017), while in the review of Diomidis (2014) in longer time scales (~10 years) corrosion rates are estimated to be even lower than 0.5 $\mu m.year^{-1}$.

In an anoxic aqueous medium, the anodic reaction is the oxidation of metal iron to ferrous ion. Initially, it leads to the production of electrons at the interface between the metal and the medium, and then to the interface between the metal and the layer of corrosion product. The half-equation corresponding to this reaction is:

$$Fe_{(s)} \rightarrow Fe^{2+}_{(aq)} + 2e^- \quad \text{(R2.5)}$$

Reaction 2.5: Anodic half-reaction of iron corrosion in anoxic medium

The anodic reaction takes place simultaneously with the cathodic reaction. In the absence of oxygen, in aqueous medium, the redox couple controlling the equation is H_2O/H_2. The water will be reduced by the electrons created by the anodic reaction to lead to the production of dihydrogen. The half-reaction of this reaction corresponding to this reaction is:

$$2H_2O + 2e^- \rightarrow 2OH^- + H_2 \quad \text{(R2.6)}$$

Reaction 2.6: Half-cathodic reaction of iron corrosion in an anoxic medium

The balance reaction of corrosion of iron in an anoxic aqueous medium, therefore, corresponds to:

$$Fe_{(s)} + 2\,H_2O \rightarrow Fe^{2+}_{(aq)} + 2\,OH^- + H_2 \quad \text{(R2.7)}$$

Reaction 2.7: Balance reaction of iron corrosion in anoxic medium

This reaction involves charge transfer between the electronic conductor (metal) and the ionic conductor (aqueous solution). The created hydrogen will be able to be released in gaseous form. The ferrous ions created can complex with hydroxyl ions in solution and/or precipitate in the form of oxides, hydroxides and oxy-hydroxides. They can for example precipitate in the form of ferrous hydroxides $Fe(OH)_2$ according to the following reaction:

$$Fe^{2+}_{(aq)} + 2\,OH^- \rightarrow Fe(OH)_2 \quad \text{(R2.8)}$$

Reaction 2.8: Precipitation reaction of ferrous oxide

This reaction is influenced by various environmental factors; in fact, ferrous hydroxide is only rarely observed because it quickly transforms into another form. For example, an increase in temperature will cause the Schikorr reaction giving rise to the formation of magnetite (Fe_3O_4) according to the reaction (Andra, 2005b):

$$3\,Fe(OH)_2 \rightarrow Fe_3O_4 + 2\,H_2O + H_2 \quad \text{(R2.9)}$$

Reaction 2.9: Schikorr reaction

There are also different chemical degradation processes that are likely to occur under deep geological disposal facility conditions. In a carbonated environment, the balance reaction of corrosion is:

$$Fe_{(s)} + 2\,HCO_3^- \rightarrow Fe^{2+}_{(aq)} + 2\,CO_3^{2-} + H_2 \quad \text{(R2.10)}$$

Reaction 2.10: Balance reaction of iron corrosion in an anoxic carbonated medium

Furthermore, pore waters contain species like chlorides, carbonates, phosphates, silicates, etc., which can combine with iron and give solid compounds more stable than oxides. For example, in the presence of carbonates and the absence of oxygen:

$$Fe + 2\,NaHCO_3 \rightarrow FeCO_3 + H_2\uparrow + Na_2CO_3 \qquad (R2.11)$$

Reaction 2.11: Formation of siderite in anoxic carbonated medium

Also, in the case of deaerated carbonated water, chukanovite ($Fe_2(OH)_2CO_3$) is a well-known corrosion product:

$$2\,Fe^{2+} + HCO_3^- + 2H_2O \leftrightarrow Fe_2(OH)_2CO_3 + 3H^+ \qquad (R2.12)$$

Reaction 2.12: Chukanovite formation in a slightly basic medium

State of the art of the studies dealing with corrosion under anoxic conditions:

Archeological artefacts

Characterization of archeological samples conditioned in anoxic aqueous environment in different sites revealed principally the presence of siderite ($FeCO_3$), chukanovite ($Fe_2(OH)_2CO_3$) and magnetite (Fe_3O_4) and other formations depending on the electrolyte. Studies from Saheb et al. (2008), with ferrous archaeological artefacts collected in anoxic soils from two different archeological sites in (Nydam Mose, Denmark and in Saint Louis, France), indicated that the main corrosion product observed on the metal surface for both sites was siderite ($FeCO_3$). Iron hydroxicarbonate ($Fe_2(OH)_2CO_3$) has also been identified on some samples. The thickness layer varies between 0.5 and 5 mm and between 1 and 3mm for the danish and the french site, respectively. In similar study Saheb et al. (2010), used archeological artefacts from a third site (Glinet, France), where the burial soil is characterized by anoxic conditions and calco-carbonated aqueous environment. The main phases constitutive of the corrosion layer are siderite ($FeCO_3$), an iron carbonate containing hydroxide groups (probably chukanovite), and magnetite (Fe_3O_4). Additionally, Michelin et al. (2013), studied the corrosion products collected on a 450-year-old archaeological iron sample in carbonated medium. Analyzes of the aqueous medium composition indicated that the sample taken from about 1 m deep, has been corroded in an anoxic environment. This study indicates that there was a continuous layer of about 100 nm at the metal/corrosion products interface, composed of a mixture of iron oxides (maghemite and magnetite) or an intermediate compound between these two phases (proportion phase is 1/3 magnetite and 2/3 maghemite). According to the authors,

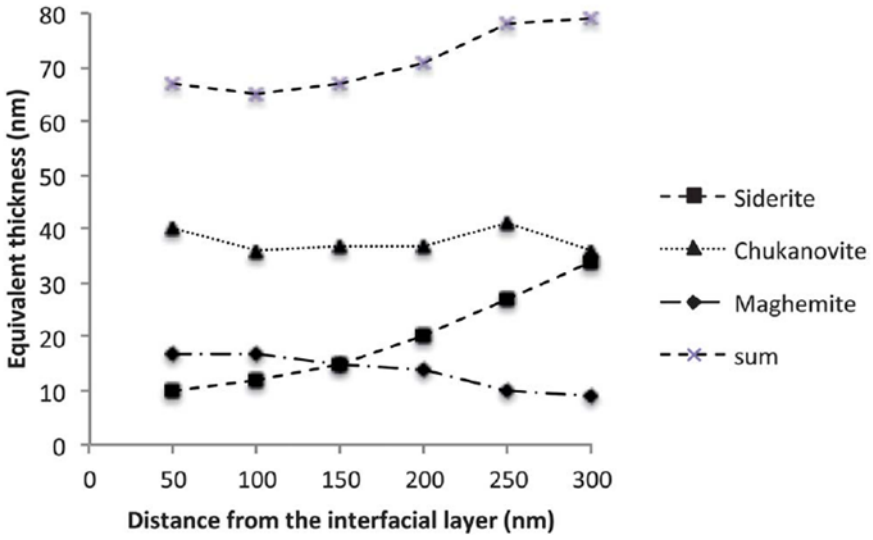

Figure 2.1.1: Equivalent thicknesses of the different phases obtained from the adjustment of the extracted spectra (Michelin et al., 2013)

this supports the hypothesis that the presence of an oxide layer controls the corrosion properties of the system. As we can see in Figure 2.1.1, beyond the metal interface, the corrosion products were mainly carbonate species of Fe (II), siderite ($FeCO_3$) and chukanovite ($Fe_2(OH)_2CO_3$), with a small amount of Fe(III) species.

Pure water

Previous studies testing the simple case of immersed steel in pure water have been performed at different temperatures. Jelinek et al. (1982) measured the H_2 evolution of anoxic corrosion of steel during 40 days with temperatures ranging between 60-90°C. The authors conclude that the temperature variation does not have a significant impact on H_2 evolution, finding magnetite as the main corrosion product. Magnetite identification is in accordance with the work of Brusch et al. (1969) performed under anoxic conditions and using pure water and temperatures ranging from 37°C to 200°C, during approximately 208 days.

In the work of Badet (2014) metallic samples have been immersed in pure deaerated water under anoxic conditions. The corrosion rate measured by weight loss method after 99 days of experiment indicated a mean value at 0.5 $\mu m.year^{-1}$. Although, no corrosion product was able to be identified.

Near neutral pH

Japanese studies (Taniguchi et al., 2004) have tested the performance of carbon steel coupons in contact with compacted bentonite immersed in two types of synthetic groundwater at 80°C. The first solution had a pH range of 8.3-8.7 while the second was slightly more alkaline with a pH around 9.2. After 4 years of exposure both tested media give corrosion rates lower than 1µm.year^{-1}. The main corrosion products identified is siderite ($FeCO_3$), and in some cases chukanovite ($Fe_2(OH)_2CO_3$), but no magnetite was found.

Necib et al. (2017) performed experiments with carbon steel samples immerged during 36 months under anoxic conditions in two environments: i) liquid synthetic pore water (COx rock) at pH 7.2 and ii) gas emanating from COx rock, at a temperature of 85°C. The pH evolution in the liquid medium indicated an acidic transient period during which the corrosion rate was high (250 µm.year^{-1}), forming ferrous hydroxychloride (β-Fe_2-$(OH)_3Cl$), mackinawite and siderite at the surface of the metallic samples. Although, for the near neutral pH the rate was around 10 µm.year^{-1} with the identified formation of magnetite, Fe-silicate and ferrous hydroxychloride. Concerning the samples exposed to gas phase, they showed a low corrosion rate, with a mean value around 10 µm.year^{-1}, and magnetite was also the main corrosion products identified.

This is in accordance with the study of Schlegel et al. (2016), working on samples collected during the Necib et al. (2017) study. The identified corrosion products were poorly crystalized chukanovite, siderite and magnetite. It is emphasized the influence of temperature, pH, bacterial activity and dissolved elements on corrosion products formation. Moreover, in a more recent work, Schlegel et al. (2021) studied carbon steel samples in saturated clay water medium for up to six years. The authors detected mainly the presence of magnetite but also chukanovite, Fe silicate, and siderite with a corrosion rate lower than 1 µm.year^{-1}.

Some anoxic corrosion studies have also been performed at higher temperature. Bataillon et al. (2001), exposed metallic samples in a mixture consisting of clay and argillite/granitic water for 328 hours. The identified corrosion product is consisted of a mixed layer of magnetite and maghemite, while in the outer zone the corrosion product is mainly siderite.

In the study of Mohamed-Said et al. (2017), a numerical model is developed to simulate the evolution of the corrosion rate of carbon steel sample put in contact with Cox argillite rock at 90°C under anoxic conditions, and to compare these simulations with experimental results obtained during a previous study. According to this experimental work, siderite is the main corrosion product that can precipitate forming a protective corrosion layer. The simulation indicate that the corrosion rate is about 150 µm.year^{-1} in the beginning of the experiment and about 3 µm.year^{-1} after 3.2 years. This corrosion rate decrease is due to the progressive

formation of a corrosion product layer with the effect to decrease both the active metal surface and the transport of aqueous species.

Higher pH

Marsh & Taylor (1988) studied the behaviour of carbon steel samples immersed in two different medium at 90°C. More specifically, steel immersed in a synthetic granitic groundwater-bentonite paste (pH=9.4) system for 208 days indicated a corrosion rate of 0.1 μm.year^{-1}, while tests performed on a longer exposure time and using seawater indicated a higher corrosion rate of 6 μm.year^{-1}. Relatively few experimental results arising from post-mortem analyses are provided, with the exception of the suggestion that a layer of magnetite (Fe_3O_4) has been formed on samples exposed to a synthetic granitic groundwater-bentonite paste system.

In the study of Kreiss (1991), we find measurements of H_2 evolution arising from the anoxic corrosion of steel in cementitious medium (pH=12.8), in neutral medium (pH=7) with addition of chloride, and in granitic groundwater (pH=8.5) with sodium, potassium and calcium hydroxides additions. Results showed that the corrosion behaviour of carbon steel observed in solution with similar pH, depends a lot on the chemical composition of the corrosion medium. Thus, the $Ca(OH)_2$ addition resulted to the slowest rate for hydrogen generation, as it participates in the oxide film growth on the corroding iron surface, resulting in a more protective film.

Smart et al. (2001) carried out numerous experiments on the anaerobic corrosion of carbon steel and cast iron. Corrosion rates were measured through the generated volumes of hydrogen. The synthetic solutions used for samples immersion had chemical compositions similar to that of the pore water of Aspo's granitic rock and that of bentonite equilibrated pore water. This work was carried out at different temperatures, using pristine samples and also samples with pre-formed oxide films upon the surfaces (magnetite (Fe_3O_4) or siderite ($FeCO_3$)). In all tests, the corrosion rate decreases with increasing exposure time, while the thickness of the layer of corrosion products increases. The results show that the mean corrosion rates were low, highlighting that, even if initially both solutions showed comparable results, after 63 days of immersion the bentonite-equilibrated water indicated hydrogen generation rate almost four times lower than in Aspo groundwater (Figure 2.1.2). The higher pH of bentonite-equilibrated water (pH=10.5), in comparison with the one of Aspo groundwater (pH=8), favours the formation of magnetite and decreases the solubility of Fe^{2+} ions, leading to more rapid formation of a protective magnetite film. The initial anaerobic corrosion rate of carbon steel measured at 30°C, 50°C and 85°C ranged from 10 to 30 μm.year^{-1}, but as the oxide film was

formed the rate decreased to values inferior to 0.1 μm.year^{-1}. Finally, the authors conclude that the initial corrosion rate increases with increasing temperature.

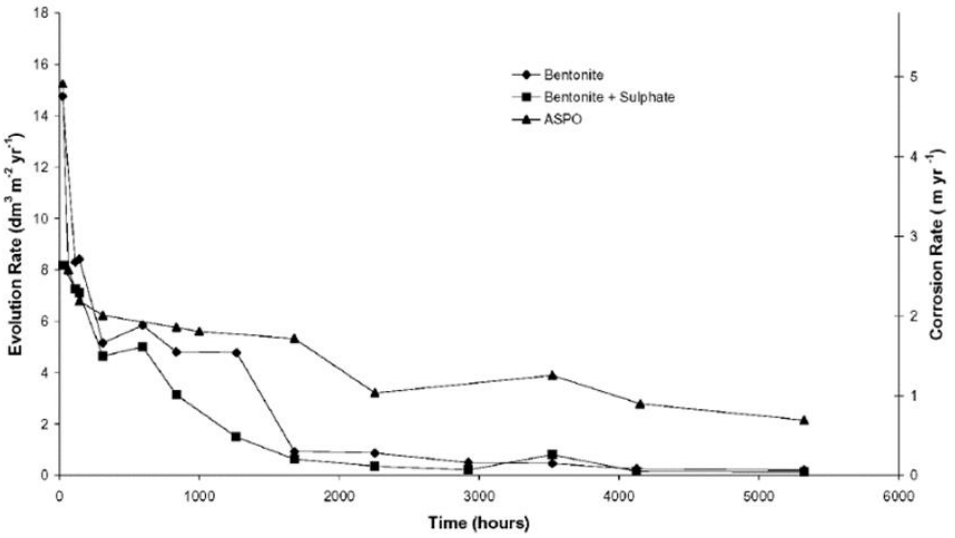

Figure 2.1.2: Evolution of the hydrogen produced by the anaerobic corrosion of carbon steel in an artificial and anoxic underground aqueous medium (Smart et al., 2001)

In another work, Smart et al. (2004) have measured in anoxic conditions the evolution of hydrogen production when carbon steel wires are brought into contact with bentonite slurry (pH=10.5) at 30°C and 50°C for about 20 months. The comparison between (i) carbon steel into bentonite slurry and (ii) carbon steel and cast iron in artificial groundwaters (7.0 < pH < 8.1) showed that the initial corrosion rate of carbon steel is higher for the tests performed in bentonite compared to the one performed in artificial groundwater, although the long-term corrosion rates seem to be equivalent (Figure 2.1.3). The higher initial corrosion rate was explained by Fe(II) adsorption by the bentonite which retarded the formation of a protective corrosion product film. Mixtures of magnetite, hematite and goethite were identified as corrosion products.

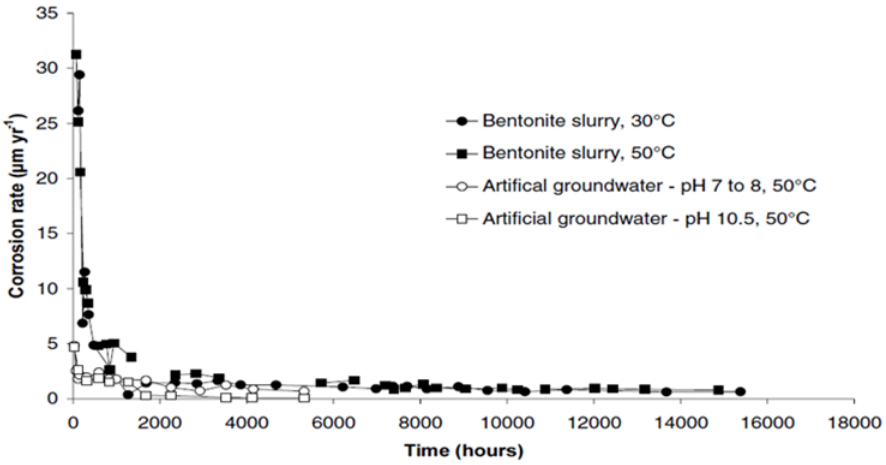

Figure 2.1.3: Results of anaerobic corrosion in bentonite suspension at 30°C and 50°C, in relation to the data obtained for steel in artificial groundwater (Smart et al., 2004)

In a more recent study, Smart et al. (2017a) measured for almost 6.5 years the corrosion rate on both pristine and pre-corroded carbon steel wires put in contact with compacted bentonite and Opalinus clay pore water at a temperature of 60°C. After five years, the corrosion rate exported from gas generation measurements reached a value of 0.5 µm.year^{-1} for both kind of samples. Regarding corrosion products characterization, the pristine wires were mainly covered by magnetite but the presence of some carbonate species and oxyhydroxides has also been identified. For the pre-corroded carbon steel wires, the authors also note the additional presence of hematite, as the samples have been exposed to air during the initial formation of corrosion film. Furthermore, Smart et al., (2014) in ambient temperature and in higher pH (13.4) studied the impact of sulphides on anaerobic corrosion. They concluded that the presence of sulphide and thiosulphate in synthetic cementitious solution did not cause any increase of the corrosion rate up to 290 days.

In parallel, short-term experiment (100 days) have been performed by Senior et al. (2017), using three types of test specimens (backfill grout, bare steel rods, steel rods encased in backfill grout) immersed in pore waters. No characterization has been made for corrosion products but the authors observed at the end of the experiment that the samples have been passivated with a corresponding corrosion rate lower than 0.01 µm.year^{-1}. In a more recent study, Senior et al. (2020) compared the corrosion rates of steel, either bare or encased within mortar, tested in water vapour or immersed in artificial rock pore water and Portlandite groundwater with dissolved calcium hydroxide to represent aged cement waters at 50°C. The test took place for approximately 4.5 years and suggest a lower corrosion rate for the samples associated to the Portlandite groundwater. In both cases, the corrosion rate was found to be lower than 0.001 µm.year^{-1}.

In the study of Kaneko et al. (2004), H_2 measurements were made for the anoxic corrosion of carbon steel in order to estimate the impact of chloride concentration in saturated medium with $Ca(OH)_2$ ($10.5 < pH < 14.0$). The tests duration was varying from 100 to 1000 days in temperatures between 20 and 45°C. The results showed that chloride concentration inferior to 5000 ppm has an insignificant effect on the corrosion rate. Short term experiments performed with high (20000 ppm) and low (< 5000 ppm) chloride concentration, indicated corrosion rate values of 0.1 $\mu m.year^{-1}$ and 0.05 $\mu m.year^{-1}$, respectively. For the long term tests performed without chloride addition, the corrosion rate was lower than 0.02 $\mu m.year^{-1}$. Characterisation of the corrosion product was not performed; however it is assumed by the authors the presence of magnetite.

Finally, one can note the work of Kursten et al. (2017) involving carbon steel samples immersed in young cementitious pore water (pH~13.6) at 80°C. Corrosion rate values measured by hydrogen production monitoring were about 0.03 $\mu m.year^{-1}$ and associated SEM and Raman characterizations showed that the corrosion product layer was mainly composed of magnetite (Fe_3O_4).

The corrosion products identified in the upper studies are summarized in Table 2.2. Depending on the selected aqueous medium different corrosion products are formed as following:

Aqueous medium	Corrosion products	References
Pure water (neutral pH)	Magnetite	Brusch & Pearl, 1969; Jelinek & Neufeld, 1982
Artificial ground water solution (near neutral pH)	Magnetite Maghemite Siderite Chukanovite, Fe-silicate, Ferrous hydroxychloride	Bataillon et al., 2001; Necib et al., 2017; Schlegel et al., 2016, 2021; Schlegel et al., 2021; Taniguchi et al., 2004
Artificial bentonite/cement solution (high pH)	Magnetite Siderite Hematite Goethite Carbonated oxy-hydroxides	Kaneko et al., 2004; Kursten et al., 2017; Smart et al., 2001, 2004, 2017a

Table 2.2: Summary of corrosion products identified under anoxic conditions

2.2 Ionizing radiation

2.2.1 Ionizing radiation and the interaction with matter

The interaction between ionizing radiation and matter is complete in 10^{-15} second and gives rise to electronically excited ions and molecules which are concentrated in tracks along the path of ionizing species. The penetrating electromagnetic waves X-rays and γ-rays are characterized by their wavelength. X-rays are generated when high-voltage electrons strike a metallic target and emit most of their energy at considerably longer wavelengths. Gamma-rays (γ-rays) are produced by the nuclear decay of unstable elements. Rays with longer wavelengths (lower energy) penetrate less easily into the material, called "soft radiation", while those of higher energy penetrate further and are called "hard radiation" (Allen, 1961; Woods & Pikaev, 1993).

The absorption of the rays takes place according to several and quite different processes, happening simultaneously, but this process is dependent on the wavelength. For low energies, most of the absorption is due to the photoelectric effect: i.e., all the energy of the photon is transmitted to the electron in the material. All the excess energy represented most of the photon's energy will therefore appear as the kinetic energy of an electron, making it capable of electrically charging other molecules.

For energies above 200 keV, another process called Compton effect becomes greatest. Here, the photon interacts with an electron in the material but instead of giving all its energy to the electron, it gives only a part of it, the rest is in the form of a scattered photon of longer wavelength (lower energy). This scattered photon in general is sufficiently penetrating to escape from the material. Therefore, although the original photon disappears and the original beam is attenuated, not all the corresponding energy has gone into the sample but only the part that was given to the involved electron.

For energies above 10 MeV, another process called pair-formation becomes important. When these high energy photons pass very close to an atomic nucleus, they can with some probability be converted into a pair of positive and negative electrons (Allen, 1961).

2.2.2 The mechanism of water radiolysis

The following diffusion model (Figure 2.2.1) is adapted to describe the processes involved in the radiolysis of water. Initially, the species are created locally around the traces of the particles forming a very heterogeneous spatial distribution. As it is shown in the following figure, there are three stages:

- the physical stage

- the physico-chemical stage

- the chemical step

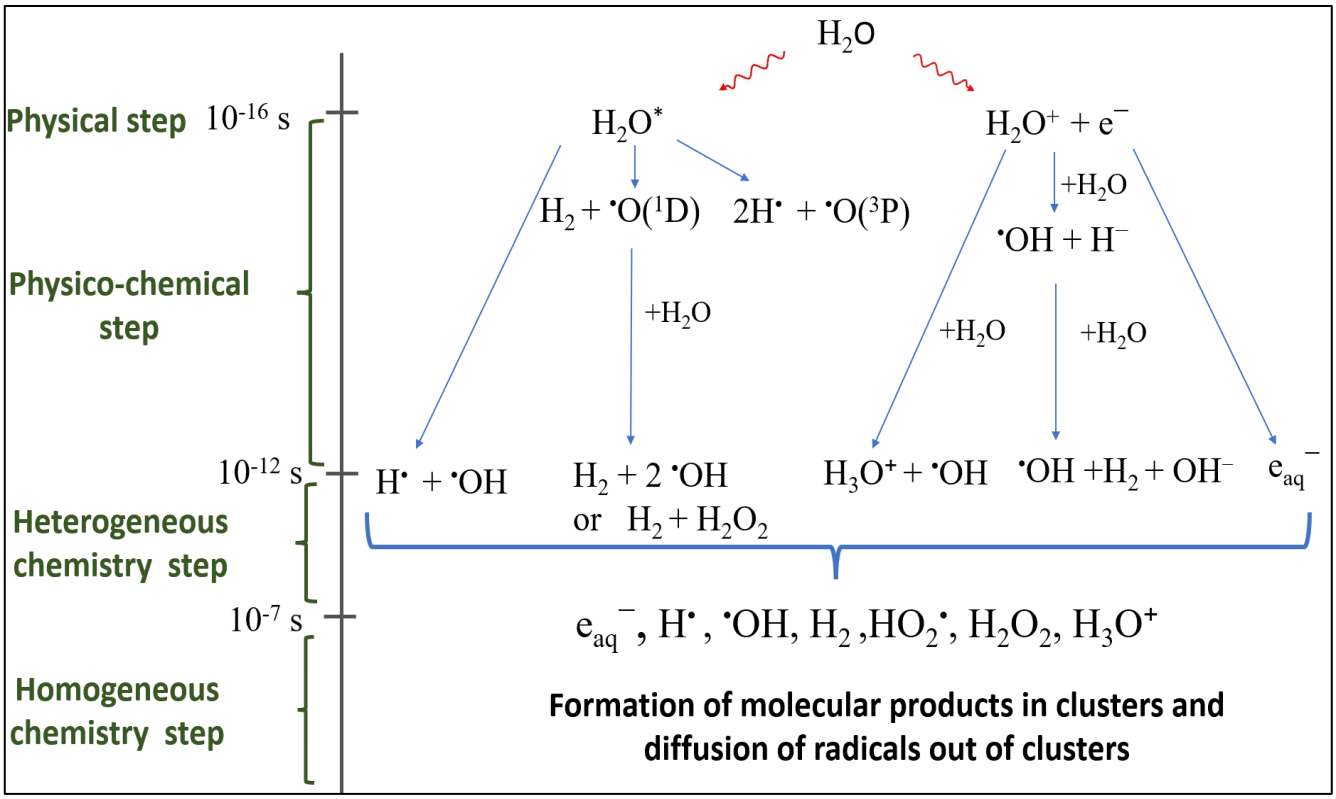

Figure 2.2.1: The formation of radiolytic species during the three stages of water radiolysis

I) Physical stage

The action of ionizing radiation indicates the passage of charged particles through matter. The Coulomb interaction between the electrostatic field of these particles and that of the electrons of matter slow down the incident particles and the primary radiolytic effect. For the water molecule, if the exchanged energy during this interaction is big enough, then the electron is ejected from the water molecule and there is « ionization ». Conversely, if the exchanged energy is weak, the electron remains bonded to the water molecule, but it is transferred to a higher energy level, which causes the excitation of the water molecule (Crumiere, 2012).

$$H_2O \rightarrow H_2O^+ + e^- \quad \text{(R2.13)}$$

$$H_2O \rightarrow H_2O^* \quad \text{(R2.14)}$$

The physical stage is completed after 10^{-15} seconds. At this stage, the present species are: e^-, H_2O^+ and H_2O^*. The ejected electron (or secondary electron) sometimes has enough energy to charge other water molecules. Energy losses below the ionization potential of a molecule should only appear as molecular excitation.

If the energy loss exceeds far from the ionization potential, another fast electron will be produced, which will carry excess energy and have enough energy to create other ionizations in turn. In addition to these secondary ionizations, other excitations will also occur. Thus, an average primary event involving 100 eV will give rise to a small cluster of ionizations and excitations. Since the path of this electron (sub-excited electron) is frequently deflected by collisions, the ions will not be aligned, but they will form in a spherical region. These groups are sometimes called "spurs" (Allen, 1961).

II) Physico-chemical stage

At this stage a thermal equilibrium is established in the system between 10^{-15} and 10^{-12} seconds. The ejected electrons (e^-) have given their kinetic energy by ionizing or exciting other water molecules. They are then defined as sub-excited electrons (e^-_{sub}). These sub-excited electrons will then thermalize (e^-_{th}) and reach a kinetic energy of the order of 0.025eV. This procedure is followed by hydration of the electrons (e^-_{aq}). These hydrated electrons will orient the water molecules around them.

$$e^- \longrightarrow e^-_{sub} \longrightarrow e^-_{th} \longrightarrow e^-_{aq} \quad \text{(R2.15)}$$

There will be electrons which will not react according to the reaction chain presented above. The electrons of sub-excitation can, before their thermalization, be attached to a molecule of water, dissociated immediately to give (H^-) and ($^\bullet OH$):

$$e^- + H_2O \rightarrow H^- + {}^\bullet OH \quad \text{(R2.16)}$$

The hydride ion (H^-) will then react with a new water molecule to form dihydrogen (H_2) and hydroxyl anion (OH^-):

$$H^- + H_2O \rightarrow H_2 + OH^- \quad \text{(R2.17)}$$

In parallel, the H_2O^+ ion is not stable, and it reacts quickly with a molecule of water to form the H_3O^+ ion and the $^\bullet OH$ radical:

$$H_2O^+ + H_2O \rightarrow H_3O^+ + {}^\bullet OH \quad \text{(R2.18)}$$

The main rupture reaction of the excited water molecule (homolytic dissociation) leads to the production of the ($^\bullet$OH) and ($H^\bullet$) radicals. In order to stabilize, excited water molecules can also produce dihydrogen (H_2) and singlet oxygen ($O^\bullet(^1D)$). The latter, as unstable, will react with water to form a molecule of hydrogen peroxide (H_2O_2) or two hydroxyl radicals ($^\bullet$OH) (Tabata et al., 1991; Truppin-Wasselin, 2000):

$$H_2O^* \rightarrow H^\bullet + {}^\bullet OH \quad \text{(R2.19)}$$

$$H_2O^* \rightarrow H_2 + O(^1D) \rightarrow H_2 + 2\,{}^\bullet OH \text{ (or } H_2O_2\text{)} \quad \text{(R2.20)}$$

The formation of oxygen atoms in the triplet state ($O^\bullet(^3P)$) has been observed but this path of de-excitation is considered to be negligible:

$$H_2O^* \rightarrow 2H^\bullet + O^\bullet(^3P) \quad \text{(R2.21)}$$

Thus, at the end of this physico-chemical stage, the present radiolytic species in water are: e^-_{hyd}, $H^\bullet$, $^\bullet$OH, H_3O^+, OH^-, H_2, and H_2O_2.

III) The chemical stage

This stage is divided into two subcategories, heterogeneous chemistry and homogeneous chemistry.

A) Heterogeneous chemistry step:

During this stage, radical reactions within the spurs take place. Due to their high concentration recombination reactions are favored (Le Caër, 2011):

$$^\bullet OH + {}^\bullet OH \rightarrow H_2O_2 \qquad k = 5.5 \times 10^9\ M^{-1}.s^{-1} \quad \text{(R2.22)}$$

$$^\bullet OH + e^-_{aq} \rightarrow OH^- \qquad k = 3.0 \times 10^{10}\ M^{-1}.s^{-1} \quad \text{(R2.23)}$$

$$^\bullet OH + H^\bullet \rightarrow H_2O \qquad k = 2.0 \times 10^{10}\ M^{-1}.s^{-1} \quad \text{(R2.24)}$$

$$e^-_{aq} + H_3O^+ \rightarrow H^\bullet + H_2 \qquad k = 2.3 \times 10^{10}\ M^{-1}.s^{-1} \quad \text{(R2.25)}$$

$$e^-_{aq} + e^-_{aq} + 2H_2O \rightarrow H_2 + 2OH^- \qquad k = 5.5 \times 10^9\ M^{-1}.s^{-1} \quad \text{(R2.26)}$$

$$e^-_{aq} + H^\bullet + H_2O \rightarrow H_2 + OH^- \qquad k = 2.5 \times 10^{10}\ M^{-1}.s^{-1} \quad \text{(R2.27)}$$

$$H^\bullet + H^\bullet \rightarrow H_2 \qquad k = 7.8 \times 10^9\ M^{-1}.s^{-1} \quad \text{(R2.28)}$$

$$H_3O^+ + OH^- \rightarrow H_2O \qquad k = 1.4 \times 10^{11}\ M^{-1}.s^{-1} \quad \text{(R2.29)}$$

B) Homogeneous chemistry step:

During this stage (>10^{-7} seconds), the species that can escape from the spurs are called "primary products" of water radiolysis. These radical and molecular products are distributed homogeneously in the solution volume:

$$H_2O \rightarrow e_{aq}^-, H^\bullet, {}^\bullet OH, HO_2^\bullet, H_3O^+, OH^-, H_2, H_2O_2$$

(Auclair, 2001; Le Caër, 2011; Trupin-Wasselin, 2000).

2.2.3 Linear energy transfer (LET)

It is defined as the amount of energy (dE) deposited by the charged particle along its path (dx) in the solution. The LET SI unit is ($J.m^{-1}$) but ($keV.\mu m^{-1}$) is more commonly used. It is calculated by the Born-Bethe formula (Trupin-Wasselin, 2000):

$$LET = -\frac{dE}{dx} = \frac{4\pi Z^2 e^4}{m_e v^2} N.n. \ln\left(\frac{2m_e v^2}{I}\right) \qquad (E2.1)$$

Where: e is the charge of the electron

m_e is the mass of the electron at rest

v is the speed of the particle

N is the number of atoms or molecules of the target per volume unit

n is the number of electrons in the atom or the molecule

Z is the charge of the particule atomic number of the retarder material

I is the average excitation or ionization potential of the retarder material

Depending on the LET value of the incident ion, the spurs will be more/less close to each other. As it is seen in Figure 2.2.2, increasing LET leads to more dense spurs. If the energy (E) deposited by the electrons (or photons) of the radiations is less than 100 eV, then there is the formation of clusters with spherical geometry. If the energy remains below 500 eV a mixture of several spurs, called “blob” is formed. In this case, the secondary electrons are energetic enough to form other clusters very close to each other. If the energy varies between 500 eV and 5000 eV there is formation of "short tracks". However, due to the higher energies of the secondary electrons, the formation of an even greater number of spurs over a shorter distance

is observed. Finally for an energy exceeding 5000 eV there is the formation of a "branch track" which has a linear trajectory but different from the main trajectory (Crumiere, 2012).

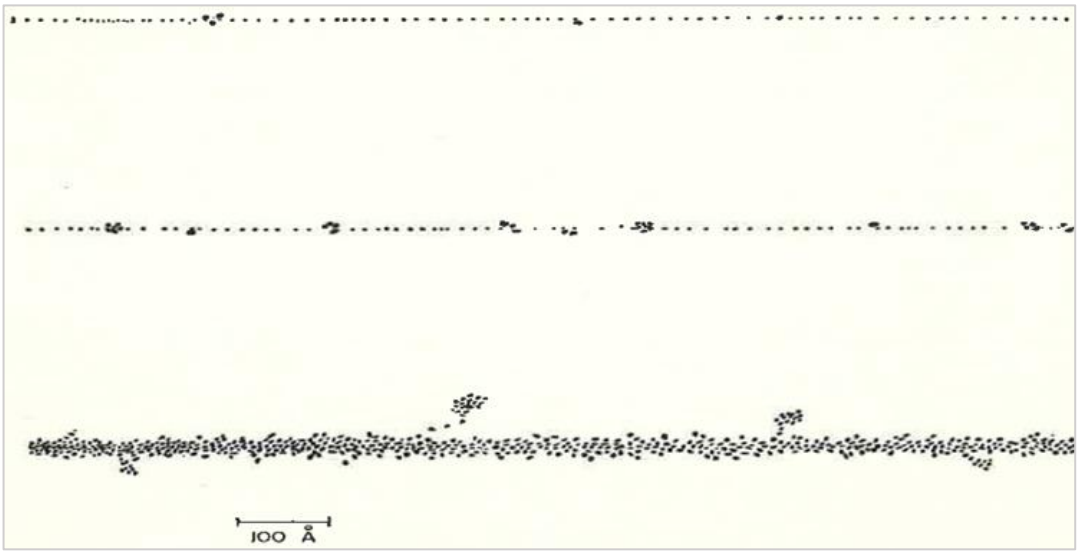

Figure 2.2.2: Schematic figure of the dependence of ionization by the energy. Each point represents an ionization in water produced by an energy deposit of 20eV. The first line for electrons of 40 kev (LET 0.08 eV/Å), in the center for deuterons of 180MeV (LET 0.5 eV/Å) and below the alpha of 5.5 MeV (LET 9eV/Å) (Allen, 1961)

2.2.4 Radiolytic yields

I) Definition

The radiolytic yield G_E is defined as the number of formed or destroyed species per unit of deposited energy. It is expressed in (µmol.J^{-1}), but also in (number of molecules for a deposited energy of 100 eV).

The conversion between these two units is: 1 molecule/100 eV = 0.1036 µmol J^{-1}.

$$G_E = \frac{[E]_t}{\mathrm{c} \times D_t} \qquad \text{(E2.2)}$$

In the above equation, G_E is the radiolytic yield of species E, $[E]_t$ is the concentration of the species E at time t (in mol.dm^{-3}), D_t is the dose received in solution at time t (J.kg^{-1}) and c it is a conversion factor (dimension of a density, kg.dm^{-3}).

The global or apparent radiolytic yields, denoted G_E, correspond to the radiolytic yields measured long after (several minutes) the passage of the radiation. The chemistry initiated by

the presence of the radicals formed and the direct action of ionizing radiation on the values of the measured yields are also two values which can influence the values of the radiolytic yields.

In parallel, the primary radiolytic yields, denoted g_E, correspond to the radical and molecular yields of the radiolytic species escaped from recombination. These radiolytic species are formed and distributed uniformly in the solution, per unit of energy deposited in the liquid (Auclair, 2001).

II) Parameters that can impact primary radiolytic yields

The values of the radiolytic yields can be influenced by the pH of the solution, the LET of the radiation and other parameters such as the quantity and the nature of dissolved species in solution, high pressures, high temperatures and high dose rates, happening simultaneously sometimes. The variations in radiolytic yields have been more studied in acidic than in alkaline media. In fact, studies in alkaline solutions are made more difficult due to the low number of solutes which can be used to determine the radiolytic yields by a capture method. Capture methods use chemical scavengers (chemical reagents in solution) which react specifically with a radical to form a stable product which could be dosed later. The scavengers that are used are either metal cations that precipitate in a solution with a high pH, or molecules that are destroyed at these pH values. Furthermore, the LET acts on the recombination in the ionization track and therefore the yields of the radicals are reduced while the yields of the molecules increase (Ferradini & Jay-Gerin, 2000).

1) Influence of pH

<u>Acidic medium</u>

To test the evolution of radiolytic yields in an acidic medium, initial work was carried out under gamma radiation using H_2SO_4 solution. For pH below 3, the H_3O^+ ions capture the majority, even all the hydrated electrons (e_{aq}^-) present in the spurs to form $H^\bullet$ (Buxton et al., 1988):

$$e_{aq}^- + H_3O^+ \rightarrow H^\bullet + H_2O, \qquad k = 2.25 \times 10^{10}\ M^{-1}.s^{-1} \qquad \text{(R2.30)}$$

$H^\bullet$ radical is not as reactive as hydroxyl radical ($^\bullet OH$). Thus, $^\bullet OH$ will react either with hydrated electron or the hydrogen radical ($H^\bullet$) (Elliot, 1994):

$$e_{aq}^- + {}^\bullet OH \rightarrow OH^- \qquad k = 3.02 \times 10^{10}\ M^{-1}.s^{-1} \qquad \text{(R2.31)}$$

$$H^\bullet + {}^\bullet OH \rightarrow H_2O \qquad k = 1.53 \times 10^{10}\ M^{-1}.s^{-1} \qquad \text{(R2.32)}$$

Due to higher rate of (R2.31), the $H^{\bullet}$ radical will remain less active within the spur or it will escape from it, increasing the associated radiolytic yield with increasing acidity.

The radiolytic hydrogen yield does not vary since it is not involved in any reaction.

All these values concerning the radiolytic yields in acidic solutions are mainly for ^{60}Co or accelerated electrons, which are considered as LET (~ 0.3 keV/μm) (Ferradini & Jay-Gerin, 2000).

Alkaline medium

Likewise, it can be assumed that the mechanisms for alkaline solutions work in the same way as in the acidic solutions. The hydroxide ions ($^{\bullet}OH$) deprotonate through the Reaction 2.32 (Ferradini & Jay-Gerin, 2000):

$$^{\bullet}OH + OH^{-} \rightarrow O^{\bullet-} + H_2O \qquad k = 6.3 \times 10^{9}\ M^{-1}.s^{-1} \qquad (R2.32)$$

When the pH values are high enough, the previous reaction consume practically all of the $^{\bullet}OH$ radicals, which could lead to the formation of hydrogen peroxide through Reaction 2.34 (Elliot, 1994). Consequently, this can decrease the yield of hydrogen peroxide:

$$O^{\bullet-} + O^{\bullet-} \rightarrow O_2^{2-} \qquad k = 10^{8}\ M^{-1}.s^{-1} \qquad (R2.33)$$

$$^{\bullet}OH + {}^{\bullet}OH \rightarrow H_2O_2 \qquad k = 5.5 \times 10^{9}\ M^{-1}.s^{-1} \qquad (R2.34)$$

The replacement of the $^{\bullet}OH$ radical by the $O^{\bullet-}$ radical, also because of their different rate constants between Reaction 2.35 (Christensen et al., 1994) and Reaction 2.36 (Matheson & Rabani, 1963), will increase the radiolytic yield of hydrated electron:

$$e_{aq}^{-} + {}^{\bullet}OH \rightarrow OH^{-} \qquad k = 3 \times 10^{10}\ M^{-1}.s^{-1} \qquad (R2.35)$$

$$e_{aq}^{-} + O^{\bullet-} \rightarrow 2\ OH^{-} \qquad k = 2.2 \times 10^{10}\ M^{-1}.s^{-1} \qquad (R2.36)$$

As it is shown in Figure 2.2.3, the radiolytic yield of H_2 seem to remain unchanged by variations in pH in alkaline regions, however several studies give contradictory results (Ferradini & Jay-Gerin, 2000).

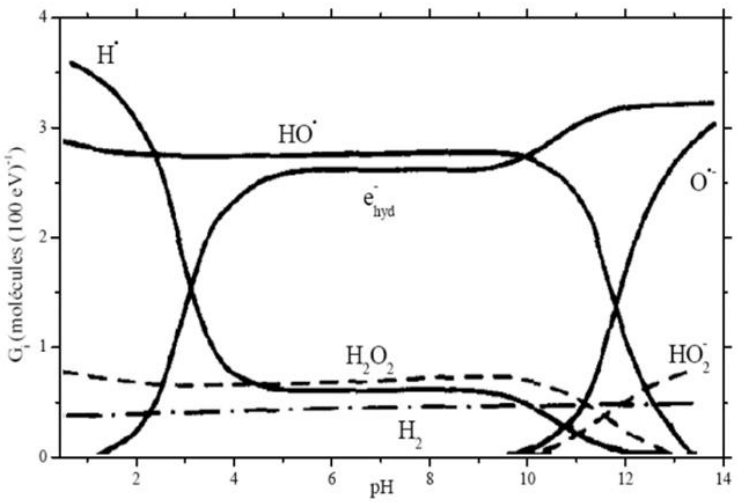

Figure 2.2.3: Evolution of radiolytic yields as a function of pH (Getoff, 1999)

2) The influence of LET

The Linear energy transmission (LET) is a very important factor for the variation of radiolytic yields. An increase of the LET value will cause heterogeneities within the volume of the solution and it will lead to the formation of spurs which are close to each other.

•At low LET (case of gamma radiation), the spurs are separated from each other, and the yield of molecular products comes from interaction between radicals from different spurs.

•At high LET (alpha radiation case), the radiolytic products react directly in the ionization zone. The possibility of covering the spurs is greater and it will favor recombination between radicals (Auclair, 2001).

As it is shown in Figure 2.2.4, the yields of molecular products (H_2, H_2O_2) increase with increasing LET, as they come from the recombination of the radicals H• and •OH.

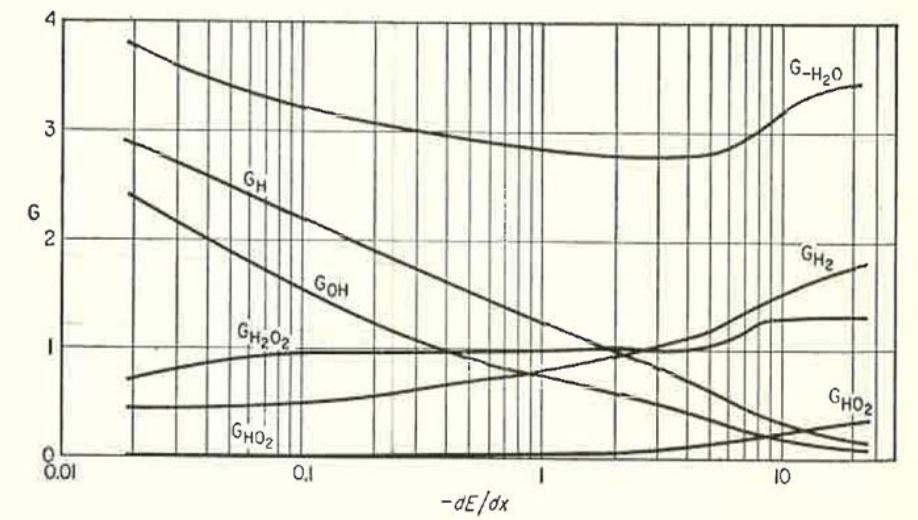

Figure 2.2.4: The influence of LET on the primary yields of radiolytic products in neutral solution (Allen, 1961)

2.3 The impact of water radiolysis on anoxic corrosion of steels

In the context of HLW disposal in deep geological disposal facility, the phenomenon of water radiolysis could effectively influence the safety of the installation. The impact of radiation on corrosion rates has been extensively studied and both enhancement and inhibition on corrosion rate have been observed. However, the mechanism that might explain these observations is still poorly understood. Corrosion process in aqueous medium can promote partial dissolution of the formed protective film, liberating iron ions in the bulk solution. Simultaneously water radiolysis will generate chemical species, whose concentrations depend on the radiation (spectrum, energy deposited in the medium), prone to intervene in the corrosion phenomena in particular by promoting various chemical and physicochemical processes such as redox reactions, gas evolution, changes in pH value or formation of precipitates (Figure 2.3.1). Therefore, it is important to study the combination of these two parallel processes thanks to experiments mimicking the representative conditions prevailing in deep geological disposal and to better understand the corrosion processes of steel. Several authors have examined the possible effect of the radiolysis of water on the behaviour non-alloy or low-alloy steels under disposal conditions.

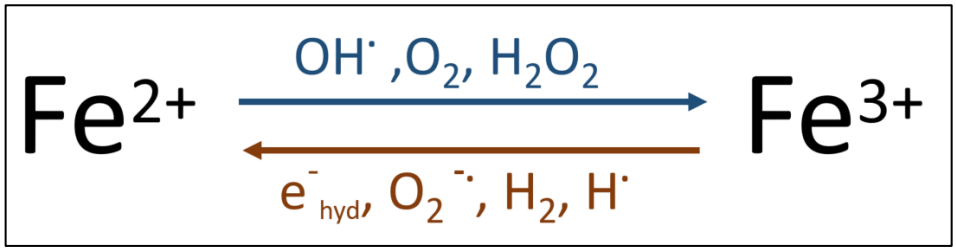

Figure 2.3.1 Oxidation-Reduction of iron ions with radiolytic species (Wren, 2005)

The following section is devoted to studies dedicated to anoxic corrosion of steel under ionizing radiation.

2.3.1 Experiments performed in pure water

Cuba et al. (2011) studied the impact of gamma radiation (total doses: 30, 60, 90, 120 kGy) on the anoxic corrosion of carbon steel samples immersed in deionized water at different temperatures (25, 50, 70°C). The generated solid corrosion products and dissolved iron species were also measured and characterized. The identified corrosion products were magnetite (Fe_3O_4) and lepidocrocite (γ-FeOOH) and the higher dissolution of corrosion product are obtained for the higher temperature and dose rate (Figure 2.3.2). The authors conclude that corrosion under gamma radiation occurs mainly by reaction with the intermediate products of water radiolysis (mainly H_2O_2 and the radicals $^{\bullet}OH$, $HO_2^{\bullet}$).

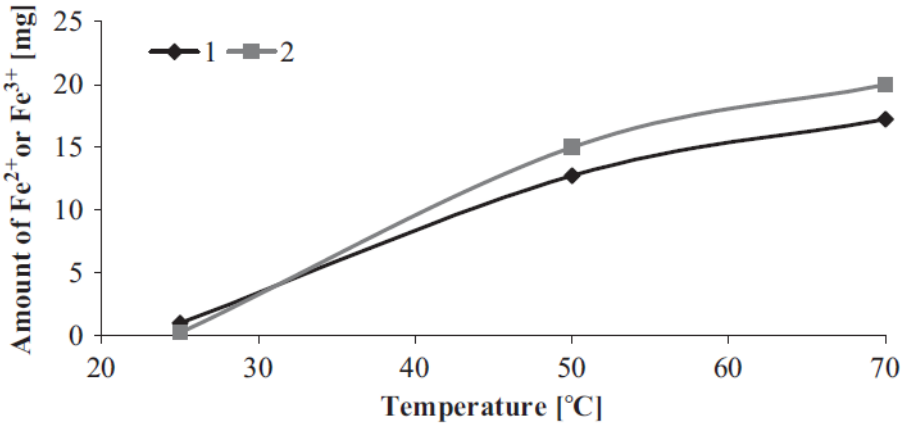

Figure 2.3.2: Dependence of total amount of 1— Fe^{2+} or 2— Fe^{3+} ions at temperature of irradiation (dose 90kGy) in deionized water saturated with nitrogen (Cuba et al., 2011)

The fact that higher corrosion product dissolution was observed in higher dose rates experiments is in accordance with the work of Neufuss et al. (2006) whose study the anoxic corrosion of carbon steel sample in deionized water under gamma radiation (total dose ranging from 0 to 120kGy) at a temperature of 70°C. The concentrations of corrosion products (sum of Fe^{2+} /Fe^{3+} ions in both solid and liquid phase) were varying from 0.28 to 1.78 $g.L^{-1}$. Additional conclusions concerning the influence of ionizing radiation on a carbon steel/water system were that (i) irradiation strongly affects the corrosion kinetics (corrosion rate increase) due to generation of oxidising agents in the aqueous medium and (ii) the type and distribution of the corrosion products depend on certain experimental parameters (temperature, presence of oxygen).

In a work of Traboulsi (unpublished) we find measurements of hydrogen production linked to the anoxic corrosion of immersed carbon steel samples in pure deaerated water under gamma radiation. Radiolysis took place after exposure to gamma radiation at dose rate of 50 $Gy.h^{-1}$ at room temperature and at neutral pH. The production of hydrogen is monitored during three successive phases: (i) anoxic corrosion pre-irradiation, ii) anoxic corrosion under irradiation and iii) anoxic corrosion post-irradiation. During the post-irradiation phase, hydrogen production increased slightly in comparison with the initial gas generation (pre-irradiation phase). The structural characterization of the metal samples indicates the presence of both magnetite (Fe_3O_4) and lepidocrocite (γ-FeOOH).

Badet (2014) carried out a characterization of the corrosion products layers observed on the surface of pure iron samples, immersed in deaerated water in a close system under anoxic conditions, with or without carbonate and submitted to gamma radiation (< 1$kGy.h^{-1}$) at ambient temperature. In dearated water without carbonate, the only detected corrosion product was magnetite (Fe_3O_4), except for the samples which have undergone the highest cumulative dose, where traces of lepidocrocite (γ-FeOOH) were also identified. Regarding the medium with carbonates, chukanovite ($Fe_2(OH)_2CO_3$) is the main detected corrosion product regardless the irradiation conditions. For the high irradiation conditions, ferric (Fe (III)) phases could be detected. These ferric species (ferrihydrite, goethite) are observed in minor proportion compared to chukanovite, and are not systematic. Their appearance could be explained by the radiolysis oxidation of Fe^{2+} ions into Fe^{3+} ions which will be accumulated at higher dose to then precipitate upon the chukanovite crystals. Concerning the corrosion rates, they were evaluated in the two tested media (with or without carbonates). For the pure water experiments performed at a dose rate of 0.3 $kGy.h^{-1}$ the corrosion rate was initially close to 2.5 $\mu m.year^{-1}$ but it decrease over time at value lower than 1 $\mu m.year^{-1}$ after 99 days of exposure.

In the carbonated medium, at the same dose rate, the initial corrosion rate is recorded around 7 μm.year^{-1}, passing then at 1 μm/year after 340 days. However, there is an important increase in the corrosion rate with an increase in the accumulated dose (830 kGy).

Vandenborre et al., (2013) studied the effect of alpha radiation (1.2–22.5 Gy.h^{-1}) on corrosion processes, by immersing pure iron and carbon steel samples in pure water. The obtained results demonstrate the formation of lepidocrocite (γ-FeOOH) in the case of carbon steel samples, and the formation of magnetite (Fe_3O_4) in the case of pure iron. In addition, the authors mentioned a non-negligible consumption of hydrogen in the case of pure iron samples tests, in comparison with the carbon steel samples tests. For this reason, the authors proposed a chemical mechanism explaining that the H_2 consumption is directly linked to the detected magnetite phase. More specifically, the Fe(III) species in solution can be partially reduced by H_2 species produced by water radiolysis. Particularly, in the case of the pure iron surface, the Fe(III) reduction into Fe(II) can explain the magnetite phase formation/precipitation at the metallic surface with the associated H_2 consumption. Furthermore, in the case of pure iron samples tests, they indicated that lepidocrocite (γ-FeOOH) is only an intermediate phase which is partially reduced to form magnetite (Fe_3O_4). These results are in agreement with those presented in the literature where it is presented that gamma radiation can induce a transformation of different iron oxy-hydroxides phases, like goethite (α-FeOOH) or akaganeite (β-FeOOH), into magnetite (Fe_3O_4) (Wang & Xin, 1999). Finally, the authors emphasized the importance of determining the contents of hydrogen peroxide (H_2O_2) in solution because of its essential role in the oxidation reaction of the iron surface.

The great importance of hydrogen peroxide in the corrosion process under irradiation has also been mentioned by Raiman et al., (2017). In this study, stainless steel sample are immersed in water (neutral pH) at high temperature and exposed to alpha radiation with maximum duration of 72 hours. Radiation has been found to increase corrosion potential, with H_2O_2 being the dominant radiolysis product contributing to this raise. Hematite (α-Fe_2O_3) was the main formed oxide, and is attributed to the oxidation of magnetite (Fe_3O_4).

Fujita et al., (2000) also states the presence of magnetite in pure water at higher temperatures. In this study, carbon steel samples in anoxic conditions with and without gamma radiation (0.48 kGy.h^{-1}) have been examined. It is emphasized the strong enhancement of corrosion rate associated to irradiated samples, almost six times higher than the non-irradiated ones. The authors suggested that since Fe_3O_4 is formed, further corrosion could be suppressed.

2.3.2 Experiments with synthetic water

I. Near neutral pH

Eriksen & Jacobsson (1983), tried to estimate the radiolytic production of hydrogen arising from compacted bentonite (containing dissolve Fe^{2+} ions in solution) samples exposed to gamma rays (0.5 $Gy.h^{-1}$). Compacted bentonite was equilibrated with slightly acidified synthetic solution (pH 6.5) and then in contact with synthetic pore water and has been irradiated for almost 10 days as it is seen in Figure 2.3.3. The H_2 concentration in the gaseous phase at the lower dose rate has been measured at 17 x 10^{-6} $mol.L^{-1}$ while for the highest dose rate the production of H_2 was 30 times higher, showing the dependence of hydrogen production on dose rate. Furthermore, the extracted Fe^{2+} from bentonite solution was measured in concentration 8.6 x 10^{-6} $mol.L^{-1}$ and the authors conclude especially on high dose rates, that there is strong H_2 dependence on the concentration of $^{\bullet}OH$ scavengers in the solution. $^{\bullet}OH$ radical can consume H_2 and therefore the increased H_2 values in their experiments are explained by the presence of $^{\bullet}OH$ scavengers e.g. Fe^{2+}/HCO_3^- able to consume faster $^{\bullet}OH$ radical.

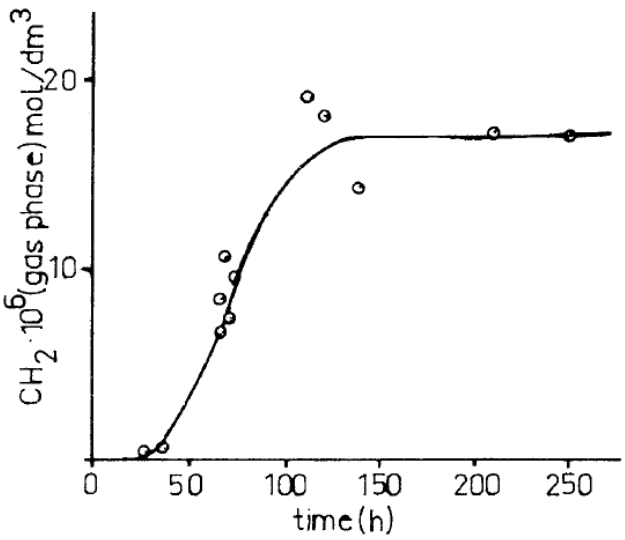

Figure 2.3.3: H_2 concentration in gas phase over time, using ^{137}Cs at 0.5$Gy.h^{-1}$ (Eriksen & Jacobsson, 1983)

In the work of Cuba et al. (2011) using carbon steel samples immersed in granitic groundwater under gamma radiation, no observation neither characterization of the formed corrosion products was performed but the total amount of Fe^{2+} and Fe^{3+} found in solid and liquid phase varying between 0.3 to 48.0 mg for 30 kGy and 120 kGy total dose, respectively. Temperature variations (25, 50, 70°C) were found to affect the corrosion system directly via a change of corrosion reaction rate, and indirectly by a change of solubility of various compounds, including corrosion products. The results are in good agreement with the work of Neufuss et

al., (2006), studying the concentration of dissolved corrosion products on irradiated iron samples immersed in granitic groundwater at 70°C and exposed to similar dose rates. Moreover, these results indicate that the presence of impurities in granitic water doesn't seem to significantly affect the corrosion process.

II. High pH

Smart et al. (2008) conducted long term experiments (several months) aimed at studying the effect of gamma radiation on carbon steel anaerobic corrosion in conditions mimicking the environment prevailing in a deep geological disposal. Experiments were carried out at two different temperatures (30°C and 50°C), for two dose rates (11 $Gy.h^{-1}$ and 300 $Gy.h^{-1}$) and in two different chemical environments, artificial granitic porewater (pH~8.8) and equilibrated-bentonite water (pH~10.4). Figure 2.3.4. shows that radiation increase the rate of corrosion for both dose rates, but the greatest increase has been observed at the highest dose (Figure 2.3.4.b). The enhancement of the corrosion rate is greater in synthetic groundwater than in bentonite-equilibrated groundwater, which had a higher ionic strength and alcaline pH. In addition, after 4000 hours of irradiation at a dose rate of 11 $Gy.h^{-1}$, the synthetic groundwater had a corrosion rate lower than 1 $\mu m.year^{-1}$ while the equilibrated bentonite had 0.05 $\mu m.year^{-1}$. The main corrosion product observed was magnetite (Fe_3O_4), although the authors indicated that radiation at higher dose rates can lead to the formation of a few additional unidentified iron oxy-hydroxide (FeOOH) species. It was observed that the corrosion products formed at higher dose rate (300 $Gy.h^{-1}$) had a more brownish coloration compared to the specimens produced at the lower dose rate or even without irradiation, which were blacker. These results suggest that the presence of radiolytic species in the solution leads to the formation of different higher oxidation state iron corrosion products.

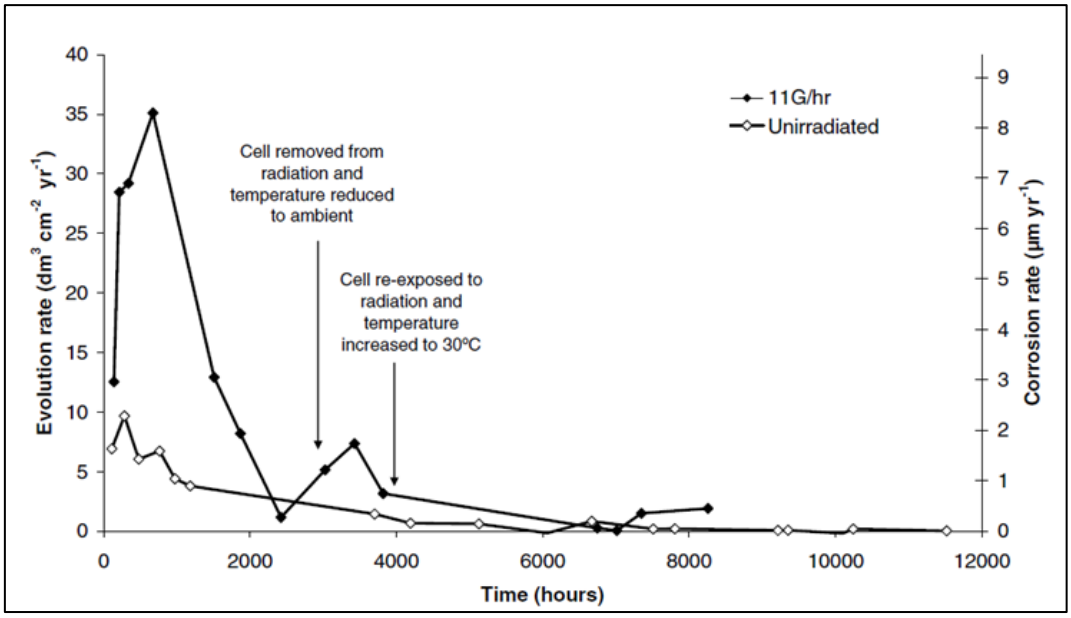

(a)

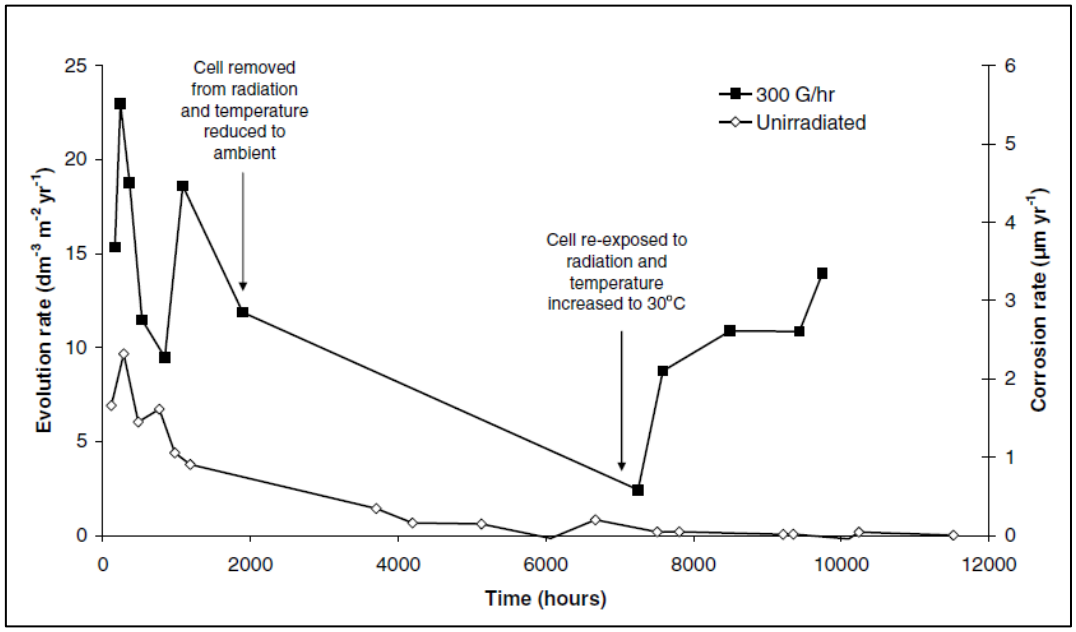

(b)

Figure 2.3.4: Hydrogen evolution rates and corrosion rates for carbon steel in synthetic granitic pore water at 30°C, with and without irradiation a) at 11Gy.h^{-1}, b) at 300Gy.h^{-1} (Smart et al., 2008)

Marsh and Taylor (1988) performed experiments using carbon steel samples immersed in two different solutions, a synthetic granitic groundwater (pH 9.4) and a synthetic seawater and exposed to ^{60}Co gamma radiation at dose rate varying between 1000 and 1500 Gy.h^{-1}. Weight loss measurements performed on samples immersed in granitic groundwater and exposed to irradiation during 200 days indicated a corrosion rate value of 3 µm.year^{-1}, without any

localised attack. For similar irradiation duration, the samples tested in seawater solution indicated corrosion rate value of 100 μm.year^{-1}, even if after 100 days of exposure it was noted a progressive decline of the corrosion rate.

In a more recent study, Smart et al. (2017) performed experiments using gamma radiation on carbon steel samples immersed in an alkaline medium (pH~13.4) to test the impact of both cementitious solutions (YCW) and possible contaminants (Cl, $S_2O_3^{2-}$, S^{2-}) on corrosion processes. Concerning long-term measurements, the corrosion rates calculated from the hydrogen generation are less than 0.1 μm.year^{-1} (10000 h) and are in good agreement with the weight loss measurements performed in parallel. Moreover, the authors observed that the long-term corrosion rates don't seem to be impacted by the experimental conditions such as the temperature, the presence of chloride or sulphure or the radiation. For the authors, the fact that metallic samples were not pre-corroded is maybe the reason why hydrogen gas generation rate are similar for the test with or without sulphides. Also, the fact that corrosion rate is not affected by the presence of chloride in the solution is due to the significantly low concentration of oxygen, even in the presence of ionizing radiation where it was expected to have more oxidizing species. Finally, this very low corrosion rate may be connected to the formation of a thin protective layer mainly composed of magnetite.

Winsley et al. (2011) monitored the evolution of H_2 production generated by the gamma radiation (25 Gy.h^{-1}) of a close system composed by carbon steel samples immerged in alkaline solution (pH=13.4), at 25°C and 80°C. The results associated to hydrogen generation monitoring indicated that, for long term observations, there is no significant difference between the irradiated and the unirradiated samples. Moreover, the experiments aiming to test the impact of temperature variations showed that the initial corrosion rate was higher at 80ºC than at 25ºC, and that the decrease of this rate was faster at 80°C than at 25°C (Figure 2.3.5). Furthermore, the impact of chloride in test solution (100 ppm) was studied for the experiments at 80°C. The results after 5350 hours of exposure seem to indicate that chlorides don't favor a significant increase of the corrosion rate (3.6 μm.year^{-1} with Cl^- and 2.5 μm.year^{-1} without Cl^-aaddition). Finally, analyzes carried out by Raman spectroscopy indicated the presence of magnetite (Fe_3O_4) on the surface of the non-irradiated samples at 80ºC, while results associated to structural characterization of irradiated samples are not provided by the authors.

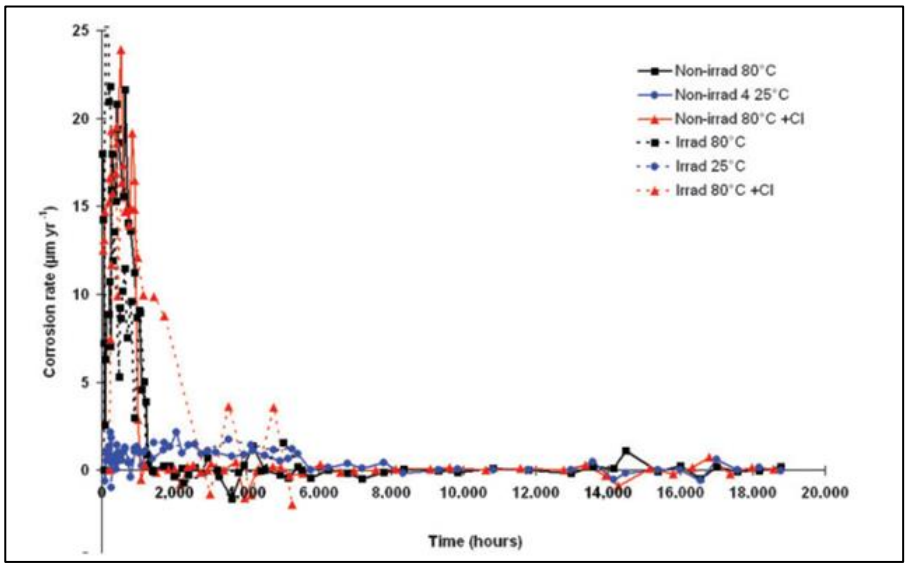

Figure 2.3.5: Evolution of corrosion rate by carbon steel in an alkaline simulant pore water with and without irradiation as a function of temperature and chloride concentration (Winsley et al., 2011)

The following tables present a summary of the above-mentioned studies with the main corrosion products observed:

Tested medium	Corrosion rate	Corrosion products	pH	Temperature (°C)	Dose	Time	Reference
Pure water	-	Magnetite, lepidocrocite	6.5	25	90 kGy (γ-rays)	-	(Cuba et al., 2011)
	5	Magnetite	6.5	25	0.3 kGy.h^{-1} (γ-rays)	15 days	(Badet, 2014)
	< 1	Magnetite				99 days	
	3.5-5.5	Magnetite lepidocrocite			1 kGy.h^{-1} (γ-rays)		
	-	Magnetite lepidocrocite	6.5	25	1.2 kGy (α-rays)	15 min	(Vandenborre et al., 2013)
	-	Magnetite, α-Fe	6.5	250	0.48 kGy.h^{-1}	651 hours	(Fujita et al., 2000)
Pure water with carbonates (10^{-2}M)	7-8	Chukanovite	7.1	25	0.3 kGy.h^{-1} (γ-rays)	15 days	(Badet, 2014)
	2	Chukanovite				109 days	
	1	Chukanovite with traces of ferrihydrite				340 days	
	2.8	Chukanovite, lepidocrocite goethite			1 kGy.h^{-1} (γ-rays)	109 days	
	1.7	Chukanovite				340 days	

Table 2.3(a): Main identified corrosion products on studies with anoxic corrosion of steel under ionizing radiation.

Tested medium	Corrosion rate	Corrosion products	pH	Temperature (°C)	Dose	Time	Reference
Synthetic groundwater	< 1	Magnetite (traces of oxyhydroxides in higher dose rates)	8.8	30	11 $Gy.h^{-1}$ (γ-rays)	166 days	(Smart et al., 2008)
Bentonite-equilibrated groundwater	0.2		10.4	50			
Synthetic alkaline porewater	< 0.1	Magnetite (presence of oxyhydroxides)	13.4	28-80	25 $Gy.h^{-1}$ (γ-rays)	5.7 years	(Smart et al., 2017)
Granitic groundwater	3	-	9.4	90	1 $kGy.h^{-1}$ (γ-rays)	200 days	(Marsh & Taylor, 1988)
Synthetic seawater	100	-	-			100 days	
Alkaline simulated porewater	2.4	-	13.4	80	25 $Gy.h^{-1}$	5500 hours	(Winsley et al., 2011)
Alkaline *simulated porewater* (Cl-addition: 100 mg/L)	3.6					6000 hours	
Alkaline simulated porewater	1.4			25		5350 hours	

Table 2.3 (b): Main identified corrosion products on studies with anoxic corrosion of steel under ionizing radiation.

In conclusion, while a range of individual studies has been performed to understand the impact of several parameters such as the dose rate (or total dose), the temperature or the physico-chemical properties of the solution, the observed effects of ionizing radiation on steel corrosion are still conflicting. Even though, most studies demonstrate that carbon steel corrosion rate is clearly enhanced by radiation exposure (Fujita et al., 2000, 2001; Marsh & Taylor, 1988; Smart et al., 2008), some others tend to indicate the contrary (Ahn & Soo, 1995; Kursten et al., 2011; Smailos et al., 1990). In parallel, while a large majority of the works cited above agreed on the fact that magnetite (Fe_3O_4) is the predominant corrosion product which is form under such experimental conditions, many key questions regarding the mid and long-term evolution of this oxide film properties, induced by the physico-chemical modifications of the solution caused by irradiation, remain unanswered.

2.4 Summary and thesis objective

This review on studies dealing with anoxic corrosion under irradiation helps us better understand the effect of water radiolysis on corrosion systems. Initially, in corrosion under anoxic conditions, it is observed that the production of hydrogen gas is accompanied by the production of ferrous iron ions which can further precipitate and influence the chemical conditions of the aqueous medium. In anoxic conditions, the corrosion rate show a progressive decrease attributed to the passivation of the metal surface through the formation of layers of mixtures mainly composed by iron oxides, hydroxides and oxyhydroxides. Therefore, after summarizing the results associated to anoxic corrosion studies, it seems that the mainly formed oxide is magnetite (Fe_3O_4). However, it appears that the nature of the formed iron oxides depends on parameters such as the temperature, the redox and the pH of the aqueous medium. Impact of ionizing radiation on anoxic corrosion processes has also been studied as irradiation is capable of modifying considerably the physico-chemical conditions of the system, due to the creation of radiolytic species which govern the redox conditions of the anoxic aqueous medium and thus, contributes to the production of hydrogen. Previous studies have identified the impact linked to the radiolysis process, which is highly dependent on parameters such as pH, LET and also, on the presence of hydrogen peroxide (H_2O_2), due to its catalytic role on corrosion processes. The relevant studies with the presence of irradiation indicated that the formed corrosion products should be affected from the tested medium, although once again, the presence of magnetite is also evident in the vast majority of the characterisations. Except magnetite, higher oxidation states of not-well crystallised corrosion products have been

reported and are attributed to exposure to higher radiation rate. However, there are still many questions, in particular regarding the processes and mechanisms associated to the production of hydrogen for an "anoxic corrosion under irradiation" system. More specifically:

- Does radiation really impact the corrosion processes and the associated corrosion rate?
- What is the origin of the gradual decrease in hydrogen production during the irradiation phase, observed in several experiments?
- How does the system behave in the presence of water whose composition is close to that of natural argillaceous pore water or slightly alkaline synthetic solution?

Thus, there are still many uncertainties concerning the phenomena of anoxic corrosion under radiation. In this perspective, this thesis work aims to study:

- The evolution of hydrogen production recorded before, during and after the irradiation for two systems: (i) the first one, containing ultrapure deaerated water, dedicated exclusively to water radiolysis processes and (ii) the second one, containing the same volume of ultrapure deaerated water and also metallic samples, dedicated to anoxic corrosion under irradiation. The two systems are monitored in parallel and under identical conditions. By subtracting the H_2 production associated to the cells containing only ultrapure deaerated water from the one generated by the cells containing pure deaerated water and metallic samples, it should permit to estimate the volume of hydrogen generated only by the process of anoxic corrosion under irradiation and to calculate the associated corrosion rate.
- The formation of oxide layers on metal surfaces and their influence on the production of hydrogen.
- The impact of irradiation on the mid to long-term properties (growth, stability, micro-porosity, conductivity) of such neoformed corrosion products
- What is the influence of temperature on these phenomena?
- The theoretical production of hydrogen linked to radiolysis via modelling work.

Therefore, in chapter 3 will be shown the experimental approach that we followed in order to answer the previous questions. In chapter 4 and 5, we will present all the obtained experimental results as well as the simulation work that we performed in parallel. In chapter 6, the results will be categorised accordingly to be further discussed and finally, in the last chapter, the conclusions of this work will be presented.

Chapter 3: Experimental setup

3.1 General approach

A schematic overview of the innovative dynamic experimental setup used in this work to study the impact of gamma-radiation on anoxic corrosion of steel processes is given in Figure 3.1.1.

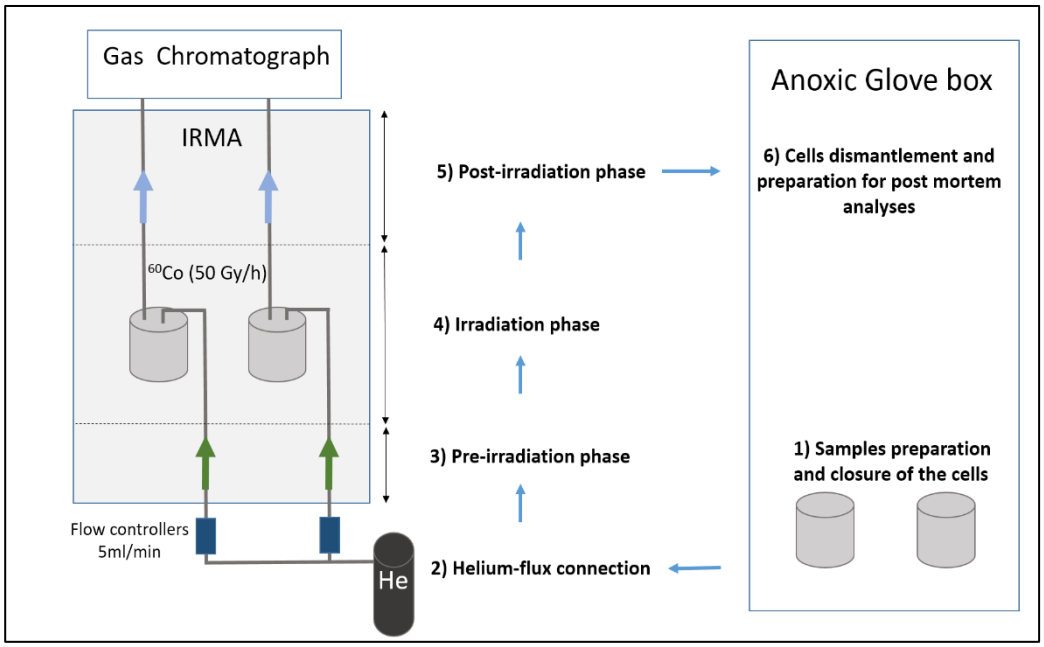

Figure 3.1.1: Experimental setup of this study to measure H_2 production from both water radiolysis and carbon steel anoxic corrosion under gamma radiation processes

It allows to distinguish between the hydrogen production attributed to anoxic corrosion and the one imputed to radiolytic process by measuring continuously the H_2 gas generated by two parallel systems: one cell containing six carbon steel samples immersed in solution, the other cell containing only the same volume of solution. These two stainless steel cells are placed into an irradiation chamber where they are exposed to gamma radiation and their H_2 evolution is recorded using an in-line gas chromatograph. The hydrogen production is monitored before, during and after irradiation under anoxic conditions and at ambient temperature.

At the end of the experiment, the cells are dismantled in an anoxic glove box to collect solid (metallic samples) and liquids (immersion solution) samples which are subjected to post-mortem analyses.

3.2 Experimental setup

3.2.1. General description

For experimental system involving metallic samples, the coupons are inserted in a dedicated borosilicate glass sample holder (Figure 3.2.1.b) which allow to maximize the carbon steel surface available for corrosion processes. The sample holder is then introduced in a borosilicate glass beaker containing a given volume of solution (mainly 200 mL) sufficient to ensure a total immersion of the coupons. The beaker is then emplaced in a stainless-steel cell made up of a cylindrical body (10.4 cm, r =11cm) (Figure 3.2.1.a) and a cover fitted with a tin seal allowing it to be hermetically closed. The cell cover is fitted with two stainless steel line allowing the circulation of a carrier gas. The input line has a sufficient length to get into the solution contained in the beaker whereas the output line internal extremity is located at the same level as the beaker upper part (Figure. 3.2.1(c-d)). Both lines are equipped with a valve on their external part to avoid any unintended oxygen contamination during cells transportation.

In parallel, an experimental system dedicated to water radiolysis study is prepared following the same procedural steps as in the case of experimental system involving metallic samples, except the introduction of the sample holder containing the coupons. To ensure that inert atmosphere prevail in our experimental cells and to avoid any further oxidation of the metallic coupons, all these preparation processes are performed in an anoxic glove box under continual nitrogen (N_2) flow. Once the cells are closed their tightness is checked via leak detector (Leybold Infinicon, UL 200).

After their preparation under inert atmosphere, both cells are hermetically closed and transported from the glove box into the irradiation chamber. Thanks to the input/output lines, the cells are then connected to the circulation system making possible to inject a carrier gas into the solution (input line) and to flow continuously the produced hydrogen gas towards a gas chromatograph (output line) via flow-controllers, set at 5 $ml.min^{-1}$.

Accordingly to a predetermined analytical sequences, hydrogen production relative to each cell is independently measured every 20 minutes before, during and after irradiation period. Once irradiation phase stopped, cell containing only ultrapure deaerated water is disconnected from the circulation system whereas cell containing metallic samples and ultrapure deaerated water remains connected for some days more. The corrosion rate estimation is due to the precise measurement of molecular hydrogen production in the cells. By subtracting the H_2 production associated to the cells containing only pure deaerated water from the one generated by the cells containing pure deaerated water and metallic samples, it should permit to estimate the volume of hydrogen generated only by the process of anoxic corrosion under irradiation. These results

are converted from hydrogen in mol.min^{-1} to corrosion rate in µm.year^{-1} based on calculations from previous studies (Smart & Rance, 2005).

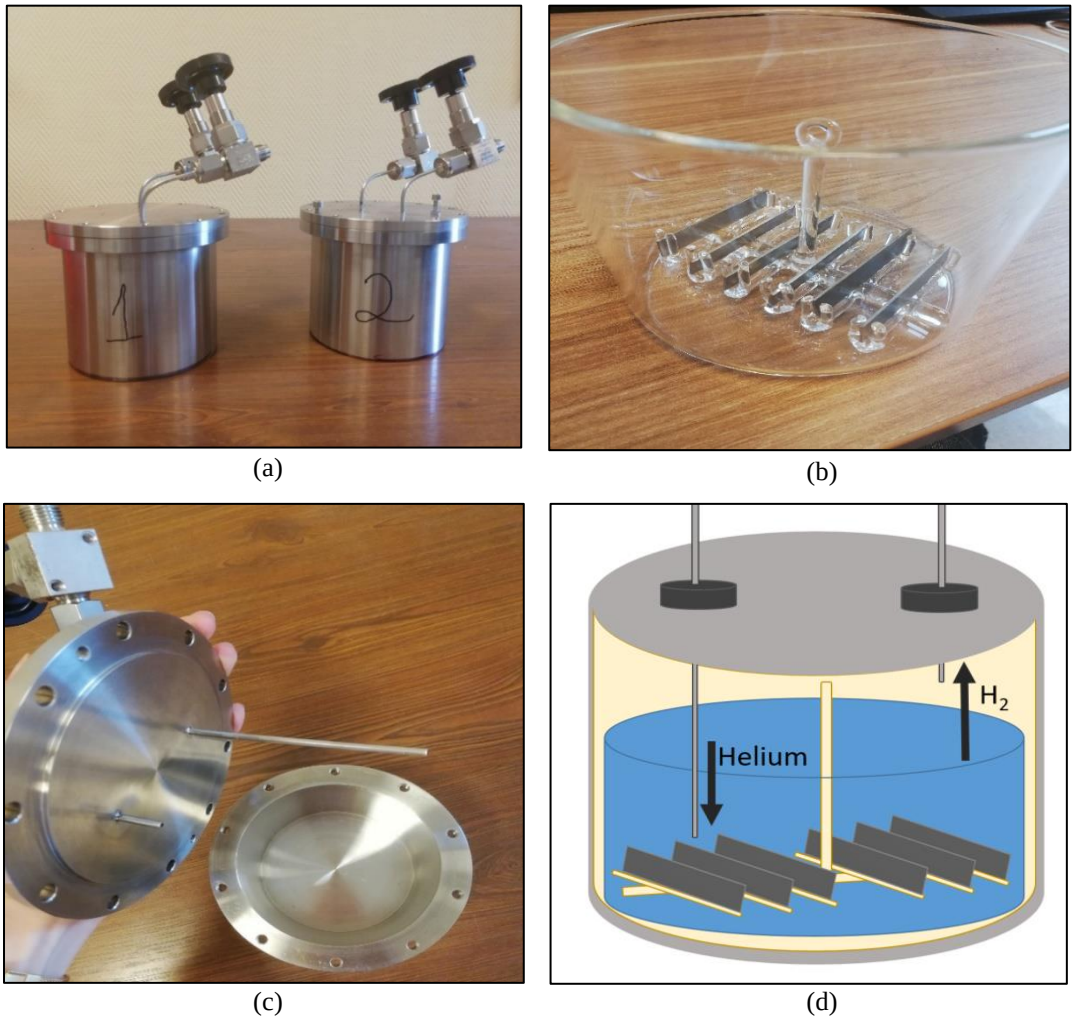

Figure 3.2.1: a) Image of the two identical stainless-steel cells, b) image of the borosilicate glass beaker and sample holder for the metallic samples, c) image of the cell's cover with the input and output line, d) schematic view of a cell 1 (with metallic samples) connected to the gas circulation system

At the end of the experimental tests, cells are disconnected from the circulation system and transported into the glove box to be dismantled, in order to collect the carbon steel coupons and the solutions under anoxic conditions.

3.2.2 Samples

3.2.2. a) Solid samples

Corrosion experiments are performed on coupons (50 x 10 x 1 mm) of commercially available S235 carbon steel (max. 0.17 wt% of C, 1.40 wt% of Mn, 0.03 wt% of St, 0.02 wt% of P, 0.02 wt% of S). To minimize the amount of surface oxide present before the start of the experiments, the metallic samples are polished in two distinct way: (i) either rough polishing using SiC paper, grad-220 and grad-1200 (Figure 3.2.2 .b) or (ii) mirror polishing using diamond paste (Figure 3.2.2.c).

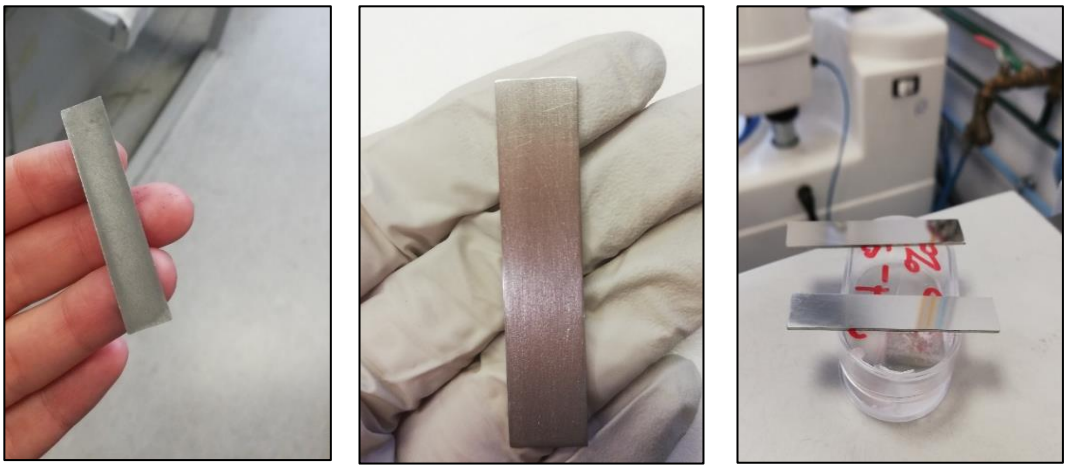

(a) (b) (c)

Figure 3.2.2: a) Image of the metallic sample before any treatment, b) image of the rough surface sample using SiC paper, c) image of the mirror-effect polishing sample

After polishing, which takes place only some hours before the experiment, the samples are cleaned for 10 minutes with ethanol in an ultrasonic bath and then they are let to dry.

3.2.2. b) Liquid samples

For each individual test, the volume of tested solution remained exactly the same for both cells (with or without metallic coupons). Before introduced into the cell, each tested solution was deaerated through agitation during several hours into the anoxic glove box. In order to test the impact of solution's chemical composition on anoxic corrosion of carbon steel, three different solutions have been used:

- Ultrapure water

  Five tests where dedicated to study the impact of ultra-pure deaerated water on carbon steel anoxic corrosion processes without any impact of other solutes and impurities (experiments A, B, C, E, F).

  The volume of ultrapure deaerated water (Millipore Alpha-Q with an electrical resistivity of 18.2 MΩ) was varying from 100 to 200 mL in order to sufficiently cover the samples and ensure their total immersion.

- Argillaceous rock synthetic pore water

  To get closer to the real deep geological disposal conditions, it is important to study the corrosion processes impacting carbon steel materials when exposed to argillaceous rock pore water. Due to the very low porosity and permeability properties of this argillite, it's not possible to sample directly neither indirectly the pore water naturally present in its porosity. Thereby, the chemical composition of this pore water is estimated thanks to diffusive exchange experiments. The chemical composition of the synthetic argillaceous rock pore water used in this study corresponds to the Upper Toarcian Tournemire argillite pore water. The final composition of this synthetic pore water is given in Table 3.2.1.

Ions	Na^+	K^+	Mg^{2+}	Ca^{2+}	Cl^-	SO_4^{2-}	HCO_3^-	pH
Concentration ($mmol.L^{-1}$)	22.0	0.3	1.0	1.6	4.5	2.5	4.0	7.5

Table 3.2.1: Chemical composition of Upper Toarcian Tournemire argillite pore water

The associated masses of salts that have been mixed to one liter of ultrapure water (Millipore Alpha-Q with an electrical resistivity of 18.2 MΩ) for the fabrication of this solution are shown in Table 3.2.2. These solutions have been prepared in the anoxic glove box and deaerated by agitation.

Salts	$MgSO_4\,7H_20$	Na_2SO_4	$NaHCO_3$	NaCl	$CaCl_2\,2H_2O$	KCl
Mass (g)	0.246	1.207	0.336	0.058	0.235	0.022

Table 3.2.2: Measured salts masses for the fabrication of 1L of Upper Toarcian Tournemire argillite pore water

Four tests were dedicated to study the impact of the synthetic argillaceous rock pore water on carbon steel anoxic corrosion processes, two full-length experiments (experiment D, G), one short-term test (experiment D++) and one short-term experiment without irradiation (experiment D+).

The volume of synthetic argillaceous rock pore water was 200 mL in order to sufficiently cover the samples and ensure their total immersion.

- MREA-TRNM solution

According to the multi-barrier concept developed for the deep geological disposal, HLW overpack will be inserted in a carbon steel casing tube within horizontal micro-tunnel drilled in the highly impermeable Callovo-Oxfordian (COx) clay rock. In parallel, it is planned to inject a bentonite-cement grout material (MREA: Matériau de Remplissage de l'Espace Annulaire) in the annular space between the hosting rock and the carbon steel liner. This grout pore water is associated with a slightly alkaline pH (10 < pH < 11) and it aimed to neutralize the transient acid disturbance to decrease the corrosion rate. Thus, to test how this MREA pore water could impact the corrosion processes of the carbon steel, a full-length experiment has been performed by using an "MREA-TRNM" synthetic solution as aqueous medium (experiment H). This "MREA-TRNM" synthetic solution composition, proposed and used in the BACUCE in situ experiment (EURAD – ACED), correspond to a theoretical mix of 75 % of hydrated bentonite/grout pore water and 25 % of Tournemire argillite pore water. This 3/1 ratio mimicked the flux of the Tournemire pore water within the system. The final composition of this synthetic pore water is given in Table 3.2.3.

Ions	Na^+	K^+	Mg^{2+}	Ca^{2+}	Cl^-	SO_4^{2-}	HCO_3^-	NO_3^-	pH
Concentration ($mmol.L^{-1}$)	7,22	1,62	0,25	1,19	1,95	2,75	1,00	0,02	10,7 –10,9

Table 3.2.3: Chemical composition of MREA-TRNM synthetic solution

The associated masses of salts that have been mixed to one litter of ultrapure water (Millipore Alpha-Q with an electrical resistivity of 18.2 MΩ) for the fabrication of this solution are shown in Table 3.2.4. These solutions have been prepared in the anoxic glove box and deaerated by agitation.

Solute	Mass (g)
$CaCl,2H_2O$	0.115
$CaCO_3$	0.041
$NaNO_3$	0.002
$Na_2SO_4,7H_2O$	0.356
$NaHCO_3$	0.084
NaCl	0.018
KCl	0.006
solution	Volume (mL)
KOH (1M)	0.76
NaOH (1M)	0.88

Table 3.2.4: Measured salts masses/volume of solution for the fabrication of MREA-TRNM, synthetic solution

3.2.3 Gas Chromatograph

3.2.3. a) Principle

Gas chromatography (GC) is a common type of chromatography used in analytical chemistry for separating and analysing compounds that can be vaporized without decomposition. It makes possible to analyse even very complex mixtures of very diverse nature and volatility. The chromatograph used for this study in order to quantify the hydrogen gas (H_2) generation within the two tested cells is a Varian-450GC.

The "heart" of the chromatograph is the column, a tube more or less permeable to gases which contains an active substance, solid or liquid, called the stationary phase. The column is continuously scanned by a carrier gas. Most frequently two types of columns are used, the filled

and the capillary columns. We used a filled column, Molsieve 5A, with a diameter 3.17 mm and length of 3 m.

The chromatographic process is discontinuous. At the initial moment, one mL sample is introduced at the top of the column. This introduction takes the form of an injection using a micro-syringe through a septum in a small chamber located upstream of the column on the gas circuit called injector, brought to a temperature appropriate to the volatility of the sample. The temperature of the column has been set at 80°C. The constituents of the injected mixture and the carrier gas are driven at the same speed. They arrive all together at the other end of the column if they were not braked in different ways by the interaction of their molecules with those of the stationary phase. That means that larger molecules need more time to pass this phase.

Thus, the constituents of the sample, leaving at the same time from the injector, will detach from each other in the course through the column, according to their affinity for the stationary phase. The arrivals are recorded by an essential organ called the detector. For our measurements we used a pulsed discharge helium ionization detector (PDHID) set at 120°C using highly pure Helium (purity 99.999%). The constituents leaving the column, flowing counter to the flow of helium from the discharge zone, are ionized by photons from the helium discharge. The resulting electrons move toward the collector electrode, where they cause changes in the standing current which are quantified as the detector output.

At the output of each compound, one will observe an upward deviation and then downward of the recorder. Each arrival of a constituent of the mixture corresponds to a peak which is detached from the baseline. The set of peaks and the baseline drawn from the injection constitute the so called “chromatogram”. On this chromatogram, the retention time (abscissa) makes it possible to qualitatively characterize the constituents of the mixture. The ordinate of the vertices or the area between the baseline and the peak is used to measure the amount of each solute separated in the sample.

The measurement of the surfaces of the peaks and the calculation of the concentrations of the constituents of the sample are obtained by means of a calculation tool (Galaxy chromatography Data System) coupled to the chromatograph which directly provides the analysis report.

Every analysis provides a chromatogram every ten minutes, making possible the quantification of hydrogen production in each cell every 20 minutes.

3.2.3. b) Calibration

To avoid any presence of impurity from previous experiments, the column is conditioned before every test by heating both the column (200°C) and the detector (280°C) during at least 24h. Afterwards, a calibration is performed in order to relate the area of the dissolved gas with the surface of the peak in the chromatogram. To achieve this, we connect gas chromatograph with standard gas bottle (mixture gas, Air Products) containing H_2, O_2 and N_2 in certain concentrations. The flow of the gas is fixed with flow controllers at 5ml.min^{-1} which is the same rate used during the experiments. The obtained area peaks during calibration are corrected with respect to the given values for gases concentration in the standard gas bottle. For H_2, the given concentration is set at 20.37 ± 3% ppm. As it is seen in Figure 3.2.1 the H_2 evolution as a function of time after calibration is measured by the gas chromatograph at 20.67 ± 0.36 ppm.

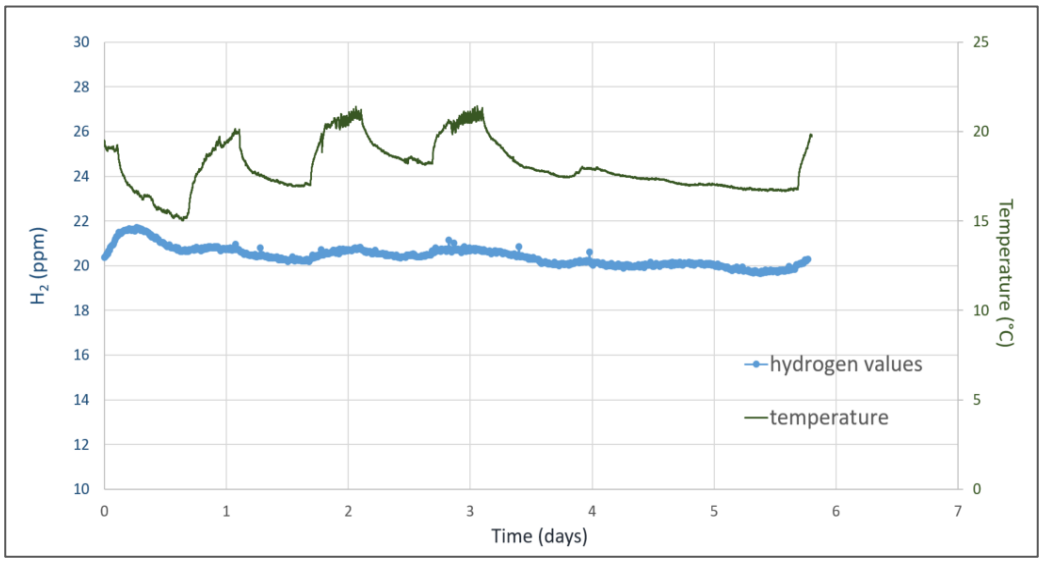

Figure 3.2.1: H_2 evolution over time during calibration using standard gas mixture with H_2 gas concentration at 20.37 ppm

3.2.4 Gamma radiation

3.2.4. a) Irradiation chamber

The IRSN-IRMA irradiation chamber (IRradiation MAterials) located at Saclay research center was used to carry out the irradiation of the cells. IRMA installation is a panoramic irradiation chamber for studying how materials react to the effects of dose and dose rate due to exposure to ionising radiation. The irradiation chamber has volume of 24 m^3. For this work, gamma radiation was performed with four cylindrical ^{60}Co sources (451.6 mm in length, 11.1 mm in diameter each) provided by MDS Nordion. The sources half-life time (t½) is 5.27 years and

their total activity during the 3 years of this study varied between 850-650 TBq. The radioactive sources are remotely handled after withdrawal from their safe repository (lead well). For temperature monitoring, two thermocouples able to provide measurements every one minute are installed into the irradiation chamber. As shown in Figure 3.2.4, the gas chromatograph is installed outside IRMA and connected in line with the irradiation chamber using the suitable metallic cables.

Figure 3.2.2: IRMA facility (Saclay research center)

3.2.4. b) Gamma radiation and dose rate

In order to achieve an estimation of the real conditions that would prevail in a deep repository, a rather low dose rate of 50 $Gy.h^{-1}$ (corresponding approximatively to five time the predicted in situ dose rate) is applied. The calculations of the theoretical distances between the sources and the cells required to obtain the desired dose rate were realized using a dedicated software (Microshield® 9.07 software) (Figure 3.2.3.a). These distances are afterwards validated by measuring the dose rate using a calibrated ionization chamber (Figure 3.2.3.b). The distance between the cells and the sources varied between 70 and 100 cm. In order to maintain a stable dose rate (~50 $Gy.h^{-1}$) for all the experiments, a lead screen of 2 cm width (or steel brick of 5 cm width) was used (Figure 3.2.3.c), depending on the total activity of the sources.

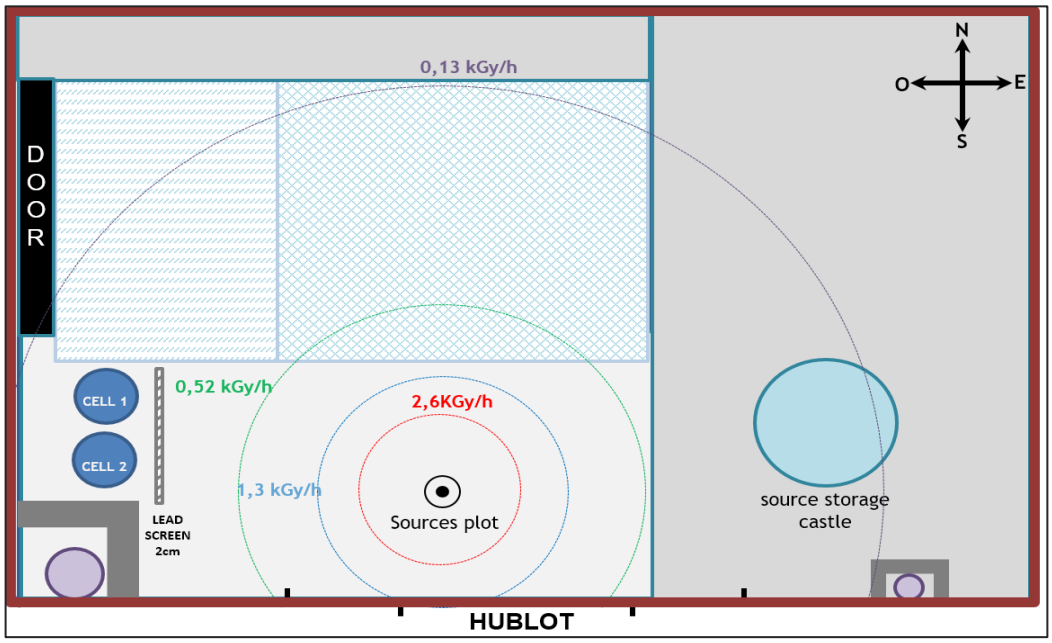

(a)

(b)

(c)

Figure 3.2.3: a) calculations of the theoretical distances between the sources and the cells realized using Microshield® 9.07 software, b) measurement of the dose rate using a calibrated ionization chamber, c) lead screen or brick systems installed to maintain a stable dose rate

A summarised description concerning the irradiation conditions of all experiments is presented in Table 3.2.5.

Table 3.2.5: Experimental conditions for all the full-length experiments

Experiment	Pre-iradiation phase (days)	Irradiation phase (days)	Post-irradiation phase (days)	Tested solution	Solution volume (ml)	Helium flow rate (ml/min)	Cell	Metallic samples	Dose rate ($Gy.h^{-1}$)	Total dose (KGy)	Total activity (TBq)	Sources
A	-	11.7	5.9	Pure water	100	30	A1	5	50.4	14.3	848.7	4
							A2	-	49.8	14.1		
B	4.9	12.0	8.7	Pure water	150	5	B1	6	51.7	14.9	825.8	4
							B2	-	51.2	14.7		
C	0.7	14.6	6.1	Pure water	200	5	C1	6	51.0	18.3	773.6	4
							C2	-	51.0	18.3		
D	1.0	12.6	5.0	TRNM solution	200	5	D1	6	50.1	15.4	138.6	1
							D2	-	50.1	15.4		
E	0.6	15.7	4.8	Pure water	200	5	E1	6	45.3	17.4	683.5	4
							E2	-	50.3	19.3		
F	1.8	11.5	3.0	Pure water	200	5	F1	6	50.5	14.3	674.7	4
							F2	-	53.7	15.2		
G	3.6	9.7	3.9	TRNM solution	200	5	G1	6	50.1	12.0	123.2	1
							G2	-	50.7	12.7		
H	3.2	12.1	-	MREA solution	200	5	H1	6	46.0	17.3	650.3	4
							H2	-	48.0	18.1		

3.2.5 Corrosion rate measurements: H_2 gas generation

The main goal of this study is to estimate the carbon steel anoxic corrosion rate associated to three successive temporal phases: pre-irradiation, irradiation, and post-irradiation phases. In this way we used the hydrogen gas generation measurement method. The corrosion rate estimation is due to the precise measurement of molecular hydrogen production in two cells: one containing solution and metallic samples and another one containing only solution. By subtracting the H_2 production associated to the cells containing only solution from the one generated by the cells containing solution and metallic samples, it should permit to estimate the volume of hydrogen generated only by the process of anoxic corrosion under irradiation. These results are converted from hydrogen in $mol.min^{-1}$ to corrosion rate in $\mu m.year^{-1}$ based on calculations from previous studies (Smart & Rance, 2005):

The general conversion factor selected when the corrosion product is not identified is given by the following equations:

$$1\ mmol\ H_2 / m^2 / yr = 0.0071\ \mu m.year^{-1} \quad \text{(E3.1)}$$

When for the case where corrosion product is identified as of magnetite (Fe_3O_4), the conversion factor is applied as following:

$$1\ mmol\ H_2 / m^2 / yr = 0.0053\ \mu m.year^{-1} \quad \text{(E3.2)}$$

3.3 Post-mortem analyses

3.3.1 Solid samples

3.3.1. a) Scanning Electron Microscopy (SEM)

Morphology and chemical composition of the corrosion products formed at the surface of the carbon steel samples are firstly investigated using a Scanning Electron Microscopy (SEM) coupled to Energy Dispersive Spectroscopy (EDS).

Scanning electron microscopes (SEMs) a highly focused electron beam is formed to scan the sample with a resolution down to the nanometer scale. Different effects can result from the interaction between the electron beam and the electrons in the sample. Part of the electron beam will be unscattered, but most of the electron beam interacts with the sample and undergoes inelastic and elastic scattering. The large part of the electron beam's energy is transformed into

heat, and then secondary effects take place. These effects can be the emission of secondary electrons, backscattered electrons and also characteristic X-rays.

The secondary electrons are generated when an incident electron changes its path and loses part of its energy, which is transferred to an atom in the sample (inelastic event) and leaves the sample with low energy. Each primary or incident electron can produce several secondary electrons, thus secondary electrons are abundant, and they are used for the imaging signal in SEM.

Backscattered electrons are generated from the collision between incident electrons and atoms in the sample, losing part of their energy and being scattered 'backwards' at 180 degrees. Some of the backscattered electrons can generate further secondary electrons as they are leaving the sample. The production of backscattered electrons is dependent on the atomic number of the present element present in the sample: the higher the atomic number, the "brighter" the region will appear (Egerton, 2005; Girao et al., 2017).

In this study, analyses are performed using a Field Emission Gun (FEG) JSM7000-F SEM apparatus (JEOL) under an accelerating voltage of 15 kV (Figure 3.3.1.a). Sample surface images are obtained using both Secondary Electron (SE) mode and BackScattered Electron (BSE) mode. EDS spectra are collected on point of interest using a silicon-drift detector (Bruker AXS).

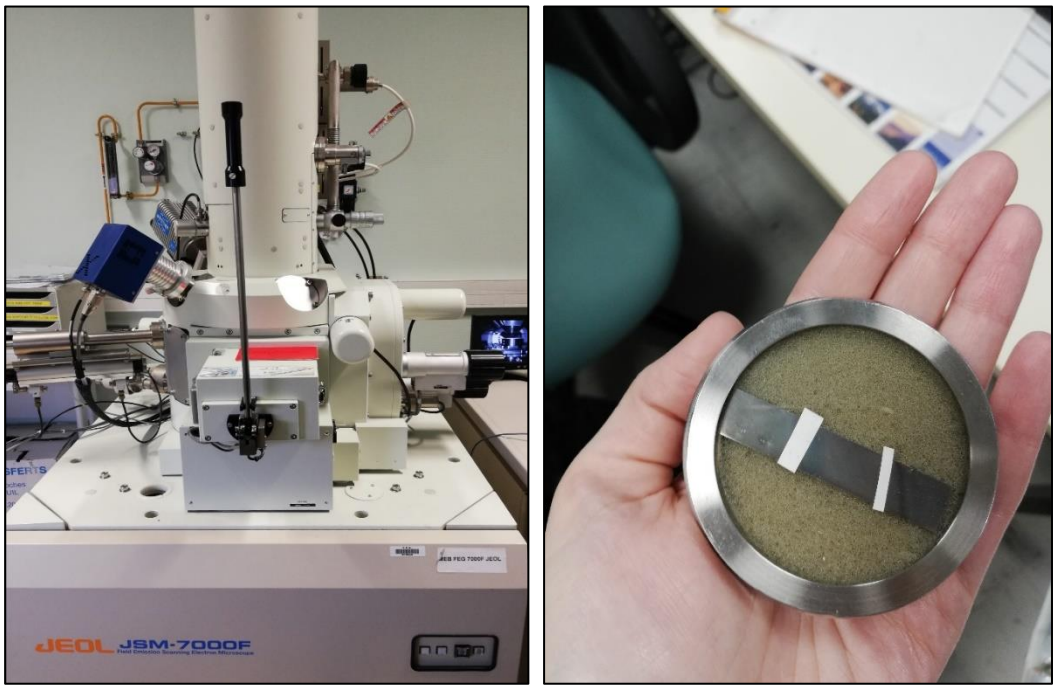

(a) (b)

Figure 3.3.1: a) FEG-SEM apparatus (JEOL), b) airtight anoxic box for samples

Samples are brought to the microscope in an airtight anoxic box (Figure 3.3.1.b) and all subsequent transfers are done rapidly (less than one minute) to minimize exposure to oxygen.

3.3.1. b) Micro-Raman spectroscopy (μRaman)

Raman spectroscopy uses a single frequency of radiation to irradiate the sample and it is the radiation scattered from the molecule, one vibrational unit of energy different from the incident beam, which is detected. In Raman scattering, the light interacts with the molecule and distorts (polarizes) the cloud of electrons round the nuclei to form a short-lived state called a 'virtual state'. The energy changes, detected in vibrational spectroscopy, are those required to cause nuclear motion. If only electron cloud distortion is involved in scattering, the photons will be scattered with very small frequency changes, as the electrons are comparatively light. This scattering process is regarded as elastic scattering and is the dominant process. For molecules it is called Rayleigh scattering. If the nuclear motion is induced during the scattering process, energy will be transferred either from the incident photon to the molecule, or from the molecule to the scattered photon. In these cases, the process is inelastic, and the energy of the scattered photon is different from that of the incident photon by one vibrational unit. This is Raman scattering.

At room temperature, most of the molecules are in the lowest energy vibrational level. Since the virtual states are not real states of the molecule but are created when the laser interacts with the electrons and causes polarization, the energy of these states is determined by the frequency of the light source used. The Rayleigh process will be the most intense process since most photons scatter this way. It does not involve any energy change and consequently the light returns to the same energy state. The Raman scattering process from the ground vibrational state leads to absorption of energy by the molecule and its promotion to a higher energy excited vibrational state. This is called Stokes scattering.

Moreover, due to thermal energy, some molecules may be present in an excited state. Scattering from these states to the ground state is called anti-Stokes scattering and involves transfer of energy to the scattered photon. The energy between the incident and scattered light appears as a frequency shift between the scattered light frequency, and the excitation frequency. The energy gap between these two vibrational levels is examined in Raman spectroscopy as the characteristic spectral patterns act as fingertips for the examined substances (Smith & Dent, 2005).

In this study, for the micro-Raman (μRaman) spectroscopy, the metallic samples are kept in airtight anoxic box equipped with a 1 mm thick glass window as it is seen in Figure 3.3.1.b.

Samples surfaces are imaged with an Olympus MX41 microscope equipped with a CCD camera. μRaman spectra are obtained using a LabRam HR800 spectrometer equipped with an Olympus MX41 microscope. YAG solid-state laser with wavelengths of 532 and 785 nm are used as excitation sources and power outputs are kept at reasonably low values (≈ 500 $\mu W/\mu m^2$) to limit thermal degradation with a spot size of 5 nm.

3.3.1. c) Optical spectroscopy

Optical-microscopy (OM) is a simple system in which the object of interest is illuminated by a transmitted light source and then a condenser lens focuses and densifies the light into a more intense one. The objective lens collects the light, and a focused real image is formed. The real image is again enlarged by the ocular lenses giving the final magnified image of the observed sample. In this study we used the CDD camera of the Olympus MX41 microscope to obtain images of the formed corrosion products upon the steel samples at the scale of μm.

3.3.2 Liquid samples

3.3.2. a) pH evolution

The acidity of the solution can have a major impact on corrosion process. Therefore, the pH of the solution has been measured before the beginning and after the end of each experiment in both cells. Every pH measurement has been made in the anoxic glove box under permanent flow of inert gas (N_2). The measurements have been made with a portable pH meter (Multi 3420, WTW) using a glass electrode (ADA S7/IDS, WTW). Additionally, the pH of the solution was initially measured with pH-paper (Merck Millipore) in order to verify the range of acidity/alkalinity.

3.3.2. b) Iron concentration measurements

In order to evaluate the corrosion product dissolution processes, we performed measurements to estimate the amount the total amount of dissolved iron (Fe_{tot}), present in the solution sampled in the cells containing metallic coupons. These samples were taken within some minutes after dismantling the cell with metallic samples, inside the anoxic glove box, to avoid any further oxidation. The total amount of dissolved iron (Fe_{tot}) in solution was also measured thanks to Inductively Coupled Plasma–Atomic Emission Spectrometry (ICP-AES). The basic aim of analytical atomic spectroscopy is to identify elements and quantify their concentrations in

various media. The procedure consists of three general steps: atom formation, excitation, and emission. Before excitation, an element that is bound in a specific matrix must be separated from that matrix so that its atomic emission spectra is free from interferences. ICP-AES uses a plasma as the atomization and excitation source. A plasma is an electrically neutral highly ionized gas that consists of ions, electrons, and atoms. Once atoms are exited or ionized in the plasma, they exit the high temperature region and electronically relax. This results in the emission of an element-characteristic photon available for detection.

In this study it was used an iCAP 7600 Duo (Thermo Electron) apparatus for the detection of total dissolved iron (Fe_{total}). The sample solution before introduced for analysis was acidified up to 2% in HNO_3 to prevent adsorption of metals onto instrument tubing or glassware prior to introduction into the plasma.

3.3.2. c) Hydrogen peroxide concentration measurements

Hydrogen peroxide (H_2O_2) is a molecular product of water radiolysis. It is quite unstable in solution; however, it is possible to measure it without using scavengers if the measurement will take place the first 24 hours after the stop of irradiation. This measurement is known as the Ghormley method (Allen et al., 1952) which is based on the interaction of hydrogen peroxide with iodide ions as following:

$$2I^- + H_2O_2 + 2H^+ \rightarrow I_2 + 2H_2O \quad \text{(R3.1)}$$

$$I_2 + I^- \rightarrow I_3^- \quad \text{(R3.2)}$$

Iodide ions are consuming hydrogen peroxide resulting to the formation of diiodine (I_2), which are complexing with iodide ions (I^-) to form triiodide (I_3^-). The latter has an absorbance measured at $\lambda = 348$ nm (Figure 3.3.2).

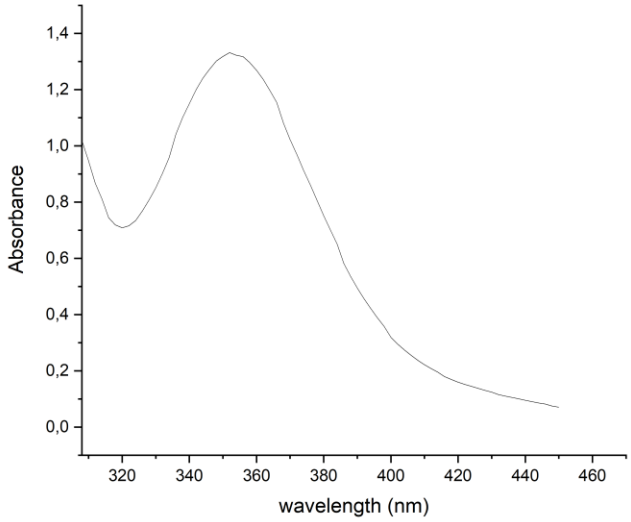

Figure 3.3.2: Absorption spectrum of I_3^- of a solution with known hydrogen peroxide concentration, using the Ghormley method

Its molar coefficient extinction coefficient at this wavelength is 25800 $M^{-1}cm^{-1}$. With this method we can easily measure indirectly the concentration of hydrogen peroxide in aqueous solutions using UV-Vis spectroscopy (UV-2600, Shimadzu). The reaction is catalysed by ion molybdate in a buffered solution (pH=6) with potassium acid phthalate. The absorbance is measured in cuvettes containing a mixture solution and the irradiated sample. As the dismantlement of cells containing the metallic samples was taking place some days the end of irradiation, the measurement of hydrogen peroxide became possible only in the cells containing the deaerated solution. All the procedure is analytically explained in annex A.

Hydrogen peroxide (H_2O_2) concentration measurement has also been performed thanks to fluorescence method. The sensitivity of fluorescence method is based on substance called "Amplex Red", by making this method 5 to 20 times more sensitive than most colorimetric analyses, leading to its wide use in the quantification of low concentrations of hydrogen peroxide. The "Amplex Red" is a non-fluorescent and colourless compound that upon enzymatic oxidation is transformed into another compound, resorufin, highly absorbing and fluorescing. Horseradish peroxidase (HRP) catalyses and oxidized Amplex Red to resorufin. Unfortunately, further oxidation of resorufin gives a non-fluorescent resazurin, leading to loss of fluorescence intensity (Towne et al., 2004). The irradiated sample solution, containing the low concentration of hydrogen peroxide, with the addition of Amplex Red is introduced in a cuvette, then in the optic cell of the spectro-fluorometer, and the fluorescence spectrum it is recorded (I1). Then, the HRP enzyme is introduced and after 1 minute of agitation the new spectrum is recorded (I2). Finally, it is also added to the cuvette a known concentration of H_2O_2

(reference) and after 1 minute of agitation the spectrum is re-measured (I3). Even if the procedure is more accurate, the florescence method had been performed only in one of the experiments in this study (experiment B).

3.3.3 Corrosion rate measurements: weight loss measurement

Additionally to the hydrogen gas production monitoring, the average corrosion rate obtained on the total duration of the experiment is also evaluated by weight loss measurement method. These gravimetric measurements were performed on dedicated metallic coupons which have been weighted initially, at the beginning of the experiment, and finally after being soaked in three successive ultrasonic baths. The solution contained in the bath is composed of 50%m distilled water + 50%m HCl (37%, VMR) containing 5 $g.L^{-1}$ of hexamethylenetetramine ((CH2)6N4, VMR) as an inhibitor of iron dissolution under acidic conditions, and the duration of each bath is 5 minutes. The weight of the coupons is measured using a high accuracy mass balance (XP205DR, METTLER TOLEDO) to allow an estimate of the average general corrosion rate (r, in µm/y). The damaged thickness (e, in µm) is calculated according to:

$$e = \frac{\Delta m}{S \times \rho(Fe)} \quad \text{(E3.3)}$$

where S is the surface area(11.2 cm^{-2} per sample), Δm is the mass difference, and ρ(Fe) is the iron density. The general corrosion rate r, is given by:

$$r = \frac{e}{t} \quad \text{(E3.4)}$$

where t is time (in year).

Chapter 4: Experimental Results

4.1 Experiments with pure water

4.1.1 H_2 gas production

Ultrapure dearated water was used, as immersion solution, for the majority of our experiments in the tested cells. Five long-term experiments, with approximately same time duration took place. The number of metallic samples, the volume of the solution as well as the flow rate of helium gas into cells were not identical in every experiment, although the conditions were exactly the same between the two cells.

1) Experiment A

In experiment A, cell A1 (ultrapure water with metallic coupons) and cell A2 (only ultrapure water) were tested with 100 ml of ultrapure deaerated water. Five carbon steel samples were sufficiently immersed in cell A1. For both cells, the helium flow rate was set at 30 $ml.min^{-1}$.

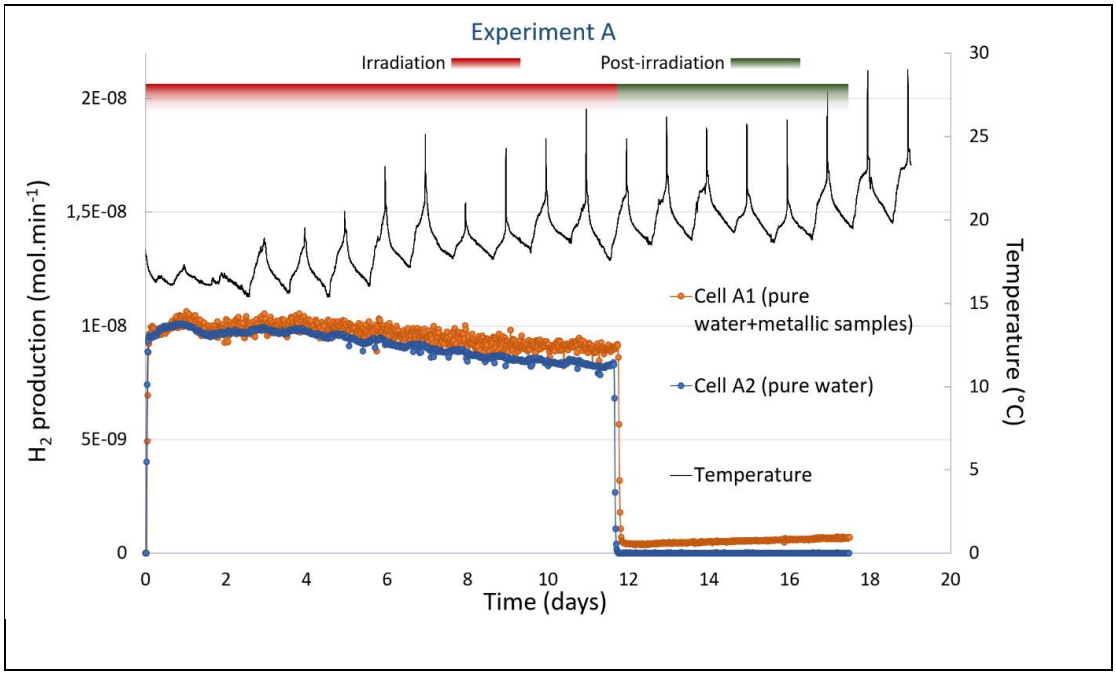

Figure 4.1.1: H_2 production and temperature evolution over time for experiment A

During this experiment, the H_2 production corresponding to the pre-irradiation phase was not recorded, resulting to study only the irradiation and post-irradiation phase. The irradiation phase

lasted 11.7 days and the gamma radiation dose rate applied was 50.4 $Gy.h^{-1}$ and 49.8 $Gy.h^{-1}$ for cell A1 and A2, respectively. For the post-irradiation phase both cells remained connected for the H_2 measurements for 5.9 days. The hydrogen evolution recorded for both cell A1 and cell A2 and the temperature evolution are shown in Figure 4.1.1.

Cell A1 (pure water + samples)

For cell A1, Figure 4.1.1 describes the two successive phases of the experiment: the radiolytic anoxic corrosion phase and the post-irradiation anoxic corrosion phase. During the radiolytic corrosion phase, we observe that H_2 evolution can be separated in two parts:

• The first part during which the amount of H_2 increases rapidly with the start of irradiation and then stabilizes for 4.5 days at an average value of 1.0×10^{-8} $mol.min^{-1}$;

• The second part during which the quantity of H_2 gradually decreases over 8.2 days to reach a minimum value of 9.2×10^{-9} $mol.min^{-1}$.

Once the irradiation stops, the amount of produced H_2 (g) decreases rapidly before obtaining a minimum value of 3.8×10^{-10} $mol.min^{-1}$. Thereafter, gas production shows a slight and gradual increase until the end of the experiment, where the value obtained is 7.1×10^{-10} $mol.min^{-1}$.

Cell A2 (pure water)

For cell A2, the Figure 4.1.1 describes the phase of water radiolysis. This parallel monitoring allows to directly measure the hydrogen production linked to water radiolysis process. This volume of radiolytic H_2 is then deducted from the one generated by the cells containing pure deaerated water and metallic samples (cells A1) to estimate the volume of hydrogen generated only by the process of anoxic corrosion under irradiation.

During the irradiation period, we observe that H_2 evolution can be separated in two parts:

• The first part during which the quantity of H_2 increases rapidly and stabilizes for 4.5 days (like cell A1) at an average value of 9.8×10^{-9} $mol.min^{-1}$;

• The second part during which the quantity of H_2 decreases progressively to a minimum value of 8.3×10^{-9} $mol.min^{-1}$ until the irradiation stops.

As expected, once irradiation ends, hydrogen production becomes zero.

Corrosion rate

To estimate the carbon steel anoxic corrosion rate associated to three successive temporal phases (pre-irradiation, irradiation and post-irradiation phases) we used the hydrogen gas generation method. The corrosion rate estimation is due to the precise measurement of molecular hydrogen production in two cells: one containing solution and metallic samples and another one containing only solution. By subtracting the H_2 production associated to the cells containing only solution from the one generated by the cells containing solution and metallic samples, it should permit to estimate the volume of hydrogen generated only by the process of anoxic corrosion under irradiation. These results are converted from hydrogen in $mol.min^{-1}$ to corrosion rate in $\mu m.year^{-1}$ based on calculations from previous studies (Smart & Rance, 2005). The obtained results are shown in Table 4.1.1. During irradiation phase, the average corrosion rate value is about 0.22 $\mu m.year^{-1}$, with maximum values reaching 0.68 $\mu m.year^{-1}$. During post irradiation phase, the average corrosion rate value is around 0.27 $\mu m.year^{-1}$, with maximum values at 0.37 $\mu m.year^{-1}$.

Corrosion rate	Irradiation phase	Post-irradiation phase
Average corrosion rate ($\mu m.year^{-1}$)	0.22 ± 0.35	0.27 ± 0.05
Maximum corrosion rate ($\mu m.year^{-1}$)	0.68	0.37

Table 4.1.1: Corrosion rates obtained for experiment A

2) Experiment B

In experiment B, cell B1 (ultrapure water with metallic coupons) and cell B2 (only ultrapure water) were tested with 150 ml of ultrapure deaerated water. Among the six metallic samples inserted in cell B1, two of them underwent special polishing treatment till obtaining a very smooth mirror-effect surface. Furthermore, helium flow rate was decreased from 30 $ml.min^{-1}$ to 5 $ml.min^{-1}$, in order to minimize the disturbance of the system.

During this experiment, the H_2 production associated with cell B1 was recorded during the pre-irradiation phase. Even though the H_2 production associated with cell B2 was expected to be zero during this phase (no irradiation means no H_2 production associated to radiolytic process), gas chromatograph measurements (>0) indicated a technical problem most probably due to residual impurities in the output line of cell B2.

Then, the experiment was interrupted for some minutes in order to flush both input and output lines with compressed air. To assure that the recorded values are representative, additional calibration had been made for both lines right before the irradiation start. The irradiation phase lasted 12 days and the gamma-irradiation dose rate applied was 51.7 $Gy.h^{-1}$ and 51.2 $Gy.h^{-1}$ for cell B1 and B2, respectively. Once the irradiation stopped, cell B2 was disconnected while cell B1 remained connected for nine days more to record the H_2 evolution corresponding theoretically to the post irradiation anoxic corrosion process. It should be mentioned that right after the end of the irradiation phase, there was no H_2 measurement for approximately 15 hours due to a technical problem with the helium flow controllers. After this pause, H_2 evolution for the post-irradiation phase was measured for further 8.7 days. The hydrogen evolution for the experiment B is shown in Figure 4.1.2.

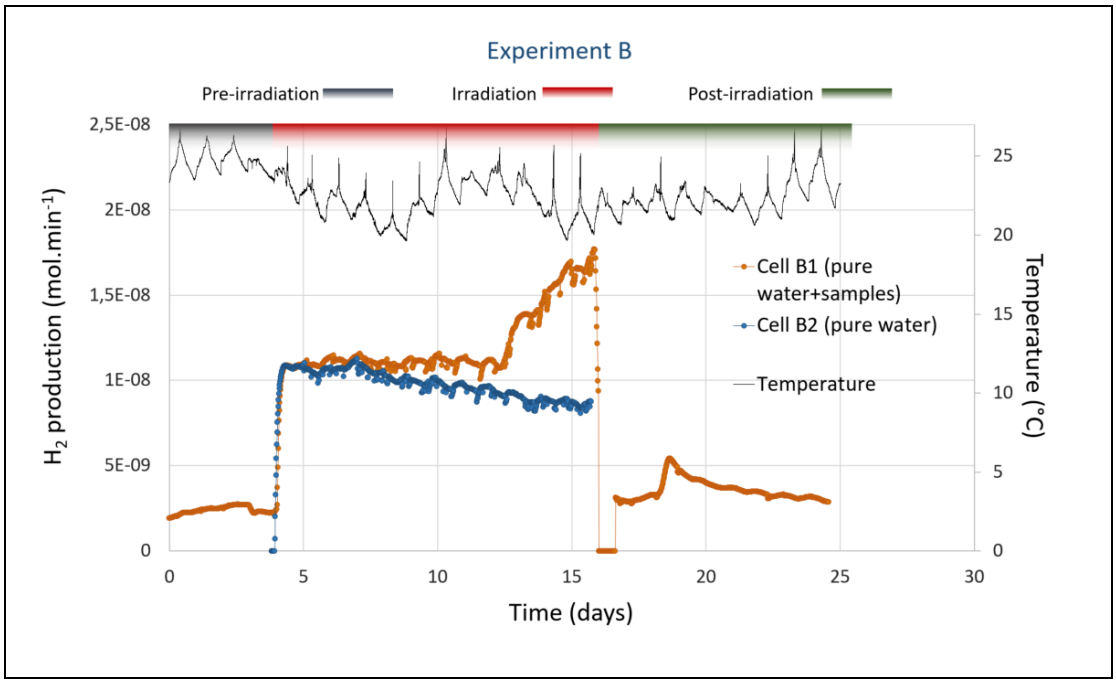

Figure 4.1.2: H_2 production and temperature evolution over time for experiment B

Cell B1 (ultrapure water + samples)

For cell B1, Figure 4.1.2 shows that the average hydrogen production value recorded during pre-irradiation phase is about 2.26 x 10^{-9} $mol.min^{-1}$.

During irradiation phase, hydrogen production from cell B1 remains higher than the one associated with cell B2, and it is stabilized almost for eight days at the value of 1.1 x 10^{-8} $mol.min^{-1}$. Afterwards, a sharp and unexplained increase is taking place, persisting till the end of irradiation phase, reaching the maximum value of 1.76 x 10^{-8} $mol.min^{-1}$. This increase could not be explained by a parallel temperature increase and is not taking place in the cell B2.

After the end of irradiation phase, H_2 production in cell B1 decreased rapidly. Due to a sudden helium flow meters breakdown, almost 15 hours of measurements were lost. After this problem H_2 production from cell B1, corresponding to the post irradiation anoxic corrosion process, was recorded at an initial value of about 3.03 x 10^{-9} mol.min^{-1}. There is then an unexplained increase up to 5.05 x 10^{-9} mol.min^{-1}. This increase is followed by a progressive decrease, stabilizing H_2 evolution at 3.13 x 10^{-9} mol.min^{-1}.

Cell B2 (ultrapure water)

For cell B2, the Figure 4.1.2 describes the phase of water radiolysis recorded during irradiation phase. During this period, we observe that H_2 production evolution can be separated in two parts:

• The first part (2.7 days) during which H_2 evolution reaches a plateau and remains stable at 1.1 x 10^{-8} mol.min^{-1}.

• The second part (almost 8 days) during which H_2 evolution starts to show a progressive decrease till the end of the irradiation, where it reaches the value of 8.4 x 10^{-9} mol.min^{-1}.

Once irradiation ends, the cell B2 is disconnected for further analyzes.

Corrosion rate

The corrosion rate values obtained for experiment B are shown in Table 4.2.2. For this experiment, we were able to monitor the hydrogen production evolution associated with cell B1 during the pre-irradiation phase and thus, to provide a more complete evolution on the corrosion rate for the three tested phases. For experiment B, we used the general conversion factor to obtain the corrosion rates as it was the only experiment where we identified more than one corrosion products upon the samples. During pre-irradiation phase, the average corrosion rate value is about 1.35 µm.year^{-1}, with maximum values at 1.54 µm.year^{-1}. During irradiation phase, the average corrosion rate value is about 0.74 µm.year^{-1}, with maximum values at 1.26 µm.year^{-1}. It should be mentioned that in the average corrosion rate under irradiation, is not included the period of the sharp H_2 increase in cell B1. During the post irradiation phase, the average corrosion rate value is about 2.01 µm.year^{-1}, with maximum values at 3.06 µm.year^{-1}. It should be mentioned that for the post irradiation this relatively higher corrosion rate is due to the hydrogen peak (t = 18.7 days) that is shown in Figure 4.1.2. After this peak, the average corrosion rate is set at 1.85 µm.year^{-1}.

Corrosion rate	Pre-irradiation phase	Irradiation phase	Post-irradiation phase
Average corrosion rate ($\mu m.year^{-1}$)	1.35 ± 0.04	0.74 ± 0.54	2.01 ± 0.07
Maximum corrosion rate ($\mu m.year^{-1}$)	1.54	1.26	3.06

Table 4.1.2: Corrosion rates obtained for experiment B

3) Experiment C

In experiment C, cell C1 (ultrapure water with metallic coupons) and cell C2 (only ultrapure water) were tested with 200 ml of ultrapure deaerated water. Among the six metallic samples inserted in cell C1, two of them underwent special polishing treatment till obtaining a very smooth mirror-effect surface. Helium flow rate was maintained at 5 $ml.min^{-1}$. During this experiment, the H_2 production associated with cells C1 and C2 was recorded during the 3 tested phases: pre-irradiation, irradiation and post-irradiation. The irradiation phase lasted 14.6 days and the gamma radiation dose rate applied was 51.0 $Gy.h^{-1}$ for both cells. Once the irradiation stopped, cell C2 was disconnected while cell C1 remained connected for six days more to record the H_2 evolution corresponding theoretically to the post irradiation anoxic corrosion process. Figure 4.1.3 shows the H_2 evolution for experiment C.

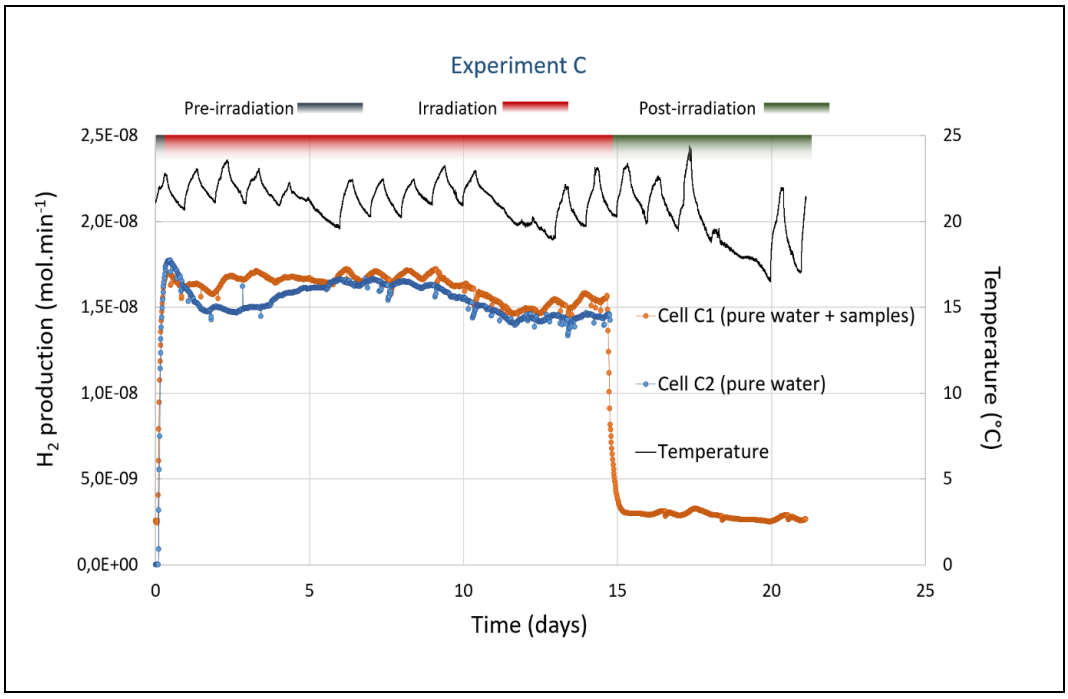

Figure 4.1.3: H_2 production and temperature evolution over time for experiment C

Cell C1 (ultrapure water + samples)

For cell C1, Figure 4.1.3 shows the hydrogen production recorded during the three successive phases of the experiment: (i) pre-irradiation anoxic corrosion phase, (ii) radiolytic anoxic corrosion phase and (iii) post-irradiation anoxic corrosion phase.

i) During pre-irradiation phase, hydrogen production was recorded for only two hours. However, these few measurements indicated a stable average value of about 2.5×10^{-9} mol.min^{-1}, in the same level with the pre-irradiation phase in experiment B (2.3×10^{-9} mol.min^{-1}).

ii) During radiolytic anoxic corrosion phase, hydrogen production is rapidly increased till a stabilization "plateau", followed by three successive steps:
   - The first step during which H_2 production stabilized for 8.8 days, with an average value of 1.6×10^{-8} mol.min^{-1};
   - The second phase during which H_2 production gradually decreased over 2.4 days, from 1.7×10^{-8} mol.min^{-1} to 1.5×10^{-8} mol.min^{-1};
   - The third phase during which H_2 production seems to be once again stabilized obtaining the average value of 1.5×10^{-8} mol.min^{-1}.

iii) During post irradiation anoxic corrosion phase, hydrogen production decreased rapidly to reach the value of 3.0×10^{-9} mol.min^{-1}. Thereafter, H_2 production seems to be stabilized until the end of the experiment, with an average value of about 2.8×10^{-9} mol.min^{-1}.

Cell C2 (ultrapure water):

For cell C2, the Figure 4.1.3 describes the phase of water radiolysis recorded during irradiation phase. During this period, we observe that H_2 production evolution can be separated in four parts:

• The first part (5 days) during which H_2 evolution shows an unexpected evolution as there is a sudden drop and then a re-increase to reach the same H_2 production value as the one before this "curve-shape" evolution. It is the first time that we observe this "curve-shape" evolution for H_2 production right after reaching the initial plateau. This evolution is not observed for cell C1 and could not be attributed to temperature variations.

• The three other parts (8.9 days) during which H_2 evolution is quite similar to the one of Cell C1: i) a first stabilization phase with an average value of 1.6×10^{-8} mol.min^{-1}, ii) a progressive decrease from 1.6×10^{-8} mol.min^{-1} to 1.4×10^{-8} mol.min^{-1}, iii) a second stabilization phase with an average value of 1.4×10^{-8} mol.min^{-1}.

Once irradiation ends, the cell C2 is disconnected for further analyzes.

Corrosion rate

The corrosion rate values obtained for experiment C are shown in Table 4.1.3. For this experiment, we were able to monitor the hydrogen production evolution associated with cell C1 during the three tested phases. During pre-irradiation phase, the average corrosion rate value is about 1.05 µm.year^{-1}, with maximum values at 1.08 µm.year^{-1}. During irradiation phase, the average corrosion rate value is about 0.34 µm.year^{-1}, with maximum values at 1.05 µm.year^{-1}. During post irradiation phase, the average corrosion rate value is about 1.19 µm.year^{-1}, with maximum values at 1.37 µm.year^{-1}.

Corrosion rate	Pre-irradiation phase	Irradiation phase	Post-irradiation phase
Average corrosion rate (µm.year^{-1})	1.05 ± 0.03	0.34 ± 0.4	1.19 ± 0.09
Maximum corrosion rate (µm.year^{-1})	1.08	1.05	1.37

Table 4.1.3: Corrosion rates obtained for experiment C

4) Experiment E

For experiment E, cell E1 (ultrapure water with metallic coupons) and cell E2 (only ultrapure water) were tested with 200 ml of ultrapure deaerated water. The six metallic samples inserted in cell E1 didn't undergo special polishing. Helium flow rate was maintained at 5 ml.min^{-1}.

During this experiment, the H_2 production associated with cells E1 and E2 was recorded during the 3 tested phases: pre-irradiation, irradiation and post irradiation. The irradiation phase lasted 15.7 days and the gamma radiation dose rate applied was 45.3 Gy.h^{-1} and 50.3 Gy.h^{-1} for cell E1 and E2, respectively. Once the irradiation stopped, cell E2 was disconnected while cell E1 remained connected for five days more to record the H_2 evolution corresponding theoretically to the post-irradiation anoxic corrosion process. Figure 4.1.4 shows the H_2 evolution for experiment E.

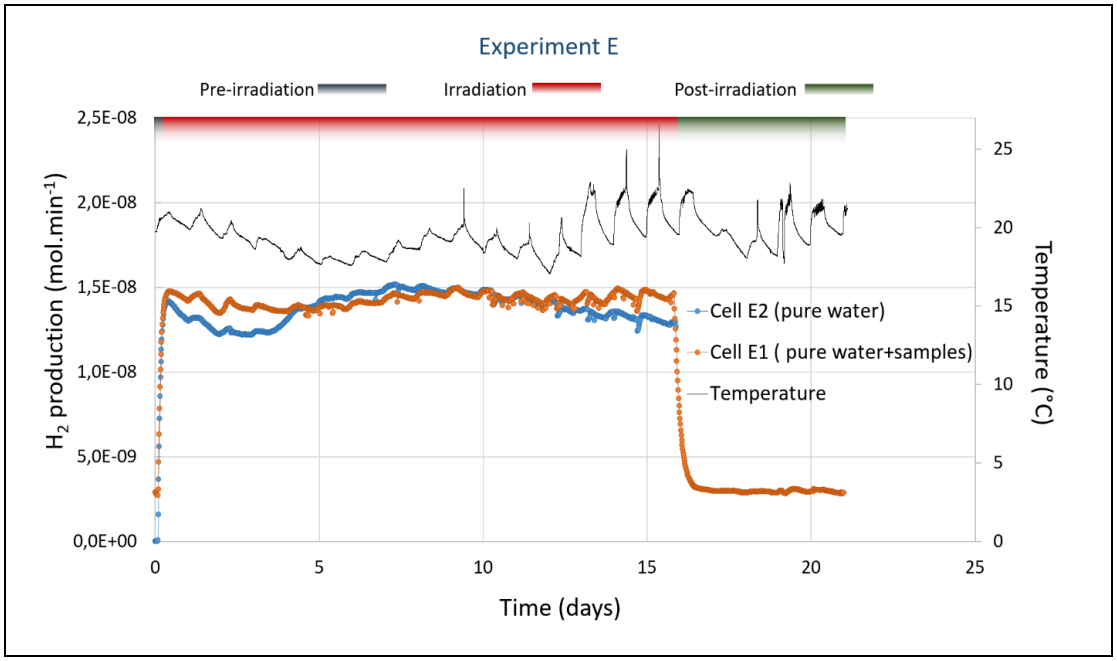

Figure 4.1.4: H_2 production and temperature evolution over time for experiment E

Cell E1 (ultrapure water + samples)

For cell E1, Figure 4.1.4 shows that the average hydrogen production value recorded during pre-irradiation phase is about 2.8 x 10^{-9} mol.min^{-1}, in good agreement with the results obtained during this phase in experiment B and C.

During irradiation phase, hydrogen production from cell E1 seems stable over time, obtaining an average value of 1.42 x 10^{-8} mol.min^{-1}.

After the end of irradiation phase, H_2 production in cell E1 decreased rapidly and reached an average value of 3.2 x 10^{-9} mol.min^{-1}. H_2 production is then stabilized over time at a value of about 3.0 x 10^{-9} mol.min^{-1}. These values are very similar to the ones obtained for experiment C, where the experimental conditions were exactly the same.

Cell E2 (ultrapure water)

For cell E2, the Figure 4.1.4 describes the phase of water radiolysis recorded during irradiation. During this period, we observe that H_2 production evolution can be separated in three parts:

• The first part (4.5 days) during which H_2 production exhibits the same "curve-shape" evolution that is observed for cell C2 (sudden drop to 1.21 x 10^{-8} mol.min^{-1} and then a re-increase to 1.51 x 10^{-8} mol.min^{-1}).

• The second part during which H_2 production shows a stabilization for almost 6 days, with an average value of 1.46 x 10^{-8} mol.min^{-1}.

• The third part (5.3 days) during which H_2 production decreases from 1.42 x 10^{-8} mol.min^{-1} to 1.26 x 10^{-8} mol.min^{-1}.

As in previous experiments, once irradiation ends, cell E2 is disconnected for further analyzes.

Corrosion rate

The corrosion rate values obtained for experiment E are shown in Table 4.1.4. For this experiment, we were able to monitor the hydrogen production evolution associated with cell E1 during the three tested phases. During pre-irradiation phase, the average corrosion rate value is about 1.16 µm.year^{-1}, in good agreement with results associated to experiment C. During irradiation phase, the average corrosion rate value is about 0.20 µm.year^{-1}, with maximum values at 0.78 µm.year^{-1}. It is worth noting that the calculations of the corrosion rate associated with irradiation phase don't take into account the period during which hydrogen production from cell E2 (ultrapure water) is higher than the one originating from cell E1 (ultrapure water + metallic samples). During post-irradiation phase, the average corrosion rate value is about 1.23 µm.year^{-1}, with maximum values at 1.35 µm.year^{-1}. These values are here again very close to the one obtained during the same post irradiation phase for experiment C.

Corrosion rate	Pre-irradiation phase	Irradiation phase	Post-irradiation phase
Average corrosion rate (µm.year^{-1})	1.16 ± 0.04	0.20 ± 0.38	1.23 ± 0.04
Maximum corrosion rate (µm.year^{-1})	1.21	0.78	1.35

Table 4.1.4: Corrosion rates obtained for experiment E

1) Experiment F

For experiment F, cell F1 (ultrapure water with metallic coupons) and cell F2 (only ultrapure water) were tested using 200 ml of ultrapure deaerated water. The six metallic samples inserted in cell F1 didn't undergo special polishing. Helium flow rate was maintained at 5 ml.min^{-1}. During this experiment, the H_2 production associated with cells F1 and F2 was recorded during the 3 tested phases: pre-irradiation, irradiation and post irradiation. The irradiation phase lasted

11.5 days and the gamma radiation dose rate applied was 50.5 $Gy.h^{-1}$ and 53.7 $Gy.h^{-1}$ for cell F1 and F2, respectively. Once irradiation stopped, cell F2 was disconnected while cell F1 remained connected for three days more to record the H_2 evolution corresponding theoretically to the post-irradiation anoxic corrosion process. Figure 4.1.5 shows the H_2 evolution for experiment F.

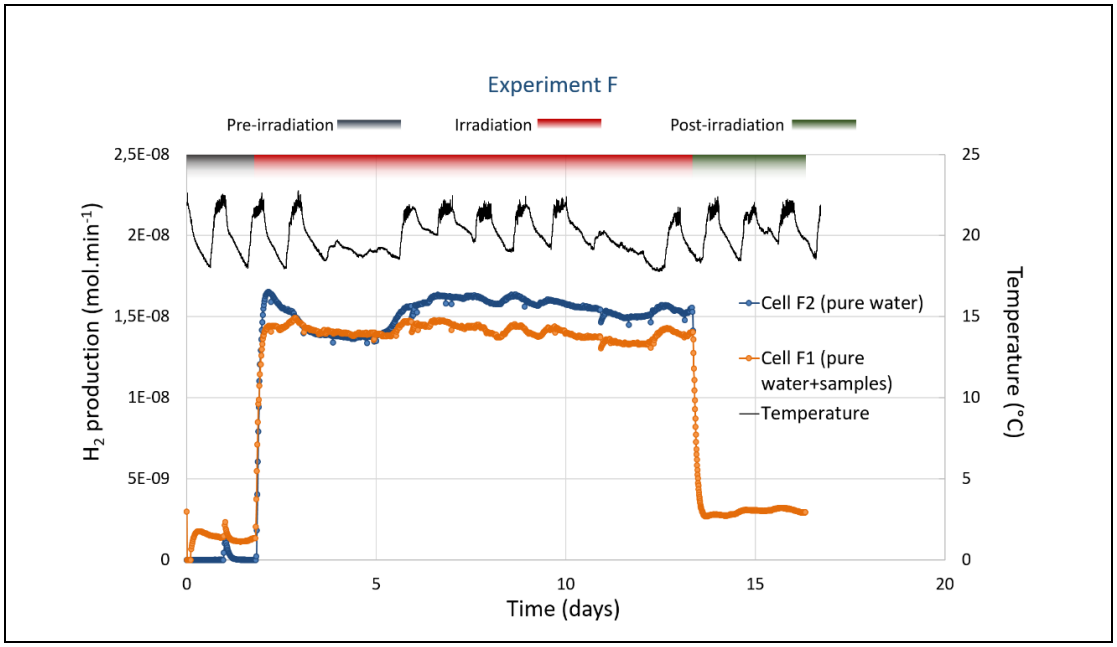

Figure 4.1.5: H_2 production and temperature evolution over time for experiment F

Cell F1 (pure water + samples)

For cell F1, Figure 4.1.4 shows that the average hydrogen production value recorded during pre-irradiation phase is about 1.28 x 10^{-9} $mol.min^{-1}$, almost the half comparing with the results obtained for cells B1, E1, C1 during the same pre irradiation phase. The small increase that is observed at t=1.5 days, is due to the re-launch of the gas chromatograph sequence, as we identified a small presence of oxygen in the cells.

During irradiation phase, hydrogen production from cell F1 seems stable over time, obtaining an average value of 1.41 x 10^{-8} $mol.min^{-1}$.

After the end of irradiation phase, H_2 production in cell F1 decreased rapidly and then stabilized over time at a value of about 3.0 x 10^{-9} $mol.min^{-1}$. These values are equivalent to the ones obtained during the post irradiation phase for experiments C and E, where the experimental conditions were exactly the same.

Cell F2 (pure water)

For cell F2, the Figure 4.1.5 describes the phase of water radiolysis recorded during irradiation. During this period, we observe that H_2 production evolution can be separated in two parts:

• The first part (4.2 days) during which H_2 production exhibits the same "curve-shape" evolution that is observed for cell C2 and E2.

• The second part during which H_2 production seems to be more or less stabilized with an average value of 1.57 x 10^{-8} mol.min^{-1}.

As in previous experiments, once irradiation ends, cell F2 is disconnected for further analyses.

Corrosion rate

The corrosion rate values obtained for experiment F are shown in Table 4.1.5. For this experiment, we were able to monitor the hydrogen production evolution associated with cell F1 during the three tested phases. During pre-irradiation phase, the average corrosion rate value is about 0.56 µm.year^{-1}, almost the half of the values obtained for the other experiments for the same pre irradiation phase.

During irradiation phase, it was not possible to calculate the corrosion rate as the hydrogen production on cell F2 (ultrapure water) was constantly superior to cell F1 (ultrapure water + metallic samples).

During post irradiation phase, the average corrosion rate value is about 1.25 µm.year^{-1}, with maximum values at 1.35 µm.year^{-1}. These values are again very close to the one obtained during the same post irradiation phase for experiments C and E.

Corrosion rate	Pre-irradiation phase	Irradiation phase	Post-irradiation phase
Average corrosion rate (µm.year^{-1})	0.56 ± 0.03	-	1.25 ± 0.06
Maximum corrosion rate (µm.year^{-1})	0.87	-	1.35

Table 4.1.5: Corrosion rates obtained for experiment F

Table 4.1.6 summarized the average values of hydrogen production associated to each studied phase (pre irradiation, irradiation, post irradiation) for the five experiments involving ultrapure water.

Experiment	Cell	Pre-irradiation (H_2 ($x10^{-9}$ $mol.min^{-1}$))	Irradiation (H_2 ($x10^{-9}$ $mol.min^{-1}$))	Post-irradiation (H_2 ($x10^{-9}$ $mol.min^{-1}$))
A	A1	-	9.62 ± 0.42	0.66 ± 0.09
	A2	-	9.18 ± 0.57	-
B	B1	2.26 ± 0.04	11.0*± 0.22	3.13 ± 0.11
	B2	0	9.72 ± 0.78	-
C	C1	2.51 ± 0.06	16.18 ± 0.74	2.83 ± 0.21
	C2	0	15.43 ± 0.88	-
E	E1	2.81 ± 0.07	14.21 ± 0.37	2.96 ± 0.07
	E2	0	13.78 ± 0.86	-
F	F1	1.28 ± 0.07	14.1 ± 0.41	2.97 ± 0.14
	F2	0	15.28 ± 0.83	-

*Table 4.1.6: Hydrogen production associated to each studied phase (pre-irradiation, irradiation, post-irradiation) for the five experiments involving ultrapure water (*measurements before t=12.35)*

Figure 4.1.6 compares the different corrosion rate values associated to each studied phase (pre irradiation, irradiation, post irradiation) for the five experiments involving ultrapure water.

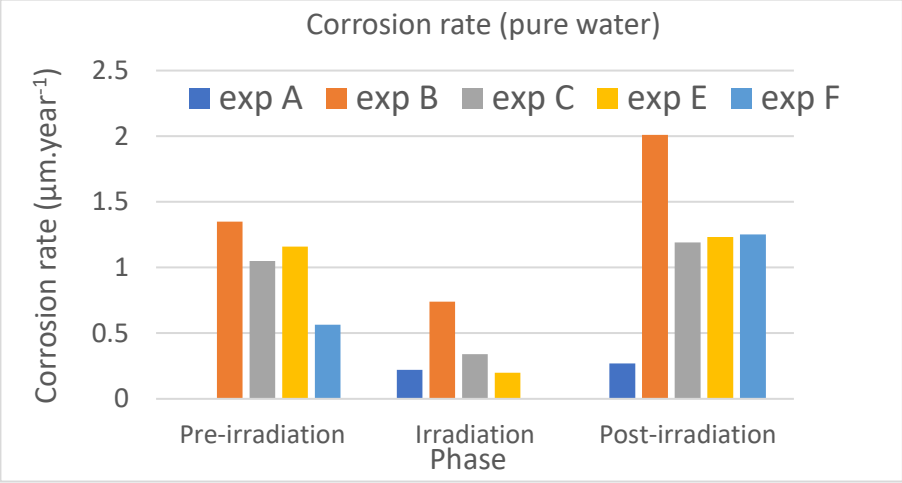

Figure 4.1.6: Corrosion rate values associated to each studied phase (pre-irradiation, irradiation, post-irradiation) for the five experiments involving ultrapure water

4.1.2 Solid Samples

At the end of the experimental tests, the cells are disconnected from the circulation system and moved from the irradiation chamber into the glove box to be dismantled in order to collect the carbon steel coupons and the solutions under anoxic conditions.

The solid samples are taken out, and after rinsing with a few drops of ethanol, they are drying in the anoxic glove box. Afterwards, they are primarily placed in airtight boxes to prevent further oxidation. For all experiments (A, B, C, E and F), one rough-polished sample ("R-sample") is used for structural characterization. For experiments B and C, a supplementary smooth mirror-effect surface sample ("P-sample") is also used for structural characterization. In parallel, depending on the experiment, two or three samples were used for the weight loss measurements. The rest of the samples have been kept for additional analyses.

Concerning the structural characterization, the procedure remains the same for all the experiments: (i) morphology and chemical composition of the corrosion products formed at the surface of the carbon steel samples are firstly investigated using a Scanning Electron Microscopy (SEM) coupled to Energy Dispersive Spectroscopy (EDS), then (ii) the samples are characterized by optical imaging and micro-Raman (μRaman) spectroscopy.

I. Experiment A

SEM - EDS analyses

Compared to its initial appearance, the metallic sample removed from cell A1 at the end of the experiment did not show any significant difference, except the edges which were darker than the other surfaces. Even if the short time scale of our corrosion experiments doesn't permit the formation of a thick corrosion product layer, SEM-EDS analyses allows to identify regions where corrosion products were visible (Secondary Electron (SE) mode and/or BackScattered Electron (BSE) mode) (Figure 4.1.7).

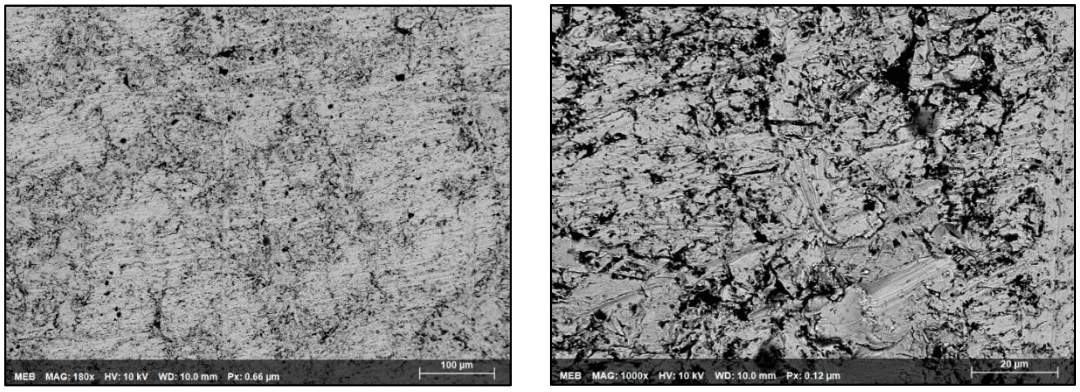

(a) (b)

Figure 4.1.7: SEM images for "AR-sample" at a) 100 µm, b) 20 µm

Optical imaging and Raman spectroscopy

Thanks to observations by optical microscopy, it was possible to distinguish areas affected by corrosion processes (purple coloring) (Fig. 4.1.8.a). These areas were investigated by µRaman spectroscopy in order to identify the nature of the oxides observed. Thus, the faint presence of magnetite (Fe_3O_4), in very small quantity, was highlighted thanks to its characteristic peak at 672.24 cm^{-1} (Fig. 4.1.8.b).

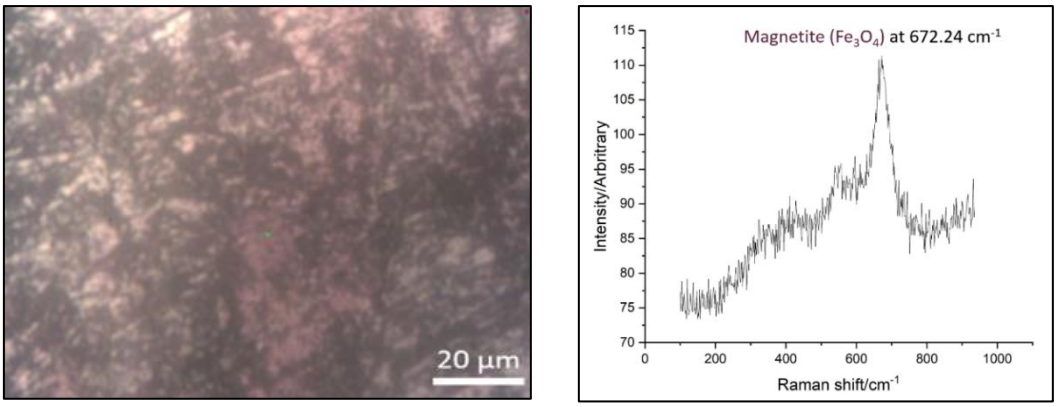

(a) (b)

Figure 4.1.8: a) Optical imaging at 20 µm and b) Raman spectrum for experiment A

II. Experiment B

SEM - EDS analyses

For experiment B, one rough sample (“BR-sample”) and one smooth mirror-effect surface sample (“BP-sample”) were used for the structural characterization. Compared to their initial appearances, “BR-samples” showed a slightly darker color while “BP-samples” became more blurry. SEM-EDS analyses enabled to visualize some formations upon the samples’ surfaces (Figure 4.1.9).

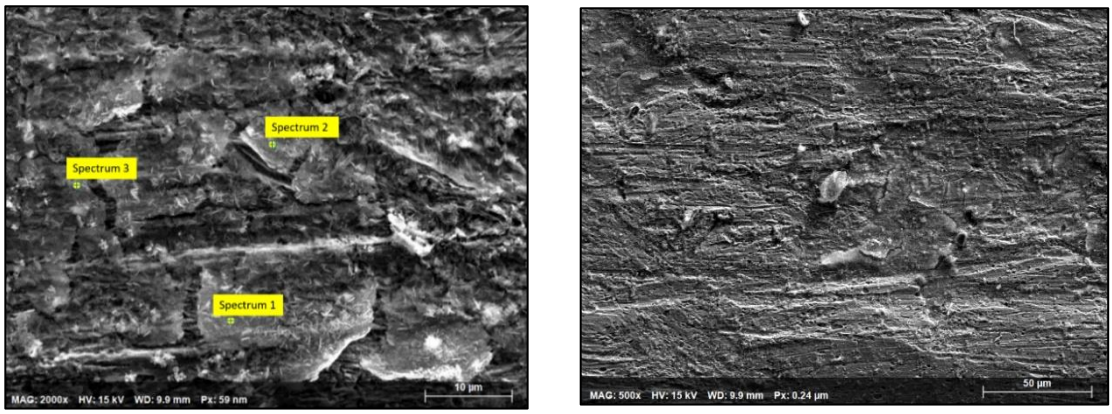

(a) (b)

Figure 4.1.9: SEM images for “BR-sample”at a) 10 µm, b) 50 µm

Figure 4.1.9 shows that there is some thin crystal formation on the “BR-sample” surface. Associated EDS mapping indicates the presence of iron, oxygen and also silicon (Table 4.1.6).

	C	O	Si	Fe
Spectrum 1 (%)	0	50.67	1.34	47.98
Spectrum 2 (%)	0	50.11	0.23	49.64
Spectrum 3 (%)	0	50.37	0.68	48.37

Table 4.1.6: EDS analyses of selected zones for BR-coupon. Selected zones are illustrated in Figure 4.1.9.a.

Figure 4.1.10 shows that there is the formation of hexagonal-shaped nanoplates, not homogeneously distributed on the surface of the “BP-sample”.

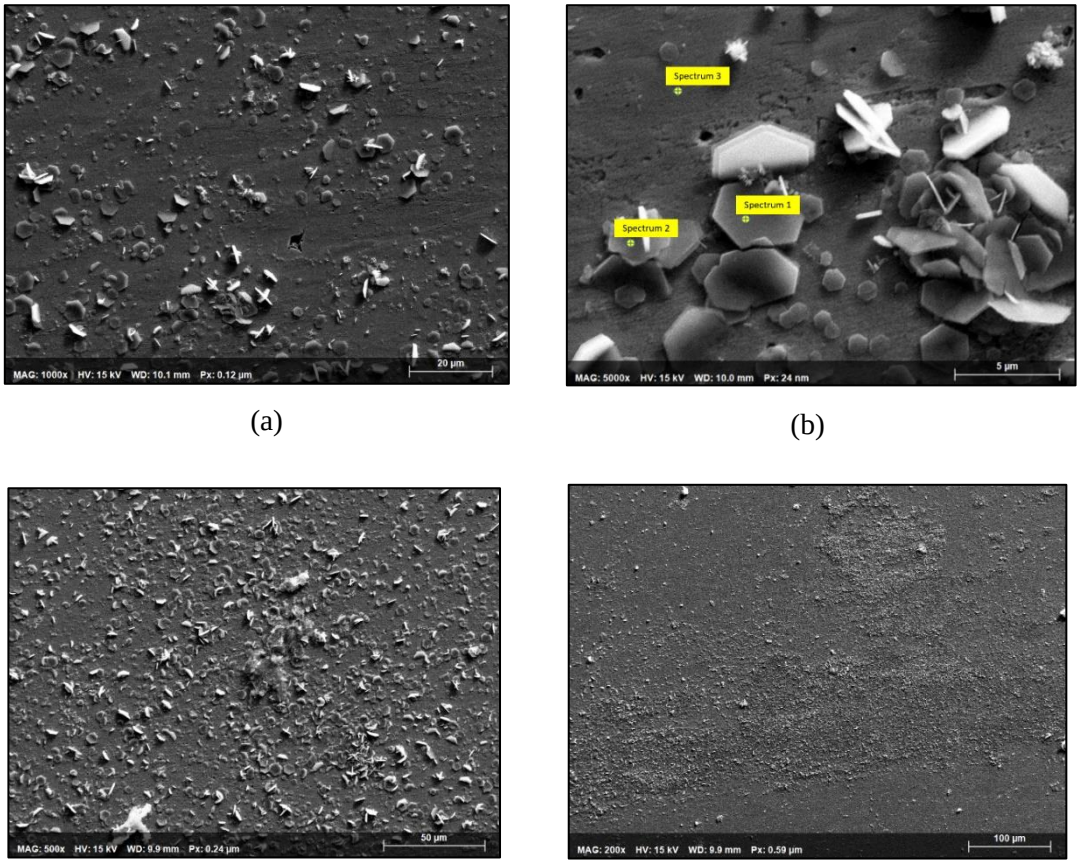

(a) (b)

(c) (d)

Figure 4.1.10: SEM images for "BP-sample"at a) 20 µm, b) 5 µm, c) 50 µm, d) 100 µm

EDS mapping performed on "BP-sample" surface, indicates the presence of iron, oxygen and also silicon (Table 4.1.7).

	O	Si	Fe
Spectrum 1 (%)	50.96	1.92	47.11
Spectrum 2 (%)	50.67	1.34	47.98
Spectrum 3 (%)	50.04	0.08	49.87

Table 4.1.7: EDS analyses of selected zones for BP-coupon. Selected zones are illustrated in Figure 4.1.10.b

Optical imaging and Raman spectroscopy

Thanks to optical microscopy observations, it was possible to distinguish areas affected by corrosion processes for both type of sample (Figure 4.1.11).

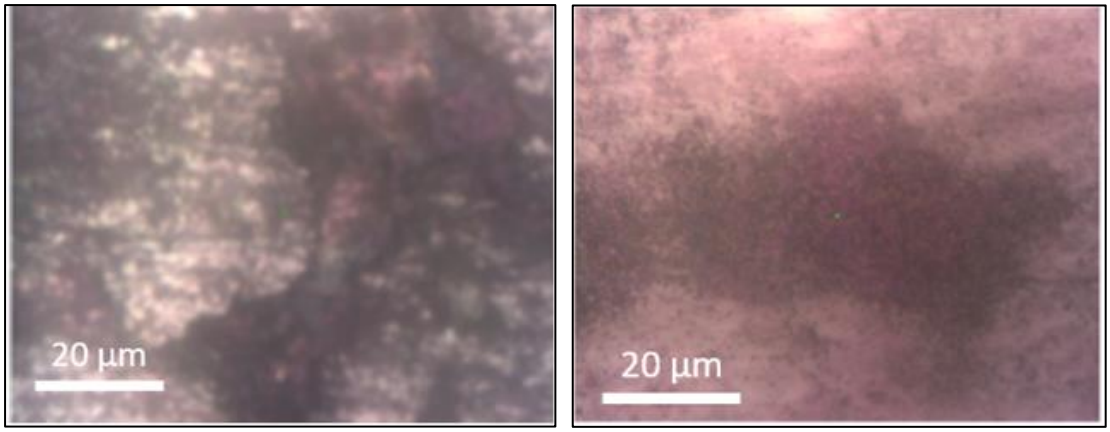

(a) (b)

Figure 4.1.11: Optical imaging at 20 µm for a) "BR-sample" and b) "BP-sample"

The associated Raman-spectrum showed that for both "BR-sample" (Figure 4.1.12.a) and "BP-sample" (Figure 4.1.12.b) magnetite is the main corrosion product formed on the metallic surface. Surprisingly, the "BP-sample" also revealed the presence of feroxyhyte (δ-FeOOH) with its characteristic bands at 417.22 cm^{-1} and 728 cm^{-1} (Figure 4.1.12.c).

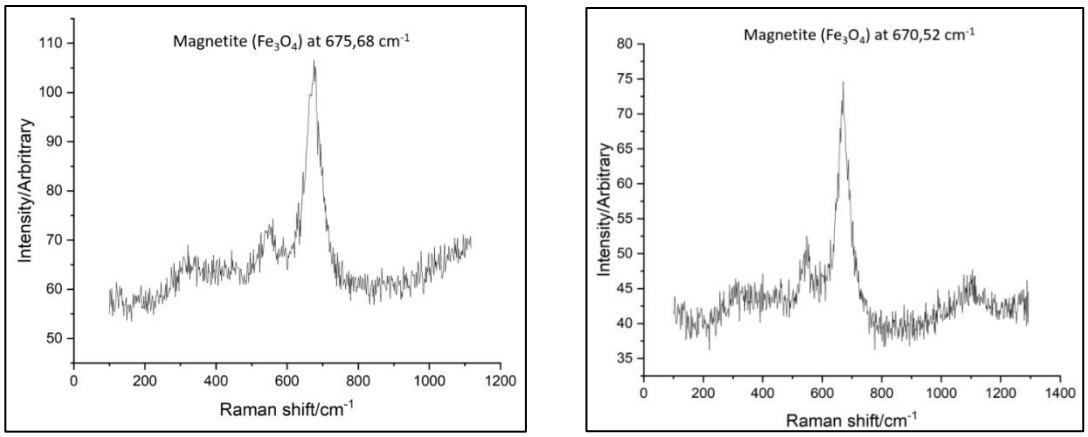

(a) (b)

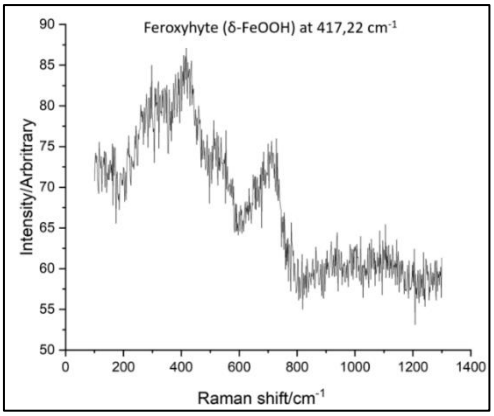

(c)

Figure 4.1.12: Raman spectrum for a) "BR-sample" (identification of magnetite), b) "BP-sample" (identification of magnetite) and c) "BP-sample" (identification of feroxyhyte)

III. Experiment C

SEM - EDS analyses

In the same way as for experiment B, experiment C used one rough sample ("CR-sample") and one smooth mirror-effect surface sample ("CP-sample") for the structural characterization. Compared to their initial appearances, "CR-samples" obtained a slightly darker coloration and "CP-sample" had lost their initial shine.

SEM-EDS analyses enabled to visualize the formation of hexagonal-shaped nanoplates, homogeneously distributed on the surface of the "CR-sample" (Figure 4.1.13).

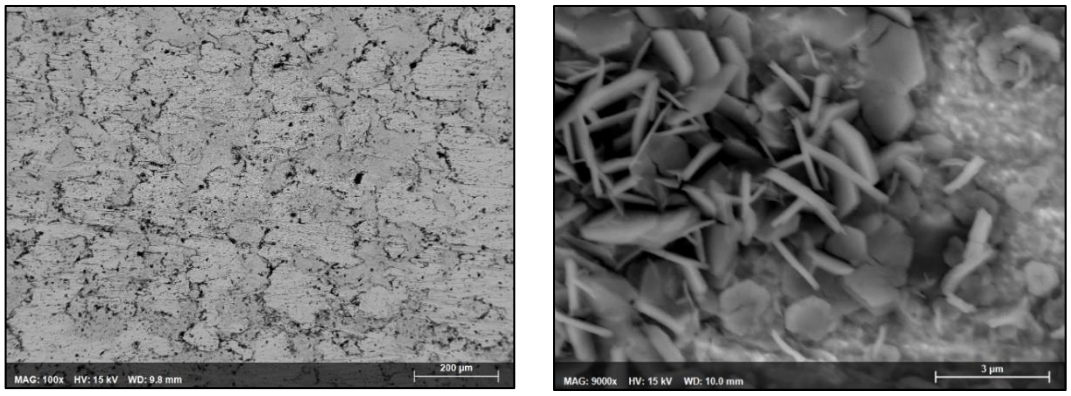

(a) (b)

Figure 4.1.13: SEM images for "CR-sample" at a) 200 µm and b) 3 µm

EDS mapping performed on "CR-sample" make possible to visualize (in white color) the zone where iron, oxygen and silicon are present (Figure 4.1.14).

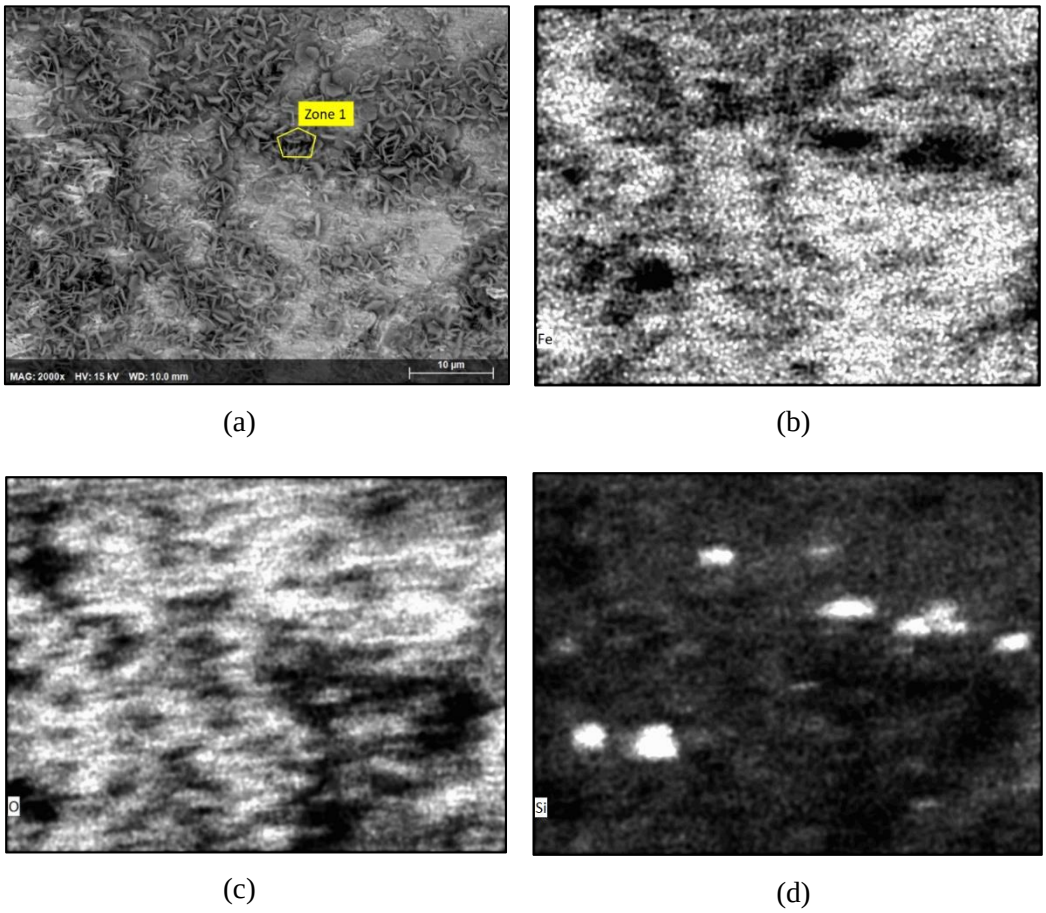

(a) (b)

(c) (d)

Figure 4.1.14: SEM images and elemental mapping for "CR-sample": a) illustration of the selected zone for elemental mapping, b) presence of iron (white color), c) presence of oxygen (white color) and d) presence of silicon (white color)

	O	Si	Fe	C	S	Na
Zone 1 (%)	51.23	11.92	29.87	6.59	0.11	0.25

Table 4.1.8: EDS analyses of selected zones for "CR-sample". Selected zone is illustrated in Figure 4.1.14.a

Moreover, elemental mapping was performed on a small area of "CR-sample" (selected zone illustrated in Figure 4.1.14.a) and the associated results are presented in Table 4.1.8. It shows the presence of iron and oxygen, probably due to an oxide presence, but also the presence of silicon.

Figure 4.1.15 shows that it is not evident to observe any corrosion product formation on the surface of "CP-sample". However, elemental mapping performed on the surface of such sample shows the presence of iron and oxygen (no big amount of silicon was identified) (Table 4.1.9).

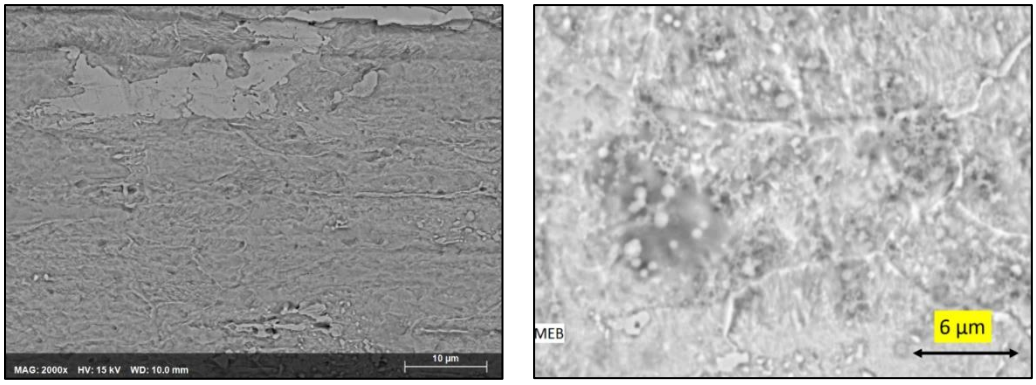

(a) (b)

Figure 4.1.15: SEM images for "CP-sample"at a) 10 µm and b) 6 µm

	O	Si	Fe	C	S	Na
CP-sample (%)	24.83	0.79	65.32	8.82	0.09	0.13

Table 4.1.9: EDS analyses of selected zone for "CP-sample"

Optical imaging and Raman spectroscopy

Thanks to optical microscopy observations, it was possible to distinguish areas affected by corrosion processes for both "CR-sample" and "CP-sample" (Figure 4.1.16).

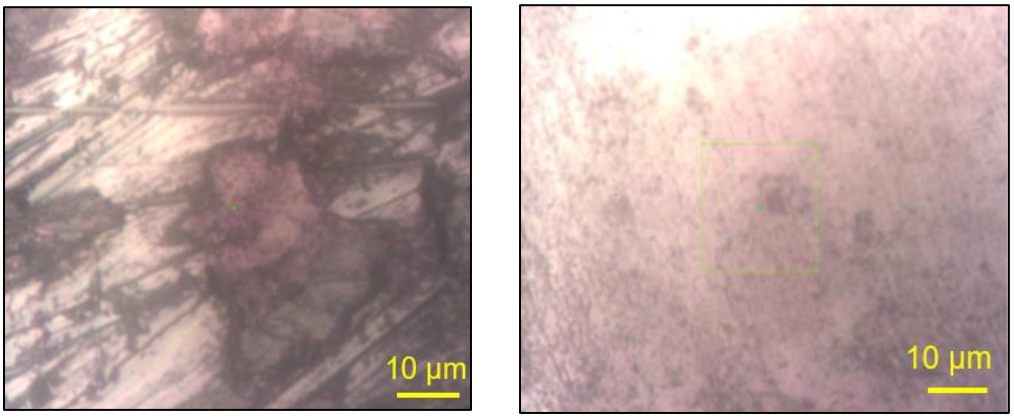

(a) (b)

Figure 4.1.16: Optical imaging at 10 µm for a) "CR-sample" and b) "CP-sample"

The associated Raman-spectrum showed that upon "CR-sample" magnetite was formed at 675.68 cm^{-1} (Figure 4.1.17.a). Concerning "CP-sample", we could mainly identify some hints

of magnetite presence at 672.24 cm^{-1} (Figure 4.1.17.b), although only one spectrum revealed a significant presence of magnetite at 679.12 cm^{-1} (Figure 4.1.17.c).

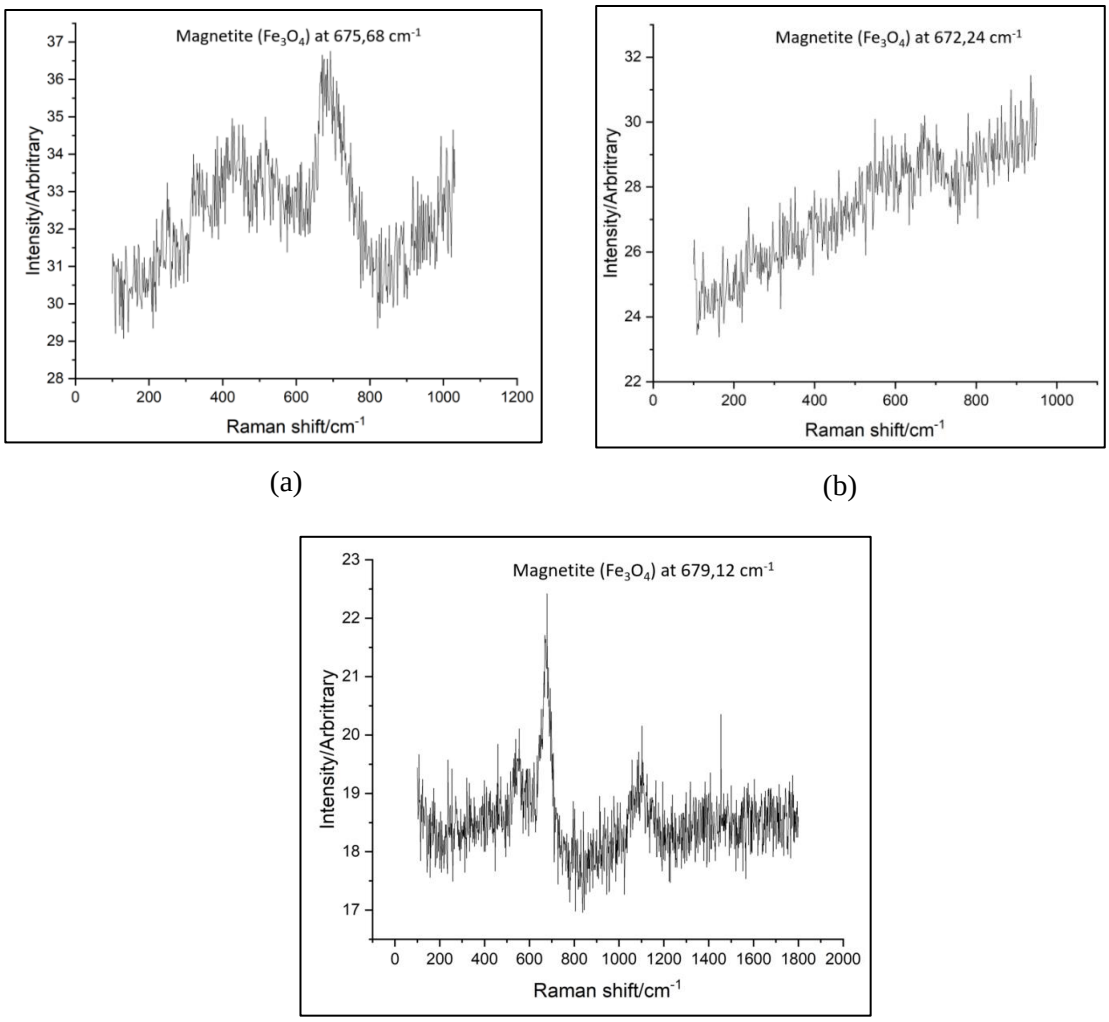

Figure 4.1.17: Experiment C: Raman spectrum for a) "CR-sample" (identification of magnetite), b) "CP-sample" (identification of magnetite) and c) "CP-sample" (identification of magnetite)

IV. Experiment E

SEM - EDS analyses

For experiment E, one rough sample ("ER-sample") was used for the structural characterization. Compared to its initial appearance, "ER-samples" didn't show any significant color change. SEM-EDS analyses enabled to visualize some iron oxides formations (hexagonal-shaped nanoplates, homogeneously distributed) upon the sample surface (Figure 4.1.18).

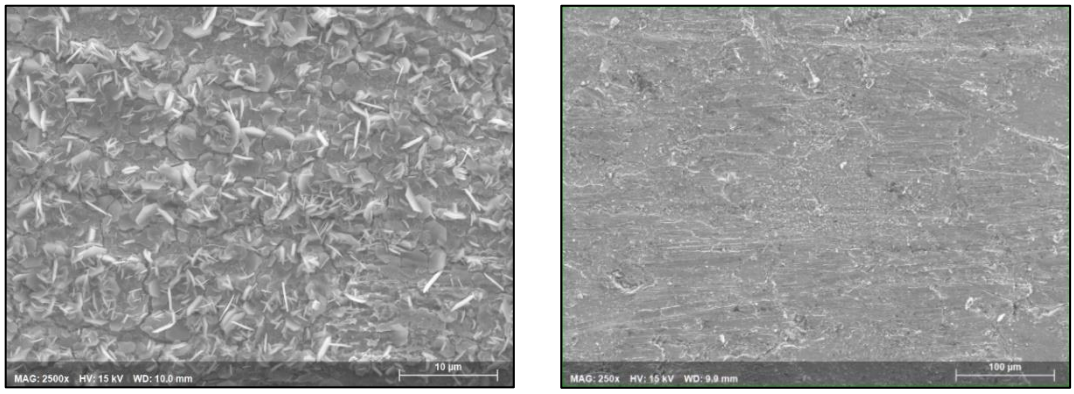

(a) (b)

Figure 4.1.18: SEM images for "ER-sample"at a) 10 µm, b) 100 µm

EDS mapping performed on "ER-sample" make possible to visualize the zone where iron, oxygen and silicon are present (Figure 4.1.19). Associated results are presented in Table 4.1.10.

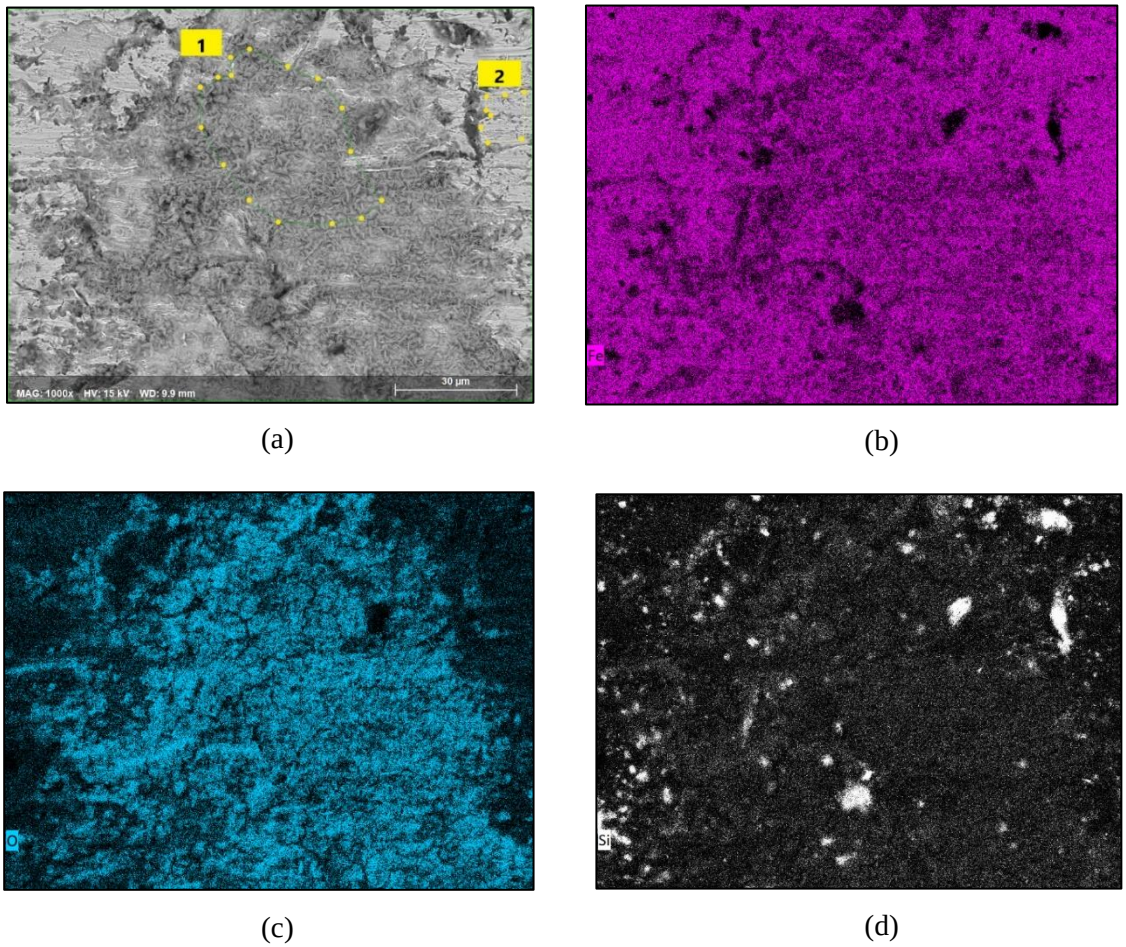

(a) (b)

(c) (d)

Figure 4.1.19: SEM images and elemental mapping for "ER-sample": a) illustration of the selected zone for elemental mapping, b) presence of iron (violet color), c) presence of oxygen (blue color) and d) presence of silicon (white color)

	C	O	Al	Si	Ca	Fe
Zone 1(%)	9.19	37.75	0.19	4.14	0.0	48.72
Zone 2(%)	12.44	13.26	0.10	2.21	0.0	71.99

Table 4.1.10: EDS analyses of selected zones for "ER-sample"

Optical imaging and Raman spectroscopy

Thanks to optic microscopy observations, it was possible to distinguish areas affected by corrosion processes for "ER-sample" (Figure 4.1.20).

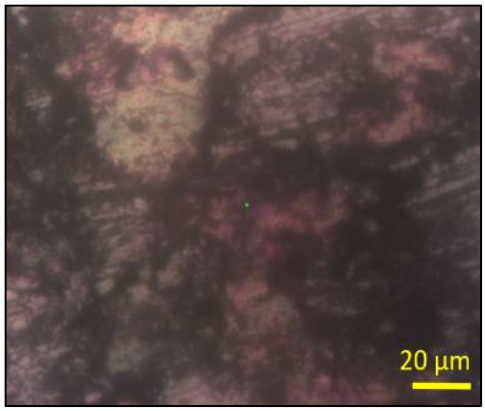

Figure 4.1.20: Optical imaging for the sample of experiment E at 20µm

Unfortunately, the associated Raman investigation didn't allow to identify any presence of corrosion product on "ER-sample".

V. Experiment F

For experiment F, one rough sample ("ER-sample") was planned to be used for structural characterization. Unfortunately, we observed that experiment F samples have undergone active oxidation since their surfaces were partially covered by a dark/orange layer. The condition of the samples was not appropriate to give representative results, as this oxidation could happen during the experiment or during their storage. Thus, we don't present any µRaman result associated with experiment F.

Weight loss measurement method

Additionally to the hydrogen gas production monitoring, the average corrosion rate obtained on the total duration of the experiment is also evaluated by weight loss measurement method. These gravimetric measurements were performed on dedicated metallic coupons which have been weighted initially, at the beginning of the experiment, and finally after being soaked in three successive ultrasonic baths with acidic solution.

It should be noted that we didn't use the same US-bath for all the experiments. A new, US-bath was used for experiment E and experiment F, while in the previous experiments (B-C) a less effective US bath was used. Initially, we thought that this change could potentially generate differences among the results, although as it is shown in Table 4.1.11, the corrosion rate in the experiments with the pure water are not far enough with each other (excepted for experiment F sample which has been potentially oxidized).

Experiment	# samples	time (years)	$\Sigma(\Delta m_{(g)})$	r ($\mu m.year^{-1}$)
B	3	0.0704	0.003	1.69 ± 0.08
C	2	0.0587	0.005	4.82 ± 0.34
E	1	0.0582	0.001	1.94 ± 0.27
F	2	0.0447	0.0238	30.23 ± 2.13

Table 4.1.11: Summarized results for the corrosion rate calculated with weight loss measurement method and associated to the experiments with pure water

4.1.3 Liquid Samples

For each experiment, solutions that have been sampled in both cells (with and without metallic coupons) have undergone *post mortem* analyses. For the cells dealing with ultrapure water only, solution has been sampled right after the end of the irradiation phase to measure the concentration of hydrogen peroxide (H_2O_2). For the cells dealing with ultrapure water and metallic coupons, solution has been sampled right after the end of the post irradiation phase, to measure the dissolved iron ions concentrations. In addition, pH measurements have been performed on solutions before and after the experiment for all the tested cells.

pH evolution

All the pH measurements took place after calibration of the pH-meter using 3 different buffer solutions at 3 different pH (4, 7, 10). Table 4.1.12 summarized the results of the pH evolution for all the experiments with pure water.

pH / Experiment	Cell 1 (pure water + samples) before the experiment	Cell 1 (pure water + samples) after the experiment	Cell 2 (pure water) before the experiment	Cell 2 (pure water) after the experiment
A	6.5	5.6	6.7	5.3
B	6.7	5.0	6.5	4.6
C	6.5	5.4	6.5	4.5
E	6.5	6.0	6.5	4.4
F	6.3	7.1	6.4	4.9

Table 4.1.12: pH evolution (before and after the experiment) for all the cells tested with ultrapure water

We can observe that, for both type of cell, an acidification of the solutions occurs during the experiment. Moreover, the biggest pH decreases correspond to the solutions sampled in the cell dealing with ultrapure water only. However, the pH evolution recorded for cell F1 differs from this general trend, as it is the only cell showing an increase in the pH after the end of the test.

Hydrogen peroxide concentration

Hydrogen peroxide concentrations have been measured only for cells dealing with ultrapure water for experiments B, C and F. All the H_2O_2 measurements were carried out within the day of the irradiation end. The results of these measurements are shown in Table 4.1.13.

Experiment	A	B	C	E	F
$[H_2O_2]$ ($\mu mol.L^{-1}$)	-	11.86	0.52 ± 0.09	-	0.59 ± 0.09

Table 4.1.13: H_2O_2 concentration in cells containing ultra-pure deaerated water

Experiment C and experiment F indicate very close H_2O_2 concentrations values, while experiment B show a concentration two orders of magnitude higher than the other two. This difference may be attributed to two reasons. Firstly, we used the fluorescence method for experiment B, while for experiment C and F, we performed the measurement thanks to Ghormley method. Secondly, the solution sampled just after the irradiation phase of experiment B was quite blurry (Figure 4.1.21). This observation could signify the presence of impurities within the cell B2 which could potentially have an impact on hydrogen peroxide concentration.

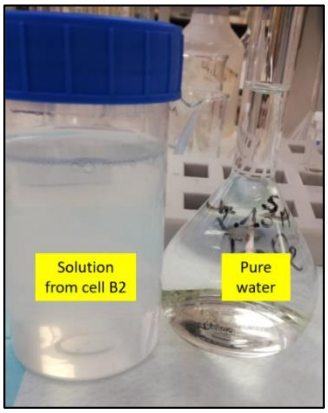

Figure 4.1.21: Blurry solution sampled in cell B2 after the irradiation phase

Concentration of dissolved iron

For all experiments, the total dissolved iron concentrations measured by Inductively Coupled Plasma – Atomic Emission Spectrometry (ICP-AES) are shown in Table 4.1.14. The results are in good agreement with each other, varying between 0.21-0.34 mmol.L^{-1}. Exception to this is the result associated to experiment A, with a value which is one order of magnitude lower than the other four experiments with pure water.

Experiment	A	B	C	E	F
$[Fe_{total}]$ (mmol.L^{-1})	0.02	0.33 ± 0.0004	0.34 ± 0.002	0.25 ± 0.07	0.21 ± 0.0005

Table 4.1.14: Total dissolved iron concentrations measured by ICP-AES for the cells dealing with ultrapure water only

Iron incorporation to the glass matrix

It is noteworthy to mention that after the end of every experiment, we observed a non-removable grey line on both the glass beaker (situated around the liquid/gas interface) and the glass sample holder involved in the cells containing solution and metallic samples (Figure 4.1.22.b). This grey line most probably results from incorporated iron ions into the glass matrix. To confirm this hypothesis, we performed additional tests in order to remove the iron ions from the glass matrix and estimate their quantity. Using HCl solution, partial acid attack was achieved on two glass beakers: the cell A1 beaker and a pristine one. The results of this second test revealed that the presence of iron corresponds to 0.871 mg while the pristine one had only 0.004 mg. Therefore, the iron entrapment hypothesis is confirmed as the iron presence in the pre-used glass beaker/sample holder was found to be two orders of magnitude higher than the pristine one.

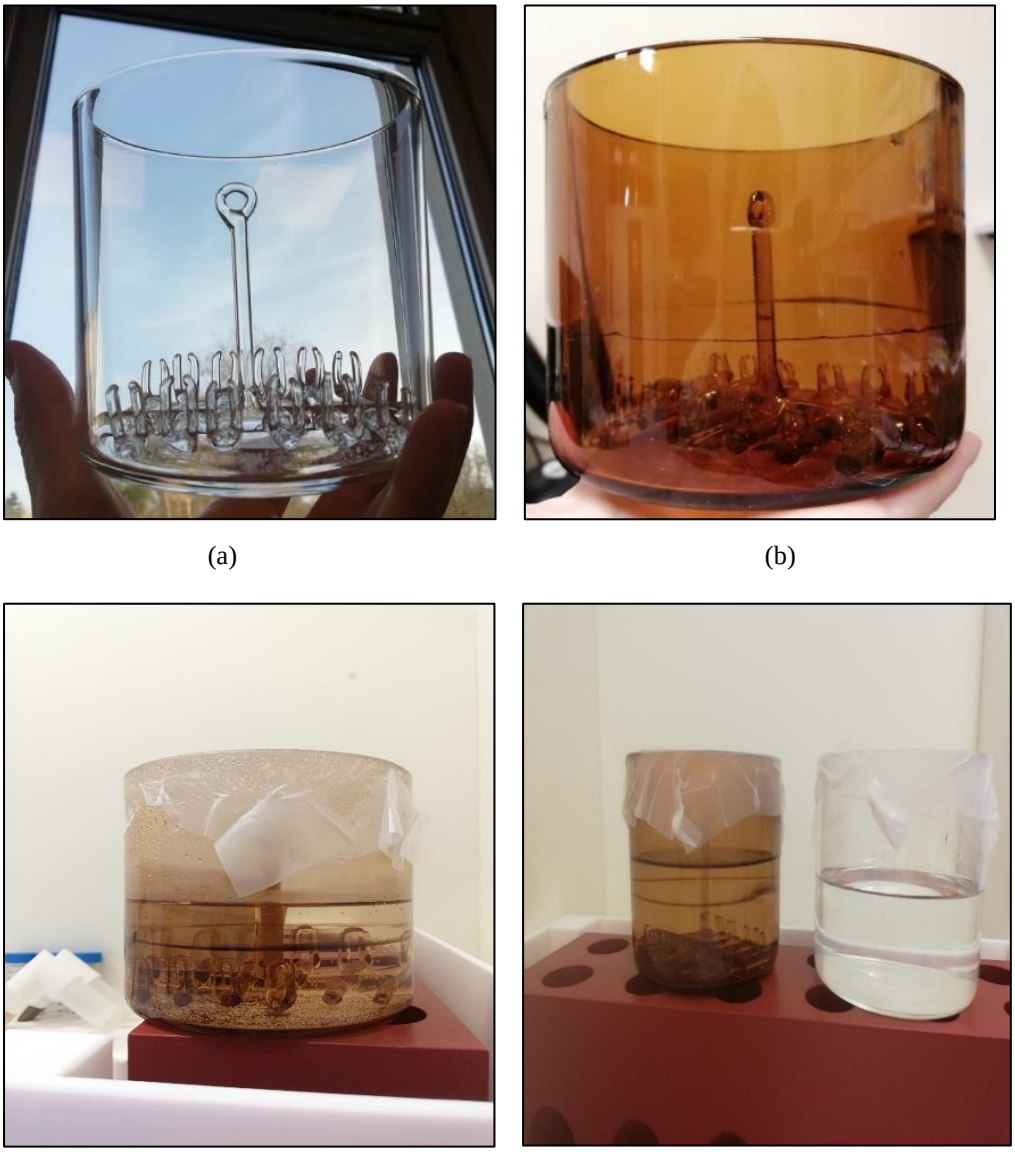

(a) (b)

(c) (d)

Figure 4.1.22: Glass beaker and the sample holder a) before the experiment, b) after the experiment, c) during first test over the hotplate, d) during second test with pristine beaker over the hotplate.

4.2 Experiments with synthetic pore water

4.2.1 H_2 gas production

Tournemire argillaceous rock synthetic pore water (TRNM synthetic pore water) has been used in order to get closer to the real deep geological disposal conditions, i.e., when carbon steel material corrosion processes involved argillaceous rock pore water. Four tests were dedicated to study the impact of the synthetic argillaceous rock pore water on carbon steel anoxic corrosion processes, two full length experiments (experiment D, G), one short term test (experiment D++) and one short term experiment without irradiation (experiment D+).

1) Experiment D

In experiment D, cell D1 (TRNM synthetic pore water with metallic coupons) and cell D2 (only TRNM synthetic pore water) were tested with 200 ml of TRNM synthetic pore water. Six carbon steel samples were sufficiently immersed in cell D1. Among these six metallic samples, two of them underwent special polishing treatment till obtaining a very smooth mirror-effect surface ("DP-sample") and the four others where roughly polished ("DR-sample"). For both cells the helium flow rate was set at 5 $ml.min^{-1}$.

The irradiation phase lasted approximately 12.6 days and the gamma radiation dose rate applied was 50.1 $Gy.h^{-1}$ for both cells. Once the irradiation stopped, cell D2 was disconnected while cell D1 remained connected for five days more to record the H_2 evolution corresponding theoretically to the post irradiation anoxic corrosion process. Figure 4.2.1 shows the H_2 evolution for experiment D.

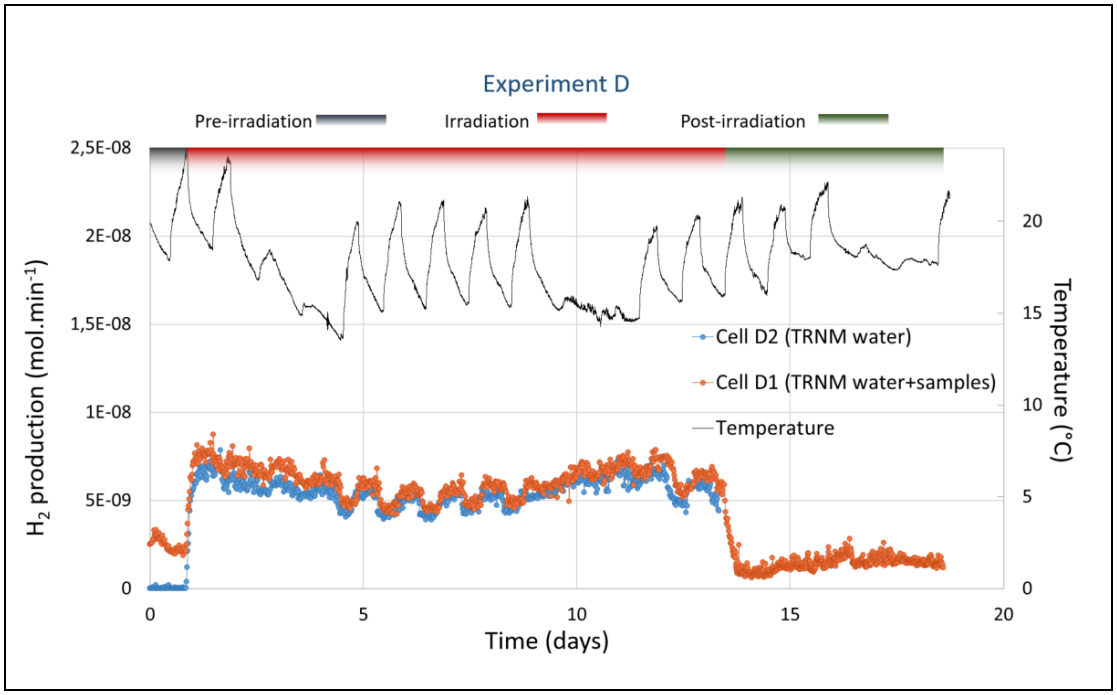

Figure 4.2.1: H_2 production and temperature evolution over time for experiment D

During the gas chromatograph calibration tests which took place just before the beginning of experiment D, we observed that the given H_2 concentration values were approximately the half of the real concentration (~10.7 ppm instead of 20.37 ppm). Due to lack of time for further tests, the experiment started.

Cell D1 (TRNM synthetic pore water + samples)

For cell D1, Figure 4.2.1 shows the hydrogen production recorded during the three successive phases of the experiment: (i) pre-irradiation anoxic corrosion phase, (ii) radiolytic anoxic corrosion phase and (iii) post-irradiation anoxic corrosion phase.

i) During pre-irradiation phase, hydrogen production evolution shows a first decrease followed by a more stable phase almost for 9 hours before the irradiation start. These measurements indicated a stable average value of about 2.15 x 10^{-9} mol.min^{-1}.

ii) During radiolytic anoxic corrosion phase, hydrogen production is rapidly increased till a stabilization "plateau". After this, and for all the irradiation phase, hydrogen production seems to fluctuate with the temperature variations. On average H_2 obtained the value of 6.11 x 10^{-9} mol.min^{-1}, approximately the half of the values obtained during ultrapure water tests.

iii) After the end of irradiation phase, hydrogen production evolution recorded for cell D1 decreased rapidly to then stabilize over time at a value of about 1.42 x 10^{-9} mol.min^{-1}.

In comparison with the previous tests performed with ultrapure water and metallic samples, we observed a decrease in the hydrogen production

Cell D2 (TRNM synthetic pore water):

For the cell D2, Figure 4.2.1 represents the water radiolysis of the synthetic pore water. During these 12.2 days of irradiation, the H_2 production seem to be alike the one recorded in cell D1, as we observe similar evolution with great temperature dependence. The average value of hydrogen production is about 5.52 x 10^{-9} mol.min^{-1}, constantly inferior of cell D1.

Corrosion rate

For this experiment, we were able to monitor the hydrogen production evolution associated with cell D1 during the three tested phases. During pre-irradiation phase, the average corrosion rate value is about 0.88 µm.year^{-1}, slightly lower than the results associated to ultrapure water experiments. During irradiation phase, the average corrosion rate value is estimated at 0.29 µm.year^{-1}, with maximum values at 0.98 µm.year^{-1}. During post-irradiation phase, the average corrosion rate value is about 0.59 µm.year^{-1}. It is worth noting that for the post-irradiation rate we observe a decrease comparing with the pre-irradiation phase. Once more, due to the identified problem during the calibration, these values correspond to the hydrogen measurements exported from the gas chromatograph, although its proper function need to be further verified.

As the calibration problem persisted, in order to better understand if the obtained values for experiment D were reliable, two additional short-term tests took place, with and without irradiation:

- Experiment D+ was performed without irradiation in order to measure the hydrogen arising of anoxic corrosion of steel immersed in synthetic pore water;
- Experiment D++ was performed under irradiation in order to measure and compare the H_2 production results associated to water radiolysis using synthetic pore water and ultrapure water.

2) Experiment D+

Since the pre-irradiation H_2 production is measured only for short period of time, we decided to perform this experiment to test if the hydrogen production evolution during this pure anoxic corrosion period was in the same order of magnitude as the associated phase of experiment D. We performed the experiment using only the cell D1 (TRNM water + metallic samples), with 200ml of synthetic pore water solution and 6 metallic samples (with rough surfaces), following the same procedure as in experiment D. The cell was placed out of IRMA hall, and we recorded H_2 production evolution for 5.6 days, using helium as carrier gas with a 5 $ml.min^{-1}$ flow rate.

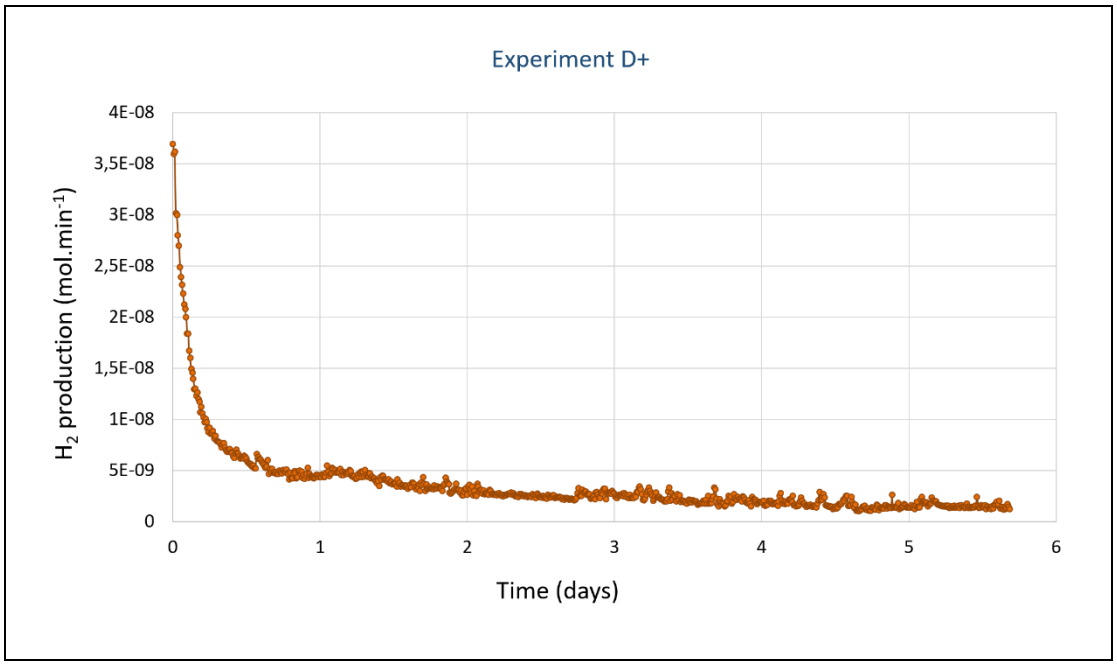

Figure 4.2.2: H_2 production evolution over time for experiment D+

As Figure 4.2.2 shows, initial hydrogen production values recorded during the first 12 hours are very high. This is certainly due to residual gas in the output lines. All this gas volume is progressively evacuated and after the first 24 hours we obtain a more stable evolution which is gradually decreased even more, probably due to the beginning of the formation of a corrosion layer upon the metallic surfaces. Hydrogen production in experiment D+ after the first day, was on average at 2.47 x 10^{-9} $mol.min^{-1}$, quite similar for the associated average value during experiment D (2.15 x 10^{-9} $mol.min^{-1}$). This assured us about the repeatability of experiment D, at least as far it concerns the pure anoxic corrosion under the same conditions. This hydrogen value corresponds to an average corrosion rate at 1.02 $\mu m.year^{-1}$.

3) Experiment D++

Thanks to experiment D+, we confirmed that the calibration problem that we faced before the beginning of experiment D persisted. Using a bottle of mixture gas with known concentrations of (H_2, O_2, N_2), gas chromatograph continued to not measure the indicated concentration. In order to verify if this problem extends to both input lines of gas (as we use two entries for the parallel use of two cells), we continued with experiment D++. This experiment performed under irradiation and without metallic sample aiming to test: i) H_2 production values under irradiation for both input lines, and also ii) the difference of H_2 production obtained either for ultrapure water or TRNM synthetic pore water. The procedure was the same as it is for every experiment, using the anoxic glove box and prepare 200 ml of the two tested solutions. The D++ cell1 (TRNMwater) and the D++ cell 2 (ultrapure water) were connected in IRMA chamber where they were under gamma-irradiation (dose rate = 50 $Gy.h^{-1}$) for almost 4.8 days. The results of experiment D++, combined with the results from cell D2 and cell C2 are shown in Figure 4.2.3.

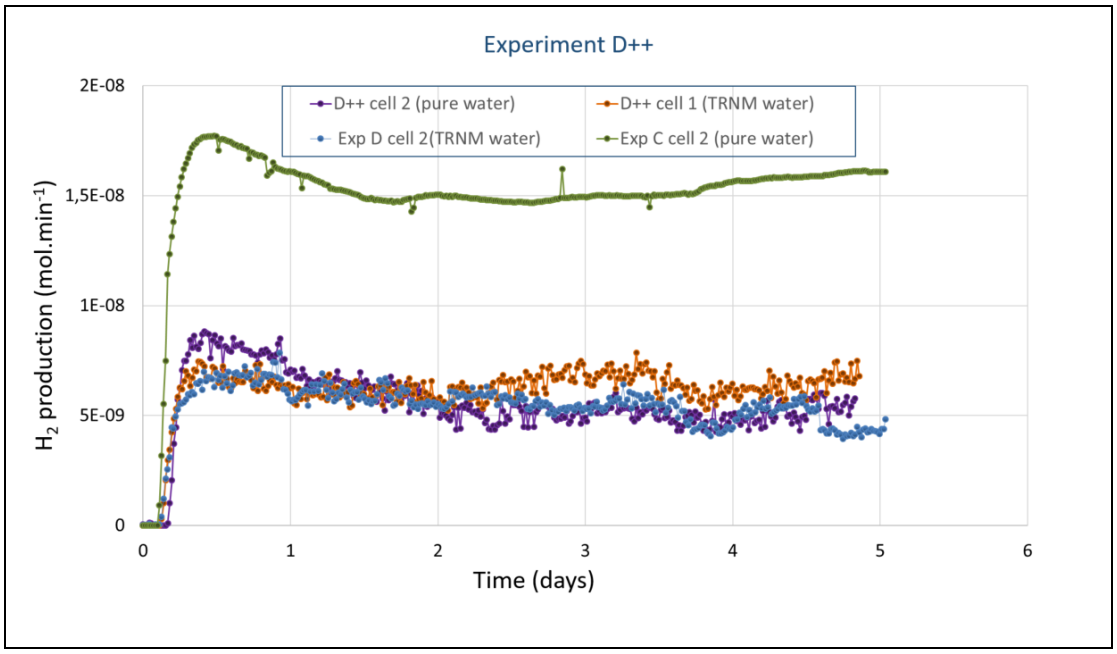

Figure 4.2.3: H_2 production evolution over time for experiment D++ (violet and orange lines), cell D2 (blue line) and cell C2 (green line)

The Figure 4.2.3 makes easy the comparison of the results from experiment C, D and D++. As we can see, cell D2 (TRNM synthetic pore water) and D++ cell1 (TRNM synthetic pore water) had quite similar evolution over time. On the contrary, this was not the case between cell C2 (ultrapure water) and D++ cell 2 (ultrapure water). As the conditions were identical between experiment C and D++ (volume of solution, anoxic condition, dose rate, Helium flux) it was supposed to have results in similar levels. Moreover, the proper calibration, and also the reproducibility of the results during experiments with pure water (exp A, B, C, E, F) make the results of cell C2 reliable, acting as a reference for the H_2 production associated with ultrapure

water under irradiation test. The H_2 production during experiment D++ in cell 2 (ultrapure water) was almost the half of H_2 production in cell C2 (ultrapure water). As the calibration before experiment C had not indicated any problem while the calibration before experiment D, D+, D++ was showing the half quantity of hydrogen, makes us conclude that the H_2 values that we obtained from experiment D are reliable as it concerns the tendencies but not the absolute values.

The results of this last experiment made necessary the intervention of a technician to repair the gas chromatograph, by installing a backflushed pre-column, able to capture possible impurities that could affect the PDHID detector's efficiency. Additional performed tests provided the proper calibration of the apparatus.

4) Experiment G

In experiment G, cell G1 (TRNM synthetic pore water with metallic coupons) and cell G2 (only TRNM synthetic pore water) were tested with 200 ml of ultrapure deaerated water. Six carbon steel samples were sufficiently immersed in cell D1. All of them underwent rough polishing treatment ("GR-sample"). For both cells the helium flow rate was set at 5 $ml.min^{-1}$.

The irradiation phase lasted 9.7 days and the gamma-radiation dose rate applied was 50.1 $Gy.h^{-1}$ and 50.7 $Gy.h^{-1}$ for cell G1 and cell G2, respectively. Within this irradiation phase, due to a technical problem impacting the two helium flow controllers, we were not able to measure H_2 production for 2.76 days. Although, based on the hydrogen tendency associated to both cells before and after this technical problem, we can assume that no unexpected evolution took place during these days. Once the irradiation stopped, cell G2 was disconnected while cell G1 remained connected for four days more to record the H_2 evolution corresponding theoretically to the post irradiation anoxic corrosion process. Figure 4.2.4 shows the H_2 evolution for experiment G.

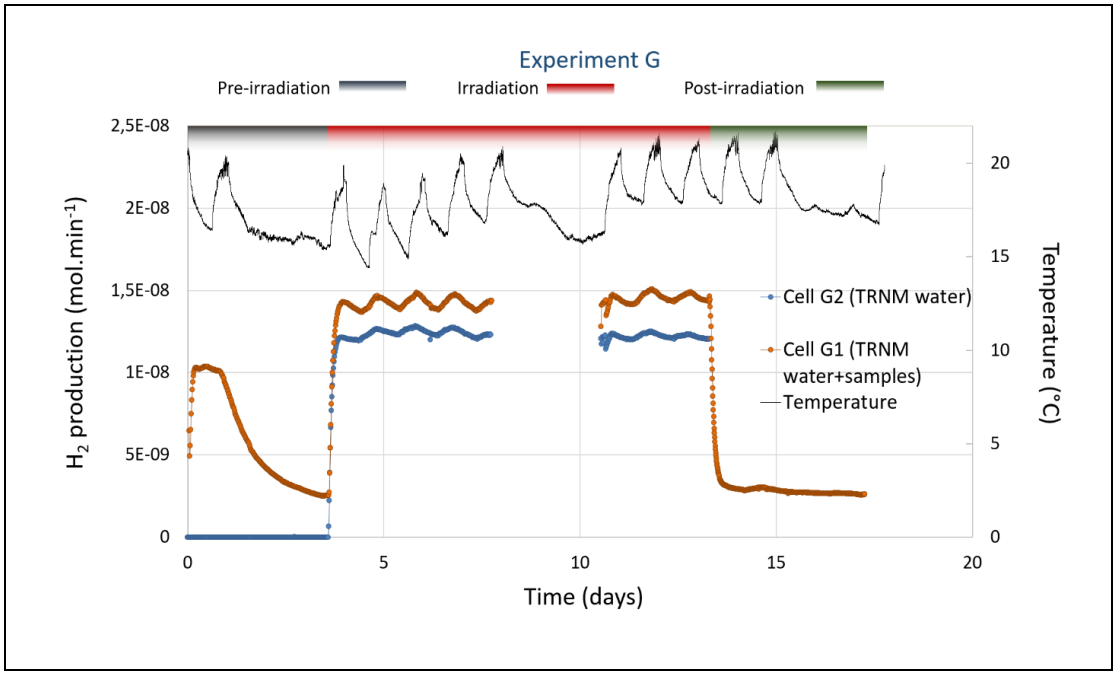

Figure 4.2.4: H_2 production and temperature evolution over time for experiment G

Cell G1 (TRNM synthetic pore water + samples)

For cell G1, Figure 4.2.4 shows the hydrogen production recorded during the three successive phases of the experiment: (i) pre-irradiation anoxic corrosion phase, (ii) radiolytic anoxic corrosion phase and (iii) post-irradiation anoxic corrosion phase.

i) During pre-irradiation phase, hydrogen production increase for few hours and reach a first plateau with a stable average value of about 1.01 x 10^{-8} mol.min^{-1}. Then, hydrogen production a slow decrease for 2.4 days. After, hydrogen evolution shows a stabilization for approximately 7 hours. During these seven hours, hydrogen on average is at 2.57 x 10^{-9} mol.min^{-1}.

ii) During radiolytic anoxic corrosion phase, hydrogen production indicates a stable evolution over time with small fluctuations due to temperature variations. The hydrogen production average value is 1.43 x 10^{-8} mol.min^{-1}, in the same order with hydrogen production obtained with experiments using pure water (1-1.62 x 10^{-8} mol.min^{-1}). Throughout the irradiation phase, the H_2 production recorded in cell G1 remain superior to the one measured in cell G2.

iii) During post irradiation anoxic corrosion phase, hydrogen production decreased rapidly to reach the average value of 2.78 x 10^{-9} mol.min^{-1}.

Cell G2 (TRNM water):

For cell G2, the Figure 4.2.4 describes the phase of synthetic porewater radiolysis recorded during irradiation. Hydrogen evolution is nearly identical with the one in cell G1, as we have similar tendencies with great temperature dependence. The average value during irradiation period was 1.23 x 10^{-8} mol.min^{-1}, constantly inferior of cell G1.

Corrosion rate

The corrosion rate values obtained for experiment G are shown in Table 4.2.2. For this experiment, we were able to monitor the hydrogen production evolution associated with cell G1 during the three tested phases.

During pre-irradiation phase, the first stabilization phase with an average H_2 production value of 1.01 x 10^{-8} mol.min^{-1} corresponds to a corrosion rate of 4.22 µm.year^{-1}. After the progressive decrease, H_2 production stabilized once again at the value of 2.52 x 10^{-9} mol.min^{-1}, which correspond to 1.06 µm.year^{-1}. These results indicate similar rates for tests involving TRNM synthetic pore water in comparison to the one performed with ultrapure water.

During irradiation phase, the average corrosion rate value is about 0.83 µm.year^{-1}, with maximum values at 1.08 µm.year^{-1}. During post irradiation phase, the average corrosion rate value is about 1.16 µm.year^{-1}.

Corrosion rate	Pre-irradiation phase	Irradiation phase	Post-irradiation phase
Average corrosion rate (µm.year^{-1})	1.06* ± 0.06	0.83 ± 0.35	1.16 ± 0.06
Maximum corrosion rate (µm.year^{-1})	4.22	1.08	1.31

*Table 4.2.1: Corrosion rates obtained for experiment G (*Average corrosion rate right before irradiation launch)*

Table 4.2.2 summarized the average values of hydrogen production associated to each studied phase (pre-irradiation, irradiation, post-irradiation) for the two experiments involving TRNM synthetic pore water. Additional experiment (D++) showed that the gas chromatograph was measuring the half of the produced H_2 quantity during experiment D. Therefore, the results on the following table for experiment D have been multiplied by a factor two.

Experiment	cell	Pre-irradiation (H_2 ($x10^{-9}$ $mol.min^{-1}$))	Irradiation (H_2 ($x10^{-9}$ $mol.min^{-1}$))	Post-irradiation (H_2 ($x10^{-9}$ $mol.min^{-1}$))
D	D1	4.22 ± 0.24	12.22 ± 1.71	2.85 ± 0.70
	D2	0	11.04 ± 1.48	-
G	G1	2.52*± 0.06	14.33 ± 0.30	2.78 ± 0.14
	G2	0	12.30 ± 0.22	-

*Table 4.2.2: Average H_2 production values for experiments with TRNM synthetic pore water (*average corrosion rate right before irradiation launch)*

Additionally, the corrosion rate results from experiment D* (with H_2 values multiplied by a factor 2) are listed on Table 4.2.3.

Corrosion rate	Pre-irradiation phase	Irradiation phase	Post-irradiation phase
Average corrosion rate ($\mu m.year^{-1}$)	1.76 ± 0.11	0.51 ± 0.33	1.18 ± 0.39
Maximum corrosion rate ($\mu m.year^{-1}$)	2.02	1.79	2.33

Table 4.2.3: Corrosion rate on experiment D, after H_2 measurements multiplied by a factor of two*

Figure 4.1.6 compares the different corrosion rate values associated to each studied phase (pre-irradiation, irradiation, post-irradiation) for the two experiments involving TRNM synthetic pore water. One can note that, after multiplying by a factor of 2, the values of H_2 production obtained for experiment D thanks to the altered gas chromatograph, there is good accordance between these data and the one obtained from experiment G. However, we still observe a difference between the two experiments during pre-irradiation phase. The higher values from experiment D are attributed to the shortest time exposure (1 day) compared with experiment G (3.6 days), limiting the formation a more protective layer, and thus leading to a higher corrosion rate.

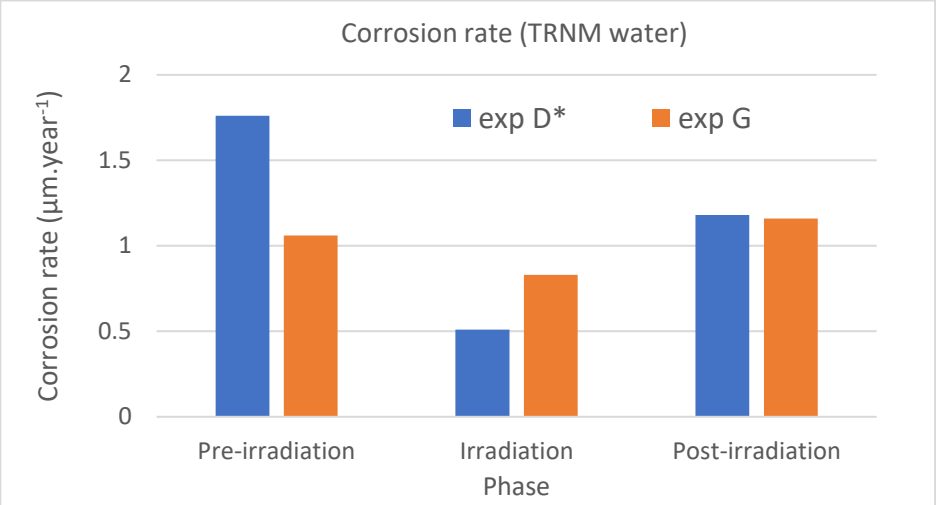

Figure: 4.2.5: Corrosion rate values associated to each studied phase (pre-irradiation, irradiation, post-irradiation) for the experiments involving TRNM synthetic pore water (H_2 values multiplied by a factor 2)*

4.2.2 Solid samples

The preparation of the metallic samples removed from cells involving TRNM synthetic pore water followed the same procedure as the one with the samples immersed in pure water. However, only samples from the two full-length experiments (experiments D and G) have been structurally characterized.

I. Experiment D

SEM-EDS analyses

For experiment D we used two different kind of steel surfaces. Four samples with rough surfaces (DR-samples) and two samples with smooth surfaces (DP-samples) have been used. SEM-EDS analyses were performed on both samples.

The "DR-samples" exhibited the presence of corrosion products (long-shaped and/or sea urchin-shape crystals) homogeneously distributed on the surface of the coupons (Figure 4.2.6).

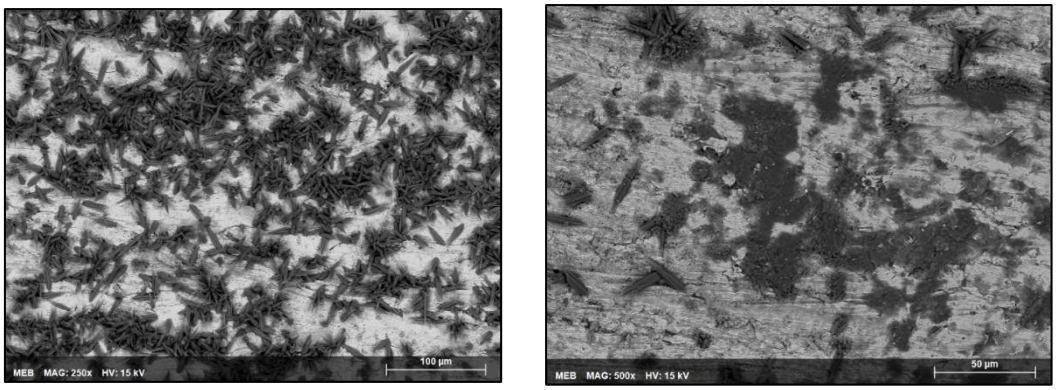

(a) (b)

Figure 4.2.6: SEM images for "DR-sample" at a) 100 µm, b) 50 µm

The composition of such crystals has been studied thanks to SEM-EDS mapping (Figure 4.2.7 and Table 4.2.4).

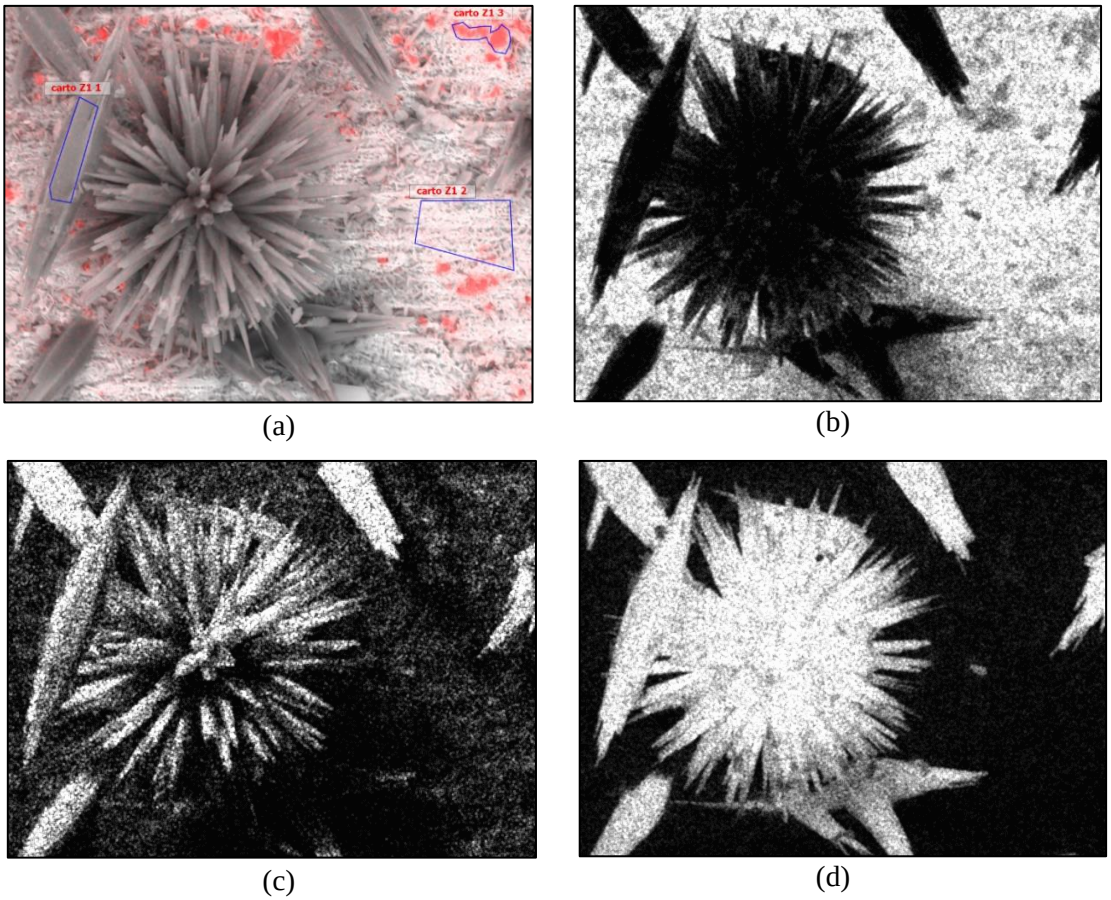

(a) (b)

(c) (d)

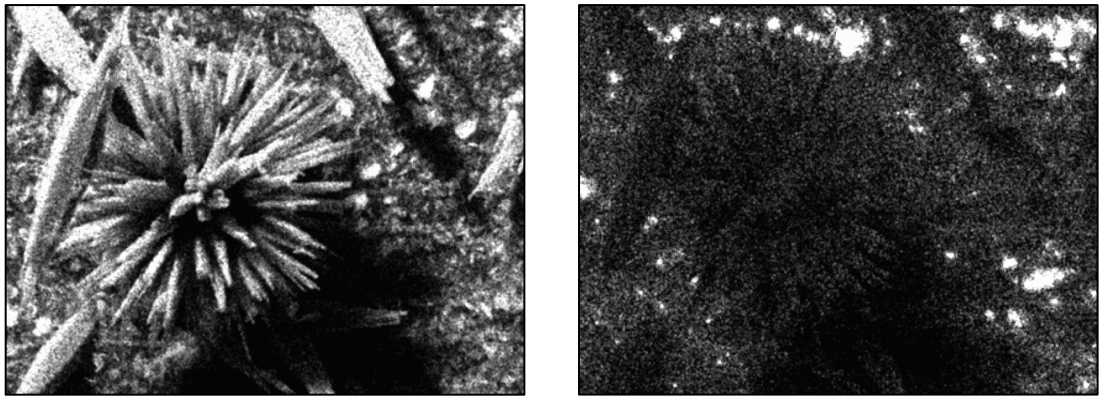

(e) (f)

Figure 4.2.7: SEM images and elemental mapping for "DR-sample": a) illustration of the selected zone for elemental mapping, b) presence of iron (white color), c) presence of carbon (white color), d) presence of calcium (white color), e) presence of oxygen (white color) and f) presence of silicon (white color)

	Fe	C	O	Ca	Na	Mg	Al	Si	S	Cl
Z1(%)	1.30	9.93	68.47	20.06	0.13	0.00	0.00	0.04	0.05	0.01
Z2(%)	72.20	3.30	22.45	0.75	0.02	0.16	0.03	0.93	0.13	0.03
Z3(%)	50.49	17.67	17.23	0.59	0.00	0.06	0.07	13.66	0.21	0.00

Table 4.2.4: EDS analyses of selected zones for "DR-sample". Selected zones are illustrated in Figure 4.2.7

The first zone (Z1 1) is covering a part of the long-shaped crystal, mainly composed by calcium, oxygen and carbon, probably indicating the presence of calcium carbonate species. The second zone (Z1 2) is to take a reference from the background, while the third zone (Z1 3) was a region with small elements mainly composed by iron, carbon, oxygen and silicon.

The long-shaped crystals observed on "DR-samples" have undergone additional SEM-EDS mapping. Even though, their presence was evident almost everywhere on the coupon surface, we also observed few special small cluster-region where hexagonal formation is identified (Figure 4.2.8).

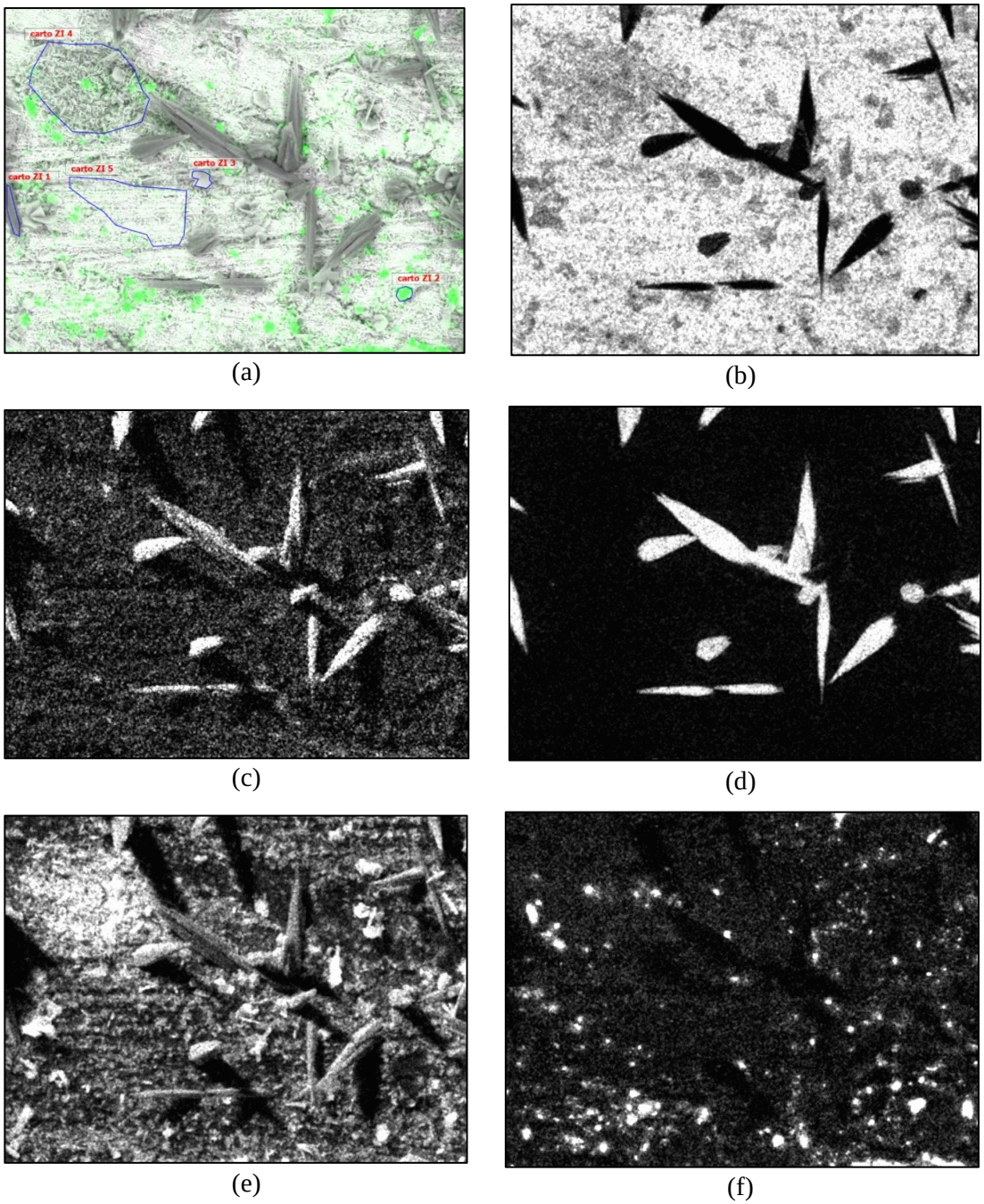

Figure 4.2.8: Experiment D: SEM images and elemental mapping for "DR-sample": a) illustration of the selected zone for elemental mapping, b) presence of iron (white color), c) presence of carbon (white color), d) presence of calcium (white color), e) presence of oxygen (white color) and f) presence of silicon (white color)

Table 4.2.5 presents the results associated to the elemental mapping characterization performed on these "DR-samples".

	C	O	Na	Mg	Al	Si	S	Cl	Ca	Fe
Z1(%)	9.63	55.50	0	0.03	0.01	0.157	0.16	0	30.01	4.49
Z2(%)	10.85	25.86	0.11	0	0.02	32.80	0.28	0.17	0.37	29.50
Z3(%)	1.29	35.63	0.18	0.70	0	1.05	0.27	0	1.33	59.53
Z4(%)	2.34	51.48	0	0.42	0.14	1.64	0.15	0	0.33	43.46
Z5(%)	3.81	25.16	0	0.13	0.1	0.78	0.09	0.01	0.37	69.53

Table 4.2.5: EDS analyses of selected zones for "DR-sample". Selected zones are illustrated in Figure 4.2.8

The first zone (Z1 1) is covering a long-shaped crystal, and as in Figure 4.2.7, this formation was found to be mainly composed by carbon, oxygen and calcium. The second zone (Z1 2) down and right on the image is composed mainly by silicon, but also by carbon, oxygen, and iron. The third zone (Z1 3) was found to be primarily by oxygen and iron, as also the fourth zone (Z1 4). Finally, the fifth zone was chosen as a background surface, mainly made by iron and oxygen. The results showed by both Figure 4.2.8 and Table 4.2.5 indicate that the chemical composition of the long-shape crystal (zone 1) is characterized by a high calcium content. In parallel, when we studied the cluster-region where hexagonal formation is identified (zone 4), we observed the presence of both iron and oxygen, probably indicating the presence of corrosion products. SEM-EDS analyses performed on "DP-sample" (mirror polishing) show that the quantity of crystal formed at the surface of the coupon is less than the one observed on the "DR-sample" (Figure 4.2.9). Moreover, the distribution of these crystal seems to be more localized for the "DP-sample" than for the "DR-sample".

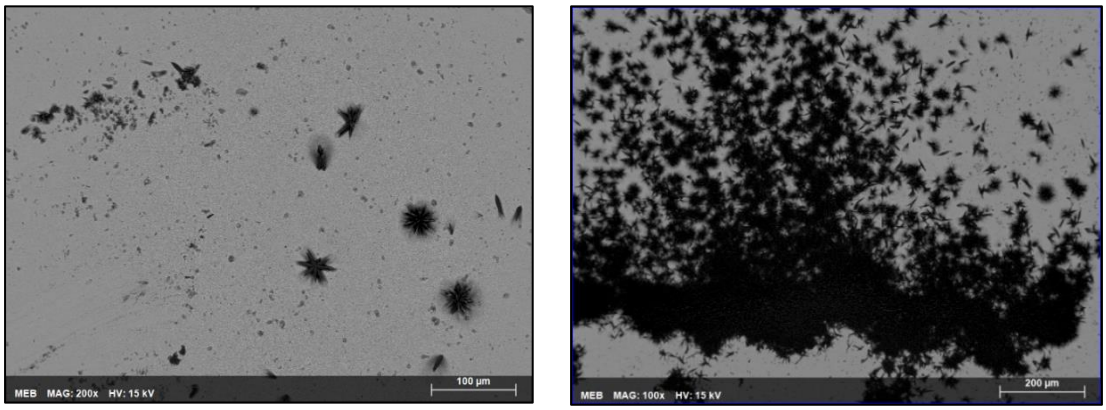

(a) (b)

Figure 4.2.9: SEM images for "DP-sample"at a) 100 µm, b) 200 µm

The composition of such “star-shape” well crystallized formation has been investigated thanks to SEM-EDS mapping (Figure 4.2.10).

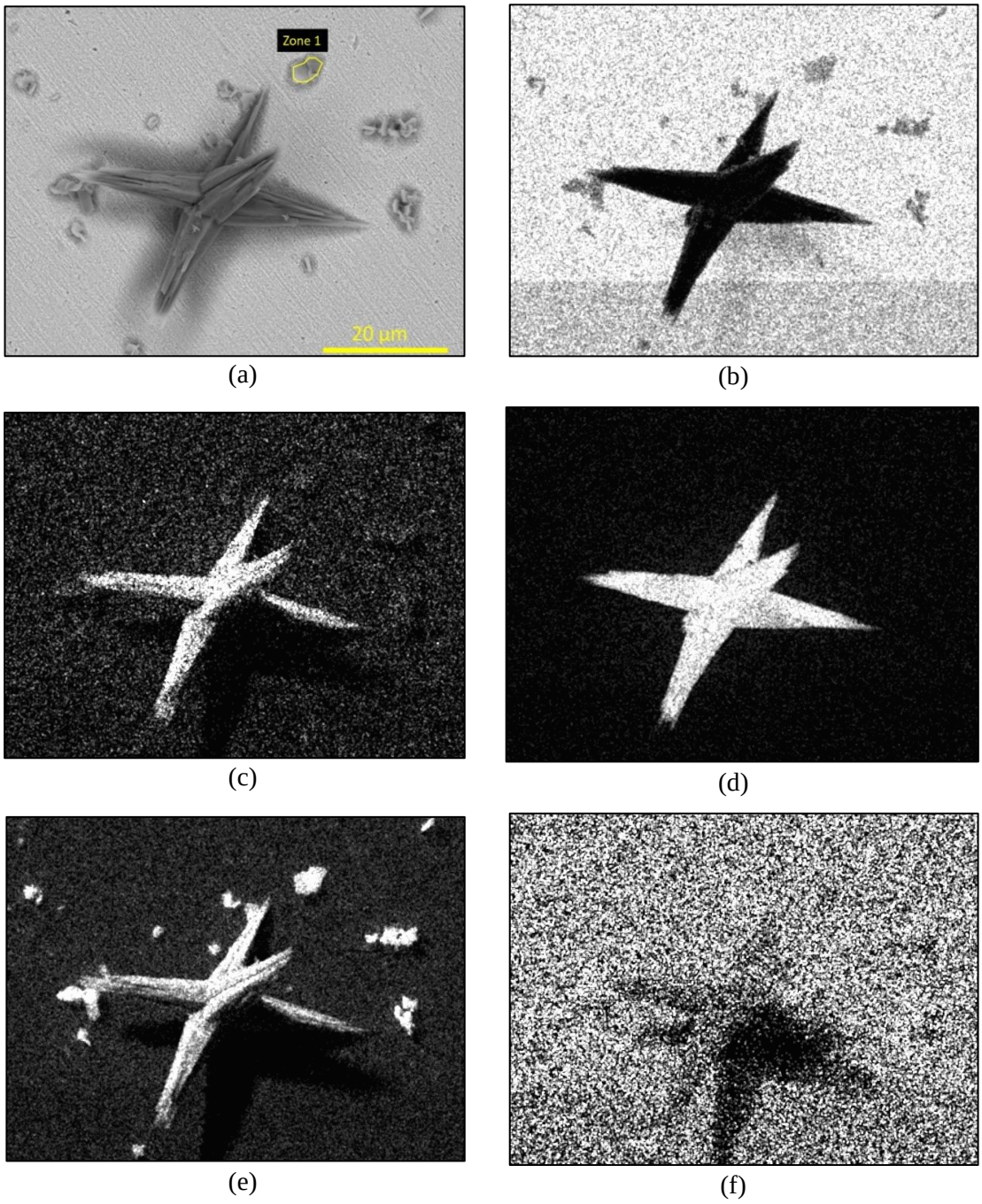

Figure 4.2.10: SEM images and elemental mapping for “DP-sample”a) illustration of the selected zone for elemental mapping, b) presence of iron (white color), c) presence of carbon (white color), d) presence of calcium (white color), e) presence of oxygen (white color) and f) presence of silicon (white color)

It appears that these “star-shape” crystals are mainly composed from calcium, carbon and oxygen, something which could mean the presence of calcium carbonate species, just like in “DR sample”.

Not so far from these “star-shape” crystals, we can also observe small clusters composed by fine hexagonal crystals (zone 1 on Figure 4.2.10.a). The EDS analyses performed on this zone indicated mainly the presence of both iron and oxygen that could correspond to corrosion product (Table 4.2.6).

	F	C	O	Ca	Na	Mg	Al	Si	S	Cl
Z1(%)	43.40	1.39	54.13	0.34	0.20	0.06	0.13	0.14	0.19	0.02

Table 4.2.6: EDS analyses of selected zones for “DP-sample”. Selected zone is illustrated in Figure 4.2.10

Optical imaging and Raman spectroscopy

Optical microscopy observations were performed on both “DR-sample” and “DP-sample” (Figure 4.2.11).

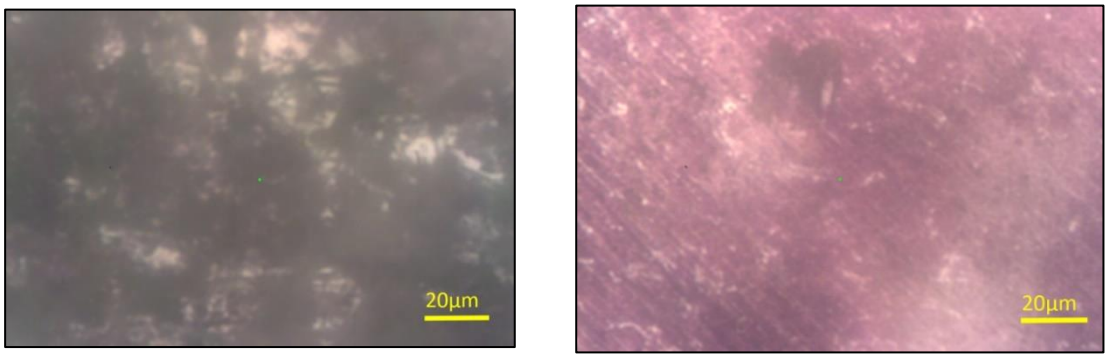

(a) (b)

Figure 4.2.11: Optical imaging at 20 µm for a) “DR-sample” and b) “DP-sample”

Optical imaging revealed that the vast majority of “DR-sample” surface has been covered by a layer which does not allow to visualize the metallic surface (Figure 4.2.11.a). Relevant areas were investigated by µRaman analyzes in order to identify the nature of this layer (Figure 4.2.12).

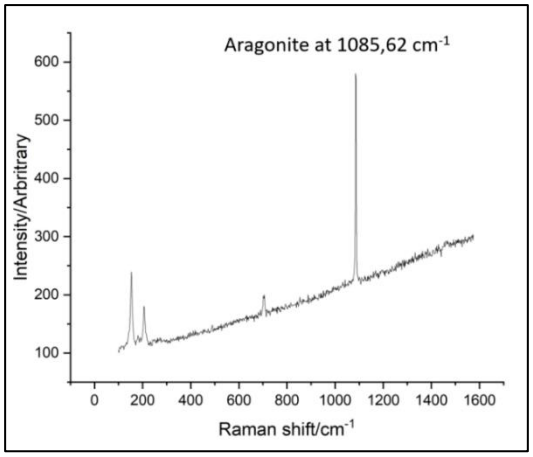

(a)

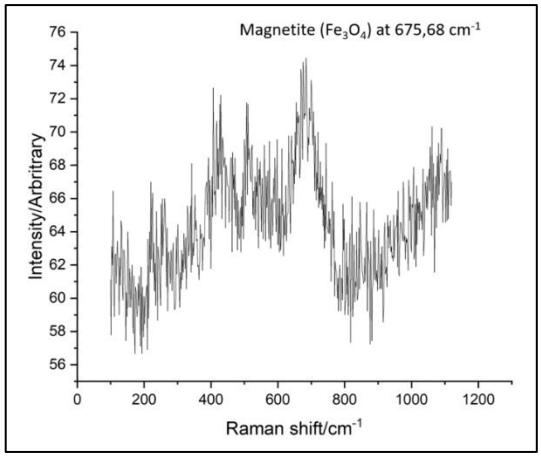

(b)

Figure 4.2.12: Raman spectrum for a) "DR-sample" (identification of aragonite), b) "DR-sample" (identification of magnetite)

µRaman analyzes performed on "DR-sample" showed that the main component of this layer is aragonite ($CaCO_3$), present almost everywhere on the surface, with a specific peak at 1085.62 cm^{-1} (Figure 4.2.12.a).

However, it should be notice that another formation has been identified with a specific peak at 675.68 cm^{-1} (Figure 4.2.12.b) characteristic of magnetite (Fe_3O_4).

Regarding "DP-sample", optical imaging revealed that the majority of the surface of the coupon is not covered by a layer in comparison with "DR-samples" (Figure 4.2.11.b). SEM-EDS analyses already showed that the crystals distribution was more localized.

Relevant areas were investigated by µRaman analyzes in order to identify the nature of these formation (Figure 4.2.13).

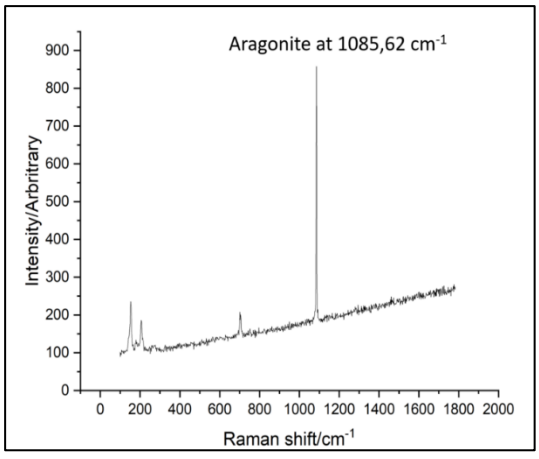

(a)

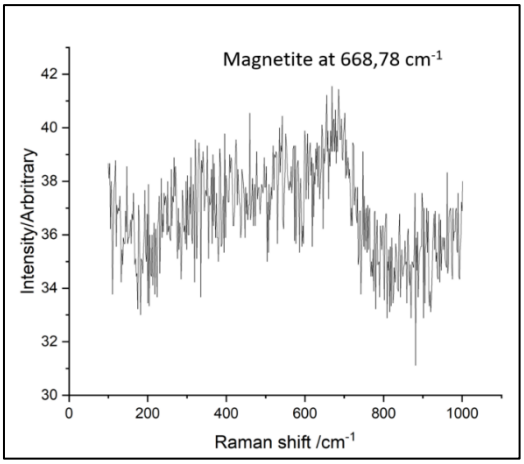

(b)

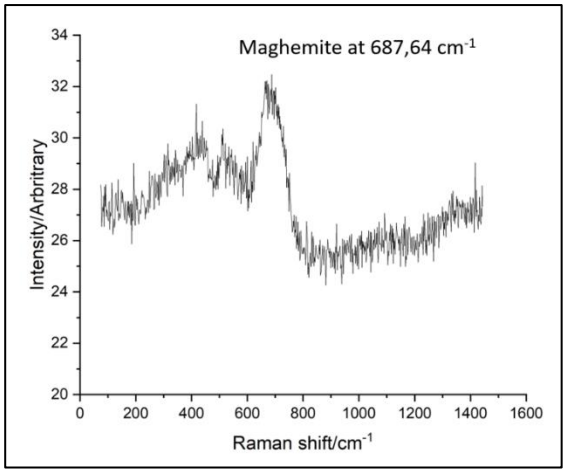

(c)

Figure 4.2.13: Raman spectrum for a) "DP-sample" (identification of aragonite), b) "DP-sample" (identification of magnetite), c) "DP-sample" (identification of maghemite)

μRaman analyzes were performed in two stages:

- First investigation allowed to identified the presence of aragonite ($CaCO_3$) (Figure 4.2.13.a) and also the faint presence of magnetite (Fe_3O_4) (Figure 4.2.13.b).
- A second set of investigation has been performed one week after the first characterization. The obtained results show that aragonite is still present, but we also observed the presence of a mixed phase between maghemite (γ-Fe_2O_3) and magnetite (Fe_3O_4) with a peak at 687.64 cm^{-1} (Figure 4.2.13.c).

  However, the presence of maghemite is attributed to a magnetite oxidation that occurred probably within these seven days between the two set of analyses.

II. Experiment G

SEM - EDS analyses

For experiment G we used six samples with rough surfaces (GR-samples). SEM-EDS analyses were performed, and "GR-samples" exhibited similar formations as those observed on experiment D coupons. The metallic surfaces are covered with long and narrow crystallized formations (Figure 4.2.14.a), although we can see thin polygonal formations scattered upon the samples (Figure 4.2.14.b).

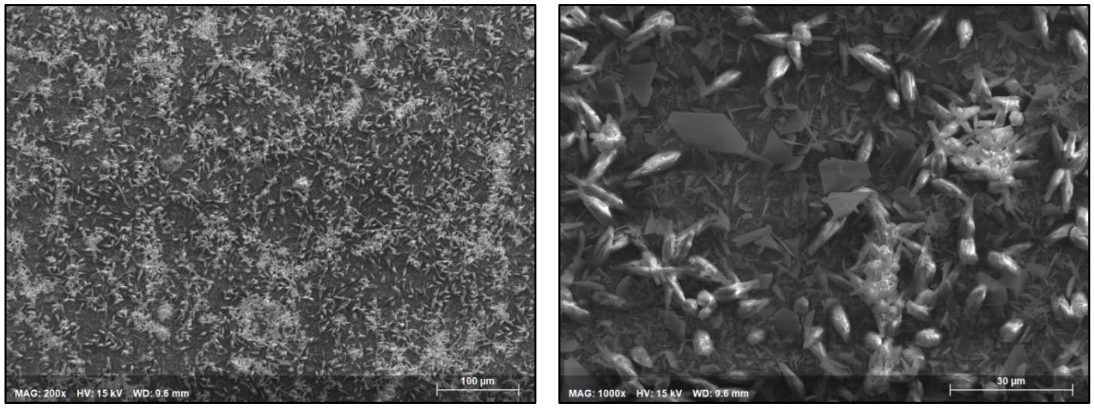

Figure 4.2.14: SEM images for "GR-sample" at a) 100 µm, b) 30 µm

The composition of such formations has been studied thanks to SEM-EDS mapping (Figure 4.2.15 and Table 4.2.7).

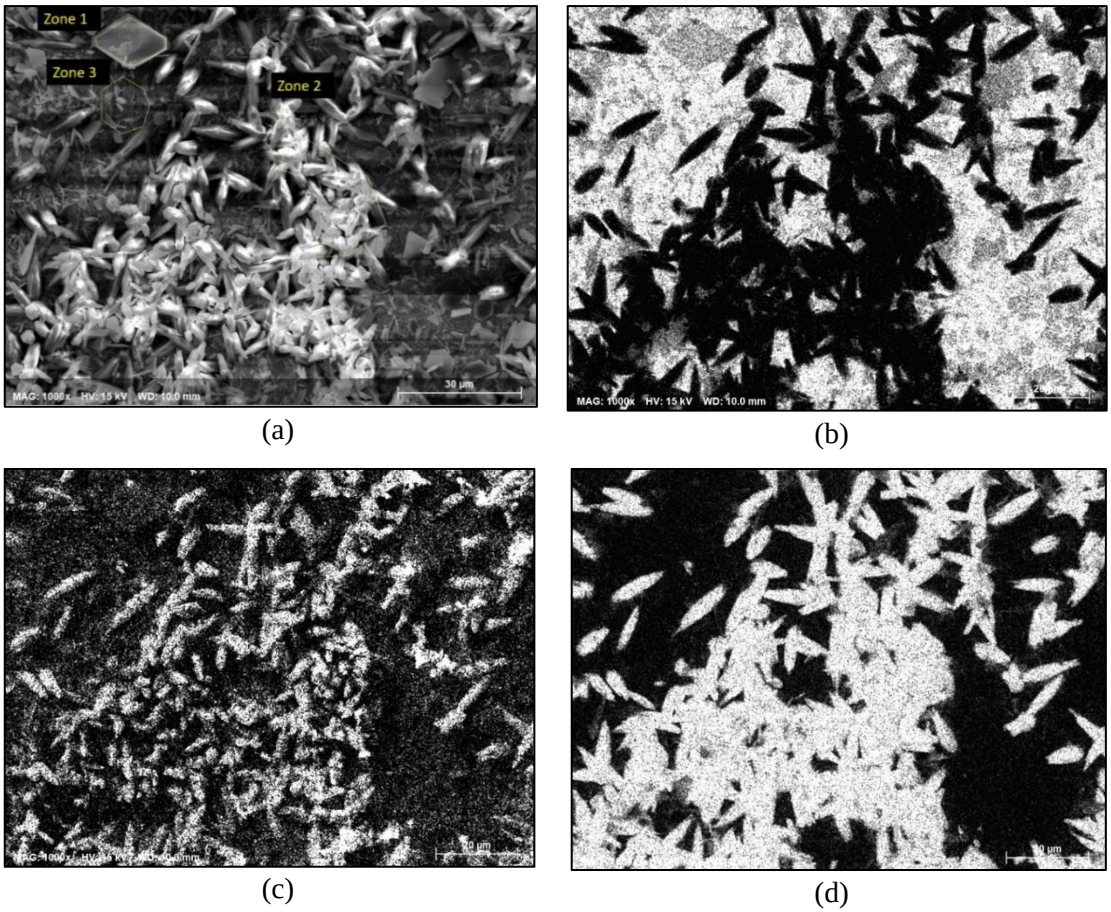

(a) (b)

(c) (d)

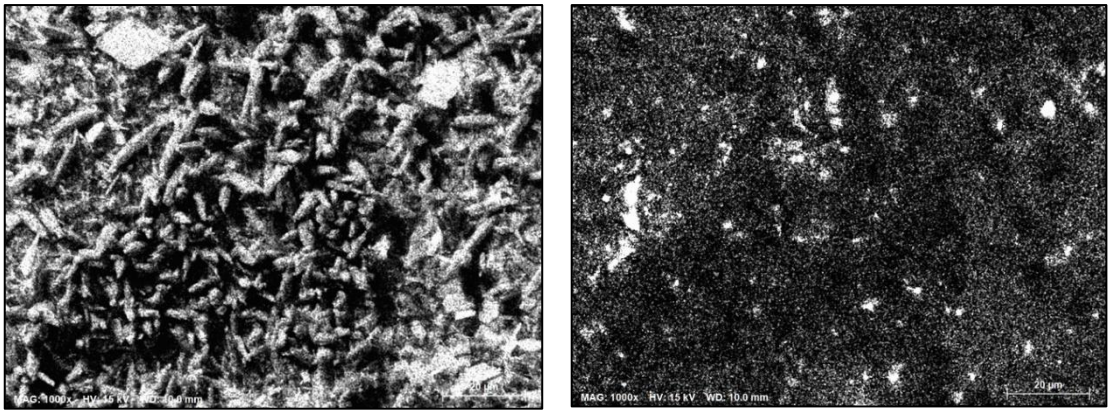

(e) (f)

Figure 4.2.15: SEM images and elemental mapping for "GR-sample": a) illustration of the selected zones for elemental mapping, b) presence of iron (white color), c) presence of carbon (white color), d) presence of calcium (white color), e) presence of oxygen (white color) and f) presence of silicon (white color)

Spectrum	C	O	Si	Ca	Fe
Z1(%)	6.25	62.32	0.19	0.82	30.40
Z2(%)	15.62	61.23	0.14	20.61	2.39

Table 4.2.7: EDS analyses of selected zones for "GR-sample". Selected zones are illustrated in Figure 4.2.15

Elemental mapping indicated that the long narrow crystals are mainly composed of calcium, oxygen, and carbon, suggesting the presence of calcium carbonate formation (zone 2 in Figure 4.2.15.a). In parallel, the thin hexagonal crystal is mainly from iron and oxygen indicating the possible presence of iron oxide (zone 1 in Figure 4.2.15.a).

We performed additional SEM-EDS analyses focused on the small cluster scattered upon the samples. We observed smaller and larger thin crystals (Figure 4.2.16.a).

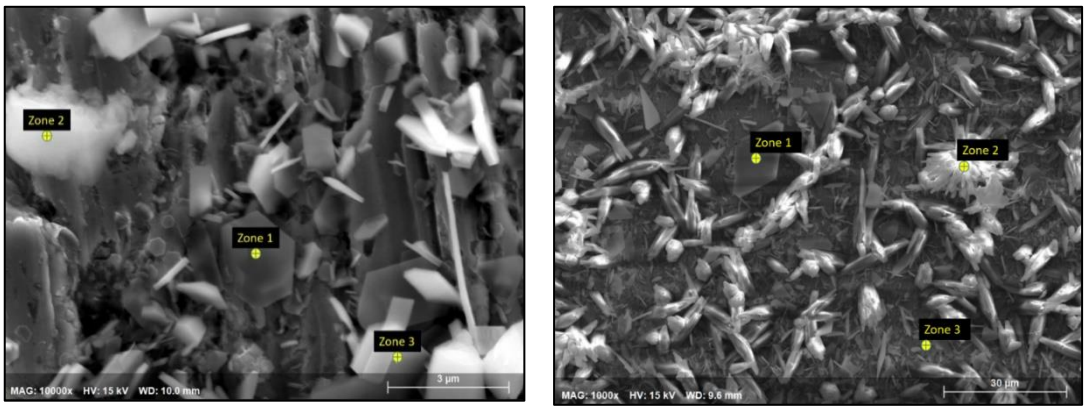

(a) (b)

Figure 4.2.16: SEM images for "GR-sample" at a) 3 µm, b) 30 µm

The EDS analyses associated to the three spots (Figure 4.2.16.a) are shown in Table 4.2.8.

Spectrum	C	O	Si	Ca	Fe
Zone 1(%)	5.46	38.95	0.81	0.28	54.50
Zone 2(%)	11.85	47.6	1.55	19.66	19.32
Zone 3(%)	8.27	43.83	0.0	1.11	46.78

Table 4.2.8: EDS analyses of selected zones for "GR-sample". Selected zones are illustrated in Figure 4.2.16.a

In the first zone (zone 1) is spotted a hexagonal crystal mainly by iron and oxygen, probably due to the presence of iron oxide. In the second zone (zone 2) is spotted a not crystallized formation by oxygen by carbon, oxygen, calcium and iron, while in the third zone (zone 3) is spotted a thin crystal composed primarily by oxygen and iron, ant in a smaller extent by carbon.

Moreover, Figure 4.2.16.b shows the formation of "sea urchin-shape" formations as previously observed in experiment D. Their composition is shown in Table 4.2.9.

Spectrum	C	O	Ca	Fe
Zone 1(%)	3.20	71.74	0.45	24.61
Zone 2(%)	5.55	36.70	55.53	2.22
Zone 3(%)	3.84	23.03	0.59	72.54

Table 4.2.9: EDS analyses of selected zones for "GR-sample". Selected zones are illustrated in Figure 4.2.16.b

In Figure 4.2.19.b the first zone (zone 1) is pointing out a crystal consisted of oxygen and iron. In the second zone (zone 2) the "sea urchin-shape" formation is composed by calcium, oxygen and carbon as a similar formation in experiment D, possibly due to a calcium carbonate presence. Finally, the third zone (zone 3) has selected as a background reference, consisting of iron and oxygen. The oxygen presence even in the background zone could possibly signify an oxidation of the metallic sample.

Optical imaging and Raman spectroscopy

Optical microscopy observations were performed on "GR-sample" (Figure 4.2.17).

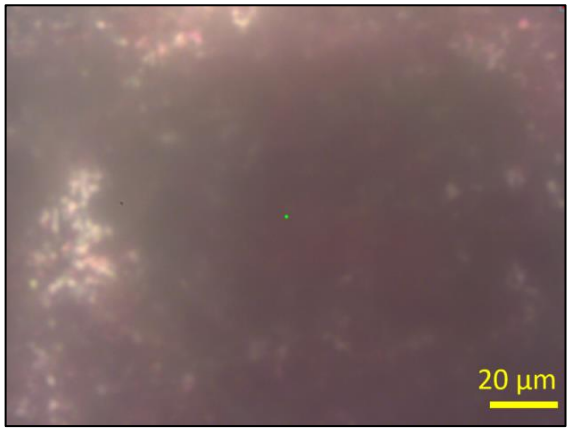

Figure 4.2.17: Optical imaging for "GR-sample" at 20 µm

Optical microscopy images obtained for experiment G are comparable to the one from experiments D: the metallic surface is almost fully covered with a thin layer mainly composed by calcium carbonate, leaving only a few regions exposing bare sample (Figure 4.2.17).

Through Raman spectroscopy we detected the presence of aragonite ($CaCO_3$) at 1085.62 cm^{-1} as the only calcium carbonate polymorph, and the presence of maghemite (γ-Fe_2O_3) at 720.31 cm^{-1} (Figure 4.2.18). However, the presence of maghemite could signify just the transformation of the initially corrosion product e.g., magnetite, as the presence of oxygen was significant in all the SEM –EDS analyses.

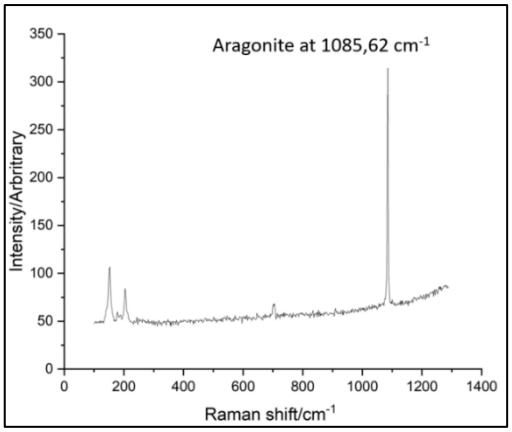

(a)

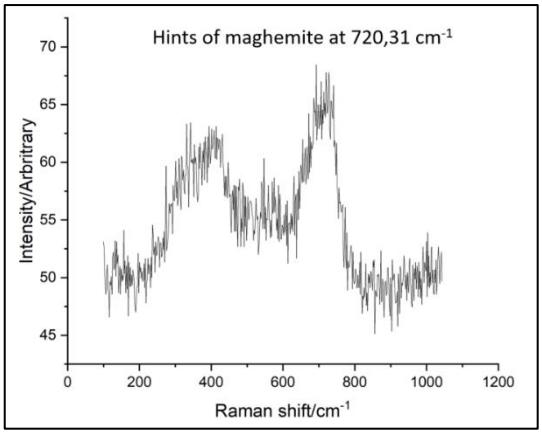

(b)

Figure 4.2.18: Raman spectrum for a) "GR-sample" (identification of aragonite), b) "GR-sample" (identification of maghemite)

Weight loss measurement method

Additionally, to the hydrogen gas production monitoring, the average corrosion rate obtained on the total duration of the experiment is also evaluated by weight loss measurement method. These gravimetric measurements were performed on dedicated metallic coupons which have been weighted initially, at the beginning of the experiment, and finally after being soaked in three successive ultrasonic baths with acidic solution.

Table 4.2.10 presents the corrosion rates values calculated for both experiment with TRNM synthetic pore water (experiments D and G).

Experiment	# samples	time (years)	$\Sigma(\Delta m_{(g)})$	r ($\mu m.year^{-1}$)
D	2	0.05117	0.0252	27.96 ± 1.97
G	2	0.0472	0.0363	43.59 ± 3.08

Table 4.2.10: Summarized results for the corrosion rate calculated with weight loss measurement method and associated to the experiments with TRNM synthetic pore water (experiments D and G)

Results obtained from weight loss method for experiment D and G indicated much higher corrosion rates (27.96 and 43.59 $\mu m.year^{-1}$, respectively) than the one obtained via hydrogen gas production monitoring (1.18 and 1.16 $\mu m.year^{-1}$, respectively). Two hypotheses can be proposed to explain such a difference: (i) the important mass balance gap between initial and final metallic coupon mass can be due, to a certain extent, to the formation of corrosion product

and (ii) the probable oxidation of the samples during their storage (Raman-spectroscopy characterization shows that "GR-sample" was oxidized).

4.2.3 Liquid samples

For experiments D and G, solutions have been sampled in both cells (with and without metallic coupons) and have undergone post mortem analyses. For the cells dealing with TRNM synthetic pore water only (cells D2 and G2), solution has been sampled right after the end of the irradiation phase to measure the concentration of hydrogen peroxide (H_2O_2). For the cells dealing with TRNM synthetic pore water and metallic coupons (cells D1 and G1), solution has been sampled right after the end of the post irradiation phase to measure the dissolved iron ions concentrations. In addition, pH measurements have been performed on solutions before and after the experiment for all the tested cells.

pH evolution

All the pH measurements took place after calibration of the pH-meter using 3 different buffer solutions at 3 different pH (4, 7, 10). Table 4.2.11 summarized the results of the pH evolution for all the experiments with TRNM synthetic pore water.

pH / Exp.	Cell 1 (TRNM water + samples) before the experiment	Cell 1 (TRNM water + samples) after the experiment	Cell 2 (TRNM water) before the experiment	Cell 2 (TRNM water) after the experiment
D	8.75	9.22	8.75	9.20
G	8.15	9.34	8.15	9.13

Table 4.2.11: pH evolution (before and after the experiment) for all the cells tested with TRNM synthetic pore water (experiments D and G)

It should be mentioned that the theoretical pH values for Tournemire synthetic pore water have been reported at a lower value (pH~7.5) than the ones measured for experiments D and G before the beginning of the experiment. Both experiments, show an increase in their pH after the end of the experiment, suggesting similar values for both cells.

Hydrogen peroxide concentration

Hydrogen peroxide concentrations have been measured for cells D and G dealing with TRNM synthetic pore water. These H_2O_2 measurements were carried out within the day of the irradiation end and no chemical scavenger has been added in the solution to stabilize H_2O_2. Due to the slightly alkaline pH value (~9) after irradiation, we added some drops of HCl acidic solution to the sample before mixing it with the Ghormley reagents in order to stabilized the solution (Auclair, 2001). The results of these measurements are shown in Table 4.2.12.

Experiment	D	G
$[H_2O_2]$ ($\mu mol.L^{-1}$)	0.38 ± 0.04	0.35 ± 0.07

Table 4.2.12: H_2O_2 concentration in cells containing TRNM synthetic pore water

Both tests showed equivalent results, highlighting the reproducibility of our experiments.

Concentration of dissolved iron

For cells D1 and G1, the total dissolved iron concentrations measured by Inductively Coupled Plasma – Atomic Emission Spectrometry (ICP-AES) are shown in Table 4.2.13. The results are in good agreement with each other indicating slightly lower values than the ones obtained with pure water, varying between 0.21-0.34 $mmol.L^{-1}$ under identical conditions (He flux, number of samples, volume of solution).

Experiment	D	G
$[Fe_{total}]$ ($mmol.L^{-1}$)	0.10 ± 0.002	0.07 ± 0.02

Table 4.2.13 Total dissolved iron concentrations measured by ICP-AES for the cells dealing with TRNM synthetic pore water in the presence of iron

4.3 Experiments with cementitious grout solution

4.3.1 H_2 gas production

MREA – TRNM synthetic solution has been used in one full-length experiment to study the impact of such solution (mimicking the flux of Tournemire pore water within the MREA system) on carbon steel anoxic corrosion processes.

Experiment H

In experiment H, cell H1 (MREA – TRNM synthetic solution with metallic coupons) and cell H2 (only MREA – TRNM synthetic solution) were tested with 200 ml of MREA – TRNM synthetic solution. Six carbon steel samples were sufficiently immersed in cell H1. These six metallic samples where roughly polished ("HR-sample"). For both cells, the helium flow rate was set at 5 $ml.min^{-1}$.

The irradiation phase lasted approximately 12.1 days and the gamma radiation dose rate applied was 46.0 $Gy.h^{-1}$ and 48.0 $Gy.h^{-1}$ for cell H1 and cell H2, respectively.

Unfortunately, the irradiation phase has been stopped due to technical failure of the gas chromatograph preventing hydrogen concentration measurements. Thus, we had to stop the experiment and to dismantle the two cells without post-irradiation phase. Figure 4.3.1 shows the H_2 evolution for experiment H.

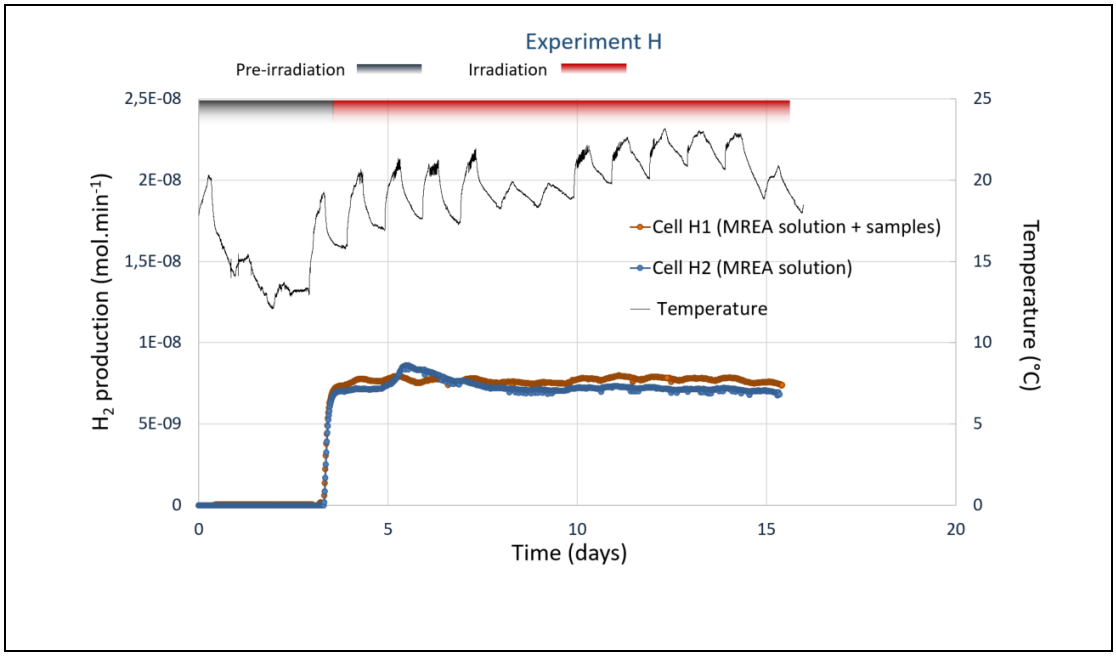

Figure 4.3.1: H_2 production and temperature evolution over time for experiment H

Cell H1 (MREA – TRNM synthetic solution + samples)

For cell H1, Figure 4.3.1 shows the hydrogen production recorded only during two successive phases of the experiment: (i) pre-irradiation anoxic corrosion phase and (ii) radiolytic anoxic corrosion phase.

i) During pre-irradiation phase, hydrogen monitoring shows a stable evolution, independent of temperature fluctuation, and exhibits very low H_2 production values compared to previous experiments. These measurements indicated a stable average value of about 0.39 x 10^{-10} mol.min^{-1}, with a maximum value recorded at 0.57 x 10^{-10} mol.min^{-1}.

ii) During radiolytic anoxic corrosion phase, hydrogen production is rapidly increased till a stabilization "plateau". Then, hydrogen production shows a stable evolution over these 12 days of irradiation, with an average value at 7.68 x 10^{-9} mol.min^{-1}. There is no temperature impact on H_2 evolution. Hydrogen production in cell H1 had higher values than cell H2, exception to this is a small interval within the fifth day of the experiment where H1 indicated slightly lower hydrogen values.

Cell H2 (MREA – TRNM synthetic solution)

For the cell H2, Figure 4.3.1 represents the water radiolysis of a more alkaline solution. During these 12.1 days of irradiation, the hydrogen production indicates similar tendency with cell H1. The average value during the irradiation period was 7.30 x 10^{-9} mol.min^{-1}, slightly lower compared to cell H1. The obtained hydrogen production values are significantly lower compared with previous experiments using ultrapure water or TRNM synthetic pore water. Table 4.3.1 summarizes the average hydrogen gas production values obtained for both cells.

Experiment	cell	Pre-irradiation (H_2 (x10^{-9} mol.min^{-1}))	Irradiation (H_2 (x10^{-9} mol.min^{-1}))
H	H1	0.04 ± 0.02	7.68 ± 0.14
	H2	0	7.30 ± 0.37

Table 4.3.1: Average hydrogen gas production values obtained for the experiment with MREA – TRNM synthetic solution

Corrosion rate

The corrosion rate values obtained for experiment H are shown in Table 4.3.2. For this experiment, we were able to monitor the hydrogen production evolution associated with cell E1 only during two tested phases. During pre-irradiation phase, the average corrosion rate value is about 0.02 µm.year^{-1}. This value is very low compared with the range of corrosion rate value obtained for experiment involving ultrapure water or TRNM synthetic pore water ($0.56 < r < 1.76$ µm.year^{-1}).

During irradiation phase, the average corrosion rate value is about 0.2 µm.year^{-1}. On the one hand this rate is lower than the corresponding rate using ultrapure water and/or TRNM synthetic pore water, on the other hand this rate is clearly higher than the one observed during pre-irradiation phase rate (0.02 µm.year^{-1}). This is the first time in this work that we observe such an irradiation impact on the corrosion rate.

Corrosion rate	Pre-irradiation phase	Irradiation phase
Average corrosion rate (µm.year^{-1})	0.02 ± 0.001	0.21 ± 0.22
Maximum corrosion rate (µm.year^{-1})	0.09	0.48

Table 4.3.2: Corrosion rates obtained for experiment H

4.3.2 Solid samples

For experiment H, we used six samples with rough surfaces (HR-samples). These "HR-samples" have been used for SEM-microscopy, Raman spectroscopy, optic microscopy while some steel samples have been used for weigh loss measurements.

SEM-EDS analyses

SEM-EDS analyses were performed, and "HR-samples" exhibited an homogeneous neoformed thin and small crystals distribution on the coupon surface (Figure 4.3.2).

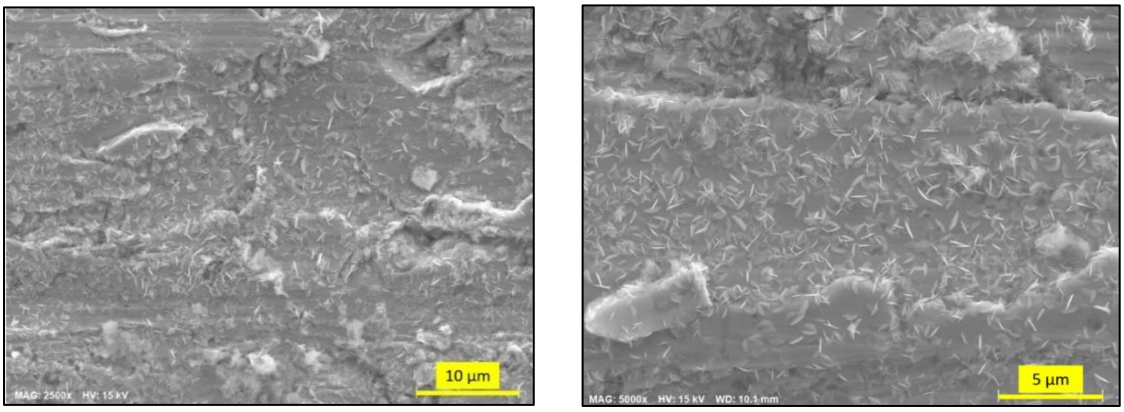

(a) (b)

Figure 4.3.2: SEM images for "HR-sample"at a) 10 µm, b) 5 µm

The composition of such formations has been studied thanks to SEM-EDS mapping (Figure 4.3.3 and Table 4.3.3).

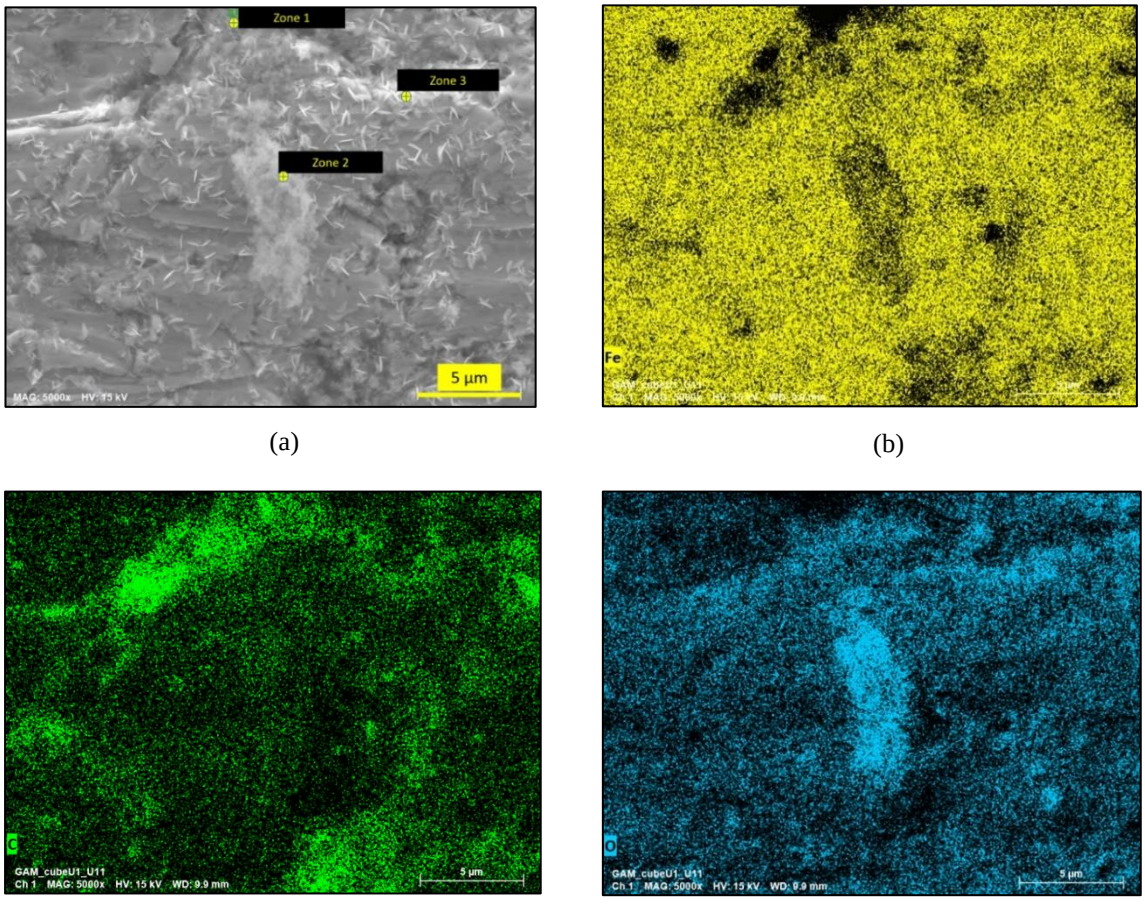

(a) (b)

(c) (d)

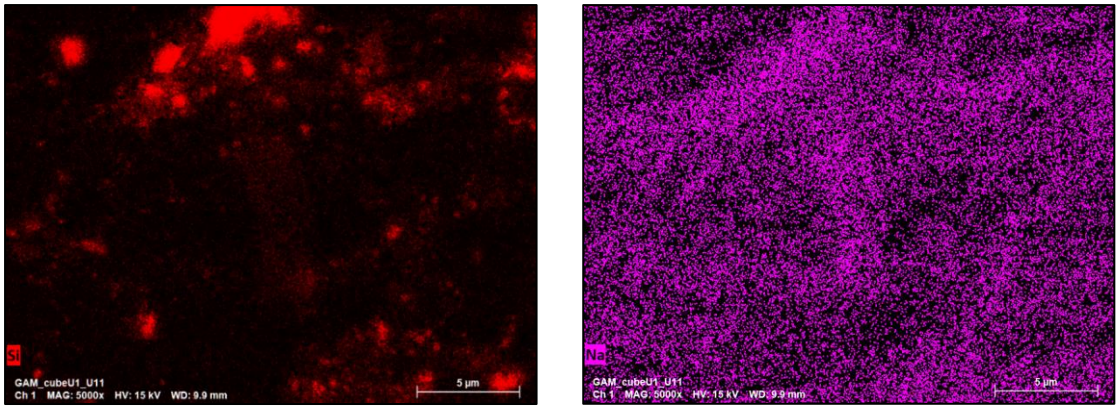

(e) (f)

Figure 4.3.3: SEM images and elemental mapping for "HR-sample": a) illustration of the selected zone for elemental mapping, b) presence of iron (yellow color), c) presence of carbon (green color), d) presence of oxygen (blue color), e) presence of silicon (red color) and f) presence of sodium (violet color)

The elemental mapping in Figure 4.3.3 showed that zone 1 exhibits high presence of oxygen and silicon. Moreover, the zone 1, as the zone 3 are mainly composed by oxygen and iron. Surprisingly, it was found in all three spot-zones the presence of dysprosium (Table 4.3.3).

	C	O	Na	Mg	Al	Si	Ka	Fe	Dy
Zone 1 (%)	0.0	64.00				27.33		7.35	1.32
Zone 2 (%)	0.0	52.87	0.47	4.0	0.65	2.86	0.28	33.01	5.85
Zone 3 (%)	0.0	53.02				2.73		37.64	6.62

Table 4.3.3: EDS analyses of selected zones for "HR-sample". Selected zones are illustrated in Figure 4.3.3

Optical imaging and Raman spectroscopy

Optical microscopy observations were performed on "HR-sample" (Figure 4.3.4.a). The image shows relevant area where iron oxides may have formed. This area have been investigated thanks to Raman spectroscopy analyses (Figure 4.3.4.b).

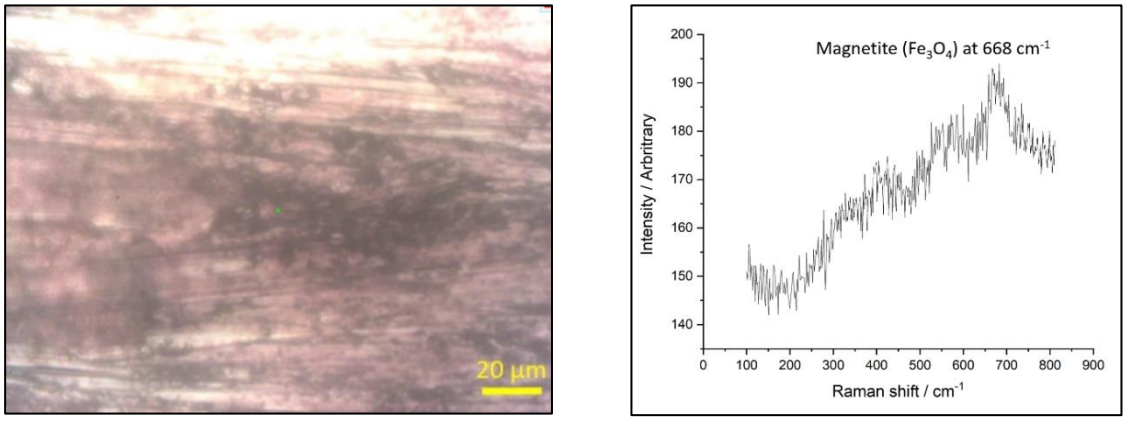

(a) (b)

Figure 4.3.4: a) Optical imaging at 20 µm and b) Raman spectrum for "HR-sample"

Figure 4.3.4.b shows that magnetite (Fe_3O_4) has been identified on the surface of "HR-sample", with a specific peak at 668 cm^{-1}.

Weight loss measurement method

Additionally, to the hydrogen gas production monitoring, the average corrosion rate obtained on the total duration of the experiment is also evaluated by weight loss measurement method. Table 4.3.4 presents the corrosion rates values calculated for experiment H (MREA – TRNM synthetic solution).

Experiment	# samples	time (years)	$\Sigma(\Delta m_{(g)})$	r (µm.$year^{-1}$)
H	2	0.0547	0.0013	1.42 ± 0.10

Table 4.3.4: Corrosion rate calculated obtained by weight loss measurement method for "HR-samples" (experiments H, MREA – TRNM synthetic solution)

As previously observed, corrosion rate obtained by weight loss method measurements (1.42 µm.$year^{-1}$) is higher than the one estimated by hydrogen gas measurements (< 0.48 µm.$year^{-1}$) for experiment H. Even though, weight loss method for this experiment indicates relatively low corrosion rate compared with experiments with pure water/ synthetic porewater, the corrosion rate by H_2 measurements during irradiation phase is in the same order of magnitude with the majority of the associated rates in experiments with pure water/synthetic pore water.

4.3.3 Liquid samples

For experiment H, solutions have been sampled in both cells (with and without metallic coupons) and have undergone *post mortem* analyses. Even if experiment H had been interrupted during irradiation phase all the *post mortem* analyses have been performed as in the previous experiments. The cells dismantlement was done inside the anoxic glove box and pH evolution, concentration of hydrogen peroxide (H_2O_2) and total dissolved iron ions concentrations (Fe_{total}) have been estimated.

pH evolution

pH measurements took place after calibration of the pH-meter using 3 different buffer solutions at 3 different pH (4, 7, 10). Table 4.3.5 presents the results of the pH evolution for experiments H dealing with MREA – TRNM synthetic solution.

pH / Experiment	Cell H1 (MREA – TRNM synthetic solution + samples) before the experiment	Cell H1 (MREA – TRNM synthetic solution + samples) after the experiment	Cell H2 (MREA – TRNM synthetic solution) before the experiment	Cell H2 (MREA – TRNM synthetic solution) before the experiment
H	12.3	12.4	12.3	12.4

Table 4.3.5: pH evolution (before and after the experiment) for experiment H (MREA – TRNM synthetic solution)

These results show that no clear pH evolution occurred during experiment H.

Hydrogen peroxide concentration

Hydrogen peroxide concentrations have been measured for cell H2 dealing with MREA – TRNM synthetic solution. These H_2O_2 measurements were carried out within the day of the experiment and no chemical scavenger has been added in the solution to stabilize H_2O_2. Due to the alkaline pH value, we added some drops of HCl acidic solution to the sample before mixing it with the Ghormley reagents in order to stabilize the solution. The concentration of hydrogen peroxide was found to be 0.27 ± 0.08 $\mu mol.L^{-1}$. This concentration is in the same order of

magnitude with the previous measurements of hydrogen peroxide with ultrapure water/ TRNM synthetic pore water.

Experiment	H
$H_2O_2(\mu mol.L^{-1})$	0.27 ± 0.08

Table 4.3.6: H_2O_2 concentration for experiment H (MREA – TRNM synthetic solution)

Concentration of dissolved iron

Even though the neoformed corrosion products were shown to be very homogeneously distributed upon the samples, their dissolution didn't take place in big extent during experiment H. This has been depicted on the concentration of total iron, measured at 0.89 ± 0.02 $\mu mol.L^{-1}$, almost 3 order of magnitude lower than the associated concentration on experiments with pure water. This could be expected as increased pH favors Fe^{2+}/Fe^{3+} stability, leading to more protective conditions for the metallic surfaces.

Table 4.3.7 summarizes the average H_2 values for pre-irradiation, irradiation and post-irradiation phase, using the three tested solutions. Finally, Table 4.3.8 shows summarizes the average corrosion rates as they have been derived from the H_2 gas generation method.

Solution	Experiment	Cell	Pre-irradiation (H_2 ($x10^{-9}$ $mol.min^{-1}$))	Irradiation (H_2 ($x10^{-9}$ $mol.min^{-1}$))	Post-irradiation (H_2 ($x10^{-9}$ $mol.min^{-1}$))
Pure water	A	A1	-	9.62 ± 0.42	0.66 ± 0.09
		A2	-	9.18 ± 0.57	-
	B	B1	2.26 ± 0.04	11.0 ± 0.22	3.13 ± 0.11
		B2	0	9.72 ± 0.78	-
	C	C1	2.51 ± 0.06	16.18 ± 0.74	2.83 ± 0.2
		C2	0	15.43 ± 0.88	-
	E	E1	2.81 ± 0.07	14.21 ± 0.37	2.96 ± 0.07
		E2	0	13.78 ± 0.86	-
	F	F1	1.28 ± 0.07	14.1 ± 0.41	2.97 ± 0.14
		F2	0	15.28 ± 0.83	-
TRNM water	D	D1	4.30 ± 0.2	12.22 ± 1.71	2.85 ± 0.70
		D2	0	11.04 ± 1.48	-
	G	G1	2.52 ± 0.1	14.33 ± 0.30	2.78 ± 0.14
		G2	0	12.30 ± 0.22	-
MREA-TRNM solution	H	H1	0.04 ± 0.02	7.68 ± 0.14	-
		H2	0	7.30 ± 0.37	-

Table 4.3.7: Average hydrogen production associated to each studied phase (pre-irradiation, irradiation, post- irradiation) for every tested solution

Solution	Experiment	Pre-irradiation (CR in µm.year^{-1})	Irradiation (CR in µm.year^{-1})	Post-irradiation (CR in µm.year^{-1})	Identified products
Pure water	A	-	0.22 ± 0.35	0.27 ± 0.05	Magnetite (Fe_3O_4)
	B	1.35 ± 0.04	0.74 ± 0.54	2.01 ± 0.07	Magnetite (Fe_3O_4) Feroxyhyte (δ-FeOOH)
	C	1.05 ± 0.03	0.34 ± 0.40	1.19 ± 0.09	Magnetite (Fe_3O_4)
	E	1.16 ± 0.04	0.20 ± 0.38	1.23 ± 0.04	-
	F	0.56 ± 0.03	-	1.25 ± 0.06	-
TRNM water	D	1.76 ± 0.11	0.51 ± 0.33	1.18 ± 0.29	Aragonite ($CaCO_3$) Magnetite (Fe_3O_4) Maghemite (γ-Fe_2O_3)
	G	1.06 ± 0.06	0.83 ± 0.35	1.16 ± 0.06	Aragonite ($CaCO_3$) Maghemite (γ-Fe_2O_3)
MREA-TRNM solution	H	0.02 ± 0.001	0.21 ± 0.22	-	Magnetite (Fe_3O_4)

Table 4.3.8: Average corrosion rate (CR) values associated to each studied phase (pre-irradiation, irradiation, post-irradiation) and identified formation upon the metallic surfaces for every tested solution

Chapter 5: Modeling the experimental results

5.1 Introduction to the deterministic model

In the previous chapter we saw that water radiolysis products can play a major role on corrosion process. Radiolysis of aqueous solution will generate several radiolytic species, which are highly reactive and able to modify the chemistry of the solution, and molecules such as molecular hydrogen and hydrogen peroxide. The various possibilities of interactions between them with various constant rates leads to a multi-timescale reactivity and makes necessary a simulation of the concentration evolution over time in order to predict the concentration at a long term. CHEMSIMUL® software (Kirkegaard et al., 2008) was chosen for the numerical simulation of species under the irradiation phase. It was developed at Riso National Laboratory in Denmark, as a collaboration between chemists and applied mathematicians, based on the translation of chemical reactions to coupled ordinary differential equations. The simulation returns the concentrations of the chemical species in the reaction system as a function of time as a result of solving numerically these equations. This program is used for simulation on radiation chemistry, where bursts of radiation is modeled by a pulse with a specific duration of time and a provided dose. By choosing one single pulse with time duration equal to the irradiation period we can obtain the concentration of the desired chemical species over time (e.g., hydrogen), which will permit us to compare it with the experimental results. As a first attempt the hydrogen evolution of the ultrapure deaerated system will be presented. Progressively, the addition of the iron and the impurities concentrations coming from the more complex solution (synthetic pore water) will complete this work.

The most important input parameters in CHEMSIMUL software are:

-Reaction equations in chemical notation

-The concentration of each species present in solution

-The initial and final simulation time

-The G-values of the radiolytical species (yield of produced molecules per 100eV), the total absorbed dose and the number of pulses

5.2 Limitations and assumptions

CHEMSIMUL® simulates an ideal process with uniform distribution of reactants and external effects e.g., irradiation. The program is constructed to simulate homogeneous kinetics in an homogeneous system combined eventually with transport into and out of the reaction zone. An important parameter in this study, is the controlled gas extraction that takes place. The constant helium addition with the constant extraction of the produced gas within the experimental cell, introduced the major challenge of this work. The simulation becomes more difficult due to lack of equilibrium between the liquid and the gaseous phase as all the formed gas is extracted with a given rate. By making the assumption that the helium gas flow will evacuate all the gas formed within the cell, we introduce the proposal that hydrogen and oxygen will be extracted at the same rate than the helium extraction rate.

Moreover, the cases where iron is present in the solution, we take into account Fe-species in the bulk solution and not reactions in solid state. Therefore, we are aware of a primary difference between experimental and theoretical results in the presence of iron, as the hydrogen from anoxic corrosion is not taken into consideration in our simulation tests.

Finally, the evolution of hydrogen gas from experimental data and simulation will be illustrated in the same graph for their best comparison.

5.3 Reaction groups

In order to obtain the simulation of each experimental test, the input reactions have been categorized into 8 groups according to the different initial chemical composition of the solution. Thus, the simulation work will be achieved with the combination of different groups each time. The reaction groups are shown in Table (5.3.1) and all the reactions are in Annex B.

Group	Reactions	Number of Reactions
1	Reactions of water radiolysis of pure liquid water	31
2	Reactions in gas phase for pure water	9
3	Reactions of gas extraction	3
4	Reactions between radiolytic products and Fe-species	23
5	Reactions between radiolytic and carbonated species	5
6	Reactions between radiolytic and chloride species	43
7	Reactions between carbonated and chloride species	6
8	Reactions between carbonated and iron species	1

Table 5.3.1: Groups of reactions used in this study

In group 1, there are all the reactions related to radiolysis of pure water in the liquid phase. These reactions have been found via the NIST database (NIST, 2002) and Buxton et al. (1988). In group 2, we added the reactions in the gaseous phase under irradiation also using the NIST database (NIST, 2013).

Group 3 is dedicated to the reactions for the gas extraction. These reactions are taken into account in order to mimic the semi-open experimental system that is used in our work. The rates of the gas extraction have been calculated using the assumption that all the helium entering in the cell pushes all the gas towards the output of the cell. The experimental extraction rate has been calculated to be 1.32×10^{-9} $mol.L^{-1}.s^{-1}$ for an helium rate of 5 $ml.min^{-1}$.

Simulation of hydrogen gas results to be a linear graph expressed in $mol.L^{-1}$ (moles of hydrogen gas per 1L of solution) over time (s). The hydrogen gas ($mol.L^{-1}$) is multiplied with the volume of solution (0.2 L) in order to obtain the results in moles (mol) in the gaseous phase over time (s). After that, we calculate the derivative ($mol.s^{-1}$) over time (s). Therefore, the simulated extraction rate has been determined so to i) maintain the linearity of the hydrogen gas and to ii) maintain the slope of the graph as close as possible to 1.32×10^{-9}($mol.L^{-1}.s^{-1}$).

At last, the necessary adjustment for the simulated extraction rate has been set at 5.15×10^{-4} $M.s^{-1}$. The conversion of our experimental results from ($mol.min^{-1}$/days) to ($mol.s^{-1}$/s) is mandatory in order to compare results.

Group 4 represents the relevant reactions occurring between radiolytic and Fe-species. These reactions have been selected according to Eh-pH diagram (Figure 5.3.1), for Fe-species present in solution with constant rates determined in previous studies (Bjergbakke et al., 1989; Bouniol, 2010; Eriksen et al., 1989) Furthermore, in this group has been added a reaction (Re200 in Annex B), able to insert in the system the constant Fe^{2+} release in the bulk solution, arising

from anoxic corrosion of steel, and with the assumption that the initial concentration of Fe^{2+} at the beginning of irradiation to be $[Fe^{2+}]=0.01M$.

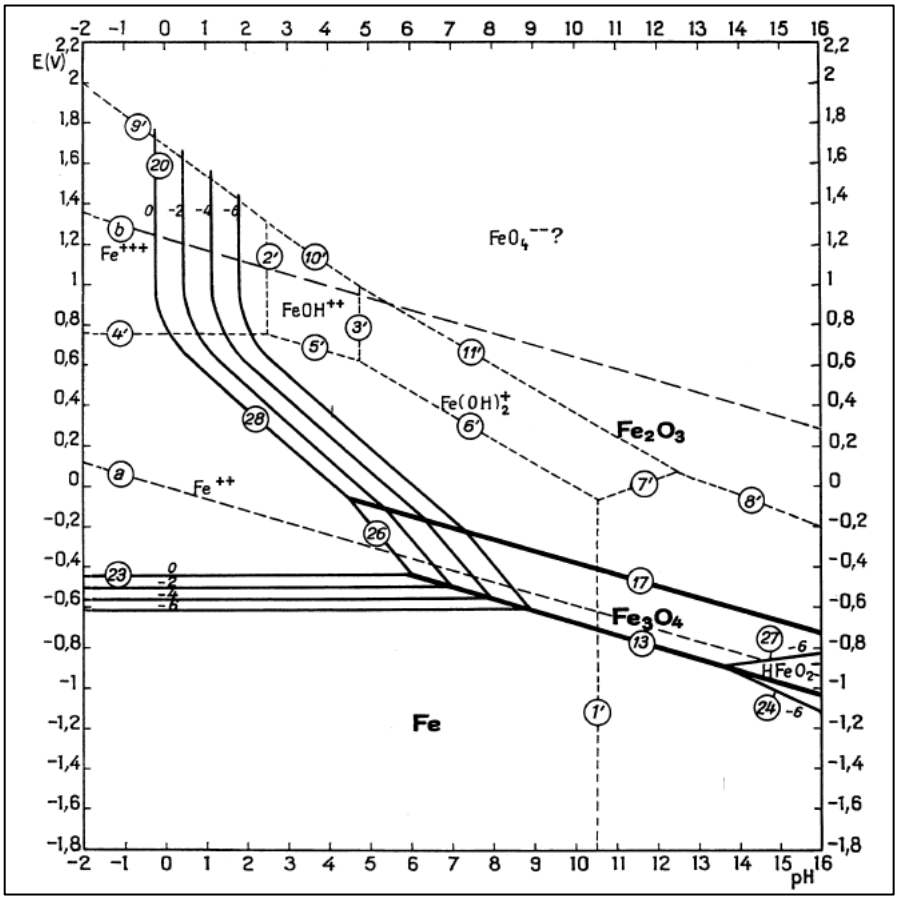

Figure 5.3.1: Potential-pH equilibrium diagram for the system iron-water, at 25°C (considering as solid substances only Fe, Fe_3O_4 and Fe_2O_3)(Pourbaix, 1974)

In group 5, the major reactions with carbonated species and radiolytic products have been selected as well as in group 6, we placed the reactions with chloride ions in pore waters (Bjergbakke et al., 1984). In group 7 we placed the reactions between chloride and iron species (Bjergbakke et al., 1984) while in the final group, group 8, we placed a reaction between iron and carbonates (Eriksen et al., 1989).

As it has been stated before, the hydrogen gas results from experimental/simulation data will be illustrated in $mol.s^{-1}$ over time (s). Moreover, the evolution of H_2O_2 and H^+ will be presented as concentration ($mol.L^{-1}$) over time (s).

5.4 Input data

For each experiment the input data can be different. The mandatory domains that are inserted by the user are: (i) the initial concentration of each species, (ii) the total irradiation dose and (iii) the total duration of the irradiation. The initial chemical composition of the tested solutions are presented in Chapter 4. Since radiation source was the same for every experiment, the applied radiolytical yields associated to each chemical component remained the same for all the tested solutions (pure water/TRNM water) (Table 5.4.1).

G(OH)	2.67
G(E[-])	2.66
G(H[+])	2.76
G(OH[-])	0.1
G(H)	0.55
G(H2)	0.45
G(H2O2)	0.72
G(H2O)	-6.87

Table 5.4.1: The radiolytic yields for γ-rays (in molecule/100eV)

The irradiation time, and therefore the total irradiation dose varied for every experiment and were dependent on the experimental conditions. Consequently, for each tested solution we used the experimental conditions of a representative experiment. More specifically, for the case of pure water we used the experimental conditions of experiment C, for the TRNM water we used the experimental conditions of experiment G. All the upper data are summarized in Table 5.4.2.

	Pure water (cell C2)	Pure water +Fe (Cell C1)	TRNM water (cell G2)	TRNM water +Fe (Cell G1)
Time (s)	1.26×10^6		8.38×10^5	
Total dose (kGy)	18.3	18.3	12.7	12.1

Table 5.4.2: Total irradiation time and total dose for the three tested solutions

On the following figures aiming to compare experimental data with simulation results, the left hand y-axis represents the H_2 production experimentally obtained and the right hand y-axis represents the simulated H_2 production.

5.5 Simulation of pure water

The simulation of pure water has been performed using the concentrations that are shown on Table 5.5.1. This simulation effort is to get close in the experimental conditions of experiment C.

Concentration	Pure water (cell C2)	Pure water +Fe (cell C1)
Con[H2O]	55.56	55.56
Con[H+]	$1.0x10^{-7}$	$1.0x10^{-7}$
Con [OH-]	$1.0x10^{-7}$	$1.0x10^{-7}$
Con[H2]	0	0
Con[H2G]	0	0
Con[O2G]	0	0
Con[VAP]	0	0
Con[Fe(++)]	-	10^{-5}

Table 5.5.1: The initial concentrations (in mol.L^{-1}) for the case of pure water

5.5.1 Pure water

For ultrapure deaerated water, experimental conditions correspond to the ones in the cell C2(ultrapure deaerated water without metallic sample). In this case, we use the reaction groups 1, 2 and 3 (Table 5.3.1). Figure 5.5.1 shows the merged results of H_2 production associated to both experimental results and simulation.

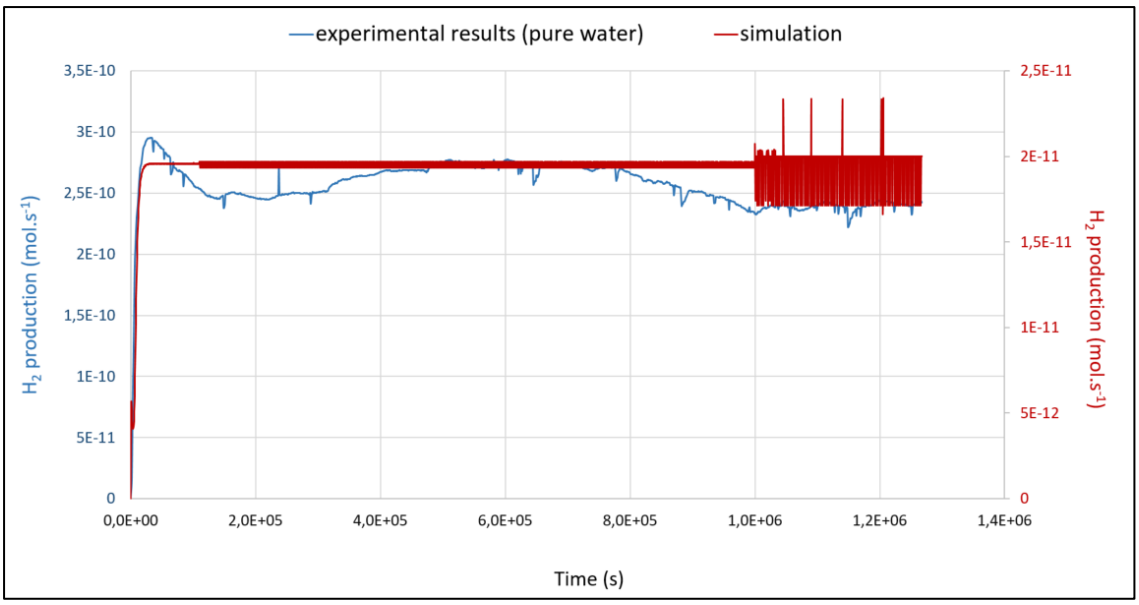

Figure 5.5.1: H_2 evolution graph from experimental results and simulation work for the case of pure water under irradiation

As it is shown, the evolution of the two graphs over time is similar. Once the irradiation starts, the two graphs reach their maximum peak. Afterwards, a "plateau" phase is observed during the whole irradiation period. The observed fluctuations on experimental data are attributed to the temperature variations, occurring in daily basis, while on simulation data the observed noise is more attributed to a very slight decrease on the hydrogen in liquid phase. The plateau level for experimental data is between 2.22 - 2.94 x 10^{-10} mol.s^{-1} while for the simulation data it varies between 1.66 - 2.33 x 10^{-11} mol.s^{-1}, which reveals almost one order of magnitude difference. The higher experimental values could be attributed to the difficulties on pure water simulation under low-LET radiation. Impurities arising from anything in contact with the pure water solution could lead to interaction of very reactive radicals e.g., •OH and this could give, higher hydrogen, as the maintenance of a totally ultra-pure water system in practice is almost impossible.

As it is depicted in Figure 5.5.2, the simulation of hydrogen peroxide aiming to represent the fate of hydrogen peroxide revealed a final concentration $[H_2O_2]_s$ = 2.90 x 10^{-7} M, indicating a very slight decrease over time. This is quite close with our experimental value, measured within 24 hours after the end of irradiation ($[H_2O_2]_E$ = 5.20 x 10^{-7} M).

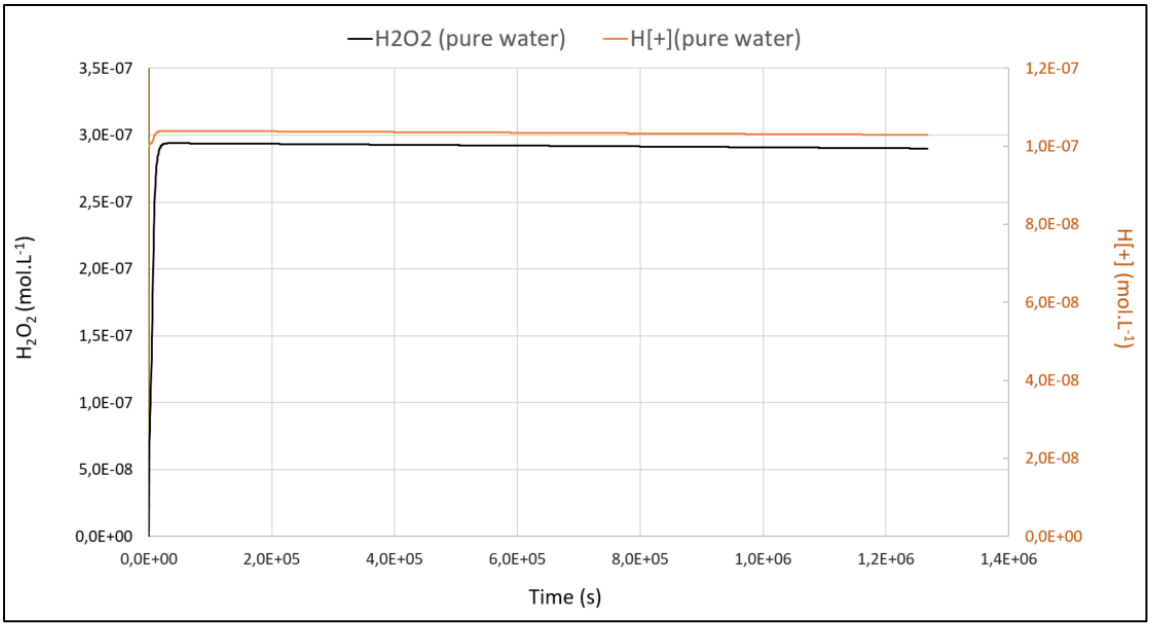

Figure 5.5.2: H_2O_2 and H^+ evolution from simulation work for the case of pure water under irradiation

In the same figure, the simulated value of the H^+ ion was found to be $[H^+]_s = 1.03 \times 10^{-7}$ M. While the pH measurement right after the end of irradiation indicated a pH value at 4.46, resulting to a concentration of H^+ ion in the order of 10^{-5} M.

5.5.2 Pure water and interface with iron

For this case, the experimental conditions applied, correspond to the ones in the cell C1 (pure water + metallic sample). For the associated simulation exercise, we use the reaction groups 1, 2, 3 and 4 (Table 5.3.1). In Figure 5.5.3 are shown the merged results of experimental data and simulation results (secondary axis).

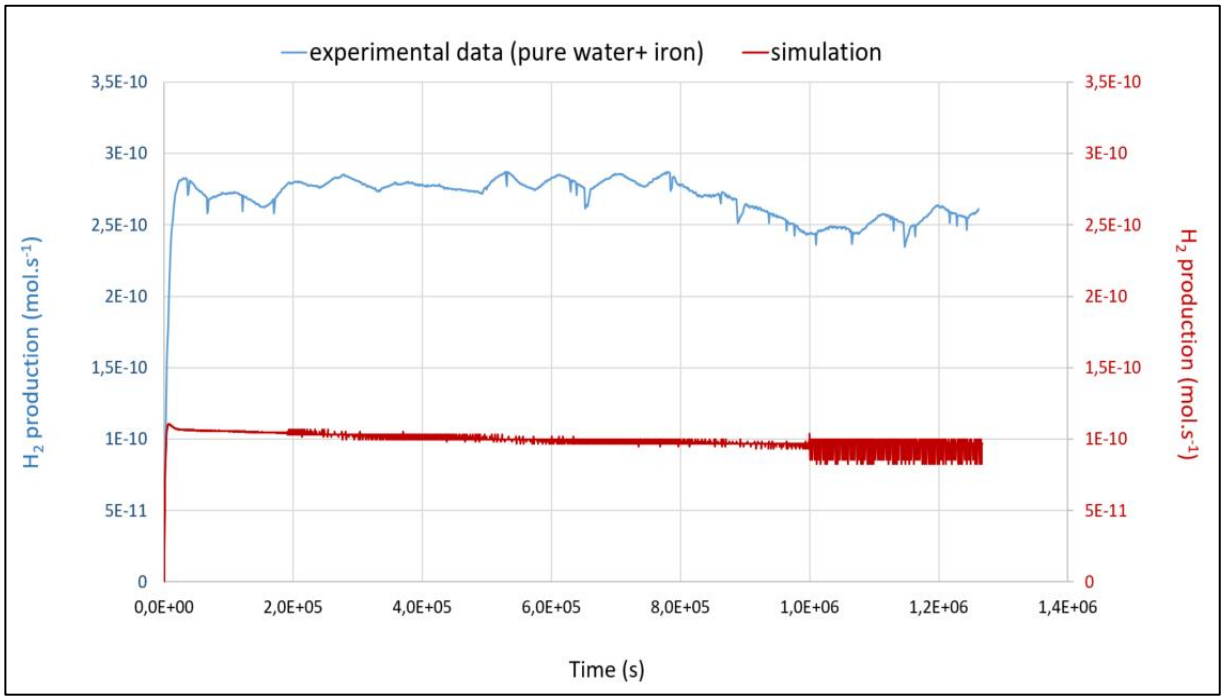

Figure 5.5.3: H_2 evolution graph from experimental results and simulation work for the case of pure water with iron presence under irradiation

In Figure 5.5.3, we confirm that the presence of iron, considered as "impurity" in the system of pure water, generates higher simulated results closer to our experimental data. The evolution of hydrogen gas over time in both graphs is comparable. As in Figure 5.5.1, the Figure 5.5.2 shows that once the irradiation starts, the two graphs obtain within some hours their maximum value. The experimental data are among 2.35 - 2.87 x 10^{-10} mol.s^{-1} while the simulation curve reaches the maximum value at 1.11 x 10^{-10} mol.s^{-1} and has a small decrease till the final value of 9.67 x 10^{-11} mol.s^{-1}. It is crucial to point out that experimental data evolution takes into account the contribution of anoxic corrosion on the global H_2 production. Unfortunately, this contribution is not taken into account in the simulation work as it does not comprise reactions in solid state. However, with a rough calculation of the H_2 difference between the cells C1 and C2, the H_2 excess in cell C1 due to iron presence is 0.75 x 10 mol.min^{-1} which is equal to 0.13 x 10^{-10} mol.s^{-1}. Despite this addition, the simulated H_2 production is still lower than the experimental one.

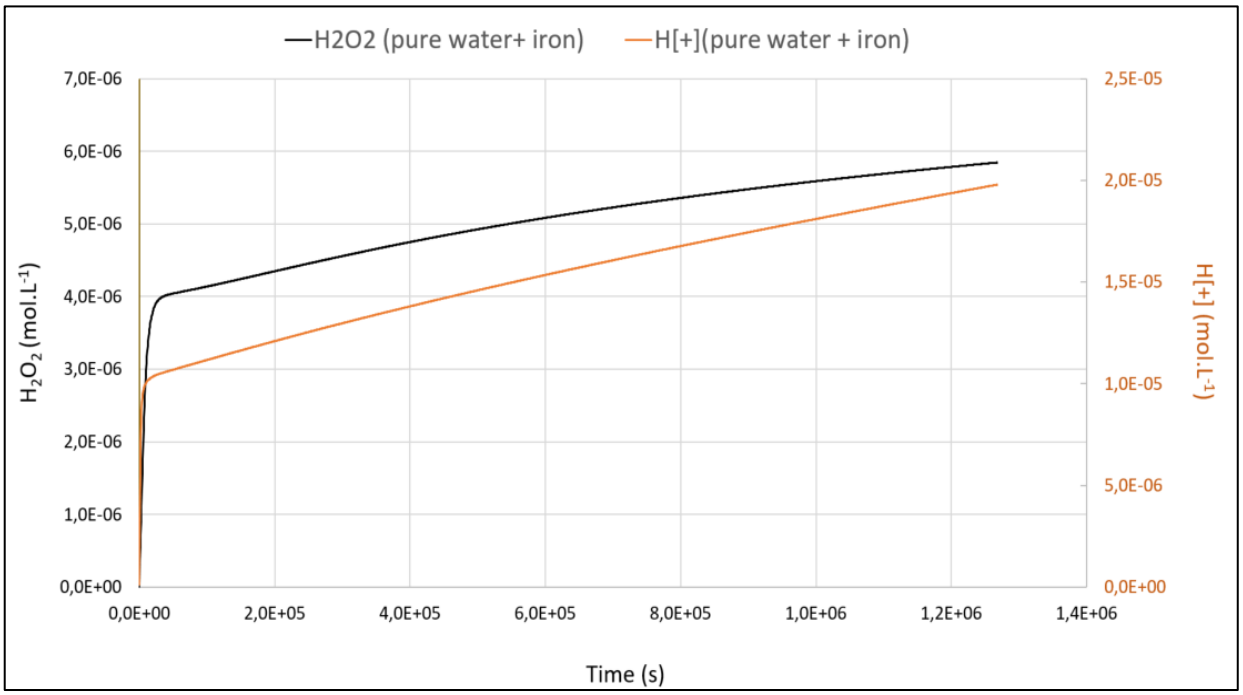

Figure 5.5.4: H_2O_2 and H^+ evolution from simulation work for the case of pure water under irradiation

Figure 5.5.4 shows that, in presence of iron in the system, hydrogen peroxide final concentration is about 5.84 x 10^{-6} M, almost one order of magnitude higher compared with the simulated results associated to ultrapure deaerated water without metallic sample. Even though, iron addition is not able to impact directly hydrogen peroxide's production, one can note that interactions of hydrated electron (e^-) with Fe^{3+} or $Fe(OH)_2^{2+}$ could represent competition reactions. Indeed, these scavenged hydrated electrons are no more available to react with H_2O_2 and thus, H_2O_2 concentration in solution increases with time.

Figure 5.5.4 also shows that the simulated value of the H^+ ion at the end of the irradiation was found to be $[H^+]_s$ = 1.97 x 10^{-5} M. This is not very far from our pH measurement in cell C1 (pure water + iron) which was about 5.4, resulting to a $H[^+]_E$ concentration close to 0.39 x 10^{-5} mol.L^{-1}.

5.6 Simulation of synthetic pore water (TRNM synthetic pore water)

The simulation of the tests involving TRNM synthetic pore water has been performed using the solution chemical composition that is shown in Table 5.6.1. It is worth mentioning that only reactions involving chlorine and carbon species have been added in the input file and not all the

residual ions of the synthetic pore water, due to their significant higher constant rates. This simulation work aims to reproduce the experimental results obtained for experiment G.

Concentration	TRNM synthetic pore water(cell G2)	TRNM synthetic pore water+Fe (cell G1)
Con[H2O]	55.56	55.56
Con[H+]	1.0×10^{-8}	1.0×10^{-8}
Con [OH-]	1.0×10^{-6}	1.0×10^{-6}
Con[H2]	0	0
Con[H2G]	0	0
Con[O2G]	0	0
Con[VAP]	0	0
Con[Cl(-)]	0.0045	0.0045
Con[HCO3(-)]	0.004	0.004
Con[Fe(++)]	-	0.01×10^{-3}

Table 5.6.1: The initial concentrations for the case of synthetic pore water

5.6.1 TRNM synthetic pore water

For the case of TRNM synthetic pore water, the experimental conditions correspond to the ones observed for cell G2. For the associated simulation exercise, we used the reactions from groups 1, 2, 3, 5, 6 and 7 (Table 5.3.1). Figure 5.6.1 shows the merged results of experimental data and simulation results (secondary axis).

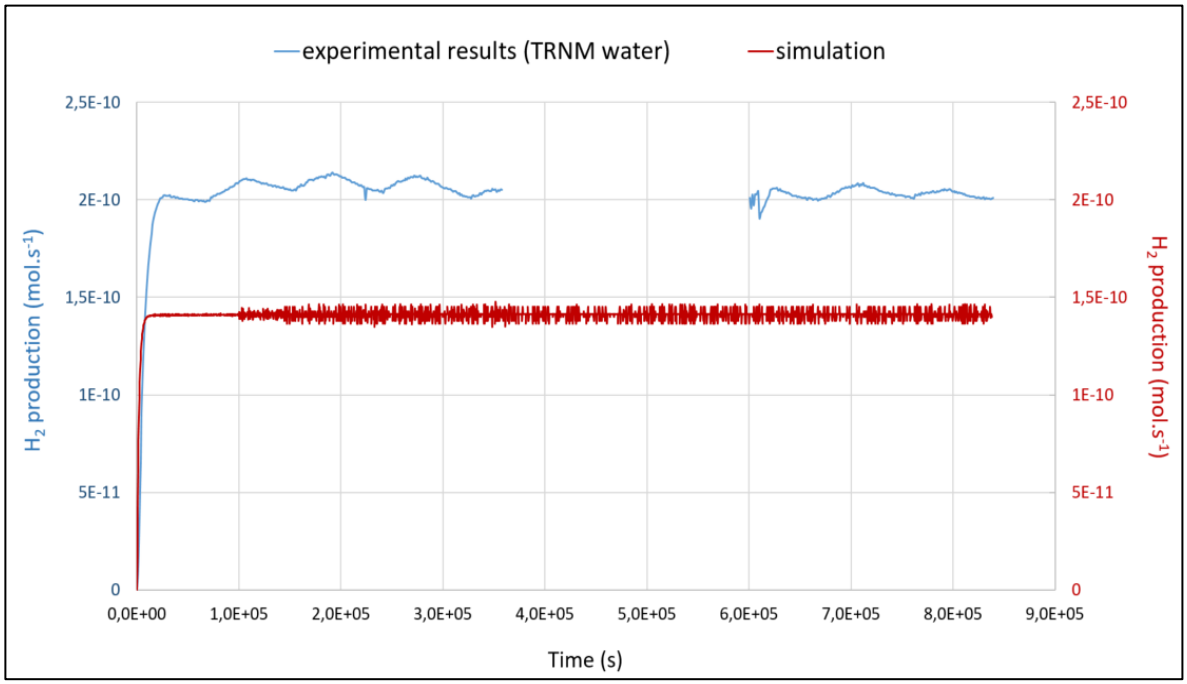

Figure 5.6.1: H_2 evolution graph from experimental results and simulation work for the case of synthetic pore water under irradiation

The evolution of the curves associated to experimental H_2 values and modelled H_2 results over time is similar. Once the irradiation starts, the two curves reach their maximum peak. Afterwards, a "plateau" phase is observed during the whole irradiation period. H_2 production experimental data range between 1.9 - 2.1 x 10^{-10} mol.s^{-1} while the simulation data vary between 1.3 - 1.5 x 10^{-10} mol.s^{-1} indicating comparable results.

As it is depicted in Figure 5.6.2, the simulation aiming to represent the fate of hydrogen peroxide (H_2O_2) revealed a final concentration equal to 3.6 x 10^{-7} mol.L^{-1}. This result is in good accordance with our experimental value, measured within 24 hours after the end of irradiation, [H_2O_2] = 3.5 x 10^{-7} mol.L^{-1}.

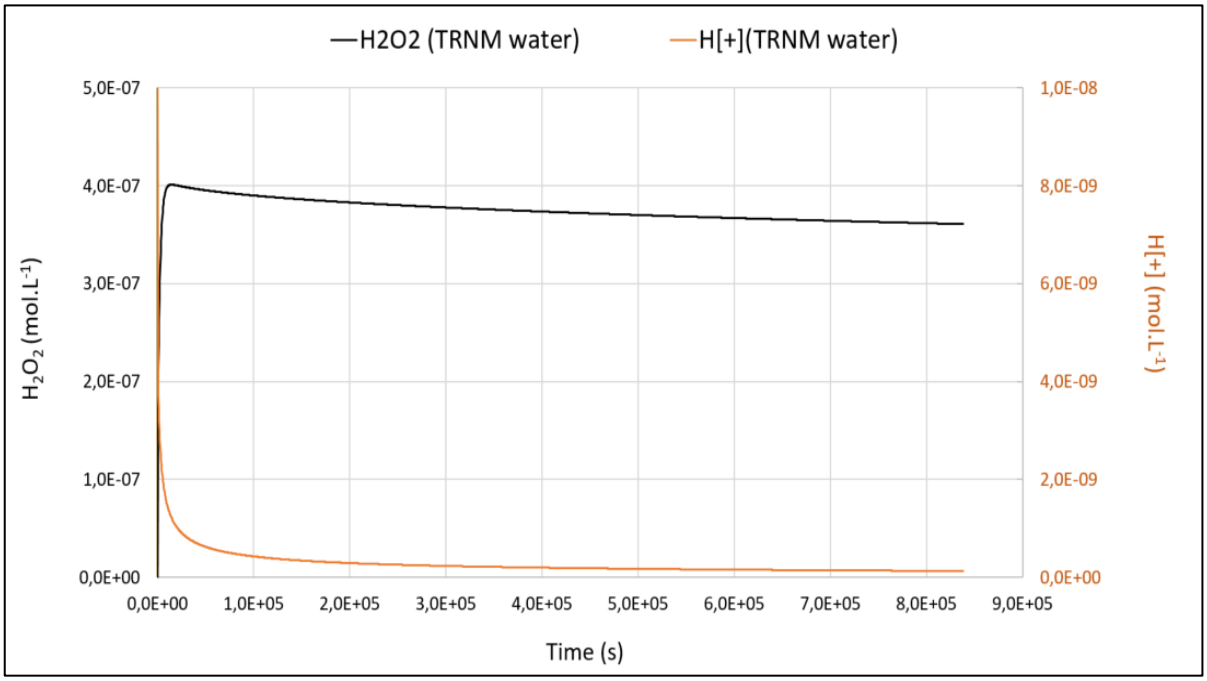

Figure 5.6.2: H_2O_2 and H^+ (secondary axis) evolution from simulation work for the case of TRNM water under irradiation

Figure 5.6.2 also shows the simulated value of the H^+ ion production (secondary axis). The stabilized $H[^+]_s$ concentration is about 1.3 x 10^{-10} mol.L^{-1}. In parallel, the pH measurements performed right after the end of irradiation indicated a pH value of 9.1, resulting to a $H[^+]_E$ concentration equal to 7.9 x 10^{-10} mol.L^{-1}.

5.6.2 TRNM synthetic pore water + iron sample

For this case, the experimental conditions applied correspond to the ones observed for cell G1 (TRNM synthetic pore water + metallic sample). For the associated simulation exercise, we used the reactions from groups 1, 2, 3, 4, 5, 6 and 8 (Table 5.3.1). In Figure 5.6.3 are shown the merged results of experimental data and simulation results (secondary y-axis).

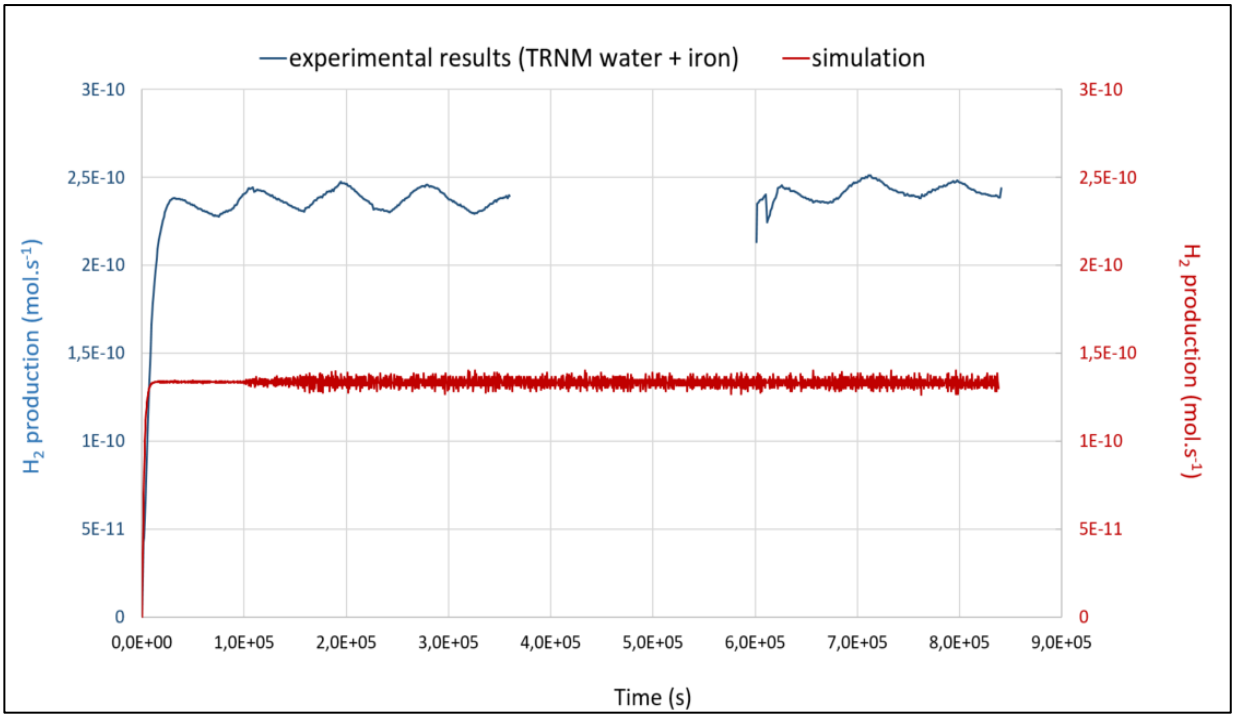

Figure 5.6.3: H_2 evolution graph with experimental results and simulation work for the case of synthetic pore water in the presence of iron under irradiation

As in Figure 5.6.1, the curves in Figure 5.6.3 reach a maximum value, and then a "plateau" phase is observed during the whole irradiation period.

H_2 production experimental data set ranges between 2.1 - 2.5 x 10^{-10} mol.s^{-1} while the simulation data set varies between 1.3 - 1.4 x 10^{-10} mol.s^{-1} indicating comparable results. These results are also close to the ones in absence of iron sample (see Figure 6.3.1). Although, an additional H_2 volume could be estimated by hydrogen difference between cell G1 and G2, on average 2.0 x 10^{-9} mol.min^{-1} equal to 0.34 x 10^{-10} mol.s^{-1}. This could increase simulated H_2 but not higher than 1.7 x 10^{-10} mol.s^{-1}. Even though experimental curve remains higher than the simulated one, the results seem to not differ appreciably.

Figure 5.6.4 shows that, in presence of iron in the system, hydrogen peroxide final concentration (left hand y-axis) is about 7.1 x 10^{-6} mol.L^{-1}, one order of magnitude higher compared with the simulated results associated to TRNM synthetic pore water without metallic sample (i.e., 3.6 x 10^{-7} mol.L^{-1}). As previously observed, the interactions between scavenged hydrated electrons (e_{aq}^-) and iron compounds will induce a decrease in (e^-) concentration. Thus, hydrated electrons are no more available to react with H_2O_2 and thus, H_2O_2 concentration in solution increases with time.

Figure 5.6.4 also shows that the simulated $H[^+]_s$ concentration value at the end of the irradiation is the same with the Figure 5.6.2, 1.29 x 10^{-10} mol.L^{-1}. This simulated H^+ concentration value corresponds to a pH value of 9.8 when our experimental pH measurement in cell G1 (TRNM synthetic pore water + iron sample) which was about 9.3. The fact that the pH evolution in the presence/absence of iron remains the same shows that Fe-reactions are not of significant importance for $H[^+]$ evolution.

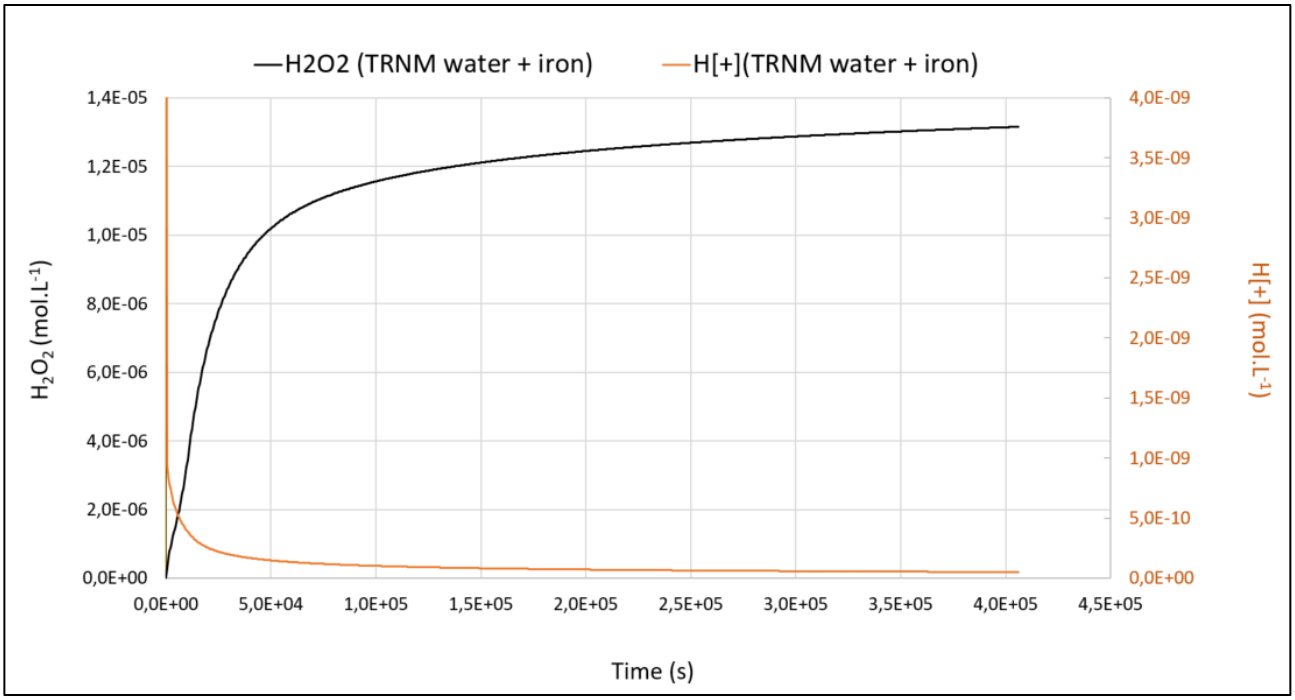

Figure 5.6.4: H_2O_2 and H^+ evolution from simulation work for the case of TRNM water in the presence of iron under irradiation

This simulation work aims to mimic our experimental conditions during irradiation using either pure deaerated water or TRNM synthetic pore water, with or without iron presence. The biggest difference between experimental and simulated values is observed for tests involving ultrapure water. The fact that simulated values are one order of magnitude lower than experimental ones may be attributed to the fact that it is difficult to obtain experimentally a "real and ideal" ultrapure water as modelled by Chemsimul. The presence of even really low amount of impurities in our solution could thus impact the H_2 production and induce such difference between experimental and simulated results. In this way, modelling exercises performed with addition of possible impurities in the aqueous solution, either Fe-species or synthetic pore water components, generate graphs much closer to our experimental results. The fact that other radiolytic species concentration (e.g., H_2O_2 and H^+) are close to our experimental values makes

us conclude that the used input dataset sufficiently represents the conditions prevailing during irradiation phase of our experiments. Thus, simulation allow to determine some parameters values that have not been experimentally measured, as the H_2O_2 concentration of the solution associated to cells involving metallic samples. Simulated H_2O_2 concentration obtained for such tests exhibit values one to two order of magnitude higher than the ones experimentally measured for test without metallic coupons. Certainly, our semi-open system creates a lot of uncertainties mainly due to the constant gas extraction. Although, species evolution and final concentrations seem to be in good accordance with the greater part of our measurements.

Chapter 6: Discussion

The primary motivations of the work presented in this manuscript is to investigate the impact of gamma radiation on carbon steel anoxic corrosion processes in order to (i) quantify the H_2 production and (ii) estimate the associated corrosion rate allowing an accurate dimensioning of the metallic elements used in the French high-level radioactive waste deep geological disposal design (Cigeo project). The adopted experimental setup allows distinguishing between the H_2 production related to water radiolysis and the one related to anoxic corrosion, making possible the estimation of associated corrosion rate. Finally, *post mortem* analyses were performed on the metallic samples surface to identify neoformed corrosion products, and chemical characteristics of the solution were determined (pH, Fe_{total} and H_2O_2). In parallel, the obtained experimental data are compared to simulated data resulting from different modelling exercises.

This discussion section deals with the inter-connexion of the results and the literature. After briefly discussing the reliability of our experimental set-up relative to the different solution volume and/or helium flow rate that have been used, the second part of the discussion will be devoted to the radiolytic processes associated to the tests involving cells without metallic sample. In a third part, the corrosion processes impacting the cells with metallic samples when submitted to radiation will be discussed. Finally, the two different techniques for corrosion rate estimation, i.e., gas generation and weight loss, will be compared.

6.1 Reliability of the experimental set-up

The reliability of the results is crucial for discussing with the reality of phenomena expected in the future life of the nuclear waste disposal depicted in the Cigeo project. In order to verify the reliability of our experimental setup and the representativeness of the obtained results, we had to firstly check if the volume of solution used in our tests could be a parameter impacting the H_2 production provided by water radiolysis.

Impact of the solution volume

When comparing the mean hydrogen production rate obtained during irradiation phase for cell B2, tested with 150 mL of ultrapure water (i.e., 9.7×10^{-9} mol.min^{-1}), with the mean rate derived from cells C2, tested with 200 mL of ultrapure water (i.e., 1.5×10^{-8} mol.min^{-1}), we observed that the ratio between the volumes used in these different set of test (i.e., 0.75) is similar to the

ratio between the associated obtained H_2 production rates (i.e., 0.65). Thus, in order to obtain comparable results of H_2 production associated to water radiolysis process, we decided from Experiment C to perform all the additional tests with a volume of solution equal to 200 mL.

Impact of the gas flow

In parallel, we had also to verify if the flow rate of the carrier gas (He), used to flow continuously the produced hydrogen gas towards a gas chromatograph, could impact the H_2 production associated to water radiolysis process.

When comparing the mean hydrogen rate obtained during irradiation phase for cell A2, tested with 100 mL of ultrapure water subjected to a He flow rate of 30 $mL.min^{-1}$ (i.e., 9.2 x 10^{-9} $mol.min^{-1}$), with the mean rate derived from cells B2, tested with 150 mL of ultrapure water subjected to a He flow rate of 5 $mL.min^{-1}$ (i.e., 9.7 x 10^{-9} $mol.min^{-1}$), we observed that carrier gas flow rate does not seem to impact notably the H_2 production associated to water radiolysis process. Moreover, regarding the impact of the volume of solution used in the tests on hydrogen production (see above), the H_2 production associated to cell A2 would be higher with 200 mL than the one with 100 mL, although the results associated to these two experiments are not significantly different. Nevertheless, in order to obtain comparable results of H_2 production associated to water radiolysis process and to limit the perturbation possibly associated with an intense solution bubbling, we decided that from experiment B, all the tests will be performed with a He flow rate of 5 $mL.min^{-1}$.

6.2 Radiolytic processes in solution without metallic coupons

In order to better understand the impact that radiolysis processes could have on corrosion phenomena, we propose to firstly focus on the results related to the cells tested with the same volume (200 mL) of solution (ultrapure water, TRNM synthetic pore water, MREA-TRNM synthetic solution) without metallic sample and subjected to the same helium flow rate of 5 $mL.min^{-1}$.

In ultrapure water (cells C2, E2, F2), we observe that once the irradiation phase starts, water radiolysis process takes place: we can immediately observe an intense production of H_2 (Figure 6.1.1). This is mainly due to recombination reactions occurring in the earliest stage consequently to the ionization of water molecules (Tabata et al., 1991).

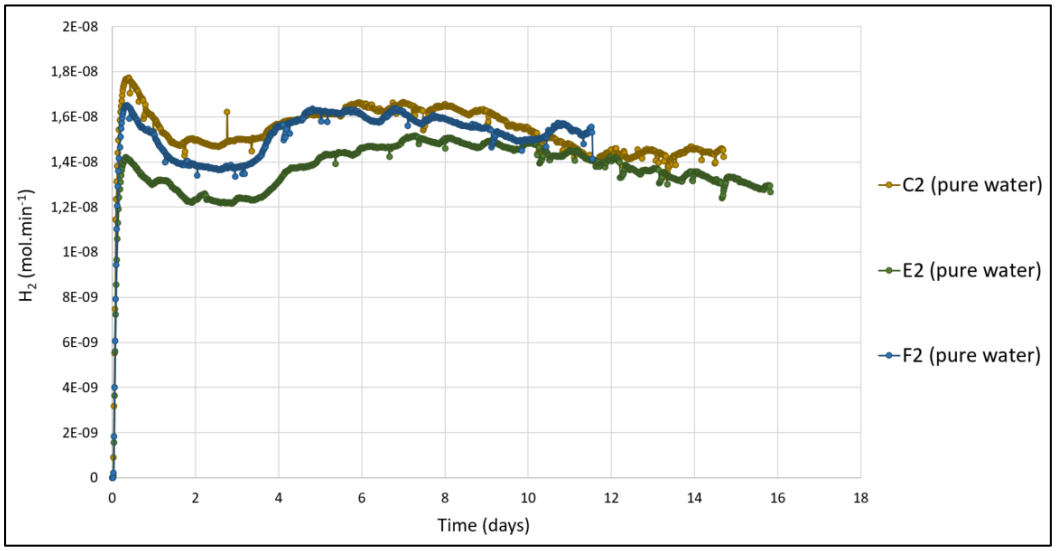

Figure 6.1.1: H_2 evolution over time for cells C2/E2/F2 tested with ultrapure water

According to Pastina et al., (1999) the reactions (R6.1), (R6.2) and (R6.3), which highlight the importance of hydrated electron (e_{aq}^-) regarding molecular hydrogen formation, are responsible for the majority of H_2 formation:

$$e_{aq}^- + e_{aq}^- + 2\,H_2O \rightarrow H_2 + 2\,OH^- \qquad k = 0.55 \times 10^{10}\ M^{-1}.s^{-1} \qquad (R6.1)$$

$$e_{aq}^- + H^\bullet + H_2O \rightarrow H_2 + OH^- \qquad k = 2.50 \times 10^{10}\ M^{-1}.s^{-1} \qquad (R6.2)$$

$$H^\bullet + H^\bullet \rightarrow H_2 \qquad k = 0.78 \times 10^{10}\ M^{-1}.s^{-1} \qquad (R6.3)$$

These reactions occur in spurs following the ionization processes (Hatano et al., 2010). Furthermore, H_2 can be consumed by reacting towards $^\bullet OH$ according to the following reaction (R6.4):

$$^\bullet OH + H_2 \rightarrow H^\bullet + H_2O \qquad k = 4 \times 10^7\ M^{-1}.s^{-1} \qquad (R6.4)$$

but not in a big extent as this reaction is relatively slow. Moreover, the use of a semi-open and gas-flow system does not permit to H_2 gas to remain in the liquid phase; then it escapes to this reaction.

Regarding the results associated with the cells involving more complex chemical solution, as TRNM synthetic pore water (cells D2, G2) or MREA-TRNM synthetic solution (cell H2), we also observe that once the irradiation phase starts, water radiolysis process takes place and we can immediately observe an intense production of H_2 (Figure 6.2.2).

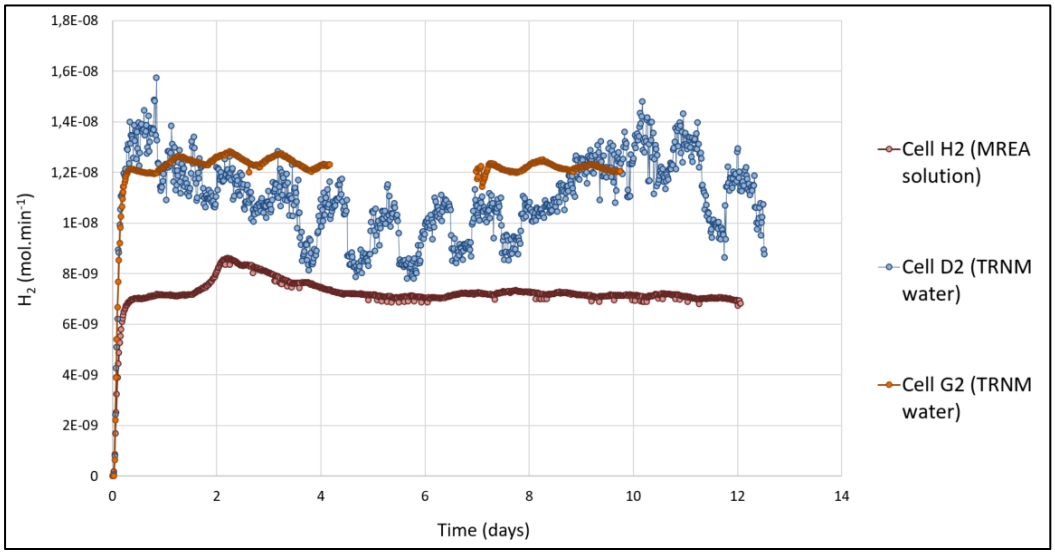

Figure 6.1.2: H_2 evolution over time for cells D2/G2 tested with TRNM synthetic pore water and for cell H2 tested with MREA-TRNM synthetic solution

However, when comparing the mean hydrogen production rate obtained during irradiation phase of ultrapure water (i.e., ~ 1.5 x 10^{-8} mol.min^{-1}), with the mean rate derived from either TRNM synthetic pore water (i.e., ~ 1.1 x 10^{-8} mol.min^{-1}) or MREA-TRNM synthetic solution (i.e., ~ 7.3 x 10^{-9} mol.min^{-1}), we observe that included impurities in the solution induces a small decrease of the H_2 production.

According to literature, such H_2 production decrease would be linked to the presence of solutes in solution. On the one hand, if solution exhibits high solute concentrations (generally >1M, depending on the species reactivity), reactions between radical species and solutes could prevent radical-to-radical reactions and thus impact the radiolytic yield (G-values) of molecular species such H_2 (Schwarz, 1955). On the other hand, if solution exhibits low to intermediate solute concentrations, solutes cannot compete with radical-to-radical reactions, but they are still able to form reactive species prone to impact the formation of H_2O_2 which remains and accumulates in solution unlike H_2 (Jonsson, 2012).

Pastina et al. (1999) suggested that H_2 yield generally exhibits a steady decrease with increased scavenging capacity for hydrated electron (which is considered as the main precursor of molecular hydrogen). Such scavenging capacity is calculated according to the following equation (E6.1):

$$SC = k \times [S] \qquad \text{(E6.1)}$$

Where SC is the scavenging capacity (s^{-1}), k is the constant rate of the reaction involving the hydrated electron/scavenging solute and [S] is the scavenging solute concentration.

In that work, the authors showed that solute can really induce a decrease of H_2 yield if their associated scavenging capacity is above 10^8 s^{-1}. Nonetheless, our experimental results seem to indicate that, even for lower scavenging capacity (inferior to 10^4 s^{-1}) solute would slightly impact H_2 production.

According to some authors (Bjergbakke et al., 1984; Bouniol, 2004) even though Cl-products will react very fast, their importance is insignificant due to the fast backwards reactions. This is in accordance with the work of Eriksen et al. (1989), suggesting that in the presence of chloride (Cl^-) the concentration of $^\bullet OH$ radical does not decrease significantly and the H_2 consumption process through (R6.4) continues. Nevertheless, these impurities are known to react with a great efficiency towards $^\bullet OH$ and their scavenging capacity is to be considered.

In the spurs diffusion model as, it has been described by (Schwarz, 1969), e_{aq}^-, $H^\bullet$, $^\bullet OH$, and H_2O_2 are involved in the non-homogeneous stage. Since $^\bullet OH$ can be scavenged in the non-homogeneous stage of the radiolysis process, the chemical system tends to diminish the G-values of H_2O_2 and meanwhile to increase the G-value of e_{aq}^-. Therefore, if $^\bullet OH$ is consumed, e_{aq}^- can serve to form H_2 and $G(H_2)$ should increase, which is not what we observe in our results. Then we discard $^\bullet OH$ scavenging as the origin of $G(H_2)$ decrease. For some authors, the presence in solution of solutes able to scavenge $^\bullet OH$ radical could have a significant impact on H_2 production by introducing new reactions able to compete with reaction (R6.4). Indeed, the presence in the system of inorganic solute such as carbonate (HCO_3^-) will induce the following reaction (R6.5):

$$^\bullet OH + HCO_3^- \rightarrow CO_3^- + H_2O \qquad k = 1.5 \times 10^7\ M^{-1}.s^{-1} \qquad \text{(R6.5)}$$

Such $^\bullet OH$ radical scavenging should thus limit the direct consumption of H_2 and lead to an increase of hydrogen gas production. In this context, the work of Bouniol (2004) suggests that inorganic solutes are able to impact radiolytic yield for concentrations ranging from 10^{-3} - 10^{-2} $mol.L^{-1}$.

In parallel, Tabata et al. (1991) suggested that radiolytic yields can be impacted for solute concentration above 10^{-3} $mol.L^{-1}$. Since our synthetic solutions (TRNM synthetic pore water and MREA-TRNM synthetic solution) involved some solutes with concentration in the order of the millimole, it might be assumed that H_2 radiolytic yield has been impacted by the presence of solute.

Moreover, MREA-TRNM synthetic solution contains nitrate (NO_3^-) which is known to impact significantly H_2 production through (Bouniol, 2004):

$$e_{aq}^- + NO_3^- \rightarrow NO_2 + 2OH^- \qquad k = 9.7 \times 10^9\ M^{-1}.s^{-1} \qquad \text{(R6.6)}$$

The upper reaction, in competition with reaction (R6.1), can significantly decrease molecular hydrogen yield (Bouniol, 2004; Draganic & Draganic, 1971; Iwamatsu et al., 2018; Schwarz, 1969). In that respect, the low amount of nitrates present in the MREA-TRNM synthetic solution (0.02 mM) would scavenge some hydrated electron and thus, participate to a low extent to decrease H_2 production associated to cell H2. In the work of Pastina et al. (1999), 0.0057 M of NO_3^- affects the $G(H_2)$ of 0.04 (from 0.47 to 0.43).

Inversely, other studies tend to indicate that the solution's ionic strength, a parameter linked directly to the solute concentration, has no significant impact on H_2 radiolytic yield (Peled & Czapski, 1970).

Another important parameter prone to impact the H_2 radiolytic yield evolution is the pH range of the tested solution. However, when performing a bibliographic review of the studies dealing with the impact of the pH on the evolution of radiolytic yields, one realizes that it remains a field with a lot of unanswered questions and contradictory results, especially for the highest pH values.

Some authors (Joseph et al., 2008) suggest that under gamma rays, both H_2 and H_2O_2 radiolytic yields are not impacted, for solution exhibiting a pH ranging from 5 to 8. Compared with measurements done for pH values ranging from 5 to 8, this work also indicates that for pH value above 10, H_2 and H_2O_2 concentrations increased by two orders of magnitude and one order of magnitude, respectively. For other authors (Buxton & Dainton, 1965; Cheek & Linnenbom, 1963), H_2 yield starts to decrease only if the pH of the solution is above 13. However, these works also suggested that hydrogen peroxide yield starts to decrease for pH above 10. In parallel, the work of Hayon (1965) shows that both H_2 and H_2O_2 radiolytic yields exhibit a decrease when the pH of the solution is above 11.

To explain such radiolytic yield evolution in alkaline media, several reactions have to be taken into account. According to Trupin et al. (1999) for pH values above 12, $^{\bullet}OH$ radical will deprotonate through the reaction (R6.7):

$$^{\bullet}OH + OH^- \rightarrow O^{\bullet-} + H_2O \qquad k = 6.3 \times 10^9\ M^{-1}.s^{-1} \qquad \text{(R6.7)}$$

Reaction (R6.7) shows that an important quantity of $O^{\bullet-}$ radical will be created. Through reactions (R6.8) and (R6.9):

$$^{\bullet}OH + O^{\bullet-} \rightarrow HO_2^- \qquad k = 10^9\ M^{-1}.s^{-1} \qquad \text{(R6.8)}$$

$$O^{\bullet-} + O^{\bullet-} \rightarrow O_2^{2-} \qquad k = 10^8\ M^{-1}.s^{-1} \qquad \text{(R6.9)}$$

this $O^{\bullet-}$ radical is able to participate to an additional formation of H_2O_2 for solution having a pH above 12 (Trupin et al., 1999). However, due to the fact that the main production of H_2O_2 is associated to a reaction (R6.10):

$$^{\bullet}OH + {}^{\bullet}OH \rightarrow H_2O_2 \qquad k = 5.5 \times 10^{9}\ M^{-1}.s^{-1} \qquad (R6.10)$$

exhibiting a faster constant rate than both reaction (R6.8) and (R6.9), $O^{\bullet-}$ radical will not be able to react with $^{\bullet}OH$ radical. Thus, $O^{\bullet-}$ radical will then diffuse into the spurs and/or react with other radical species, without participating anymore to H_2O_2 production. This phenomenon can thus explain the hydrogen peroxide decrease observed for experiments performed in alkaline media (Trupin et al., 1999).

From radiolytic H_2 production point of view, this production of $O^{\bullet-}$ radical will also play a role. Indeed, the main reaction consuming H_2 involves $^{\bullet}OH$ radical (R6.4):

$$^{\bullet}OH + H_2 \rightarrow H^{\bullet} + H_2O \qquad k = 4.0 \times 10^{7}\ M^{-1}.s^{-1} \qquad (R6.4)$$

Due to the high constant rate of reaction (R6.7), a large part of $^{\bullet}OH$ radical will not be able to react with H_2 through reaction (R6.4). Nevertheless, according to the work of Bouniol (2004), an additional source of H_2 consumption will arise with the presence of $O^{\bullet-}$ radical through reaction (R6.11):

$$O^{\bullet-} + H_2 \rightarrow e_{aq}^{-} + H_2O \qquad k = 1 \times 10^{8}\ M^{-1}.s^{-1} \qquad (R6.11)$$

Therefore, even if the decrease of H_2O_2 radiolytic yield mentioned above could contribute to have more hydrated electrons available to produce H_2, the global production of molecular hydrogen should decrease for tests performed in alkaline media.

These assumptions are in good agreement with our experimental results. When comparing the mean radiolytic H_2 production associated to the tests performed with ultrapure deaerated water (i.e., ~1.5×10^{-8} mol.min^{-1}) to the one associated to the tests performed with the TRNM synthetic pore water (i.e., ~ 1.2×10^{-8} mol.min^{-1}), one can realize that the presence of solute in solution can induce a decrease of molecular hydrogen production. In the same way, when comparing the mean radiolytic H_2 production associated to the tests performed with TRNM synthetic pore water to the one associated to the test performed with MREA-TRNM synthetic solution (i.e., ~ 7.3×10^{-9} mol.min^{-1}), we conclude that alkaline pH condition can also cause a reduction of H_2 production.

However, a question remains when comparing the H_2O_2 evolution in test performed with MREA-TRNM synthetic solution to the one obtained for lower pH conditions. The alkaline conditions prevailing for MREA-TRNM synthetic solution would induce a large consumption

of •OH radical through reaction (R6.7) and so, to induce a decrease of the hydrogen peroxide production. Nonetheless, the H_2O_2 concentration associated with cell H2 (2.7×10^{-7} mol.L^{-1}) tested with alkaline solution is in the same order with the ones obtained for cells tested with near neutral pH solution (3.5×10^{-7} mol.L^{-1}). This observation may be explained by the presence in MREA-TRNM synthetic solution of nitrate (NO_3^-) species which are known to scavenge hydrated electron through reaction (R6.12) (Wasselin-Trupin et al., 2002):

$$NO_3^- + e_{aq}^- \rightarrow NO_3^{2-} \qquad k = 9.7 \times 10^9\ M^{-1}.s^{-1} \qquad \text{(R6.12)}$$

Reaction (R6.12) will thus limit hydrogen peroxide degradation caused by its interaction with hydrated electron (R6.13):

$$H_2O_2 + e_{aq}^- \rightarrow {}^{\bullet}OH + OH^- \qquad k = 1.1 \times 10^{10}\ M^{-1}.s^{-1} \qquad \text{(R6.13)}$$

If we now consider the global evolution of the molecular hydrogen production all along the irradiation phase, we observe that cells C2, E2 and F2 (tested with ultrapure water) indicate quite similar evolution and correspond to average values of 1.5×10^{-8} mol.min^{-1}, 1.4×10^{-8} mol.min^{-1} and 1.5×10^{-8} mol.min^{-1}, respectively. For these cells, the initial H_2 production peak related to the beginning of the irradiation phase is followed by a sharp decrease taking place during the first 48h. After this, we observe a stabilization phase (during approximately 2 or 3 days) which is followed by a progressive increase (during approximately 2 days) and then by a second stabilization period (during approximately 3 or 4 days). Finally, cells C2, E2 displayed a progressive decrease of their H_2 production until the end of the irradiation phase. In parallel, H_2 production associated to F2 cell remained constant until the end of the irradiation phase.

According to the literature (Pastina & LaVerne, 2001), a possible explanation for this progressive H_2 decrease arises from the formation of other radiolytic products with compatible reaction rates. The major factor that could inhibit H_2 formation is the presence of hydrogen peroxide (H_2O_2). The latter, as its concentration rises, is able to scavenge the main precursor of hydrogen, i.e., the hydrated electron (e_{aq}^-), as shown by reaction (R6.13), and thus, to inhibit the formation of molecular hydrogen derived from reactions (R6.1) and (R6.2). The fact that H_2O_2 was still identified in the solution collected in cells C2 and F2 just after the end of irradiation (0.5×10^{-6} mol.L^{-1} and 0.6×10^{-6} mol.L^{-1}, respectively) suggests that such process could take place during our experiments.

Regarding the global evolution of the molecular hydrogen production all along the irradiation phase, we notice that cells D2, G2 and H_2 (tested with TRNM synthetic pore water or MREA-TRNM synthetic solution) do not exhibit the same fluctuations as the one observed for ultrapure water. A first hypothesis that can explain such phenomenon could be the fast interaction of the solutes with radicals, and especially with hydrated electron which is known to be the main H_2

precursor, accelerating somehow an equilibrium phase. Additionally, as it has been previously discussed, the presence of organic solutes in the solution makes possible the reaction (R6.5) and thus, limits the amount of •OH radical able to react directly with H_2 through reaction (R6.4). Consequently, H_2 production decrease is attenuated, and we observe a more stable molecular hydrogen production evolution all along the irradiation phase.

In parallel with the data obtained thanks to experimental work, simulation exercises have also been performed with Chemsimul software (Chapter 5). The associated results showed that the hydrogen production for ultrapure water test simulation is under-estimated compared to experimental data. Moreover, the fluctuations observed during the experimental tests are not reproduced by the simulation. However, these tests showed a good agreement between simulated and experimental H_2O_2 concentrations.

In the same way, results associated to tests performed with TRNM synthetic pore water show that the simulated mean value of hydrogen production and the experimental one, are compatible. In addition, these tests also showed that the simulated concentration of H_2O_2 was in good agreement with the experimental measurement.

Also, when comparing experimental and modelled H_2 production evolution, we notice that the small H_2 variations experimentally monitored are not reproduced by the model. Indeed, these H_2 variations seems to be linked with the daily temperature fluctuation observed in the IRMA technical hall (maximum variation range from 15 to 25 °C). However, the work of Tabata et al. (1991) tends to indicate that molecular and radical yields are not impacted for temperatures below 65°C. Actually, we suspect that the PDHID detector (use in gas chromatograph to detect and measure the H_2) exhibits a great sensitivity to temperature variation. Indeed, such H_2 variations have also been observed during gas chromatograph calibration phase where no radiolytic process take place. Therefore, these H_2 variations are probably due to an experimental artefact and not caused by a physicochemical phenomenon. Moreover, in previous simulation tests, we tried to verify the temperature impact with variations up to 10°C and the results do not indicate any significant difference in H_2 evolution in this fluctuation range.

6.3 Corrosion processes

After considering some issues associated with water radiolysis processes, this part is more focussed on the question of anoxic corrosion processes taking place during the three studied phases: (i) pre-irradiation, (ii) irradiation and (iii) post-irradiation phases. We propose to discuss the results related to the cells tested with the same volume (200 mL) of solution

(ultrapure water, TRNM synthetic pore water, MREA-TRNM synthetic solution), in the presence of 6 carbon steel samples and subjected to the same He flow rate (5 $mL.min^{-1}$). Moreover, due to technical problems happening during the preparation of cell F1 and leading to a potential oxidation of the system, we decided to dismiss the results associated to this cell.

6.3.1 Pre-irradiation phase

Considering the results associated with the cells involving ultrapure deaerated water (cells C1, E1), we observe that the hydrogen production values measured during the pre-irradiation phase are quite similar: 2.5 x 10^{-9} $mol.min^{-1}$ and 2.8 x 10^{-9} $mol.min^{-1}$ for C1 and E1, respectively. This production of H_2 is exclusively associated to anoxic corrosion process occurring for carbon steel sample immersed in ultrapure deaerated water and leading to magnetite (Fe_3O_4) formation, according to reaction (R6.14):

$$3\,Fe + 4\,H_2O \rightarrow Fe_3O_4 + 4\,H_2 \qquad (R6.14)$$

These H_2 measurements are then converted into corrosion rate values, using a conversion factor relevant for anoxic corrosion mechanism leading to the formation of magnetite (Fe_3O_4) as main corrosion product. The corresponding calculated corrosion rates for cells C1 and E1 ranged between 1.1 and 1.2 $\mu m.year^{-1}$ highlighting the reliability of our measurements for tests involving ultrapure water.

These results are in good agreement with literature data derived from works dealing with carbon steel anoxic corrosion occurring in pure deaerated water. For "short term" duration experiments (almost two weeks), Badet (2014) could not identify any corrosion product on the metallic sample, although he measured corrosion rate values lower than 3 $\mu m.year^{-1}$. In parallel, the review of Platts et al., (1994) mentioned the formation of magnetite as main corrosion product and proposed corrosion rate values obtained after 40 days of interaction to be lower than 1.1 $\mu m.year^{-1}$.

Regarding the results associated with the cells involving more complex chemistry solution, as TRNM synthetic pore water (cells D1, G1) or MREA-TRNM synthetic solution (cell H1), we also notice a H_2 production associated to anoxic corrosion process leading to magnetite (Fe_3O_4) formation, as previously observed for tests performed in ultrapure deaerated water (R6.14). In the case of carbonated artificial pore water, one should also consider the reaction leading to other corrosion products such as siderite ($FeCO_3$) through the overall reaction (R6.15):

$$Fe + 2\,M\,HCO_3 \rightarrow FeCO_3 + H_2 + M_2CO_3 \qquad (R6.15)$$

where M is a balancing univalent cation.

Since we did not observe any siderite on the metallic samples at the end of tests D1 and G1 (TRNM synthetic pore water), we used the same conversion factor as the one used for ultrapure deaerated water to calculate the corresponding corrosion rates. Thus, hydrogen production equal to 4.3 x 10^{-9} mol.min^{-1} and 2.5 x 10^{-9} mol.min^{-1}, lead to corrosion rate values of 1.8 and 1.1 µm.year^{-1} for D1 and G1, respectively. The higher corrosion rate observed for D1 could be attributed to the shorter exposure time of the metallic sample during pre-irradiation phase of experiment D compared to experiment G. Indeed, the review of King (2008) suggests that H_2 gas measurements provide supposedly steady state corrosion rates after 8-16 days of exposure, with decreasing trend over time due to the progressive formation of a protective corrosion layer upon the metallic surfaces.

These corrosion rate values are in good agreement with literature data derived from works dealing with carbon steel anoxic corrosion occurring in artificial/natural groundwater. Smart et al. (2001), using Aspo-groundwater (granitic pore water), measured stabilized corrosion rate values lower than 2 µm.year^{-1} after 20 days of exposure. Similar observations are noticed by Kreiss (1991) in granitic pore water, although the initial high rates for the first 42 days are in the order of 0.7 µm.year^{-1}. Studies involving carbon steel samples immersed in argillaceous rock porewater also indicate a progressive decrease of corrosion rate even in higher temperatures. An initial rate at 150 µm.year^{-1} reaches rates lower than 1 µm.year^{-1} in longer time scales (Mohamed-Said et al., 2017; Necib et al., 2017; Schlegel et al., 2021; Smart et al., 2017a).

Compared to ultrapure water, the presence of dissolved species in natural groundwater may impact the corrosion rate evolution either by the formation of additional corrosion products (siderite, chukanovite) or by the modification of the corrosion processes (appearance of localized corrosion). Indeed, Grousset (2016) indicates that due to its low-conductivity properties, siderite would offer a better protection compared to magnetite (higher conductivity properties) for carbon steel surface subjected to bio-corrosion processes. In parallel, in the review of King (2008) referring in the work of Schenk (1988) observes that the presence of relatively low chloride (Cl^-) concentration (< 80 ppm) in near neutral pH solution, will lead progressively to the passivation of the metal. However, the author supports that increasing concentration (800 < (Cl^-) < 8000 ppm) will promote low quality of the protective layer and localised corrosion processes.

Regarding the results associated with the cell involving MREA-TRNM synthetic solution (cell H1), we observed that the hydrogen production value associated to this pre-irradiation phase is lower than the ones derived for ultrapure water and TRNM synthetic pore water. Thus, the

mean hydrogen production value of 0.04 x 10^{-8} mol.min^{-1} corresponds to a low corrosion rate of 0.02 µm.year^{-1}.

This result conforms well to previous studies involving alkaline pH solution. After 50 days of interaction, Senior et al. (2017) indicates maximum corrosion rate value of 0.026 µm.year^{-1}. In parallel, for short term experiments (100 days), Kaneko et al. (2004) reports mean corrosion rates value of 0.05 µm.year^{-1}. In addition, the work of Kaneko et al. (2004) focused more specifically on the impact of chloride concentration on corrosion processes and indicated that the previous rate can be up to 0.2 µm.year^{-1} for high chloride concentrations (<5000 ppm for alkaline pH).

The work of Smart et al. (2001) showed that during tests involving alkaline solution (pH~10.5), the hydrogen production is four times less compared to tests performed with synthetic groundwater (pH~8). According to the authors, an elevated pH favors the formation of magnetite and decreases solubility of ferrous ions, leading to more rapid and protective corrosion layer. In another work, Kreiss (1991) reported the impact of calcium hydroxide in solution and noticed that it leads to low corrosion rates as the divalent calcium ion participates in the film growth upon the metallic samples, resulting to a more protective film. Finally, Cornell & Schwertmann (2003) report that in alkaline media, the hexagonal flakes of ferrous hydroxide ($Fe(OH)_2$) are gradually transformed to smaller and thicker plates of more thermodynamically-stable magnetite, leading to a faster and better passivation of the metallic surface.

6.3.2 Irradiation phase

This part is dedicated to the corrosion processes occurring during irradiation phase in the cells containing carbon steel sample and solution. The hydrogen production arising from these cells when exposed to irradiation results not only from the corrosion processes (R6.14) but also from the recombination reactions associated to radiolytic processes (R6.1 - R6.3) as it has been previously described.

Considering the results associated to the cells involving metallic samples and ultrapure deaerated water (C1 and E1), H_2 production shows similar evolution. The average values for C1 (16.2 ± 0.7 x 10^{-9} mol.min^{-1}) and E1 (14.2 ± 0.4 x 10^{-9} mol.min^{-1}) suggest that our experiments are repeatable under identical conditions. By subtracting H_2 production associated to the cells containing only ultrapure deaerated water (cells C2 and E2) from the one generated by the cells C1 and E1, it should permit to estimate the volume of hydrogen generated only by

the process of anoxic corrosion under irradiation. Thus, the average corrosion rate measured for C1 and E1 are 0.34 µm.year^{-1} and 0.20 µm.year^{-1}, respectively.

These results can be compared to the ones obtained by Badet (2014) through its work performed with deaerated pure water under gamma radiation. For a 99 days experiment and a dose rate of 1 kGy.h^{-1}, the author measured corrosion rate values ranging between 3.5 and 5.5 µm.year^{-1}. However, for a lower dose rate fixed at 0.3 kGy.h^{-1}, corrosion rate values decreased to level lower than 0.5 µm.year^{-1}. Additionally, the author noted that for "short term" experiment (15 days) performed with a dose rate of 0.3 kGy.h^{-1}, the corrosion rate remains lower than 2.5 µm.year^{-1}.

Regarding the results associated with the cells involving TRNM synthetic pore water (cells D1, G1), the mean hydrogen production also shows very similar trend with values of 12.2 ± 0.4 x 10^{-9} mol.min^{-1} and 14.3 ± 0.4 x 10^{-9} mol.min^{-1}, respectively. By subtracting H_2 production associated to the cells containing only TRNM synthetic pore water (cells D2 and G2) from the one generated by the cells D1 and G1, we calculated mean corrosion rate values of 0.51 µm.year^{-1} and 0.83 µm.year^{-1}, respectively.

These corrosion rate values can be compared with literature data derived from works dealing with carbon steel anoxic corrosion occurring in artificial/natural groundwater under γ-radiation. In his work involving carbonated medium, Badet (2014) observed that for "short term" experiments (15 days) performed at a dose rate of 0.3 kGy.h^{-1}, corrosion rate could reach value of 7 µm.year^{-1}. However, this value decreased to 1 µm.year^{-1} after 340 days of experiment. For this "mid-long term" experiment, carbon steel samples, submitted to a dose rate of 1 kGy.h^{-1}, exhibited higher corrosion rate value of 1.7 µm.year^{-1}. The work of Smart et al., (2008) involving granitic pore water and performed for similar time duration and at a dose rate of 0.3 kGy.h^{-1} indicates corrosion rate value around 3 µm.year^{-1}. The same work showed that for a lower dose rate fixed at 11 Gy.h^{-1}, corrosion rate decreased to values lower than 1 µm.year^{-1}. In parallel, the work of Marsh & Taylor (1988) involving carbon steel samples immersed in granitic groundwater during 218 days and exposed to a dose rate of 1 kGy.h^{-1}, indicates corrosion rate values around 3 µm.year^{-1}.

Considering the results associated with the cell involving MREA-TRNM synthetic solution (cell H1), we observed that the hydrogen production value associated to this irradiation phase is also lower than the ones stemmed from ultrapure water and TRNM synthetic pore water. Thus, the mean hydrogen production value of 7.7 x 10^{-9} mol.min^{-1} corresponds to a corrosion rate of 0.21 µm.year^{-1}.

This trend has been frequently observed in previous studies dealing with alkaline pH solution under γ-radiation. In the work of Smart et al. (2008), involving carbon steel samples immersed

in bentonite equilibrated groundwater (pH~10.5) at 50°C, results showed that corrosion rates values ranged between 0.05 and 0.2 μm.year^{-1} for sample exposed to a dose rate of 11 Gy.h^{-1} during 166 days. The same test performed at a higher dose rate, 0.3 kGy.h^{-1}, during 208 days indicates a corrosion rate value at 0.2 μm.year^{-1}. In a more recent work, Smart et al. (2017b) measured corrosion rate associated to carbon steel samples immersed in young cementitious pore water (pH 13.4) and exposed to a dose rate of 25 Gy.h^{-1} at 80°C. On the long term, the obtained corrosion rate values are lower than 0.1 μm.year^{-1}, in good agreement with other studies (Kursten et al., 2011; Smart et al., 2013; Winsley et al., 2011).

Corrosion rate evolution

If we focus on the evolution of the corrosion rate values all along this irradiation phase, we observed some differences between the cells involving ultrapure deaerated water. On the one hand, cell C1 indicated a slight decrease of corrosion rate over time, reaching a final value of 0.5 μm.year^{-1} after initial peak measured during the first days of irradiation at 1.1 μm.year^{-1}. On the other hand, cell E1 displays more constant corrosion rate values all along this irradiation phase. The decrease of corrosion rate observed for C1 may be attributed to the gradual formation of a thin corrosion product layer, mainly composed of magnetite (Fe_3O_4) as observed during the structural characterization of our samples, which passivate and protect the carbon steel surfaces. The formation of magnetite under anoxic conditions depends on the Schikorr reaction as it takes place due to thermodynamically less stable ferrous hydroxide ($Fe(OH)_2$) which is converted to magnetite. Even though Schikorr reaction is favored for temperature above 60°C (Linnenbom, 1958), magnetite has already been observed at ambient temperature (Diomidis, 2014).

The identification of magnetite as predominant corrosion product has previously been observed in several carbon steel anoxic corrosion studies involving ultrapure deaerated water and performed under irradiation (Badet, 2014; Cuba et al., 2011; Vandenborre et al., 2013).

In parallel, Sunderland et al. (2017) highlighted the impact of hydrogen peroxide (H_2O_2) on magnetite formation. The authors proposed a kind of surface oxidation process involving (i) a first adsorption of ferrous ions on oxide film followed by (ii) the oxidation of this adsorbed ferrous compound into adsorbed ferric compound by H_2O_2 (R6.16), to finally observe (iii) the incorporation of these Fe^{2+}/Fe^{3+} compounds into the growing oxide matrix (R6.17):

$$2\ Fe^{2+}_{(ad)} + H_2O_2 \rightarrow 2\ Fe^{3+}_{(ad)} + 2\ OH^- \quad \text{(R6.16)}$$

$$2\ Fe^{2+}_{(ad)} + 2\ Fe^{3+}_{(ad)} + 8H_2O \rightarrow Fe_3O_4 + 4\ H_2O + 8\ H^+ \quad \text{(R6.17)}$$

The authors suggested that such a mechanism promote a faster magnetite formation. In the work of Yakabuskie et al. (2011), is indicated that for deaerated water (pH~5.5) exposed to γ-radiation, the interactions between ferrous iron on the metallic surface and the radiolytic species hydrogen peroxide (H_2O_2) (R6.18):

$$2\ Fe^{2+} + H_2O_2 + 2\ H_2O \rightarrow 2\ \gamma\text{-}FeOOH + 4\ H^+ \quad \text{(R6.18)}$$

and/or hydroxyl radical (R6.19):

$$Fe^{2+} + {}^{\bullet}OH + H_2O \rightarrow \gamma\text{-}FeOOH + 2\ H^+ \quad \text{(R6.19)}$$

promote the formation of lepidocrocite (γ-FeOOH).

Lepidocrocite formation on carbon steel surface after oxidation of ferrous hydroxide by H_2O_2 has also been mentioned by Vandenborre et al. (2013) in their work involving deaerated pure water. However, the same study mentioned that the initially formed lepidocrocite is auto-reduced to magnetite (Fe_3O_4) according to the following reaction (R6.20):

$$3\ FeOOH + H_3O^+ + e^- \rightarrow Fe_3O_4 + 3\ H_2O \quad \text{(R6.20)}$$

Regarding the global evolution of the corrosion rate associated to the cells involving TRNM synthetic pore water (cells D1, G1), we observed a contrary tendency when compared to ultrapure water. Indeed D1 and G1 exhibited relatively stable evolution (mean value around 0.5 and 0.8 $\mu m.year^{-1}$, respectively) with maximum peak values (around 1.2 and 1.1 $\mu m.year^{-1}$, respectively) measured at the end of the irradiation phase. Even if the corrosion rate values are similar, the evolution trend is in contradiction with the work of Smart et al. (2008) which showed that during anoxic corrosion experiments involving synthetic ground water and performed under irradiation, the formation of magnetite lead to a decrease of the corrosion rate.

Despite the large presence of carbonate specie aragonite ($CaCO_3$) covering the majority of the carbon steel sample surface, our *post-mortem* metallic samples characterizations allowed to identify the presence of magnetite (Fe_3O_4) and maghemite ($\gamma\text{-}Fe_2O_3$), although the presence of maghemite is more attributed to oxidation of magnetite originally formed (Cornell & Schwertmann, 2003). Regarding the predominance of aragonite on the metallic samples observed under the characteristic needle-like and hubbard squash-like formations (Santos et al., 2012), since calcite is a major component of argillaceous rock (Beaucaire et al., 2008; Chautard, 2013), the presence and the precipitation of carbonated species from a synthetic argillaceous rock pore water has already been observed. The increase of aragonite with increasing Fe^{2+} concentration with the parallel inhibition of calcite has been demonstrated in the work of (Zhu et al., 2018). The authors explain that the electrochemical corrosion behavior is influenced by the deposition of calcium carbonate on carbon steel. Moreover, inhibition of calcite and

promotion of aragonite as the predominant calcium carbonate polymorph in the presence of divalent ions such as ferrous ions have been confirmed by other studies (Gutjahr et al., 1996; Meyer, 1984; Wada et al., 1995).

Considering the global evolution of the corrosion rate associated to the cell involving MREA-TRNM synthetic solution (cell H1), we observed relatively stable behaviour (mean value around 0.2 µm.year^{-1}) with maximum peak values at 0.5 µm.year^{-1}, measured at the end of the irradiation phase. Our *post-mortem* metallic samples characterizations allowed to also identify the presence of magnetite (Fe_3O_4). Compared to the observation associated to ultrapure water and TRNM synthetic pore water, magnetite crystals seem smaller and leaner. Such corrosion product has already been observed in previous works involving carbon steel sample immersed in high pH solution under irradiation (Smart et al., 2008, 2017b).

Impact of γ-radiation on corrosion rate of carbon steel

If we focus on the impact of irradiation on corrosion rate, we firstly observe a common tendency for cells involving ultrapure water and TRNM synthetic pore water: exposure to gamma radiation does not seem to induce an increase of the measured corrosion rate values. More precisely, the comparison between corrosion rate values obtained during irradiation for cells C1 and E1 (0.3 - 0.2 µm.year^{-1}, respectively) and cells D1 and G1 (0.5 - 0.8 µm.year^{-1}, respectively) and the ones gained during the short pre-irradiation phase (1.1 - 1.2 µm.year^{-1} and 1.8 - 1.1 µm.year^{-1}, respectively) suggests that the presence of gamma radiation inhibits somehow the anoxic corrosion rate of carbon steel.

This is in contradiction with studies comparing irradiated and un-irradiated carbon steel samples immersed in ultrapure deaerated water or synthetic groundwaters. Concerning the works involving ultrapure water, Badet (2014) points out a visible increase of the corrosion rate varying between 3.5 and 5.5 µm.year^{-1} for metallic samples exposed to γ-rays at dose rate of 1 kGy.h^{-1} for 99 days when compared to non-irradiated samples. However, for the same test duration with lower dose rate (0.3 kGy.h^{-1}), the author observed that the corresponding corrosion rates are not significantly different from the ones associated to the non-irradiated samples (~0.5 µm.year^{-1}). For temperature at 200°C Ershov et al., (1985) observed that metallic sample exposed to gamma radiation (12 kGy.h^{-1}) exhibited corrosion rate values three times higher compared to un-irradiated samples. In accordance with Fujita et al. (2000) working at 250°C, where it is mentioned corrosion rate enhancement up to six times, in samples exposed to gamma rays (0.48 kGy.h^{-1}).

Concerning the works involving synthetic groundwaters, the work of Badet (2014) performed in carbonated medium showed that for "short term" experiments (15 days) γ-radiation at 0.3 $kGy.h^{-1}$ does not create significant differences on carbon steel sample corrosion rate. However, the difference between irradiated and non-irradiated samples becomes significant with increasing dose. In parallel, studies involving carbon steel samples immersed in granitic pore water and exposed to γ-radiation at dose of 0.3 $kGy.h^{-1}$ for a period up to 220 days showed that corrosion rate values associated to irradiated samples (~3 $\mu m.year^{-1}$) are clearly higher than the ones corresponding to non-irradiated conditions (Marsh & Taylor, 1988; Smart et al., 2008). On the other hand, the work of Smart et al. (2008) also showed that for similar test involving a lower dose rate fixed at $11Gy.h^{-1}$, the corresponding corrosion rate value (< 1 $\mu m.year^{-1}$) is comparable to the one associated to un-irradiated conditions.

In contrast to the results obtained during tests performed with both ultrapure water and TRNM synthetic pore water, the experiment H1 involving the more alkaline solution (TRNM-MREA water) indicates a clear increase of the corrosion rate when exposed to gamma radiation (0.21 $\mu m.year^{-1}$) compared to pre-irradiation phase (0.02 $\mu m.year^{-1}$). This trend is not frequently observed in studies dealing with anoxic corrosion of metallic sample immersed in alkaline pH solution and exposed to irradiation. The work of Smart et al. (2008) indicated that for test involving carbon steel samples immersed in bentonite equilibrated groundwater at 50°C and exposed at a dose rate of $11Gy.h^{-1}$ for 83 days, corrosion rate values are similar between irradiated and non-irradiated samples. The authors also noticed that for such high pH conditions, a minimum dose rate of 0.3 $kGy.h^{-1}$ is needed to affect the corrosion rate value. In a more recent study, Smart et al. (2017b) measured corrosion rate associated to carbon steel samples immersed in young cement pore water (pH~13.4) with or without irradiation presence (25 $Gy.h^{-1}$) and they observed that on the long term, irradiation presence is not affecting the corrosion rates. These observations are in good agreement with previous studies (Kursten et al., 2011; Smart et al., 2013; Winsley et al., 2011).

In parallel to data obtained thanks to experimental work, simulation exercises have also been performed with Chemsimul® software (Chapter 5). Additionally, to the simulation tests performed to model the H_2 production associated to the radiolysis processes impacting both ultrapure water and TRNM synthetic pore water during irradiation phase, we also tried to model the H_2 production when iron is included in the system. Unfortunately, Chemsimul® software is not able to take into account the presence of solid compounds in the system. Thus, only dissolved iron ions in solution can be considered (reactions involving iron precipitation in solid phase are not considered). Hence, Chemsimul® neither considers hydrogen production associated to carbon steel anoxic corrosion nor potential corrosion rate evolution caused by

oxide film formation. In this context, the results associated to these simulation exercises are not fully representative and cannot be further discussed.

Nevertheless, when introducing dissolved iron species in the liquid phase, we observe a slight decrease of the hydrogen production overtime. This decrease could be attributed to the fast complexation of hydrated electron with Fe-species, as proposed for example by the reaction (R6.21):

$$Fe^{3+} + e_{aq}^{-} \rightarrow Fe^{2+} + H_2O \qquad k = 2 \times 10^{10}\ M^{-1}.s^{-1} \qquad (R6.21)$$

prone to induce a diminution of the H_2 production.

Thus, H_2 production obtained from cells involving only solution (C2, E2, D2, G2) do not really represent the amount of hydrogen generated by radiolysis processes occurring in cells involving metallic samples (C1, E1, D1, G1) by failing to consider such a hydrated electron scavenging mechanism. Finally, we can consider that the corrosion rate values calculated during irradiation phase for experiments C, E, D and G are slightly overestimated.

6.3.3 Post-irradiation phase

This part is dedicated to the corrosion processes occurring during post-irradiation phase in the cells containing carbon steel sample and solution. The hydrogen production arising from these cells when exposed to irradiation comes exclusively from the anoxic corrosion processes (RC6.1) as it has been previously described.

Considering the results associated to the cells involving metallic samples and ultrapure deaerated water (C1 and E1), we observed that as soon as irradiation stops, hydrogen production falls to then rapidly stabilized at values around 2.8×10^{-9} mol.min^{-1} and 3.0×10^{-9} mol.min^{-1}, respectively. These volumes of hydrogen are generated only through anoxic corrosion process, and they allow us to calculate corresponding anoxic corrosion rate, approximately at 1.2 µm.year^{-1} for both experiments. When comparing these results with the ones obtained during the pre-irradiation phase, we do not observe any diminution suggesting that, despite the formation of a thin magnetite protective layer on the surface of the metallic samples, anoxic corrosion process still continues to operate at the same rate than before irradiation. This could be due to a progressive alteration of the magnetite layer caused by radiolytic induced redox modifications of the solution.

For example, the acidification of the solutions contained in cells C1 and E1 (from 6.5 to 5.4 and 6, respectively) can impact the stability of the magnetite. According to Daub (2013), the

solubility of magnetite is equivalent to the summation of the solubility of ferrous (Fe^{2+}) and ferric (Fe^{3+}) ions and the stability of magnetite is maximum in a pH domain ranging from 10 to 11. Thus, such an acidification could promote the solubility of magnetite and inhibit the formation of a more passive and adherent layer to therefore lead to higher corrosion rates.

This acidification of the solution arises because under irradiation, hydrogen ions are produced in larger quantities than hydroxide ions. In the modelling work performed by Lapuerta (2006), to explain the pH decrease that it was observed experimentally (from 6.5 to 4.5), the author used primary radiolytical yields of α-rays (g(H+) = 0.36 and g(OH-) = 0.06) corresponding to a mean LET value associated to a 2 MeV proton. Similarly, Christensen & Bjergbakke (1986) proposed primary radiolytical yield corresponding to a low LET value associated to gamma radiation and the G-values are 2.76 and 0.10 for H^+ and OH^-, respectively. However, simulation results show that the H^+ concentration increase is not sufficient, and the author proposed the contribution of additional ferrous/ferric ions hydrolysis processes to explain the observed pH diminution (Lapuerta, 2006). Iron species hydrolysis processes occurring under irradiation have also been studied by Sutherland et al., (2017) thanks to "short term" tests (300 hours) performed in deaerated solutions with various ferrous iron concentration and under γ-irradiation for a fixed dose rate of 2.8 $kGy.h^{-1}$. The authors indicated that the high pH drop observed after irradiation (from 6 to 3.5) may be attributed to the radiolytic oxidation of ferrous ions leading to the formation of ferric ions (R6.22):

$$Fe^{2+} + {}^{\bullet}OH \rightarrow Fe^{3+} + OH^- \qquad \text{(R6.22)}$$

followed by the hydrolysis equilibrium of ferric ions (R6.23):

$$Fe^{3+} + 3\,OH^- \rightleftarrows Fe(OH)^{2+} + 2\,OH^- \rightleftarrows Fe(OH)_2^- + OH^- \rightleftarrows Fe(OH)_3 \qquad \text{(R6.23)}$$

The ferric ions hydrolysis process consumes a sufficient quantity of hydroxide ions to decrease the pH. Focusing on the final pH value, we observed that our experimental data were higher compared to the one proposed by Sutherland et al., (2017). This difference could exist because our pH measurements have been performed several days after the end of irradiation phase. Once irradiation stops, the concentration of radiolytically produced species (especially radicals) are dramatically decreased. The most stable among them, even after irradiation end, is hydrogen peroxide (H_2O_2). This very reactive species will oxidize ferrous ions available in bulk solution *via* Fenton reaction (R6.24) as it has been proposed by (Holmboe et al., 2012; Lapuerta, 2006):

$$Fe^{2+} + H_2O_2 \rightarrow Fe^{3+} + {}^{\bullet}OH + OH^- \qquad \text{(R6.24)}$$

During post-irradiation phase, this reaction will generate hydroxide ions prone to contribute to the higher pH value observed in our work in comparison with the previously mentioned studies (Lapuerta, 2006; Sutherland et al., 2017).

Nevertheless, it seems that the formation of a significant magnetite layer is inhibited during our experiments involving ultrapure deaerated water. In the work of Daub (2013), it is mentioned that in samples immersed in deaerated solution (pH~6), irradiation led to magnetite formations with more defined shape. Moreover, concerning the growth evolution of magnetite film in similar pH, Sutherland et al., (2017) reported narrow distribution of dendritic magnetite particles when exposed to irradiation. The authors also noticed aggregation and coarsening of magnetite particle caused by the continuous dissolution–precipitation processes induced by continuous irradiation. However, in the work of Yakabuskie et al. (2011) is reported that the final identified corrosion products will be due to radiolytically oxidation of the primary particles and not due to aggregation. Additionally, it is noted that for low ferrous iron concentrations, the magnetite particles grew rapidly, they exhibited a uniform-size particle, and their abundance is low. On the contrary, for high ferrous iron concentrations, irradiation did not induced change in the final size of the particles but increased their quantity.

In parallel, other parameters linked to our experimental setup can potentially impact the stability of the neoformed magnetite layer. If we refer to the work of Brusch & Pearl, (1969), highlighting the almost linear dependence of corrosion rate on the velocity of the tested flowing system, one can imagine that the 5 $mL.min^{-1}$ flow rate used for the gas flow may participate to the constant removal of the corrosion product located at the liquid/solid interface. Moreover, this could explain the linear corrosion rate increase observed in the post-irradiation phase for experiment A, using 30 $ml.min^{-1}$ as helium flow rate, and thus promoting higher dissolution.

In addition, it was pointed out by Platts et al. (1994), that any loss of ferrous ions from the system, e.g., from either adsorption and/or precipitation phenomena, can impair the formation of a thick protective corrosion product layer and lead to a renewed corrosion process. Knowing from previous studies that due to the progressive glass alteration process, the use of glass beaker and glass sample holder may induce ion-exchange mechanisms between silicon and iron ions (Carriere et al., 2020; Ducasse, 2017; Fournier et al., 2014; Gin et al., 2015) additional post-mortem analysis were performed on these glass elements and results showed that iron ions have been entrapped in the glass alteration layer, as observed in previous studies (Aréna et al., 2017; Dillmann et al., 2016). This ion exchange between iron and silicon is further confirmed by our EDS mapping characterization which indicates the presence of silicon on the surface of the metallic coupons. Furthermore, the presence of silicates has been reported that hinder lepidocrocite formation, most probably by blocking its nucleation, when in ratio Si/Fe over of 0.4 (Schwertmann et al., 1984). However, the exact concentration of silicon in the solution containing the metallic samples has not been estimated in order to conclude to safe results. Nevertheless, the decrease of iron ions concentration in the bulk solution could explain the faint presence of corrosion products upon the metallic samples while a significant part of dissolved

iron species released had been captured in the glass matrix, thus inhibiting the formation of a more significant corrosion layer.

From a radiolytic point of view, the densification of the borosilicate glass under gamma radiation has been described in previous studies (Allred, 2003; Birtch & Shelby, 2004; Manaktala, 1992; Primak, 1982) to be a dose rate and boron content dependent process. In parallel, Schatz et al. (1998), pointed out the fact that, during experiments dealing with silica suspensions under irradiation, the absorbed energy by silica nanoparticles crosses the solid/liquid interface and generates hydrated electrons in the aqueous phase as a result of an interfacial charge transfer process. This observation is in good agreement with the work of Nakashima & Tachikawa (1986), where is mentioned the possible mechanism for hydrogen production by energy transfer from silica to the aqueous solution. The authors mention that a part of the initial hole/electron formation from irradiated silica can migrate in solids and reach the surface where they excite physisorbed water, leading to hydrogen formation. Therefore, we should note these parallel mechanisms potentially able to moderately affect hydrogen production arising from our experimental set-up involving irradiated glass.

By considering now the results associated to the cells involving metallic samples and TRNM synthetic pore water (D1 and G1), we observed that as soon as irradiation stops, hydrogen production falls and then is rapidly stabilized at values around 2.8×10^{-9} mol.min^{-1} for both experiments. This volume of hydrogen allows calculating a corresponding anoxic corrosion rate value of approximately at 1.2 μm.year^{-1}. When comparing these results with the ones obtained during the pre-irradiation phase (1.8 and 1.1 for D1 and G1, respectively), we observe that cell D1, exhibited lower corrosion rate value after irradiation while cell G1 indicated a slight increase on the corrosion rate. Apparently, the magnetite layer does not seem to be impacted in the same way between these two identical experiments.

If we consider that pH evolution can be a source of causing such contradictory trends, we observe that for both cells D1 and G1, the pH increased from approximately 8.2 to 9.2. Such results can be compared to the literature data from studies involving carbon steel samples immersed in anoxic groundwater solutions under irradiation. In their work dealing with groundwater medium (pH~7), Cuba et al. (2011) showed that γ-rays (0.22 kGy.h^{-1}) induced one pH unit decrease pH (pH~6). In parallel, the work of Marsh & Taylor (1988) indicated that irradiation (1 kGy.h^{-1}) does not cause any significant pH change from the initial value (pH~9.4). Inversely, the work of Smart et al. (2008) involving granitic solution showed that irradiation (11Gy.h^{-1}) induced a slight increase of the pH (from 8.8 to 9.3). In the same way, Badet (2014) indicated that for carbonated solution (pH=7.2) exposed to total dose lower than 650 kGy, an increase can be observed in the pH varying between 7.5 and 9.

Interaction between carbonated and radiolytic species would induce a carbonated species (CO_3^{2-}) consumption which could lead to a diminution of the alkaline reserve and so to a pH decrease. In addition, as our experimental results previously showed, tests involving TRNM synthetic pore water exhibited large aragonite ($CaCO_3$) precipitation on metallic surface which occurred through the reaction (R6.25):

$$Ca^{2+} + CO_3^{2-} \rightarrow CaCO_3 \qquad \text{(R6.25)}$$

Such reaction would induce an additional consumption of carbonated species (CO_3^{2-}) contributing to further decrease pH value. Finally, the comparison between our experimental pH evolution observation and the theoretical approach given above are not conclusive.

Nevertheless, this pH increase would induce a more thermodynamic stability of magnetite, the initially formed $Fe(OH)_2$ upon the metal will be converted to a mixed Fe^{2+}/Fe^{3+} layer. This fast initial oxidation will result in a uniform oxide layer. Once the uniform layer is established further oxidation may be controlled by mass charge transport, through this uniform layer, decreasing the oxidation rate and thus, the corrosion rate (Diomidis, 2014; Platts et al., 1994). This is in good agreement with the corrosion rate decrease observed for cell D1.

Regarding the results associated to the cells involving metallic samples and TRNM-MREA solution (H1), a technical problem prevented us to monitor hydrogen production during post-irradiation phase. However, if we focus on the results associated to pH evolution, we observe that irradiation did not induce any variation when compared with the initial value (pH~12.3).

These results can be compared with the work of Bouniol (2007) where it is shown that γ-radiation is not expected to induce significant pH evolution (from 13.6 to 13.2) even after 450 days of exposure. In the same way, the work of Winsley et al. (2011) involving high alkaline medium in ambient temperature seems to indicate that irradiation has no impact neither on the corrosion rate nor on the corrosion products. Also, short term experiments of one week performed by Daub (2013) show that γ-rays induced a slight decrease (from 10.6 to 9.9) of the pH solution. This trend is also observed by Smart et al. (2008) for carbon steel samples immersed in granitic solution and exposed to γ-radiation for several months experiments which indicated a slight pH decrease (from 10.4 to 8.9).

In parallel, it is noteworthy that in the work of Daub (2013), performed in solutions with pH in the range 8.4 - 10.6, carbon steel samples under γ-rays show an acceleration of the oxide growth compared to non-irradiated ones. However, it seems that after reaching a threshold, further oxide growth on irradiated samples is suppressed, leading to thinner final corrosion deposits, while non-irradiated samples exhibit slower but almost linear oxide growth over time. This observation can suggest that irradiation inhibit the formation of a thick magnetite layer and

thus, contributes to higher corrosion rates compared to non-irradiated conditions. On the other hand, the author also noted that even after the end of the radiation exposure, corrosion potential did not recover in the pre-irradiation value but remained significantly higher, indicating a possible post-irradiation phenomenon impacting corrosion process. The author also indicate that H_2O_2 is a key radiolytic species that can impact corrosion potential under these conditions and that its chemical addition can simulate corrosion potential under irradiation.

Nevertheless, accordingly to the experimental pH domain prevailing during post-irradiation phase for experiment H, we can consider that the conditions does not favor the destabilization of the magnetite layer formed on the surface of the metallic sample. Consequently, we can assume that the corrosion rate evolution between pre- and post-irradiation phase would tend to a slight decrease.

Finally, corrosion rate trends observed between pre-irradiation and post-irradiation phases for all of our experiments, themselves associated to magnetite precipitation/dissolution trend, can be compared to the final dissolved iron species concentration measured in solution. As it has been previously discussed, corrosion products stability is enhanced with increased alkalinity. This is in good agreement with our total dissolved iron species measurements which showed that the higher amounts of iron (0.2-0.3 $mmol.L^{-1}$) where observed for experiments involving ultrapure water, corresponding to the more acid solutions. In parallel, results associated to both TRNM synthetic pore water (0.1 $mmol.L^{-1}$) and TRNM-MREA solution (0.9 $\mu mol.L^{-1}$) confirmed that even under irradiation, increasing alkalinity promotes the stability of the magnetite and thus the formation of a thicker and protective film.

6.4 Corrosion rate measurement methods

The comparison between the corrosion rate derived through hydrogen production monitoring and the ones obtained thanks to weight loss measurements showed that the latter method induced systematically higher values. If weight loss measurement results associated to ultrapure water (1.7 - 4.8 $\mu m.year^{-1}$) are in the same order of magnitude as the ones obtained during previous study using the same conditions and technique (Badet, 2014), the values corresponding to the cells testing TRNM synthetic pore water exhibited especially high values (28.0 – 43.6 $\mu m.year^{-1}$). Nevertheless, in all experiments is confirmed the fact that corrosion rates exported from weight loss measurements are higher than the ones derived from the hydrogen gas generation measurements. Such discrepancy has been mentioned before (Diomidis, 2014; Kaneko et al., 2004; King, 2008) and it could result from the fact that H_2 gas

generation provides instantaneous corrosion rate values, while the weight loss measurements give a general average corrosion rate. Since weight loss measurement seems to lead to overestimated corrosion rate values, hydrogen gas generation measurement appears to be more representative as it provides more accurate results (Diomidis, 2014).

Finally, the property of H_2 to be able to get dissolved into metals and modify their properties, known as hydrogen embrittlement, is not taken into account, and was not in the scope of this study to further investigate it.

Conclusion and Perspectives

As part of the scientific studies implemented to contribute to the long-term safety assessment of the French HL-ILW waste deep geological disposal program, the present thesis work was dedicated to study the impact of gamma radiation on carbon steel anoxic corrosion process and the resultant hydrogen gas production. Since such geological disposal principle relies on a multi-barrier system concept, large amount of metallic elements are planned to be used either to reinforce the installation structure or to manufacture the waste containers. In the specific case of HL waste disposal gallery, stainless steel primary container would be encapsulated into cylindrical carbon steel overpack and inserted in a carbon steel casing tube within horizontal micro-tunnel drilled in the clay rock. Throughout the duration of the operational phase of the project and long after the closure of the disposal facility, several corrosion processes are expected to impact these metallic elements in a series of distinct environments which will gradually impair the carbon steel component and finally induce their breakage. Over the long term, carbon steel anoxic corrosion process will progressively attack the metallic elements and produce hydrogen gas whose accumulation may significantly affect mid- and long-term safety of the disposal facility. In parallel, one can note that all these corrosion processes will take place on carbon steel component exposed to ionizing radiation originating from nuclear waste. Ionizing radiation will lead to the radiolysis of the natural percolated pore water which will result to the formation of radiolytic species prone to modify the physico-chemical conditions at the metal-water interface, and thus to impact the corrosion processes and the associated corrosion rate. Furthermore, these neoformed radiolytic species include H_2, meaning that pore water radiolysis process will also lead to an additional production of this problematic gas.

In addition to the previous studies dedicated to investigating steel corrosion under irradiation process and its associated hydrogen gas production, the present work aimed to develop an experimental setup allowing to distinguish between the H_2 production related to water radiolysis and the one related to anoxic corrosion, making possible the estimation of associated corrosion rate. By continuous measuring of hydrogen gas production that corresponds to three important stages (pre-irradiation, irradiation and post-irradiation phases), our objective was to provide new insights regarding some conflicting issues as: (i) Can irradiation induce an increase of the corrosion rate? (ii) Can irradiation impact mid- and long-term corrosion product layer properties evolution? (iii) The initial chemical properties of the solution (pH, dissolved species) could modify steel anoxic corrosion process under irradiation?

In this way, several experiments involving carbon steel samples immersed in various deaerated solution (ultrapure water, argillaceous rock synthetic pore water and low alkaline cement grout solution) were performed to measure the evolution of the corrosion rate values measured before,

during and after irradiation. The obtained experimental results, associated to the corresponding liquid and solid samples *post mortem* characterisations, allow to draw the following interesting trends:

- From a radiolytical point of view, we observed that both the presence of solute and/or higher pH conditions induce a decrease of hydrogen production. Such phenomenon may be attributed either to the solutes scavenging capacity for hydrated electron (which is considered as the main precursor of molecular hydrogen) or to the formation of reactive species able to react with radiolytic product which can finally lead to a diminution of the H_2 radiolytic yield. The role of the $O^{\bullet -}$ radical product, present in high concentration for alkaline solution submitted to irradiation and prone to consume H_2, is also proposed.
- Regarding anoxic corrosion processes, we first observed that as expected the initial chemical composition of the solution (especially pH value) impacts directly the corrosion rate values measured on carbon steel samples before their exposure to gamma radiation. The more alkaline a solution, the more is favored passivation of the metallic surface and thus, it is associated to low corrosion rate.
- Considering anoxic corrosion under irradiation processes, the obtained results from both ultrapure water and argillaceous rock synthetic pore water, tend to indicate that ionizing radiation does not induce any increase of the corrosion rate values.
- The comparison between corrosion rate values obtained before and after irradiation (pre-irradiation and post irradiation phase, respectively) suggests that despite the formation of a thin magnetite protective layer observed on the surface of the metallic samples, anoxic corrosion process still continues to operate at the same rate than before irradiation. This phenomenon may be attributed to a progressive alteration of the magnetite layer caused by radiolytic induced redox modifications of the system, such as the acidification of the solution or the formation of oxidizing water radiolysis products prone to cause structural modification of the oxide film.
- The comparison between experimental data and simulated values allows to conclude that, despite the difficulties encountered in modelling a semi-open system and/or the presence of solid iron phase, simulation can help to predict the concentration evolution associated to key radiolytic species prone to impact anoxic corrosion under irradiation processes.

Having these first conclusions in mind, it appears that additional well-devised experiments are still required to ensure a better understanding of the anoxic corrosion processes taking place under irradiation:

- First of all, experiments performed over longer time period for the three studied phase (before, during and after irradiation) would permit to a verification of whether radiolytic induced redox modifications of the system really inhibit the long-term formation of a thick magnetite protective layer on the metallic surface.
- Higher dose rate would determine if ionizing radiation can have direct impact on corrosion product structural composition and lower dose rate should allow to get closer to the expected conditions prevailing in HL waste disposal gallery.
- The impact of higher temperature on the above-mentioned processes should also be studied to investigate the corrosion product growth and properties evolution when exposed to such conditions.
- Finally, it could be really interesting to adapt our experimental setup to allow an in situ electrochemical monitoring of the metallic sample corrosion potential measured before, during and after irradiation in order to investigate possible long-term changes on the corrosion product layer properties induced by radiolytic oxidizing species.

In conclusion, all the experimental observations along with the ones that are associated to the modelling exercises gained during this thesis in combination with the additional tests proposed in perspectives, could help us to enlarge the general knowledge associated to anoxic corrosion process under irradiation. Therefore, this could contribute to the long-term safety assessment of a deep geological disposal facility.

References

Ahn, T. M., & Soo, P. (1995). Corrosion of low carbon steel in concentrated synthetic groundwater at 80 to 150°C. Waste Management, 15(7), 471–476.

Allen, A. O., Hochanadel, C. J., Ghormley, J. A., & Davis, T. W. (1952). Decomposition of water and aqueous solutions under mixed fast neutron and gamma radiation. Journal of Physical Chemistry, 56(5), 575–586.

Allen, A. O. (1961). The radiation chemistry of water and aqueous solutions. D. Van Nostrand Company, Inc.

Allred, C. (2003). Effect of radiation on silicon and borosilicate glass. Thesis, MIT.

Andra. (2005a). Dossier 2005, Argile : Évaluation de la Faisabilité du Stockage Géologique en Formation Argileuse.

Andra. (2005b). Dossier 2005, Référentiel des matériaux d'un stockage de déchets à haute activite et à vie longue, Tome 3, Corrosion des matériaux métalliques, Rap. C.RP.ASCM.04.0015.

Andra. (2005c). Referentiel de comportement des colis des déchet de haute activité à vie long.

Andra. (2005d). Dossier 2005, Référentiel du site Meuse / Haute-Marne, Présentation Générale. Rap. C.RP.ADS.04.0022.

Andra. (2005e). Dossier 2005, Argile : Tome Évolution phénoménologique du stockage géologique.

Andra. (2013). Les déchets pris en compte dans les études de conception de Cigéo, Andra, 2013.

Andra. (2020a). Dossier d'enquête publique préalable à la déclaration d'utilité publique du centre de stockage Cigéo-Pièce 1-Notice explicative, Rap. CG-TE-D-NSY-AMOA-TR0-0000-19-0004/A.

Andra. (2020b). https://www.andra.fr/.

Arena, H., Godon, N., Rebiscoul, D., Frugier, P., Podor, R., Garces, E., Cabie, M., Mestre, J. P. (2017). Impact of iron and magnesium on glass alteration: Characterization of the secondary phases and determination of their solubility constants. Appl. Geochemistry, vol. 82, pp. 119–133, 2017.

Auclair, G. (2001). Détermination des rendements radiolytiques primaires alpha en milieu alcalin. Thesis, Université Pierre et Marie Curie.

Badet, H. (2014). Effet de la radiolyse sur les systèmes de corrosion anoxiques à très long terme des alliages ferreux. Thesis, Université Pierre et Marie Curie.

Bataillon, C., Musy, C., & Roy, M. (2001). Corrosion des surconteneurs de déchets, cas d'un surconteneur en acier faiblement allié. J. Phys IV France, 11, 267–274.

Beaucaire, C., Michelot, J. L., Savoye, S., & Cabrera, J. (2008). Groundwater characterisation and modelling of water-rock interaction in an argillaceous formation (Tournemire, France). *Applied Geochemistry*, *23*(8), 2182–2197.

Bennett, D. G., & Gens, R. (2008). Overview of European concepts for high-level waste and spent fuel disposal with special reference waste container corrosion. Journal of Nuclear Materials, 379(1–3), 1–8.

Birtch, E., Shelby, J. (2004). Annealing of hydrogen-impregnated and irradiated vitreous silica. J. Non. Cryst. Solids, vol. 349, no. 1–3, pp. 156–161.

Bjergbakke, E., Sehested, K., Lang Rasmussen, O., & Christensen, H. (1984). Input files for computer simulation of water radiolysis. Danmarks Tekniske Universitet, RISO-M-243, 23.

Bjergbakke, E., Draganic, Z. D., Sehested, K., & Dracanic, I. G. (1989). Radiolytic Products in Waters Part I: Computer Simulation of Some Radiolytic Processes in the Laboratory. Radiochimica Acta, 48(1–2), 65–72.

Bouniol, P. (2004). Etat de connaisances sur la radiolyse de l'eau dans le colis de déchets cimentés et son approche par simulation. RAPPORT CEA-R-6069, CEA.

Bouniol, P. (2007). ERMITE - Experience de Radiolyse en Mini -conducteurs Irradies sur un Temps Etendu). Report Ref. RT DPC/SCCME 07-747-A, CEA.

Bouniol, P. (2010). The influence of iron on water radiolysis in cement-based materials. Journal of Nuclear Materials, 403(1–3), 167–183.

Brusch, E., & Pearl, W. (1969). Corrosion and Corrosion Product Release Behavior of Carbon Steel. Proceedings of the American Power Conference, 31, 699–705.

Buxton, G. V., & Dainton, F. S. (1965). Radical and molecular yields in the γ-radiolysis of water. 287.

Buxton, G. V., Greenstock, C. ., Helman, W. P., & Ross, A. B. (1988). Critical Review of Rate Constants for Reactions of Hydrated Electrons, Hydrogen Atoms and Hydroxyl Radicals (.OH/.O−) in Aqueous Solution. Journal of Physical and Chemical Reference Data.

Callister, W. (2000). Materials Science and Engineering, An Introduction. John Wiley & Sons Inc.

Carriere, C., Neff, D., Martin, C., Tocino, F., Delanoë, A., Gin, S., Michau, N., Linard, Y., Dillmann, P. (2020). AVM nuclear glass / steel / claystone system altered by Callovo – Oxfordian poral water with and without cement – bentonite grout at 70 ° C. Materials and Corrosion, 72, 474–482.

Chautard, C. (2013). Interactions fer / argile en conditions de stockage géologique profond : Impact d ' activités bactériennes et d ' hétérogénéités. Thesis, Université Mines ParisTech.

Cheek, B. C. H., & Linnenbom, V. J. (1963). The radiation chemistry of alkaline hypobromite solutions. Phys. Chem., 67(4).

Christensen, H. & Bjergbakke, E. (1986). Application of chemsimul for groundwater radiolysis. Nucl. Chem. Waste Manag., vol. 6, no. 3–4, pp. 265–270.

Christensen, H., Sehested, K., & Logager, T. (1994). Temperature dependence of the rate constant for reactions of hydrated electrons with H, OH and H2O2. Rad. Phys. Chem., 43(6), 527–531.

Cornell, R. M., & Schwertmann, U. (2003). The Iron Oxides: Structure, Properties, Reactions, Occurrences and Uses.Wiley-VCA.

Crumiere, F. (2012). Études de l'effet de TEL lors de la radiolyse de l'eau : rendements radiolytiques de l'hydrogène moléculaire.Thesis,Université de Nantes.

Crusset, D., Deydier, V., Necib, S., Gras, J. M., Féron, D., Burger, E., & Necib, S. (2017). Corrosion of carbon steel components in the French high-level waste

programme : evolution of disposal concept and selection of materials. Corrosion Engineering, Science and Technology, 2782, 17–24.

Cuba, V., Silber, R., Mucka, V., Pospisil, M., Neufuss, S., Barta, J., & Vokal, A. (2011). Radiolytic formation of ferrous and ferric ions in carbon steel - deaerated water system. Radiation Physics and Chemistry, 80(3), 440–445.

Daub, K., Zhang, X., Noël, J. J., Wren J.C. (2010). Effects of γ-radiation versus H2O2 on carbon steel corrosion. Electrochim. Acta, vol. 55, no. 8, pp. 2767–2776.

Daub, K. (2013). A Study of Gamma Radiation Induced Carbon Steel Corrosion. Thesis, University of Western Ontario.

Dillmann, P., Mazaudier, F., & Hœrlé, S. (2004). Advances in understanding atmospheric corrosion of iron. I. Rust characterisation of ancient ferrous artefacts exposed to indoor atmospheric corrosion. Corrosion Science, 46(6), 1401–1429.

Dillmann, P., Gin, S., Neff, D., Gentaz, L., Rebiscoul, D. (2016). Effect of natural and synthetic iron corrosion products on silicate glass alteration processes. Geochim. Cosmochim. Acta, vol. 172, pp. 287–305.

Diomidis, N. (2014). Scientific basis for the production of gas due to corrosion in a deep geological repository. Report, Nagra.

Draganic, Z. D., & Draganic, I. G. (1971). Studies on the formation of primary yields of hydrogen peroxide and molecular hydrogen (GH2O2 and GH2) in the γ radiolysis of neutral aqueous solutions. Journal of Physical Chemistry, 75(26), 3950–3957.

Ducasse, T., (2017). Apport des verres basaltiques à la validation du modèle GRAAL sur le très long terme. Thesis, Univerité de Montpellier.

Elliot, A. J. (1994). Rate Constants and G-Values for the Simulation of the Radiolysis of Light Water over the Range 0-300°C, AECL Research.

Egerton R.F. (2005). Physical principles of electron microscopy. Springer.

Eriksen, T. & Jacobsson, A. (1983). Radiation effects on the chemical environment in a radioactive waste repository. Report 83-27, SKB.

Eriksen, T. E., Ndalamba, P., Christensen, H., & Bjergbakke, E. (1989). Radiolysis of ground water: Influence of carbonate and chloride on hydrogen peroxide production. Journal of Radioanalytical and Nuclear Chemistry Articles, 132(1), 19–35.

Ershov, B. G., Milaev, A. I., Petrosyan, V. G., Kartashov, N. I., Glasunov, P. Y., & Tevlin, S. A. (1985). The effect of radiation on corrosion of steel in high-temperature water. Radiat. Phys. Chem., 26, 587–590.

Ferradini, C., & Jay-Gerin, J. P. (2000). The effect of pH on water radiolysis : A still open question-A mini review. Res.Chem.Intermed, 26, 549–565.

Feron, D., Crusset, D., Gras, J. M. (2008). Corrosion issues in nuclear waste disposal. Journal of Nuclear Materials, 379(1–3), 16–23.

Feron, D. (2012). Nuclear corrosion science and engineering. Woodhead Publishing Series in Energy.

Feron, D., & Crusset, D. (2014). Microbial induced corrosion in French concept of nuclear waste underground disposal. Corrosion Engineering, Science and Technology, 540-547.

Fournier, M., Gin, S., Frugier, P. (2014). Resumption of nuclear glass alteration: State of the art. J. Nucl. Mater., vol. 448, no. 1–3, pp. 348–363.

Fujita, N., Matsuura, C., & Saigo, K. (2000). Irradiation-enhanced corrosion of carbon steel in high temperature water - In view of a cell formation induced by γ-rays. Radiation Physics and Chemistry, 58(2), 139–147.

Fujita, N., Matsuura, C., & Saigo, K. (2001). Radiation-induced preferential dissolution of specific planes of carbon steel in high-temperature water. Radiation Physics and Chemistry, 60(1–2), 53–60.

Genin, J., Ruby, C., Gehin, A., & Refait, P. (2006). Synthesis of green rusts by oxidation of Fe(OH)2, their products of oxidation and reduction of ferric oxyhydroxides; Eh-pH Pourbaix diagrams. Comptes Rendus - Geoscience, 338(6–7), 433–446.

Getoff, N. (1999). Radiation-induced degradation of water pollutants-State of the art. Radiat. Phys. Chem., 47(4), 581–593.

Gin, S., Jollivet, P., Fournier, M., Angeli, F., Frugier, P., & Charpentier, T. (2015). Origin and consequences of silicate glass passivation by surface layers. Nat Commun 6**,** 6360.

Girao, A., Caputo, G., & Ferro, M. C. (2017). Application of Scanning Electron Microscopy–Energy Dispersive X-Ray Spectroscopy (SEM-EDS). Comprehensive Analytical Chemistry, 75(June), 153–168.

Grousset, S. (2016). Détermination de la composition isotopique du soufre pour l'étude de l'origine, biotique ou abiotique, des sulfures de fer en corrosion anoxique. Thesis, Université Pierre et Marie Curie.

Gutjahr, A., Dabringhaus, H., & Lacmann, R. (1996). Studies of the growth and dissolution kinetics of the CaCo3 polymorphs calcite and aragonite II. The influence of divalent cation additives on the growth and dissolution rates. Journal of Crystal Growth, 158(3), 310–315.

Hatano, Y., Katsumura, Y., & Mozumder, A. (2010). Charged Particle and Photon Interactions with Matter. CRC Press.

Hayon, E. (1965). Radical and Molecular Yields in the Radiolysis of Alkaline Aqueous Solutions. Trans. Faraday Soc., 61.

Holmboe, M., Jonsson, M., & Wold, S. (2012). Influence of γ-radiation on the reactivity of montmorillonite towards H2O2. Radiation Physics and Chemistry, 81(2), 190–194.

Iwamatsu, K., Sundin, S., & LaVerne, J. A. (2018). Hydrogen peroxide kinetics in water radiolysis. Radiation Physics and Chemistry, 145(August 2017), 207–212.

Jelinek, J., & Neufeld, P. (1982). Kinetics of Hydrogen Formation From Mild Steel in Water Under Anaerobic Conditions. Corrosion, 38(2), 98–104.

Jonsson, M. (2012). Radiation Effects on Materials Used in Geological Repositories for Spent Nuclear Fuel. ISRN Materials Science, 1–13.

Joseph, J. M., Choi, B. S., Yakabuskie, P., & Wren, J. C. (2008). A combined experimental and model analysis on the effect of pH and O 2(aq) on γ-radiolytically produced H2 and H2O2. Radiation Physics and Chemistry, 77(9), 1009–1020.

Kaneko, M., Miura, N., Fujiwara, A., & Yamamoto, M. (2004). Evaluation of Gas

Generation Rate by Metal Corrosion in the Reducing Environment. Engineering Report-Radioactive Waste Management Funding and Research Center(RWMC), RWMC-TRE-03003, 145.

King, F. (2008). Corrosion of carbon steel under anaerobic conditions in a repository for SF and HLW in Opalinus Clay. Report, Nagra.

Kirkegaard, Peter; Bjergbakke, Erling; Olsen, Jens V. (2008). CHEMSIMUL: A chemical kinetics software package. Danmarks Tekniske Universitet, Risø Nationallaboratoriet for Bæredygtig Energi. Denmark. Forskningscenter Risoe. Risoe-R No. 1630

Kreiss, P. (1991). Hydrogen evolution from corrosion of iron and steel in low/intermediate level waste repositories. Tecnical Report, Nagra.

Kursten, B., Druyts, F., Macdonald, D. D., Smart, N. R., Gens, R., Wang, L., Weetjens, E., & Govaerts, J. (2011). Review of corrosion studies of metallic barrier in geological disposal conditions with respect to Belgian Supercontainer concept. Corrosion Engineering Science and Technology, 46(2), 91–97.

Kursten, B., Macdonald, D. D., Smart, N. R., & Gaggiano, R. (2017). Corrosion issues of carbon steel radioactive waste packages exposed to cementitious materials with respect to the Belgian supercontainer concept. Corrosion Engineering Science and Technology, 52, 11–16.

Landolt, D. (2007). Corrosion and Surface Chemistry of Metals. EPFL Press.

Lapuerta, S. (2006). Etude de la corrosion du fer à l ' interface de différents milieux (eau , air) soumis à l ' irradiation de protons. Thesis, Université Claude Bernard - Lyon I.

Le Caër, S. (2011). Water radiolysis: Influence of oxide surfaces on H2 production under ionizing radiation. Water, 3(1), 235–253.

Linnenbom, V. J. (1958). The Reaction between Iron and Water in the Absence of Oxygen. Journal of the Electrochemical Society, 8, 322–324.

Manaktala, H. (1992). An assessment of borosilicate glass as a High-Level waste form. Cent. Nucl. Waste Regul. Anal. San Antonio, Texas.

Marsh, G. P., & Taylor, K. J. (1988). An assessment of carbon steel containers for radioactive waste disposal. Corrosion Science, 28(3), 289–320.

Matheson, M. S., & Rabani, J. (1963). Pulse Radiolysis of Aqueous Hydrogen Solutions. I. Rate Constants for Reaction of e with Itself and Other Transients. II. The Interconvertibility of e and H. 323(2), 1324–1335.

Meyer, H. J. (1984). The influence of impurities on the growth rate of calcite. Journal of Crystal Growth, 66(3), 639–646.

Michelin, A., Drouet, E., Foy, E., Dynes, J. J., Neff, D., & Dillmann, P. (2013). Investigation at the nanometre scale on the corrosion mechanisms of archaeological ferrous artefacts by STXM. Journal of Analytical Atomic Spectrometry, 28(1), 59–66.

Misawa, T., Hashimoto, K., & Shimodaira, S. (1974). The mechanism of formation of iron oxide and oxyhydroxides in aqueous solutions at room temperature. Corrosion Science, 14(2), 131–149.

Mohamed-Said, M., Vuillemin, B., Oltra, R., Marion, A., Trenty, L., & Crusset, D. (2017). Predictive modelling of the corrosion rate of carbon steel focusing on the

effect of the precipitation of corrosion products. Corrosion Engineering Science and Technology, 52, 178–185.

Monnier, J., Neff, D., Réguer, S., Dillmann, P., Bellot-Gurlet, L., Leroy, E., Foy, E., Legrand, L., & Guillot, I. (2010). A corrosion study of the ferrous medieval reinforcement of the Amiens cathedral. Phase characterisation and localisation by various microprobes techniques. Corrosion Science, 52(3), 695–710.

Nakashima, M. & Tachikawa, E. (1986). Self-radiolysis of Tritiated Water Adsorbed on Silica Gel. Appl. Radiat. Isot., vol. 37, no. 6, pp. 527–530.

Necib, S., Linard, Y., Crusset, D., Schlegel, M., Daumas, S., & Michau, N. (2017). Corrosion processes of C-steel in long-term repository conditions. Corrosion Engineering Science and Technology, 52, 127–130.

Neufuss, S., Cuba, V., Silber, R., Muska, V., Pospisil, M., & Vokal, A. (2006). Experimental simulation of possible radiation-corrosive processes in container with spent nuclear fuel after groundwater ingress. Czechoslovak Journal of Physics, 56, 365–372.

NIST database (2002). https://kinetics.nist.gov/solution/

NIST database (2013). https://kinetics.nist.gov/kinetics/index.jsp

Novakova, A. A., Gendler, T. S., Manyurova, N. D., & Turishcheva, R. A. (1997). A Mossbauer spectroscopy study of the corrosion products formed at an iron surface in soil. Corrosion Science, 39(9), 1585–1594.

Pastina, B. & LaVerne J. A. (2001). Effect of molecular hydrogen on hydrogen peroxide in water radiolysis. J. Phys. Chem. A, 105, 9316–9322.

Pastina, B., Laverne, J., & Pimblott, S. M. (1999). Dependence of Molecular Hydrogen Formation in Water on Scavengers of the Precursor to the Hydrated Electron. Journal of Physical Chemistry A, 103(29).

Peled, E., & Czapski, G. (1970). Studies on the molecular hydrogen formation (GH2) in the radiation chemistry of aqueous solutions. Journal of Physical Chemistry, 74(15), 2903–2911.

Platts, N., Blackwood, D. J., Naish, C. C., Fuel, S. N., & Co, W. M. (1994). Anaerobic oxidation of carbon steel in granitic groundwaters: A review of the relevant literature. Report 94-01,SKB

Pourbaix, M. (1974). Atlas of electrochemical equilibria in aqueous solutions. National Association of Corrosion Engineers.

Primak, W. (1982). Effects of ionization on silicate glasses. Nucl. Waste Manag. Mater. (UC-25), Argonne, Illinois.

Raiman, S. S., Bartels, D. M., & Was, G. S. (2017). Radiolysis driven changes to oxide stability during irradiation-corrosion of 316L stainless steel in high temperature water. Journal of Nuclear Materials, 493, 40–52.

Saheb, M., Descostes, M., Neff, D., Matthiesen, H., Michelin, A., & Dillmann, P. (2010). Iron corrosion in an anoxic soil: Comparison between thermodynamic modelling and ferrous archaeological artefacts characterised along with the local in situ geochemical conditions. Applied Geochemistry, 25(12), 1937–1948.

Saheb, M., Neff, D., Dillmann, P., Matthiesen, H., & Foy, E. (2008). Long-term corrosion behaviour of low-carbon steel in anoxic environment: Characterisation of archaeological artefacts. Journal of Nuclear Materials, 379(1–3), 118–123.

Santos, R. M., Ceulemans, P., & Van Gerven, T. (2012). Synthesis of pure aragonite by sonochemical mineral carbonation. Chemical Engineering Research and Design, 90(6), 715–725.

Schatz, T., Cook, A., Meisel, D. (1998). Charge carrier transfer across the silica nanoparticle/water interface. J. Phys. Chem. B, vol. 102, no. 37, pp. 7225–7230.

Schenk, R. 1988. Untersuchungen über die Wasserstoffbildung durch Eisenkorrosion unter Endlagerbedingungen. National Cooperative for the Storage of Radioactive Waste, Technical Report, Nagra.

Schlegel, M. L., Martin, F., Fenart, M., Blanc, C., Varlet, J., & Foy, E. (2021). Corrosion of carbon steel in clay compact environments at 90 °C: Effect of confined conditions. Corrosion Science, 184.

Schlegel, M., Necib, S., Daumas, S., Blanc, C., Foy, E., Trcera, N., & Romaine, A. (2016). Microstructural characterization of carbon steel corrosion in clay borehole water under anoxic and transient acidic conditions. Corrosion Science, 109, 126–144.

Schwarz, H .A., (1955), The effect of solutes on the molecular yield s in the radiolysis of aqueous solutions . J. Am. Chem. Soc. 77,4960-4964

Schwarz, H. A. (1969). Applications of the spur diffusion model to the radiation chemistry of aqueous solutions. Journal of Physical Chemistry, 73(6), 1928–1937.

Schwertmann, U., Carlson, L., Fechter, H. (1984). Iron oxide formation in artificial ground waters. Schweiz. Z. Hydrol 46/2.

Senior, Nick, Newman, R., Wang, S., & Diomidis, N. (2017). Understanding and quantifying the anoxic corrosion of carbon steel in a Swiss L/ILW repository environment. Corrosion Engineering Science and Technology, 52, 78–83.

Senior, Nicholas, Martino, T., & Diomidis, N. (2020). The anoxic corrosion behaviour of carbon steel in anoxic alkaline environments simulating a Swiss L/ILW repository environment. Materials and Corrosion, 72(1–2), 131–140.

Smailos, E., Schwarzkopf, W., Koster, R., Fiehn, B., & Halm, B. (1990). Corrosion Testing of Selected Packaging Materials for Disposal of High-Level Waste Glass in Rock Salt·Formations. Kernforschungszentrum Karlsruhe, KFK 4723.

Smart, N., Blackwood, D., & Werme, L. (2001). The anaerobic corrosion of carbon steel and cast iron in artificial groundwaters. Report, SKB.

Smart, N., Rance, A., & Werme, L. (2004). Anaerobic Corrosion of Steel in Bentonite. Mat. Res. Soc. Symp. Proc. Vol. 807 ©, 1–5.

Smart, N., & Rance, A. (2005). Effect of radiation on anaerobic corrosion of iron. Technical Report 05-05, SKB.

Smart, N. R., Rance, A. P., & Werme, L. O. (2008). The effect of radiation on the anaerobic corrosion of steel. Journal of Nuclear Materials, 379(1–3), 97–104.

Smart, N. R., Rance, A. P., Fennell, P. A. H., & Kursten, B. (2013). The anaerobic corrosion of carbon steel in alkaline media - Phase 2 results. EPJ Web of Conferences, 56.

Smart, N. R., Rance, A. P., Fennell, P. A. H., & Kursten, B. (2014). Effect of sulphur species on anaerobic corrosion of carbon steel in alkaline media. Corrosion Engineering Science and Technology, 49(6), 473–479.

Smart, N. R., Reddy, B., Rance, A. P., Nixon, D. J., & Diomidis, N. (2017a). The anaerobic corrosion of carbon steel in saturated compacted bentonite in the Swiss repository concept. Corrosion Engineering Science and Technology, 52, 113–126.

Smart, N. R., Rance, A. P., Nixon, D. J., Fennell, P. A. H., Reddy, B., & Kursten, B. (2017b). Summary of studies on the anaerobic corrosion of carbon steel in alkaline media in support of the Belgian supercontainer concept. Corrosion Engineering Science and Technology, 52, 217–226.

Smart, N., Rance, A., & Werme, L. (2004). Anaerobic Corrosion of Steel in Bentonite. Mat. Res. Soc. Symp. Proc. Vol. 807 ©, 1–5.

Smith, E., & Dent, G. (2005). Modern Raman spectroscopy—a practical approach. John Wiley and Sons Ltd.

Sutherland, T. I., Sparks, C. J., Joseph, J. M., Wang, Z., Whitaker, G., Sham T. K., & Wren, J.C. (2017) Effect of ferrous ion concentration on the kinetics of radiation-induced iron-oxide nanoparticle formation and growth. Phys. Chem. Chem. Phys., 2017,19, 695-708

Tabata, Y., Ito, Y., & Tagawa, S. (1991). CRC handbook of radiation chemistry. Boca Raton: CRC Press.

Taniguchi, N., Kawasaki, M., Kawakami, S., & Kubota, M. (2004). Corrosion behaviour of carbon steel in contact with bentonite under anaerobic condition. In Prediction of Long Term Corrosion in Nuclear Waste Systems. 2nd Int. Workshop, Nice, September 2004 (European Federation of Corrosion and Andra), 24–34.

Towne, V., Mark, W., Oswald, B., Zhao, Q. (2004). Complexities in horseradish peroxidase-catalyzed oxidation of dihydroxyphenoxazine derivatives: appropriate ranges for pH values and hydrogen peroxide concentrations in quantitative analysis. Analytical Biochemistry, 334, 290–296.

Traboulsi, A. (2015). Hydrogen production under gamma radiation.Report, IRSN

Trupin, V., Frongillo, Y., Baldacchino, G., Le Parc, D., & Hickel, G. (1999). Détermination de constantes de vitesse de réactions de recombinaison de radicaux. J. Chim. Phys., 96, 30–34.

Trupin-Wasselin, V. (2000). Processus primaires en chimie sous rayonnement. Influence du Transfert d'Energie Linéique sur la radiolyse de l'eau. Thesis, Universite de Paris-Sud.

Vandenborre, J., Crumière, F., Blain, G., Essehli, R., Humbert, B., & Fattahi, M. (2013). Alpha localized radiolysis and corrosion mechanisms at the iron/water interface: Role of molecular species. Journal of Nuclear Materials, 433(1–3), 124–131.

Verron, H. (2020). Etude expérimentale des interactions matériau cimento-bentonitique / argilite / fer et acier (MREA/COx/Fe ou acier) à 90°C en conditions de stockage géologique profond des déchets radioactifs (CIGEO).Thesis, Université de Lorraine.

Wada, N., Yamashita, K., & Umegaki, T. (1995). Effects of divalent cations upon nucleation, growth and transformation of calcium carbonate polymorphs under conditions of double diffusion. Journal of Crystal Growth, 148(3), 297–304.

Wang, S., & Xin, H. (1999). The γ-irradiation-induced chemical change from β-FeOOH to Fe3O4. Radiation Physics and Chemistry, 56(5–6), 567–572.

Wasselin-Trupin, V., Baldacchino, G., Bouffard, S., & Hickel, B. (2002). Hydrogen peroxide yields in water radiolysis by high-energy ion beams at constant LET. Radiation Physics and Chemistry, 65(1), 53–61.

Winsley, R. J., Smart, N. R., Rance, A. P., Fennell, P. A. H., Reddy, B., & Kursten, B. (2011). Further studies on the effect of irradiation on the corrosion of carbon steel in alkaline media. Corrosion Engineering Science and Technology, 46(2), 111–116.

Woods, R. J., & Pikaev, A. K. (1993). Applied Radiation Chemistry: Radiation Processing.

Wren, J. C. (2005). Radioiodine Chemistry : The Unfinished Story. European Review Meeting on Severe Accident Research, France (ERMSAR-2005).

Yakabuskie, P. A., Joseph, J. M., Keech P., Botton, G. A, D.Guzonas, D.,& Wren, J. C. (2011). Iron oxyhydroxide colloid formation by gamma-radiolysis. Phys. Chem. Chem. Phys., 13, 7167–7175.

Zhu, T., Wang, L., Sun, W., Wang, M., Yang, Z., Ji, T., Wang, S., Wang, Y., Xia, L., & Liu, G. (2018). Origin of Aragonite Scale Deposition on Carbon Steel at Ambient Circumstances. Industrial and Engineering Chemistry Research, 57(1), 401–413.

Annexes

Annex A

The Ghormley method

Hydrogen peroxide is a primary product of radiolysis and it is formed directly by the decomposition of water.

The indirect measurement of H_2O_2 is based on the reaction with iodide ions in aqueous solution according to the mechanism:

$2I^- + H2O2 + 2H^+ \rightarrow I_2 + 2H_2O$

$I_2 + I^- \rightarrow I_3^-$

The absorbance of I_3^- is measured at λ = 348 nm. Its extinction coefficient molar at this wavelength is 25800 $M^{-1}cm^{-1}$. We can then easily go back to the concentration of hydrogen peroxide in solution. The reaction is catalyzed by the ion molybdate in a buffered medium (pH = 6) with potassium acid phthalate. The absorbance is measured relative in cuvettes containing a mixture solution of two reagents and the irradiated sample.

The two reagents are mixed in equal quantities:

Reagent A (250 ml)

1) Potassium iodide (KI) : 16.5 g
2) Potassium hydroxide (KOH) : 0.5 g
3) Ammonium molybdate tetrahydrate ($(NH_4)_6Mo_7O_{24} \cdot 4H_2O$) : 0.05 g

Reagent B

1) Potassium phthalate ($C_8H_4K_2O_4$) : 3 g
2) Phthalic acid ($C_8H_6O_4$): 2 g

Annex B

Group 1

Re1:OH+OH=H2O2	A=5.5D9
Re2:OH+E[-]=OH[-]+H2O	A=3.0D10
Re3:OH+H=H2O	A=7.0D9
Re4:OH+HO2=O2+H2O	A=7.5D9
Re5:OH+O2[-]=O2+OH[-]	A=8.8D9
Re6:OH+H2O2=H2O+HO2	A=2.7D7
Re7:OH+H2=H+H2O	A=4.7D7
Re8:E[-]+E[-]=2*OH[-]+H2	A=5.5D9
Re9:E[-]+H=OH[-]+H2	A=2.5D10
Re10:E[-]+HO2=H2O2+OH[-]	A=1.3D10
Re11:E[-]+O2[-]=HO2[-]+OH[-]	A=1.3D10
Re12:E[-]+H2O2=OH+OH[-]+H2O	A=1.1D10
Re13:E[-]+H[+]=H+H2O	A=2.3D10
Re14:E[-]+H2O=H+OH[-]+H2O	A=1.03D2
Re15:E[-]+O2=O2[-]+H2O	A=1.9D10
Re16:H+H=H2	A=7.8D9
Re17:H+HO2=H2O2	A=2.0D10
Re18:H+O2[-]=HO2[-]	A=2.0D10
Re19:H+H2O2=OH+H2O	A=9.0D7
Re20:H+OH[-]=E[-]	A=2.2D7
Re21:H+O2=HO2	A=1.2D10
Re22:HO2+HO2=O2+H2O2	A=8.3D5
Re23:HO2+O2[-]=O2+HO2[-]	A=9.7D7
Re24:O2[-]+O2[-]=O2+O2[--]	A=5.0D3
Re25:HO2=O2[-]+H[+]	A=8.0D5
Re26:O2[-]+H[+]=HO2	A=5.0D10
Re27:H2O2+OH[-]=HO2[-]+H2O	A=5.0D8
Re28:HO2[-]+H2O=H2O2+OH[-]	A=5.73D4
Re30:H[+]+OH[-]=H2O	A=1.43D11
Re31:H2O=H[+]+OH[-]	A=2.599D-5
Re32:O2[--]+H2O=HO2[-]+OH[-]	A=5.0D5

Group 2

Re38:H2G=HG+HG	A=2D-10
Re39:HG+HG=H2G	A=4.0D7
Re40:HG+O2G=HO2G	A=4.5D8
Re41:HG+HO2G=OHG+OHG	A=6.5D10
Re42:HO2G+HO2G=H2O2+O2G	A=2.0D9
Re43:OHG+OHG=H2O2	A=4.0D9
Re44:HG+OHG=H2O	A=1.0D10
Re45:OHG+HO2G=H2O+O2G	A=6.0D10
Re46:OHG+H2G=H2O+HG	A=4.0D3

Group 3

Re47:H2=H2G	A=<5.15D-4
Re49:O2=O2G	A=<5.15D-4
Re54:H2O=VAP	A=<1.627D-8
Re55:CO2=CO2G	A=<5.15D-4

Group 4

Re58:Fe[++]+H2O2=Fe[+++]+OH[-]+OH	A=62
Re59:Fe[++]+H=Fe[+++]+H[-]	A=1.3D7
Re60:Fe[++]+OH=Fe[+++]+OH[-]	A=3.4D8
Re61:Fe[+++]+E[-]=Fe[++]+H2O	A=2D10
Re62:Fe[++]+O2=Fe[+++]+O2[-]	A=0.087
Re63:Fe[+++]+H=Fe[++]+H[+]	A=1D8
Re64:Fe[+++]+HO2=Fe[++]+O2+H[+]	A=1D3
Re65:Fe[+++]+O2[-]=Fe[++]+O2	A=4.0D8
Re67:Fe(OH)[++]+E[-]=Fe(OH)[+]+H2O	A=6D10
Re68:Fe(OH)2[+]+E[-]=Fe(OH)2+H2O	A=6D10
Re70:Fe[++]+OH=Fe(OH)[++]	A=4.5D8
Re72:Fe[++]+E[-]=Fe[+]+H2O	A=1.2D8
Re75:Fe[+++]+Fe[+]=2*Fe[++]	A=1D10
Re76:Fe[++]+OH[-]=Fe(OH)[+]	A=1D3
Re77:Fe(OH)[+]=Fe[++]+OH[-]	A=1.039D-1
Re78:Fe(OH)[+]+OH[-]=Fe(OH)2	A=1D4
Re79:Fe(OH)2=Fe(OH)[+]+OH[-]	A=2.265D1
Re84:Fe[+++]+OH[-]=Fe(OH)[++]	A=1D7
Re85:Fe(OH)[++]=Fe[+++]+OH[-]	A=9.224D-5
Re86:Fe(OH)[++]+OH[-]=Fe(OH)2[+]	A=1D8
Re87:Fe(OH)2[+]=Fe(OH)[++]+OH	A=9.928D-3
Re200:A[++]=Fe[++]	A=1.76D-9
Re201:Fe[++]+E[-]=Fe[+++]+OH[-]+H[-]	A=1.2D8

Group 5

Re92:OH+CO3[--]=CO3[-]+OH[-]	A=4D8
Re93:OH+HCO3[-]=CO3[-]+H2O	A=1.5D7
Re94:O2[-]+CO3[-]=CO3[--]+O2	A=3.2D8
Re95:H2O2+CO3[-]=CO3[--]+O2[-]+2*H[+]	A=4.3D5
Re96:HO2[-]+CO3[-]=CO3[--]+O2[-]+H[+]	A=3D7
Re97:O3[-]+CO3[-]=CO3[--]+O3	A=6D7
Re98:H[+]+HCO3[-]=CO2+H2O	A=1D10
Re99:OH[-]+HCO3[-]=CO3[--]+H2O	A=1D9
Re100:H2O+CO2=HCO3[-]+H[+]	A=70
Re101:H2O+CO3[--]=HCO3[-]+OH[-]	A=3.6D3
Re102:H2O+CO4[--]=HO2[-]+OH[-]+CO2	A=0.2
Re103:CO3[-]+CO3[-]=CO4[--]+CO2	A=7D6

Group 6

Re142:OH+Cl[-]=ClOH[-]	A=4.3D9
Re143:OH+HClO=ClO+H2O	A=9D9
Re144:OH+HClO2=ClO2+H2O	A=6.3D9
Re145:E[-]+Cl=Cl[-]+H2O	A=1D10
Re146:E[-]+Cl2[-]=2*Cl[-]+H2O	A=1D10
Re147:E[-]+ClOH[-]=Cl[-]+OH[-]+H2O	A=1D10
Re148:E[-]+HClO=ClOH[-]+H2O	A=5.3D10
Re149:E[-]+Cl2=Cl2[-]+H2O	A=1D10
Re150:E[-]+Cl3[-]=Cl2[-]+Cl[-]+H2O	A=1D10
Re151:E[-]+HClO3=ClO2+OH[-]+H2O	A=4D6
Re152:H+Cl=Cl[-]+H[+]	A=1D10
Re153:H+Cl2[-]=2*Cl[-]+H[+]	A=8D9
Re154:H+ClOH[-]=Cl[-]+H2O	A=1D10
Re155:H+Cl2=Cl2[-]+H[+]	A=7D9
Re156:H+HClO=ClOH[-]+H[+]	A=1D10
Re157:H+Cl3[-]=Cl2[-]+Cl[-]+H[+]	A=1D10
Re158:HO2+Cl2[-]=2*Cl[-]+O2+H[+]	A=4D9
Re159:HO2+Cl2=Cl2[-]+O2+H[+]	A=1D9
Re160:HO2+Cl3[-]=Cl2[-]+Cl[-]+O2+H[+]	A=1D9
Re161:O2[-]+Cl2[-]=2*Cl[-]+O2	A=1.2D10
Re162:O2[-]+HClO=ClOH[-]+O2	A=7.5D6
Re163:H2O2+Cl2[-]=2*Cl[-]+O2[-]+2*H[+]	A=1.4D5
Re164:H2O2+Cl2=HO2+Cl2[-]+H[+]	A=1.9D2
Re165:H2O2+HClO=Cl[-]+O2+H2O+H[+]	A=1.7D5
Re166:OH[-]+Cl2[-]=ClOH[-]+Cl[-]	A=7.3D6
Re167:OH[-]+Cl2=HCLO+Cl[-]	A=3.88D11
Re168:H[+]+ClOH[-]=Cl+H2O	A=2.1D10
Re169:H2O+Cl2O2=HCLO+HClO2	A=2D2
Re170:H2O+Cl2O2=O2+HCLO+Cl[-]+H[+]	A=1D2
Re171:H2O+Cl2O=2*HCLO	A=1D2
Re172:H2O+Cl2O4=HCLO2+HClO3	A=1D2
Re173:H2O+Cl2O4=2*O2+HClO+Cl[-]+H[+]	A=1D2
Re174:Cl[-]+Cl=Cl2[-]	A=2.1D2
Re175:Cl[-]+ClOH[-]=Cl2[-]+OH[-]	A=9D4
Re176:Cl[-]+HClO=Cl2+OH[-]	A=10
Re177:Cl[-]+Cl2=CLl[-]	A=1D4
Re178:ClOH[-]=OH+Cl[-]	A=6.1D9
Re179:Cl2[-]=Cl+Cl[-]	A=1.1D5
Re180:Cl2[-]+Cl2[-]=Cl3[-]+Cl[-]	A=7D9
Re181:Cl3[-]=Cl2+Cl[-]	A=5D4
Re182:ClO+ClO=Cl2O2	A=1.5D10
Re183:ClO2+ClO2=Cl2O4	A=1D2
Re184:Cl2O2+HClO2=HClO3+Cl2O	A=1D2

Group 7

Re209:Cl+Fe[++]=Fe[+++]+Cl[-]	A=1.05D10
Re210:ClOH[-]+Fe[++]=Fe[+++]+Cl[-]+OH[-]	A=1.0D8

Re211:Cl2[-]+Fe[++]=Fe[+++]+2*Cl[-]	A=1.0D7
Re212:Cl2+Fe[++]=Fe[+++]+Cl2[-]	A=80
Re213:HClO+Fe[++]=Fe[+++]+ClOH[-]	A=3.6D3
Re214:Cl3[-]+Fe[++]=Fe[+++]+Cl2[-]+Cl[-]	A=2.0D5

Group 8

Re193:Fe[++]+CO3[-]=Fe[+++]+CO3[--]	A=1D8